



**CLASSIFICATION OF BATTLESPACE DETONATIONS FROM
TEMPORALLY RESOLVED MULTI-BAND IMAGERY AND MID-INFRARED
SPECTRA**

DISSERTATION

Anthony N. Dills, Major, USAF

AFIT/DS/ENP/05-03

**DEPARTMENT OF THE AIR FORCE
AIR UNIVERSITY
AIR FORCE INSTITUTE OF TECHNOLOGY**

Wright-Patterson Air Force Base, Ohio

APPROVED FOR PUBLIC RELEASE; DISTRIBUTION UNLIMITED

The views expressed in this dissertation are those of the author and do not reflect the official policy or position of the United States Air Force, Department of Defense, or the United States Government.

AFIT/DS/ENP/05-03

CLASSIFICATION OF BATTLESPACE DETONATIONS FROM
TEMPORALLY RESOLVED MULTI-BAND IMAGERY AND MID-INFRARED
SPECTRA

DISSERTATION

Presented to the Faculty
Graduate School of Engineering and Management
Air Force Institute of Technology
Air University
Air Education and Training Command
in Partial Fulfillment of the Requirements for the
Degree of Doctor of Philosophy

Anthony N. Dills, BS, MS

Major, USAF

March 2005

APPROVED FOR PUBLIC RELEASE; DISTRIBUTION UNLIMITED

CLASSIFICATION OF BATTLESPACE DETONATIONS FROM
TEMPORALLY RESOLVED MULTI-BAND IMAGERY AND MID-INFRARED
SPECTRA

Anthony N. Dills, BS, MS
Major, USAF

Approved:

Date

Glen P. Perram (Chairman)

Jeffrey P. Kharoufeh (Dean's Representative)

James W. Engel (Member)

Steven C. Gustafson (Member)

Michael A. Marciniak (Member)

Ronald F. Tuttle (Member)

Accepted:

Robert A. Calico, Jr
Dean, Graduate School of Engineering and Management

Date

Abstract

The remote sensing and event classification of bright combustion or detonation sources requires enhanced understanding of fireball phenomenology, extensive collection of ground truth signatures, and the application of quantitative pattern recognition methodologies. Temporally resolved mid-infrared Fourier Transform spectra, near infrared imagery, and 3-band visible imagery has been collected remotely from ground based sensors and processed and analyzed for several conventional and enhanced high explosive materials. These sensors have been deployed in a series of five field tests to study and distinguish between (1) uncased trinitrotoluene (TNT) and enhanced novel explosive (ENE) materials at 10, 50, and 100 kg weights, and (2) two types of conventional weapons having three weights and detonated statically or aircraft delivered.

Detonation fireballs from cased munitions are largely Planckian in the mid-infrared with initial temperatures of 1200 – 1800 °K attenuated by atmospheric absorption. Temperatures often decay exponentially to ambient within 1 – 3 s for large charges of cased munitions and in less than 1 s for uncased or smaller weight charges. Occasionally, temperature profiles exhibit secondary maxima at 0.5 – 1 s after detonation. Non-Planckian spectra features, particularly in the 1950 – 2250 cm^{-1} band, are observed with 10% deviation from Planckian behavior for cased munitions and often greater than 50% deviation for uncased munitions. Fireballs from uncased explosives typically attain a maximum area in the near infrared of 100 – 200 m^2 at 20 – 200 ms after detonation. Fireball size depends on imaging frequency band, with smaller and shorter-

lived fireballs in the blue. The combination of decaying temperature and growing fireball size often produces irradiance profiles with secondary maxima at 0.25 – 0.5 s.

From the imagery currently studied, the single best feature for classification between uncased conventional (TNT) and ENE materials is the time to peak of the fireball size, t_{mp} , in the near infrared. For TNT $t_{mp} = 40 - 160$ ms and for ENE materials, $t_{mp} = 0 - 60$ ms. Feature saliency from Fisher discrimination techniques always yields t_{mp} as the most important feature, with duration of the fireball and symmetry of its area, as measured by the standard deviation in the median time and the skew in the residual of a parametric fit of the area, as secondary features. The single feature t_{mp} yields a Fisher ratio of $F = 2.9 \pm 0.3$ and 89% accuracy in robust testing of explosive type classification if the weight is known *a priori* (at 50 kg) and 87% and $F = 2.5 \pm 0.1$ if the weight is unknown. The single best feature from the 3-band visible imagery is the maximum area in the blue band, A_{mp} , of $10 - 60 \text{ m}^2$ for TNT and $40 - 280 \text{ m}^2$ for ENE. This feature provides 93% and 79% correct classification and $F = 5.4 \pm 0.2$ and 4.4 ± 0.1 for the 50 kg and unspecified weights, respectively. Combining the time to peak size in the near IR and maximum area in the blue does not significantly improve classification performance. For a five class problem of two types and three weights, combining these two features does improve the classification performance from 54% to 74% for either feature alone. The single best feature for the five class problem is the time integrated area in the blue band, but this feature is highly correlated with the corresponding peak area. In general, the fireball size derived from the image has more information about the type than the weight.

Probability density functions for each of these classification problems are estimated. The stability of the densities with respect to choice of training data sets and systematic variation among several field tests is characterized. For signatures from a single field test, the peak locations and widths of the density functions vary by about 0.5% and 14%, respectively. Combining signatures from two field tests increases these values to 1% and 17%.

The mid-infrared spectra from cased munitions can be reduced to a set of features that includes fireball temperature, area, and residuals to Planckian fits in selected spectral bands as a function of time. The residuals in the $1950 - 2250 \text{ cm}^{-1}$ band corresponding to hot CO_2 emissions are typically less than 10% and provide the best discrimination between explosive type, size, and method of detonation (static or aircraft delivered). Discrimination based only on the peak residual provides 100% accurate classification and $F = 14 \pm 1$ between static and dynamic detonation for one type and size of munition and 86% accuracy independent of type and size ($F = 11.0 \pm 1.0$). Equally impressive is the ability to distinguish between large and small weights for static detonations at 100% accuracy and $F = 99 \pm 32$ using the residual immediately after detonation. Uncased munitions exhibit highly non-Planckian behavior, offering strong classification potential for TNT and ENE materials.

Acknowledgments

I would like to express my sincere appreciation to my faculty advisor, Dr. Glen Perram, for his guidance and support throughout the course of this effort. He provides a tremendous amount of insight and experience. I would, also, like to thank the sponsors and the team players from various government agencies and corporations. Data acquisition goes much smoother with people like Sean Miller, Tom Fitzgerald and team, Paul Brooks, Mike Purcell and team, and J.P. Hagan and team. Likewise post-processing was extremely accelerated by the hard work and dedication by Adam Pugh, George Zimmer, Ben Johnson, and Andy Giebler. My sanity was kept in check by my AFIT friends Mike Hawks, Kevin Gross, Colin Tucker, Steve Cox, all the guys in my Monday morning running team, and the many friends from church like Jason, Jody, John, Tammy, Andy, Lisa, Todd, Melissa, Rob, Laura, Paul, Abby, and oh so many more. I also counted on the many words of encouragement from my parents and second parents.

My largest and most heart felt appreciation goes to the woman with whom God has blessed me to spend the rest of my life. She is the mother of our four wonderfully supportive children. She heroically ventured out and settled into a new home, in a new area of the country with very little help from me. She sacrificially and selflessly gave up her time and energy so that I could remain in Ohio for two and a half months to finish my dissertation research while she unpacked, started the kids in school, and dealt with home builders. Thank you!

Anthony N. Dills

Table of Contents

	Page
Abstract	iv
Acknowledgments.....	vii
List of Figures	xi
List of Tables	xxi
List of Symbols and Acronyms.....	xxiv
Definitions.....	xxv
I. Introduction.....	1
II. Background	6
A. Detonation of High Explosives	6
1. Energetic materials	6
2. Basic Phenomenology	8
B. Remote sensing of IR emission.....	12
1. Radiometric Quantities	12
C. Non-Ideal Explosives Blast theory	14
III. Experimental Approach	15
A. Recent Field Tests.....	15
B. Instrumentation	23
1. AFIT Bomem MR-154 FTIR instrument	23
2. 3-chip CCD camera images	32
3. Near-Infrared (NIR) imagery.....	34
IV. Developing Discrimination Tools using Image Data.....	37
A. Near-Infrared Imagery Field data	38

B.	Feature extraction.....	43
C.	Fisher discrimination, Feature saliency and stability measures of merit	45
	1. Two-class problem.....	46
	2. Class-conditional probability densities.....	49
	3. Validation with leave-one-out and determining feature saliency	53
	4. Stability of class-conditional probability densities.....	57
D.	Testing.....	62
	1. Testing with Brilliant Flash I data	62
	2. Bootstrapping with combined Brilliant Flash tests.....	65
E.	Applying discrimination tools to Cannon 3-chip color images	67
	1. Testing with Brilliant Flash I data	71
	2. Bootstrapping with combined Brilliant Flash tests.....	73
F.	Applying discrimination tools to combined NIR and 3-chip images	77
G.	Committee of classifiers for robust testing two-class discrimination.....	79
H.	Multiple-class discrimination.....	83
	1. Theory.....	85
	2. Data.....	87
	3. Scaling laws	87
	4. Results.....	91
I.	Committee of classifiers for robust testing five-class discrimination.....	101
J.	Conclusions to discrimination tools development and imagery analysis.....	105
V.	Fisher discrimination of Radiant explosives.....	107
A.	Radiant test series	108

B.	Basic spectral model description	112
C.	Feature extraction.....	118
D.	Scaling relationships of the extracted spectral features	120
E.	Committee of classifiers to discriminate Radiant events	121
F.	Conclusions to using spectra to discriminate munitions.....	124
VI.	Conclusions.....	126
A.	Impact of this research on classification.....	126
B.	Recommendations and opportunities	131
Appendix A:	NIR Fireball Areas for Brilliant Flash I	134
Appendix B:	Imagery Features from Brilliant Flash test series.....	135
Appendix C:	Brilliant Flash II Area Fits.....	145
Appendix D:	Brilliant Flash I IR Areas	154
Appendix E:	Brilliant Flash II 3-Chip Areas	163
Appendix F:	Brilliant Flash I 3-Chip Areas.....	173
Appendix G:	Scaling Laws, NIR features, BFI & BFII.....	183
Appendix H:	Scaling Laws, 3-Chip features, BFI & BFII	188
Appendix I:	Scaling Laws, Spectral Data, Radiant.....	198
Appendix J:	Spectral Features from Radiant test series.....	205
Appendix K:	Comparison plots of MR154 and MR354 InSb spectrometer data with radiometers for Brilliant Flash II events	209
Bibliography	247

List of Figures

Figure	Page
1. RDX (left) and TNT (right) are two commonly used explosive materials. [32:23]	7
2. The Planckian radiation law (dashed line) multiplied by the appropriate atmospheric transmission function fits (solid line) the source radiation (dots) by capturing temperature, area-emissivity, and wavenumber dependence. The temperature and area times emissivity of this Radiant 3B event (E298_10S) are $1648.87 \pm 0.06^\circ\text{K}$ and $1639.7 \pm 0.8 \text{ m}^2$, respectively.....	11
3. Visual Representation of Radiometric Quantities (assuming no atmospheric transmission effects).....	13
4. This graph displays the geometry of the Radiant IIIA and IIIB tests as explained in Jay Orson's thesis.[28]	20
5. The test layout geometry includes ground zero indicated by the star and the instruments located at Diddle Knoll, 3258 m to the southeast. The contour lines are spaced at 20 m terrain height increments.	22
6. Observed spectral intensity I_σ as a function of time t and wavenumber σ for Brilliant Flash II Event 05, a medium type C detonation. The FTIR temporal and spectral resolutions were 0.123 s and 4 cm^{-1}	26
7. Three records of emissions from the detonation of type C as collected by the InSb detector. Specific bands are indicated across the top and are defined explicitly in Table 9. The spectral resolution is 4 cm^{-1} . The Brilliant Flash II events shown here, from top to bottom, are 06, 05, and 10.	27
8. Comparison plots of AFIT MR154 InSb spectrometer data (dash-dot line) with the MR354 InSb spectrometer (dotted) and radiometers (close dots) for Brilliant Flash II event 31, Type A, 50 kg. Each spectrometer data is integrated over the bands, scaled to the height of the radiometer, and shifted in time if necessary to align with the radiometer. Figure (a) is from band I (4.45- 4.65 μm), figure (b) is from band II (3.88-3.99 μm), figure (c) is from band IV (2.7-3.1 μm), and figure (d) is from band V (2.15-2.3 μm)......	29
9. A second set of comparison plots of AFIT MR154 InSb spectrometer data (dash-dot line) with the MR354 InSb spectrometer (dotted) and radiometers (close dots) for Brilliant Flash II event 25, Type A, 50 kg. Each spectrometer data is integrated over the bands, scaled to the height of the radiometer, and shifted in time if necessary to align with the radiometer. Figure (a) is from	

band I (4.45-4.65 μm), figure (b) is from band II (3.88-3.99 μm), figure (c) is from band IV (2.7-3.1 μm), and figure (d) is from band V (2.15-2.3 μm).	30
10. Scaling factor for band IV using the MR154 InSb spectrometer data (\blacktriangle) and the MR354 InSb spectrometer data (Δ). The 33% lines are drawn as dotted lines with the included area shaded.....	32
11. Each of the RGB colors is extracted through post processing from the original RGB image recorded by the Cannon 3-chip CCD. The detonation recorded in the blue band is outlined in white.	33
12. The first four frames of an event are shown here for each primary color and the composite RGB image. The detonation recorded in the blue band is outlined in white.....	33
13. InGaAs camera images exhibit the relative sizes of the fireballs immediately after detonation. The images clearly show two intensity levels: one associated with the very bright fireball and the other associated with ground reflections. These images were collected during Brilliant Flash II and all represent 50-kg weights.	34
14. One representation of the range of pixel responsivity is the range of intensities I that a pixel will register for a given input source intensity. Both figures displays the number of pixels N at each registered intensity level I on a 12-bit scale. Fig. (a) represents the signal during an event frame. Its insert is a zoom of the 3550-4050 DN intensities. Fig. (b) shows the histogram for the background scene prior to detonation with 440-560 DN emphasized.	36
15. Relative NIR intensities of a 50-kg Type-C fireball as recorded by the Alpha Indigo camera: (a) pixels above 3000 DN, (b) pixels between 2400 and 3000 DN, (c) pixels below 2400 DN and above background illumination.....	36
16. (a) A single image at detonation time ($t=0$) and corresponding (b) temporal evolution of the histogram for each image. Each histogram is shown as a function of the number of pixels (N), the pixel intensity I in digital numbers (DN) along the abscissa ranging from one to 4096, and the detonation time ($-33 \text{ msec} \leq t \leq 400 \text{ msec}$). The line at $I=3000$ DN aids in calculating fireball size. The number of pixels N at the low intensities are cut off in this figure to aid clarity between the low and high intensity features. This histogram and corresponding image is from one 50-kg Type A explosive material detonated during Brilliant Flash II.....	39
17. Histogram for the number of InGaAs pixels N illuminated at various intensities I as a function of time t for: (a) Type A, (b) Type B, (c) Type C, (d) Type D, and (e) Type E 50-kg charges. The total number of pixels in the	

InGaAs array is 80,896 so that a pixel count of 1000 is about 1.2% of the detector array.....	40
18. Reducing the image data down to the temporal behavior of the fireball area provides one method of showing reproducibility within a class and distinguishability between the classes. Pattern recognition will further remove the similarities among the curves and find the best method of discrimination. The five types shown in this figure are 50-kg weights from the Brilliant Flash II test. Type A is TNT.	42
19. The extracted features from the fireball area A_{FB} curves include simple observations of the area curve (figure a) and calculated moments of a probability density P derived from the residuals R between the data and a quadratic fit f of the data (figure b). Pattern recognition techniques help prioritize which features are the most important in discriminating among the various types of explosives.	45
20. A scatter plot of Brilliant Flash II data represented by two features, t_{mp} and σ_{t_median} , shows individual class clusters (O = TNT, X = ENE) and an appropriate Fisher discrimination line (solid black line).	47
21. Class-conditional probability density functions, $p(x/c_i)$, (left ordinate, thick lines) and posterior probabilities, $P(c_i/x)$, (right ordinate, thin lines) for each class c_i (TNT dashed, ENE solid) are calculated along the Fisher line x using two features: t_{mp} and σ_{t_median} . The $p(x/c_i)$ are normalized such that the area under each curve is 1.0. The posterior probabilities represent the total probability that an event with a certain value along the Fisher line is in one of the two classes, thus at every point along the Fisher line the posteriors sum to one. For a Fisher line value $x = 1.5$, the probability the event is ENE is roughly 0.1, and that it is TNT is 0.9.	51
22. Figure (a) shows class-conditional likelihoods where the shaded areas represent the probability of a hit (red/light gray area) and the probability of false alarm (blue/dark gray area) as a function of decision threshold along x . The resulting receiver operating characteristic curve in figure (b) shows the ordinate as the probability of hit, $P(x \in R_{TNT} / x \in c_{TNT})$, and the abscissa as the probability of false alarm, $P(x \in R_{TNT} / x \in c_{ENE})$. This example is generated using the single feature t_{mp} and shows that the likelihoods cross at $x \sim 0.5$ and $x \ll -6$	52
23. Examining every feature combination from one feature to all ten feature combinations provides one quantitative method to determine how many features are necessary for classification. The "X" data points represent the N-feature combination with the highest Fisher ratio, F . The remaining dots represent all the other N-feature combinations. The 11 through 14 feature	

combinations are not shown because they did not satisfy the 100% correctly classified criteria.	55
24. Feature saliency is a product of leave-one-out and finding the best features with the highest Fisher ratio F (Fig. a) or area under the receiver operating characteristic (ROC) curve A_{ROC} (Fig. b). Once the single best feature is determined, it is fixed while finding the next best feature. The percent of iterations of the leave-one-out process that correctly classified the left-out event into one of the two possible classes is indicated, except for those that are 100%. The error bars represent the standard deviation of the mean F and mean A_{ROC} for each feature combination.	56
25. Similar to Figure 24, Feature saliency is a product of leave-one-out and finding the best features with the highest Fisher ratio F (Fig. a) or highest A_{ROC} (Fig. b), except this time features are eliminated down from 14 to 1. In this example, A_{mp} was the first feature to be eliminated.	56
26. Class-conditional probability density functions, $p(x/c_i)$, show the probability density of measuring a particular Fisher line value x given the event is in one of two classes, $c_1 = \text{ENE}$ (—) and $c_2 = \text{TNT}$ (- - -). This Fisher line is determined by maximizing the Fisher ratio using two features: t_{mp} and σ_{t_median} . The densities are normalized, thus the area under each curve is unity. The dots (·) are events used in training.	58
27. The mean standard deviation of (a) the peak centers, $\sigma_{centers}$, and (b) the peak values, σ_{peaks} , from each pair of individual $p(x/c_i)$ and from each leave-one-out iteration is a useful metric to quantify $p(x/c_i)$ stability as a function of number of features. The number of features N_f is indicated on the abscissa and the data points represent each combination of N-features. The "X" data points represent the N-feature combination with the highest Fisher ratio. Notice, as the number of features increase the stability decreases or σ 's increases.	59
28. Similar to Figure 27, the center (a, c) and peak (b, d) standard deviations of the <i>likelihoods</i> are calculated for each feature combination derived from the "best" features shown in Figure 24. The standard deviations are normalized by the separation between the class-conditional densities. The colors are described in Figure 24's caption.	60
29. Class-conditional probability density functions, $p(x/c_i)$ or <i>likelihoods</i> , for the three-feature set $\{t_{mp}, \sigma_{t_median}, t_{median}\}$ show the probability density of measuring a particular Fisher line value x given the event is in one of two classes, $c_1 = \text{ENE}$ and $c_2 = \text{TNT}$. This Fisher line is determined by maximizing the Fisher ratio using the three features. The density functions are normalized, and thus the area under each curve is 1.0. Figure (a) has each $p(x/c_i)$ from the leave-one-out process where the vertical lines are the "left-out" events	

projected onto x and colored according to the classification rules. Figure (b) contains the average $p(x/c_i)$ along with confidence intervals.....	61
30. Same as Figure 29 except the features set is a single feature: t_{mp}	61
31. Resulting feature saliency measured by the Fisher ratio when using all of Brilliant Flash II data for training and all of Brilliant Flash I for testing. The colors are described in the caption for Figure 24.	64
32. Class-conditional <i>likelihoods</i> $p(x/c_i)$ resulting from the feature sets $\{t_{mp}\}$ (Figs. a and b) and $\{t_{mp}, \sigma_{t_median}\}$ (Figs. c and d) using Brilliant Flash II data for training and Brilliant Flash I data for testing. Figures (a) and (c) contain the individual <i>likelihoods</i> generated during training and validation using leave-one-out. Figures (b) and (d) contain the average of the training <i>likelihoods</i> with confidence intervals. Solid =ENE; dashed = TNT.....	64
33. Class-conditional <i>likelihoods</i> $p(x/c_i)$ resulting from the feature set $\{t_{mp}\}$ using the first bootstrap data indicated in the first row of Table 12. Figure (a) contains the individual <i>likelihoods</i> generated during training and validation using leave-one-out. Figure (b) contains the average of the training <i>likelihoods</i> and the confidence intervals. Solid =ENE; dashed = TNT.	67
34. Class-conditional <i>likelihoods</i> $p(x/c_i)$ resulting from the feature set $\{t_{mp}, \mu_3\}$ using the first bootstrap data indicated in the first row of Table 12. Figure (a) contains the individual <i>likelihoods</i> generated during training and validation using leave-one-out. Figure (b) contains the average of the training <i>likelihoods</i> and the confidence intervals. Figure (c) displays the events features on a two dimensional scatter plot. Solid (X) = ENE; dashed (O) = TNT.....	68
35. A subjective evaluation of the five test cases' results using A_{ROC} suggests the best features shown in this figure. Using this set and order of features, each test case is evaluated and the resulting (a) Fisher ratio and (b) A_{ROC} are displayed here as a function of the feature set. Each feature set beyond t_{mp} alone has less than 22 out of the 26 events (<85%) classified correctly during the leave-one-out. Using only t_{mp} , 23 of the 26 events (88%) are classified correctly.....	69
36. The 3-chip color area plots shown here aid in feature extraction and provide an overview of their potential to distinguish TNT from the enhanced explosives detonated in the Brilliant Flash II. The two-class discrimination problem groups Types B through D into one class called ENE.....	70
37. The 3-chip color area plots shown here aid in feature extraction and provide an overview of their potential to distinguish TNT (Type A) from the enhanced explosives (Types C and D) detonated in the Brilliant Flash I series. Type B was not tested in Brilliant Flash I.....	71

38. The best features, ranked by their (a) A_{ROC} or (b) Fisher ratio F , are generated for the 3-chip images. Once a feature is determined as best, it is fixed before finding the next best feature. The data points represent the mean and standard deviation from the leave-one-out process.	72
39. The mean standard deviation of the peak (a) centers, $\sigma_{centers}$, and (b) the values, σ_{peaks} , from each pair of $p(x/c_i)$ and from each leave-one-out iteration quantifies $p(x/c_i)$ stability as a function of number of features.	73
40. Class-conditional <i>likelihoods</i> $p(x/c_i)$ resulting from the feature sets (a) $\{ A_{mp}(B) \}$ and (b) $\{ A_{mp}(B), t_{median}(R) \}$ using the Brilliant Flash II series as the training set. The left column contains the individual results from the leave-one-out; the right column is the average <i>likelihoods</i> and corresponding confidence intervals. The solid lines are ENE; the dashed lines are TNT.	74
41. A subjective evaluation of the five test cases' results using the 3-chip data suggests the best features shown in this figure. Using this set and order of features, each test case is evaluated and the resulting (a) Fisher ratio and (b) A_{ROC} are displayed here as a function of the feature set.	76
42. Class-conditional <i>likelihoods</i> $p(x/c_i)$ resulting from the feature sets (a) $\{ A_{mp}(B) \}$ and (b) $\{ A_{mp}(B), A(B) \}$ using the second bootstrap result in Table 14. Each density is a result from the leave-one-out.	76
43. The mean standard deviation of (a) the peak centers, $\sigma_{centers}$, and (b) the peak values, σ_{peaks} , from each pair of individual $p(x/c_i)$ and from each leave-one-out iteration quantifies $p(x/c_i)$ stability as a function of number of features.	77
44. (a) The range of possible class-conditional posteriors as a result of 997 tests and (b) the 997 class-conditional probability densities from robust testing for the feature t_{mp} which provides an 89% accurate prediction of events as either ENE or TNT when weight is known to be 50 kg. The Fisher ratio is 2.9 ± 0.3 for the average densities. The vertical lines represent locations along the Fisher line, x , for each test event. Solid = ENE; dashed = TNT.	82
45. (a) The range of possible class-conditional posteriors as a result of 997 tests and (b) the 997 class-conditional probability densities from robust testing for the feature t_{mp} which provides an 87% accurate prediction of events as either ENE or TNT when weight is unknown. The Fisher ratio is 2.5 ± 0.1 for the average class-conditional densities. The vertical lines represent locations along the Fisher line, x , for each test event. Solid = ENE; dashed = TNT.	82
46. (a) The range of possible class-conditional posteriors as a result of 997 tests and (b) the 997 class-conditional probability densities from robust testing for the feature $A_{mp}(B)$ which provides an 93% accurate prediction of events (ENE or TNT) when weight is known to be 50 kg. The Fisher ratio is 5.4 ± 0.2 for the	

average class-conditional densities. The vertical lines represent locations along the Fisher line, x , for each test event. Solid = ENE; dashed = TNT.	83
47. (a) The range of possible class-conditional posteriors as a result of 997 tests and (b) the 997 class-conditional probability densities from robust testing for the feature $A_{mp}(B)$ which provides an 79% accurate prediction of events (ENE or TNT) when weight is unknown. The Fisher ratio is 4.4 ± 0.1 for the average class-conditional densities. The vertical lines represent locations along the Fisher line, x , for each test event. Solid = ENE; dashed = TNT.	84
48. The extracted areas for each color, derived from Brilliant Flash I are shown here as a function of time: (a) ENE-50kg, (b) TNT-50kg. The NIR derived areas are the solid black lines; the RGB derived areas are dotted, dashed, and dash-dot, respectively.....	87
49. The extracted areas for each color, derived from Brilliant Flash II are shown here as a function of time: (a) ENE-50kg, (b) ENE-100kg. The NIR derived areas are the solid black lines; the RGB derived areas are dotted, dashed, and dash-dot, respectively.....	88
50. The extracted areas for each color, derived from Brilliant Flash II are shown here as a function of time: (a) TNT-10kg, (b) TNT-50kg, and (c) TNT-100kg. The NIR derived areas are the solid black lines; the RGB derived areas are dotted, dashed, and dash-dot, respectively.....	88
51. Four of the features extracted from the area curve derived from the NIR images possibly provide scaling law relationships. The data points and error bars are the mean and standard deviation of each feature for each weight and type (solid line for ENE, dashed line for TNT). The slopes of each line are indicated next to each line.....	92
52. The most probable time (a) and the integrated area over the detonation time (b) features extracted from the fireball area derived from the NIR images demonstrate scaling as a function of weight and type relationships. These representations help visualize the spread in the data and the uncertainty in the slopes (dotted lines). X=ENE; O=TNT.....	93
53. (a) Class-conditional posteriors and (b) class-conditional probability densities for the five classes with vertical lines drawn for each of the eleven test cases projected onto the single feature t_{mp} normalized to zero mean and unit variance. A solid (dotted) vertical line indicates a correct (incorrect) classification of the test event. The five types are ENE-50kg (thick dashed), ENE-100kg (thick solid), TNT-10kg (solid), TNT-50kg (dashed), and TNT-100kg (dotted).....	94
54. The class-conditional probability densities (lower halves) and posteriors (upper halves) are given for a few of the top features from each camera data set.	

- Figure (a) is the result from using the two features, t_{mp} and A_{mp} . Figures (b) and (c) show the results from using the 3-chip camera: (b) a single feature, $\sigma_{t_median}(R)$ and (c) two features, $\sigma_{t_median}(R)$ and $\sigma_{t_median}(G)$. Figure (d) shows the top three features as a result of combining the NIR and 3-chip camera data, $\{ t_{mp}, A_{mp}, c_3(B) \}$ 96
55. Stability of the class-conditional probability densities are quantified by the standard deviations of the density peaks (a, c, e) and centers (b, d, f) and is a function of the feature saliency defined by the test results. (a,b) utilize only NIR data, (c,d) use only 3-chip color data, and (e,f) combines the two sources. 97
56. Data projected onto the single feature, t_{mp} , best separates the five classes. The posteriors [$P(c_i/x)$ (dashed lines)] give a correct classification probability range between 30 to 100%. \blacktriangle =ENE-50kg, \blacklozenge =ENE-100kg, \bullet =TNT-10kg, \times =TNT-50kg, \blacksquare =TNT-100kg..... 99
57. Using the NIR only bootstrap results as a guide, one possible feature saliency shown in (a) is the t_{mp} , A , μ_2 , and c_1 . The Fisher ratios calculated here come from the leave-one-out using all the data. The 3-chip color results and the combined NIR and 3-chip color results are displayed in (b) and (c), respectively. The percent of the left out test events that are correctly classified labels each data point. Different training sets cause variation in t_{mp} values. 100
58. Using the 3-chip camera data (Figure a) and the combined NIR/3-chip data (Figure b), the class-conditional probability densities (lower halves) and posteriors (upper halves) are given for a (a) $t_{median}(R)$ and (b) feature set $\{ t_{mp}, t_{mp}(B) \}$. \blacktriangle =ENE-50kg, \blacklozenge =ENE-100kg, \bullet =TNT-10kg, \times =TNT-50kg, \blacksquare =TNT-100kg..... 101
59. Possible scaling laws for the Brilliant Flash types are represented by (a) the integrated near-infrared area over the detonation time A and (b) the median time $t_{median}(G)$ in the green color band. \times = ENE events; \circ = TNT events..... 102
60. (a) Class-conditional posteriors and (b) class-conditional probability densities with a Fisher ratio of 6.7 ± 0.5 for the five classes with vertical lines drawn for test cases projected onto the single feature t_{mp} normalized to zero mean and unit variance. A solid (dotted) vertical line indicates a correct (incorrect) classification of the test event. The five types are ENE-50kg (thick solid), ENE-100kg (thick dashed), TNT-10kg (thin), TNT-50kg (thin dashed), and TNT-100kg (thin dotted)..... 103
61. (a) Class-conditional posteriors and (b) class-conditional probability densities with a Fisher ratio of 4.6 ± 0.9 for the five classes with vertical lines (solid=correct, dashed=incorrect) drawn for test cases projected onto the single feature, $A_{mp}(B)$, normalized to zero mean and unit variance. The five types are

ENE-50kg (thick solid), ENE-100kg (thick dashed), TNT-10kg (thin), TNT-50kg (thin dashed), and TNT-100kg (thin dotted).....	104
62. (a) Class-conditional posteriors and (b) class-conditional probability densities with a Fisher ratio of 11 ± 1 for the five classes with vertical lines (solid=correct, dashed=incorrect) drawn for test cases projected onto the two- feature set $\{ t_{mp}, A_{mp}(B) \}$ normalized to zero mean and unit variance. The five types are ENE-50kg (thick solid), ENE-100kg (thick dashed), TNT-10kg (thin), TNT-50kg (thin dashed), and TNT-100kg (thin dotted).	104
63. Spectral comparisons of various classes of munitions show that (a) uncased explosives contain strong emissions and absorption regions not characteristic of graybody emission and (b) the cased ordnances look much like a graybody attenuated by the atmosphere.	107
64. Typical Radiant spectral data is observed intensity I_{obs} as a function of frequency σ (cm^{-1}) and time t . The data shown here is downsampled to simplify the view.....	110
65. Radiant spectra from two time steps exhibits Planckian radiation law characteristics for when the atmospheric transmission is accounted.	110
66. Temporal profiles of two types of emissions from Radiant test. Figure (a) shows an emission with a single exponential decay behavior, while Figure (b) exhibits a triple exponential decay.....	111
67. Atmospheric correction involves systematically adjusting atmospheric absorption species' concentrations to match the absorption features seen in the data.	113
68. Spectral residuals between the data and the Planckian fit for a Radiant event show a growth in the $1950\text{-}2250\text{ cm}^{-1}$ region. The two residuals shown here are calculated at detonation time, t_0 and three time steps later $3\delta t = 0.147\text{s}$	113
69. Radiant area-emissivity products A as a function of time t , as derived from the Planckian fits.	115
70. Radiant temperatures T as a function of time t , as derived from the Planckian fits.....	116
71. Radiant integrated residuals ΔI ($1950\text{-}2250\text{cm}^{-1}$) divided by the atmospheric transmission function τ as a function of time t , as derived from the Planckian fits.....	117

72. Planckian fit parameters for Radiant events of type B, medium weight, and dynamically dropped. Figures (a), (b), and (c) are the area-emissivity, temperature, and residual properties, respectively.	118
73. These fits to example area data show that Eq.(45) models the range of possible $A(t)$ behavior.	120
74. Five features extracted from the spectra that exhibit classification potential are (a) the low temperature fit parameter T_L , (b) the time constant $A_{-}t_0$ controlling the turn-on for the linear portion of $A(t)$, (c) the most probable or peak value and (d) the initial value of the integrated residual divided by the transmission profile of the atmosphere ($\Delta I_{mp}/\tau$ and $\Delta I_0/\tau$), and (e) the their ratio $R_{mp/0}$. X = static events. O = dynamic events. 10, 50, 100 kg represent A(S), B(M), and B(L), respectively.	122
75. Class-conditional probabilities (right column) and resulting range of posteriors (left column) with test data identified as vertical stems illustrates class separation and reason for high accuracies in placing a new event into the right class. Figures (a) and (b) are for the feature ΔI_{mp} which yielded a 86% accuracy of 998 test cases ($F = 11.0 \pm 1.0$) in determining if an event is static or dynamic, independently of weight. Figures (c) and (d) show the results of using ΔI_0 to distinguish large and small static events with 100% accuracy for 11 test cases ($F = 99 \pm 32$).	124

List of Tables

Table	Page
1. Experimental values of heats of detonation for pure explosive compounds. [32:132]	8
2. Molar concentrations, heat capacities, and coefficients to Eq(5) for the products of TNT detonation. []	10
3. Radiation Quantities and Units	13
4. Known data collections dates, locations, and types of events.	15
5. Data Collection Metrics. For each collection event, the types of data readily available are marked by "y", while the other types of data collected but need to be obtained by AFIT is identified with an "x".	16
6. Instrument specifications overview.	17
7. Signal response factors from using layers mesh screens.	25
8. Definition of spectral bands of interest.	27
9. Scaling factors f_{scale} used to equate the peak intensities in specific spectral bands from the MR354 and MR154 (AFIT) InSb spectrometers to the radiometers.	31
10. Record of test results where Brilliant Flash II data is the training data and Brilliant Flash I is the testing data. FR is the Fisher ratio. A_{ROC} is the area under the receiver operating characteristic curve. σ is the standard deviation.	63
11. Selecting a random set of five events from two test series, Brilliant Flash I and Brilliant Flash II, as the test set and using the remaining events for training and validation yields the following results in the percent of the test set that was classified correctly (last column) based upon a feature set sorted by the best area under the receiver operating characteristic curve (A_{ROC}). t_{mp} is consistently the "best" feature derived from the forward-back routine. FR is the Fisher ratio. σ is the standard deviation.	66
12. Record of Cannon 3-chip data test results where Brilliant Flash II data is the training data and Brilliant Flash I is the testing data. Feature saliency is found by ranking with the Fisher ratio (FR). A_{ROC} is the area under the receiver	

operating characteristic curve. σ is the standard deviation. The RGB is in parentheses.	72
13. Record of Cannon 3-chip data bootstrapping test results where Brilliant Flash I and II data are combined and a random set of five events are chosen to be test data. The best features are sorted by their Fisher ratio. FR is the Fisher ratio. A_{ROC} is the area under the receiver operating characteristic curve. σ is the standard deviation.	75
14. Record of combined NIR and Cannon 3-chip data test results for (1) Brilliant Flash II training and Brilliant Flash I testing and (2) combined Brilliant Flash I and II data with a random set of five events chosen to be test data. The best features are sorted by their Fisher ratio. FR is the Fisher ratio. A_{ROC} is the area under the receiver operating characteristic curve. σ is the standard deviation. The RGB is in parentheses. No RGB letters signifies a NIR feature.	78
15. Percentages of the 50-kg events that are correctly classified using a selected set of feature(s). The diagonal values represent single feature discrimination and the off-diagonal values represent two-feature discrimination between types.	80
16. Percentages of the 100-kg events that are correctly classified using a selected set of feature(s). The diagonal values represent single feature discrimination and the off-diagonal values represent two-feature discrimination between types.	81
17. Percentages of the weight independent events that are correctly classified using a selected set of feature(s). The diagonal values represent single feature discrimination and the off-diagonal values represent two-feature discrimination between types.	81
18. Record of 5-class IR data test results where Brilliant Flash II data is the training data and Brilliant Flash I is the testing data. Feature saliency is found by ranking with the Fisher ratio (FR). σ is the standard deviation. The RGB is in parentheses. No RGB letters signifies a NIR feature.	93
19. Record of 5-class data bootstrapping test results where Brilliant Flash I and II data are combined and a random set of five events are chosen to be test data. The best features are sorted by their Fisher ratio. FR is the Fisher ratio. σ is the standard deviation. The RGB is in parentheses. No RGB letters signifies a NIR feature.	98
20. The percent of events that are correctly classified when using an average of the class-conditional probability densities are presented for the five-class discrimination problem. The values along the diagonal are the percentage of correct classifications when only one feature is used to classify the five types.	

The off-diagonal elements are the percentages of correct classification when two features are utilized.	103
21. Type A Small (InSb, 16 cm ⁻¹) event list.	109
22. Type B Large (InSb, 16 cm ⁻¹) event list.	109
23. Type B Medium (InSb, 16 cm ⁻¹) event list.	109
24. Features and their descriptions used for discriminating spectral data.	121
25. Prediction accuracies based upon the feature used. The results in the solid box refer to the ability to distinguish static and dynamic events if Type A(S). The dashed box contains the prediction accuracy to distinguish static and dynamic events independent of weight or type. The dotted box addresses the ability to distinguish small and large static events.	123

List of Symbols and Acronyms

Symbol	Definition
NIR	near-infrared
3-chip	Cannon XL1 Video camera that records light onto three CCDs, one for each RGB color
RGB	Red (R), Green (G), Blue (B)
TNT	trinitrotoluene, $\text{CH}_3\text{C}_6\text{H}_2(\text{NO}_2)_3$
ENE	enhanced novel explosive
DN	digital number
I	intensity
$I(\sigma)$	spectral intensity
PDF	probability density function
$p(x c_i)$	class-conditional probability density of an event having a line value of x given it is in the class c_i
$P(c_i/x)$	class-conditional posterior density of an event belonging to class c_i given it has a line value x
<u>x</u>	underlined symbols denote vectors
<u><u>X</u></u>	double underlined symbols denotes matrices
F	Fisher ratio
A_{ROC}	area under the receiver operating characteristic (ROC)
<u>A</u>	fireball area integrated over the detonation time; directly proportional to the time average of the fireball size
t_{median}	median time where the integrated area is equal before and after this time
σ_{t_median}	standard deviation of the median time
t_{mp}	time to peak or most probable time
A_{median}	fireball area value at the median time
σ_{A_median}	standard deviation of the A_{median}
A_{mp}	peak or most probable amplitude of the fireball area
c_1	fit coefficient in $c_1t^2 + c_2t + c_3$ to the fireball area
c_2	fit coefficient in $c_1t^2 + c_2t + c_3$ to the fireball area
c_3	fit coefficient in $c_1t^2 + c_2t + c_3$ to the fireball area
μ_1	first moment of a probability density function
μ_2	second moment of a probability density function
μ_3	third moment of a probability density function
μ_4	fourth moment of a probability density function

Definitions

1. *weight* – the amount in kg of explosive material, *e.g.* 50 kg
2. *type* – the explosive material name, *e.g.* TNT, Type A, enhanced
3. *class* – a description of the group of events that are similar, *e.g.* all Type A 50 kg events are a single class
4. *data* – light emissions collected using a field instrument, *e.g.* an image from the InGaAs NIR camera or a spectrum from a spectrometer. The *dimensionality* of the data is dependent on space, time, and frequency as well as class, manufacturing practices, detonation conditions, environmental effects, etc.
5. *feature* – a descriptor that characterizes an aspect of event data. A *key feature* is one whose values are very similar for events in the same class but very different for events in different classes. Features can be based upon observed parameters of the data or fit parameters of a model of the data. *Feature saliency* is the ranking of features that best discriminate. *Feature dimensionality* refers to the number of features used to represent the data.
6. *pattern recognition* – a technique of taking in data and performing an action based upon the patterns found in the data. Specifically, pattern recognition uses the features extracted from the data and quantifies the ability to classify events based upon their class.
7. *cross validation and testing* – a pattern recognition technique of training a model to classify based upon a subset of data, the *training data*, with the remaining data reserved for *testing* the final classification model. Within the training data, another

subset is set aside to *validate* the training process, often with a *leave-one-out* procedure.

8. *bootstrapping* – a testing technique useful when the data is limited. This technique creates a testing data set by randomly selecting n number of N events, leaving the remaining $N-n$ events for training. Repeated bootstrapping aids in quantifying repeatable results, *e.g.* a model which quantifies classification within acceptable uncertainties.
9. *Fisher linear discrimination* – one of many pattern recognition techniques that are used to quantify class clusters (or groupings). A Fisher line is a vector in a d -dimensional feature space that maximizes the differences in the class means and minimizes the class variances along a line upon which the feature values are perpendicularly projected.
10. *committee of classifiers* – Many times a single feature or a combination of features do not adequately classify the data, *e.g.* classifying both weight and type of explosive. One approach is to use discrimination techniques to determine one set of classes before identifying subsequent classes. For example, a committee of classifiers could use one set of features to determine an event's weight (*e.g.* 50 kg) then another set of features to determine an event's type, *e.g.* Type A. This combined approach allows the committee to ascertain the final class of the event, *e.g.* Type A 50 kg.
11. *stability* – Stability is a measure of self consistency. (a) Feature saliency (see #5 above) is stable if the ranked order of features is repeatable between different approaches. (b) After the training process in pattern recognition, a key result is a set of class-conditional probability densities. A second use of stability measures the

consistency of these densities as a function of the training set used. The two metrics of density stability used in this research are the standard deviations of the locations and heights of the density peaks.

CLASSIFICATION OF BATTLESPACE DETONATIONS FROM TEMPORALLY RESOLVED MULTI-BAND IMAGERY AND MID-INFRARED SPECTRA

I. Introduction

Commercial applications routinely leverage remote sensing technologies to monitor nearly static environments and phenomena that change very slowly over time. For example, NASA's Landsat 7 satellite acquires images of earth land and coastal regions [1]. Many industries and research organizations apply various pattern recognition techniques to these images to identify crop and soil conditions [2], study forest ecology [3], and monitor earth climatology [4][5] and volcanology [6][7]. Similarly, the French space agency, Centre National d'Etudes Spatiales (CNES) uses its satellite system SPOT (Satellite Pour l'Observation de la Terre) for earth surveillance [8][9].

Remote sensing is also used to identify and characterize transient events occurring on the earth. Although less common in commercial applications, some examples include monitoring forest fires [10][11] and Kuwait oil fires [12][13]. The U.S. military is highly interested in detecting and classifying not only transient events, such as missile launches [14][15] and naval operations [16][17], but also fast transient events like gun muzzle flashes [18][19] and high-explosive detonations [20]. Fast-transient events occur on the order of milliseconds to a few seconds, and present significantly more complex remote sensing requirements than nearly static and transient phenomena occurring on the order of minutes to days.

Current remote sensors provide the ability to locate fast transient events and, in some cases, classify the event into known categories such as conventional or nuclear explosion [21][22]. Detecting and classifying such events requires either a well-defined model or a set of attributes, characteristics, or features to facilitate discrimination between viable alternative categories. Surprisingly, no such information for detonation fireballs is available. Indeed fundamental attributes such as fireball temperature, size, and duration are poorly understood and not documented in the peer reviewed scientific literature.

A modeling approach to classifying fast transient events relies on the underlying physics and chemistry principles to estimate key signatures such as fireball emission spectra or non-optical measurements such as overpressure. Classifying a fast-transient event might consist of adjusting the parameters of such a model until its signatures match those of the observed event. While explosion phenomenology codes, such as CHEETAH [23], estimate the thermochemistry of a detonation, there are no corresponding non-proprietary models for fireball emission spectra in the open literature. Furthermore, many dimensional computer models do not effectively extract key features from observed data. No approximate analytic models exist as are required for data analysis, dimensionality reduction, and feature extraction. Previous modeling work has been accomplished by the High Explosives Research and Development (HERD) Facility at Eglin AFB, Los Alamos National Laboratories (LANL), and Lawrence Livermore National Laboratories (LLNL), Sandia National Laboratories (SNL), Riverside Research Institute (RRI), SciTec Inc., and National Ground Intelligence Center (NGIC). However, without citations or references, their contributions are not available to the open public.

Furthermore, the respective capabilities are fragmented and do not provide a basis for reliable classification.

Much has been done in condensed phase and shock [24][25][26] and in gun muzzle flash [27], yet the only open source describing fireballs from detonations has been work on characterizing bomb spectra [28]. There is no open documentation of basic attributes of fireball phenomenology, accurate and verified ground truth signatures, or a quantitative multivariate statistical methodology to demonstrate repeatable classification of explosives based upon their image and spectral characteristics. One would expect to find in the literature simple descriptions of fireballs to include spectral shape and temporal behavior, typical temperature profiles, size descriptions, and temporal evolution phenomena. All of these descriptors could depend greatly on a vast amount of *a priori* situations, i.e., explosive type and weight, munitions casing, detonation dynamics, and environmental conditions such as atmospheric transmission, dust, wind, etc. All of these variables drive the need for accurate ground truth data that has been verified with multiple instruments and approaches. These instruments should, at a minimum, provide radiometrically calibrated infrared spectra and imagery. Likewise, sufficient data must be collected to demonstrate repeatability and distinguishability among explosive types and weights.

A pattern recognition approach uses multivariate statistical techniques to classify fast-transient events based on comparing their key signatures to well-developed data sets. For conventional explosions, high-quality spectra and image data from ground-truth remote sensors is available for only a few type and weight classes, with typically less than two or three events per class. Such data is prerequisite to developing a robust ability

to classify various explosive materials, weight, or delivery mechanisms based on their signature features.

Through a series of field tests beginning in the early 1990's, the United States Air Force investigated the possibility of classifying type, weight, and delivery methods of bomb explosions using remotely collected infrared spectral signatures [28][29][30][31]. Yet these tests did not adequately address repeatability. Thus additional data is needed to establish a basis for understanding fireball phenomenology from extracted spectral and image features that are reproducible for similar events and distinguishable for dissimilar events. Pattern recognition techniques can quantify classification using key features and can guide further understanding of fireball physics and chemistry phenomenology.

The approach taken in this research to address these needs includes four phases: (1) acquire new field data with new instrumentation and sufficient replications per event type to adequately establish reproducibility, (2) develop, simultaneously, simple phenomenological models to extract features from the data that show reproducibility and distinguishability, (3) apply standard pattern recognition techniques to quantify classification potential based upon a subset of features, and (4) identify a final set of key features that most accurately perform event classification using various *a priori* information.

The present work addresses the following: (1) assess the feasibility and requirements for classification of battlefield detonations using temporally resolved emission multi-band imagery and moderate resolution spectra, (2) apply appropriate quantitative classification methodologies and tools using class-conditional probability densities, (3) demonstrate successful discrimination between conventional and enhanced

explosives, and (4) establish key phenomenology requirements for further exploitation of remote imagery and spectra.

Two new field tests have been performed, generating highly calibrated spectral and imagery data. A basic characterization of fireballs is developed, including temporal evolution of temperature and size. The relative value of various extracted features for the classification of event type is established. A method for discriminating between a conventional high-explosive material and an enhanced novel explosive is demonstrated. Finally, the potential for classification of battlespace detonations is addressed, and an approach to systematically exploiting this potential is developed.

II. Background

A. Detonation of High Explosives

1. *Energetic materials*

Energetic or explosive materials react to produce energy through a process called oxidation. During oxidation, excess internal energy stored in an energetic material (compound) is released as it burns (or explodes) with oxygen to form products with lower internal energies. Assuming a constant pressure, which is clearly not valid during an explosion reaction, the difference in these internal energies (ΔU) creates a difference in enthalpy ($\Delta H = \Delta U + P \Delta V$) which is called the heat of reaction. For explosions, it is called the heat of detonation and includes only the combustion of the explosive reactants, not the heat associated with the secondary afterburn. This value is maximum when there is just enough oxidizer to burn the fuel to create products in their most oxidized state. Thus the lowest internal energy state is the highest oxidation state. Typical components of explosives are carbon, hydrogen, nitrogen, and oxygen, thus expressed as $C_xH_yN_zO_w$. The highest oxidation states of carbon, hydrogen, and nitrogen are carbon dioxide (CO_2), water (H_2O), and nitrogen molecules (N_2) which incidentally have lower energy levels than NO , NO_2 , ... N_xO_y . [32:19-20]

Two prominent explosive materials used in industry as well as for the current tests are RDX (used in Composition C-4) and trinitrotoluene (TNT) (See Figure 1). Both of these are underoxidized, meaning that during a burn there is not enough oxygen to fully burn all the fuel. TNT is considered very underoxidized. According to Cooper, the rules of thumb for assessing the products of a detonation reaction are as follows: [32:131]

1. All nitrogen goes to N_2 .
2. All the hydrogen burns with available oxygen to form H_2O .
3. Any oxygen left after step (2) burns carbon to CO .
4. Any oxygen left after step (3) burns CO to CO_2 .
5. Any excess oxygen forms O_2 .
6. Any excess carbon forms $C(\text{smoke})$.

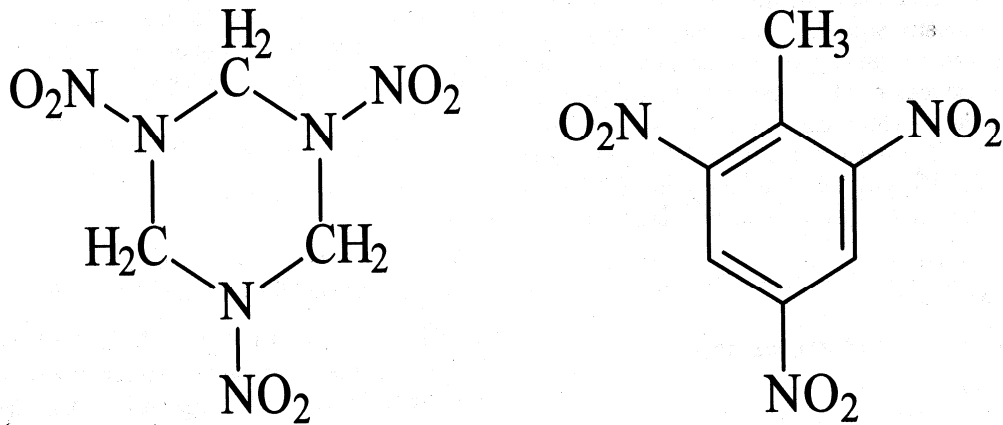
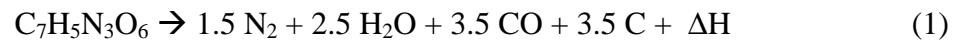
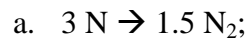


Figure 1. RDX (left) and TNT (right) are two commonly used explosive materials. [32:23]

For example, in TNT the oxidation reaction is as follows:



where possible stoichiometry include



- b. $5 \text{ H} + 2.5 \text{ O} \rightarrow 2.5 \text{ H}_2\text{O}$ (3.5 O remaining);
- c. $7 \text{ C} + 3.5 \text{ O} \rightarrow 3.5 \text{ CO}$ (all the O is used up) + 3.5 C; and
- d. 3.5 C can create black smoke if not remixed in air.

Thus an underoxidized fuel never reaches all the burning steps above unless it is detonated in air which provides enough oxygen for a secondary burn of the hot free carbons and carbon monoxide molecules. This secondary reaction, called a secondary fireball or afterburn (AB), releases additional energy for a total change in enthalpy called the heat of combustion ΔH_c :

$$\Delta H_{AB} = \Delta H_c - \Delta H_d \quad (2)$$

Cooper says that these secondary fireballs can be further fueled by casings, glues, binders, and colorants that have been mixed with the explosive. This fact should be kept in mind because some of the materials used in the novel explosives (explained later) cause a significant increase in the secondary fireball size and energy output. [32:24]

2. Basic Phenomenology

As mentioned earlier, the heat of detonation ΔH is the heat (or energy) generated during the reaction and is transferred to the energy of the products of the reaction. A few experimental values of ΔH for some common explosive materials are given in Table 1.

Table 1. Experimental values of heats of detonation for pure explosive compounds. [32:132]

Explosive	ΔH (kcal/mol)
PETN	471.1
RDX	335.4
TNT	247.5

Assuming the heat capacity at constant pressure C_p is temperature invariant and that the detonation products do not dissociate, one can use ΔH for TNT to estimate the detonation temperature to be 3725°K using the relationship

$$\Delta H = C_p \Delta T \quad (3)$$

where $\Delta T = T_{\text{detonation}} - T_{\text{reactant}}$ and the heat capacity is the sum of heat capacities for each product $C_{p,i}$,

$$C_p = \sum_{i=1}^{N_{\text{products}}} n_i C_{p,i} . \quad (4)$$

where n_i is the number of moles for the product species shown in Table 2. This final temperature is unrealistically large. Allowing for the temperature dependence of the heat capacities,

$$C_{p,i}(T) = a + bT + cT^2 + dT^3 + eT^{-2}, \quad (5)$$

where the coefficients a through e are defined in Table 2, the heat of detonation becomes an integral

$$\Delta H = \int_{T_{\text{reactants}}}^{T_{\text{detonation}}} C_{p,i}(T) dT \quad (6)$$

which matches the Table 1 value of 247.5 kcal/mol at a detonation temperature of 2994°K. Including dissociation effects would further reduce the temperature estimate to acceptable values less than 2994°K.

As the explosive material burns, releasing the energy ΔH into the products, a shock wave inside the explosive material is formed. As this detonation shock reaches the perimeter of the explosive material, it interacts with the surrounding medium, *e.g.* air, and creates an outward moving shock in the transport medium. Most of the books such as Cooper [32], Klingenberg [33], and Zel'dovich [34] concentrate on understanding and parameterizing the detonation shock and the air shock; however, no known sources exist that adequately address the spectra of afterburning fireball dynamics. The current research introduces two simple descriptions of the fireball dynamics.

Table 2. Molar concentrations, heat capacities, and coefficients to Eq(5) for the products of TNT detonation. [35]

Product	n_i	$C_p(298^\circ\text{K})$ (cal/mol*K)	a	b	c	d	e	T_{range} (K)
CO	3.5	6.967	6.110801	1.457011	0.969086	-0.63846	0.031315	298-1300
CO			8.401219	0.31073	-0.049216	0.003239	-0.784603	1300-6000
N ₂	1.5	6.961	6.236138	1.964341	-0.472309	0.038067	0.01062	298-6000
H ₂ O	2.5	8.025	7.192161	1.633011	1.62367	-0.60576	0.019632	500-1700
H ₂ O			10.0297	2.06072	0.358456	0.023451	-2.66674	1700-6000
C	3.5	4.9771	5.060971	-0.194175	0.107203	-0.01034	-0.003132	298-6000

The photons emitted from the fireball afterburn are frequency and time dependent. A simple model of the fireball assumes it is hot (on the order of several 1000°K), optically thick, and selectively radiates. A blackbody obeys the Planckian radiation law for blackbody source radiance L_{BB} or intensity I_{BB} ,

$$L_{BB}(\sigma, T(t)) = \frac{I_{BB}(\sigma, T(t))}{A\epsilon(t)} = \frac{2hc^2\sigma^3}{\exp(hc\sigma/k_B T(t)) - 1} \quad (7)$$

which depends upon the frequency σ (in cm^{-1}) and time t . Both the temperature $T(t)$ and fireball area times emissivity $A\epsilon(t)$ are functions of time for a radiatively growing, decaying, and cooling fireball. The other constants include the Planck's constant h , the speed of light c , and the Boltzmann constant k_B .

As illustrated in Figure 2, spectral data collected at a remote position, resembles a Planckian attenuated by the atmosphere with the function $\tau_{atm}(\sigma)$,

$$L_{obs}(\sigma, T(t)) = \tau_{atm}(\sigma) L_{BB}(\sigma, T(t)). \quad (8)$$

The government standard atmospheric model is **MOD**erate spectral resolution atmospheric **TRAN**smittance algorithm and computer model (MODTRAN), developed by AFRL/VSBT in collaboration with Spectral Sciences, Inc.[36] MODTRAN estimates are inadequate in describing the atmosphere with the fidelity needed to model the data. Thus the atmospheric transmission function exploits a non-linear regression approach that adjusts MODTRAN estimates of individual concentrations of the primary atmospheric absorbers, *e.g.* H_2O , N_2 , CH_4 , CO_2 which are identified in the figure below [37].

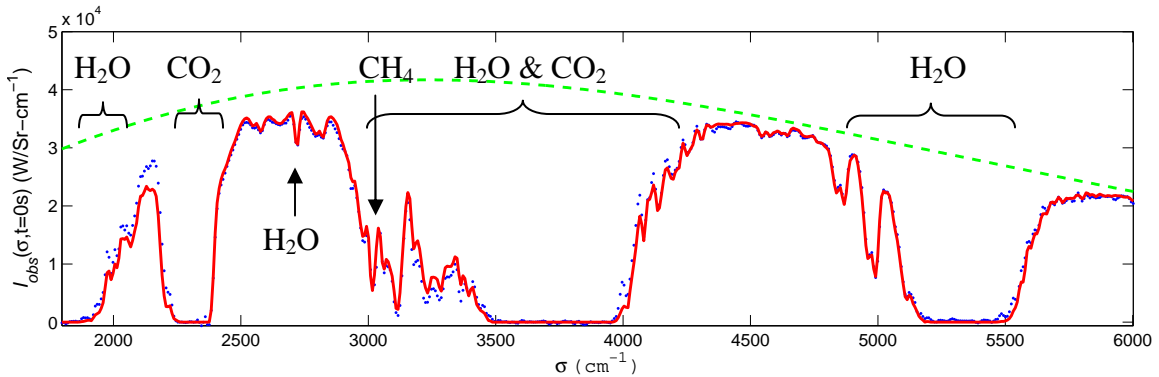


Figure 2. The Planckian radiation law (dashed line) multiplied by the appropriate atmospheric transmission function fits (solid line) the source radiation (dots). The temperature and area-emissivity of this Radiant 3B event (E298_10S) are $1648.87 \pm 0.06^\circ\text{K}$ and $1639.7 \pm 0.8 \text{ m}^2$, respectively.

With proper treatment of atmospheric absorption properties, the temperature, area, and emissivity derived from the blackbody model adequately represents most of the fireball information recorded in the spectra. Later it will be shown that the atmospheric correction is important especially if the extracted features originate from non-Planckian portions of the modeled data. Additional information about the fireball exists in the difference of the blackbody fit and the spectral data. For this reason, the analysis of spectral data presented in Chapter 5 uses solely the blackbody model. As long as the source data resembles a blackbody, then the fit parameters aid future work in phenomenology development and aid in the current work in relevant feature extraction.

B. Remote sensing of IR emission

The remote sensing of infrared signatures from bomb detonations, missile launches, and muzzle flashes provides unique data to characterize the battlespace. In particular, the spectral and temporal signatures from explosive ordnance may be used to classify the munitions type, size, and other key characteristics. Both ground-based and space-based remote sensing capabilities exist. LANSAT is a good example of a space-based remote sensing platform which collects scanning infrared imagery in eight spectral bands of the earth terrain [1]. Ground-based systems are endless. The United States Air Force Institute of Technology's (AFIT) system is a ground-based system which deploys at a safe distance and collects non-imaging Fourier Transform Infrared (FTIR) spectrum and near-infrared and visible imagery.

1. Radiometric Quantities

The amount of photons incident on a detector is dependent upon a number of standard radiometric properties: radiant flux density leaving the detonation event (M),

transmission properties along the optical path (τ_{atm}), the range z to and size of the collecting optic A_{source} , the relative orientation of the detector (*e.g.*, normal incidence), and detectivity of the detector material. All of these properties except the atmospheric effects and detector detectivity are captured in standard radiometric quantities as defined by Boyd and repeated in Table 3 below and visually represented in Figure 3. [38:14]

Table 3. Radiation Quantities and Units				
Quantity	Symbol	Units	Equation	Defining Equation
Radiant flux density at the detector (Irradiance)	E	Watt/cm ²	1	$E = \frac{d\Phi}{dA}$ $E = \frac{L \cdot A_{source}}{z^2}$ $E = \frac{I \cdot \cos(\theta)}{z^2}$
Radiant intensity at the source	I	Watt/sr	2	$I = \frac{d\Phi}{d\Omega}$
Radiance at the source	L	Watt/cm ² sr	3	$L = \left(\frac{dI}{dA} \right) * \cos(\theta)$
Spectral Radiance	$L(\sigma, t)$	Watt/ (cm ² sr cm ⁻¹)	N/A	

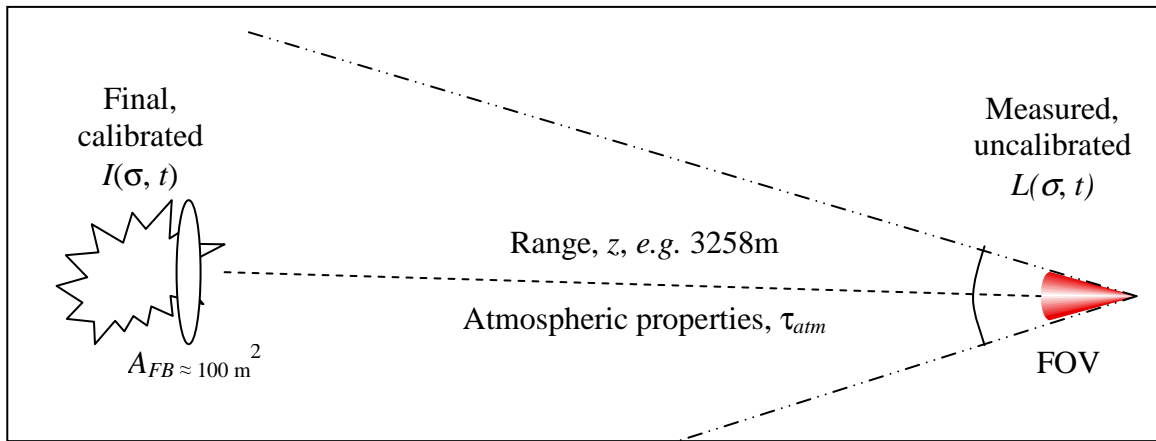


Figure 3. Visual Representation of Radiometric Quantities (assuming no atmospheric transmission effects).

C. Non-Ideal Explosives Blast theory

Non-ideal explosives mean a variety of things depending on the community. In this research effort, non-ideal refers to those high explosives fueled by ammonium nitrate, aluminum, and a variety of other non-traditional fuel additives [39]. The result of aluminum alone creates a brighter secondary flash and more intense shock front caused by an increase in the product (Al_2O_3) temperature and decrease in particle density [40]. Adding the non-traditional fuels intensify these effects as well. The community now calls the secondary flash or re-mixing stage as the thermobaric part. Thus, one will often find these explosives called thermobarics or thermobaric explosives, yet no open literature on the IR and visible emissions exist.

III. Experimental Approach

This section begins with a summary of the collected data sets from several test series, followed by a description of the instrumentation deployed by AFIT. During the discussion, data quality for the Brilliant Flash test is examined since it is the source of data collected as part of this research effort.

A. Recent Field Tests

The following tables identify the different collection tests, their basic descriptions, the types of instrument data available for analysis, and a general description of each type of instrument. Following these tables is a brief description of each collection.

Table 4. Known data collections dates, locations, and types of events.

Collection Name	Dates	Location	Types of Events	Additional Information
Radiant IIB	June 1998	Fallon NV	53 of 67 statically detonated ordnances	
Radiant IIIA	August 1999	Fallon NV	42 air dropped ordnances, 100 to 600 lbs of explosives	varied with angle between collector observation and bomb impact vector
Radiant IIIB	October 1999	Fallon NV	23 static with 3 types and 3 weights	tested repeatability
Iron Rose	June 2002	Fallon NV	58 M1/A1 tank muzzle flashes	
Brilliant Flash I	June 2002	Tyndall AFB FL	51 static, explosive material only, 2 novel mixes and TNT, 3 weights	Collected as part of this research effort

Collection Name	Dates	Location	Types of Events	Additional Information
Brilliant Flash II	June 2003	Utah Test and Training Range (UTTR)	44 static, explosive material only, 3 novel mixtures and TNT, 4 weights	Collected as part of this research effort
Chinook	September 2002	Undisclosed	16 Fuel Air Explosives (FAE)	
Northern Lights	October 2002	Undisclosed	24 volumetric explosives: FAE and Thermobaric Explosives (TBX)	

Table 5. Data Collection Metrics. For each collection event, the types of data readily available are marked by "y", while the other types of data collected but need to be obtained by AFIT is identified with an "x".

Collection Name	FTIR (MR154)	FTIR (MR354)	Radio-meter(1)	Radio-meter(2)	NIR FPA	Visible CCD	Visible Spec.	IRIS256 Imager
Radiant IIB	y		x	x				
Radiant IIIA	y		x	x				
Radiant IIIB	y		x	x				
Iron Rose		x	x	x				
Brilliant Flash I	y	x	x	x	y	y		
Brilliant Flash II	y	y	y	x	y	y	y	x
Chinook Winds Trials		x	x					x
Northern Lights Trials		x	x					x

Table 6. Instrument specifications overview.

Instrument	Spectral Range (cm⁻¹)	Spectral Resolution (cm⁻¹)	Temporal Resolution	Additional Information
FTIR MR154 (Team A/AFIT)	500-6000	1, 2, 4, 8, 16, 32	~3.6 spectra/sec (at 16 cm ⁻¹ resolution)	
FTIR MR354 (Team B)	500-6000	1, 2, 4, 8, 16, 32	~82 spectra/sec (at 16 cm ⁻¹ resolution)	
Radiometer(1) (Team B)	2153-2245 2509-2581 3226-3704 4348-4650	whole band	200 Hz	4 radiometers
Radiometer(2) NIR FPA	Not Available 0.9-1.7 μm	Not Available whole band	Not Available 30 Hz	12-bit dynamic range [41]
Visible CCD	Red Green Blue	whole band	30 Hz	3 CCDs [42]
Visible Spec	385-550 nm 470-530 nm 565-910 nm 570-800 nm 570-882 nm 655-880 nm	0.4 nm	100 Hz	0.25-m grating; 1024-element photodiode [43]
IRRIS 256 Imager (Team B)	Thermal IR (3.6-4.1 μm and 4.5-5.1 μm)	whole band	40 Hz	256x256

AFIT first participated in spectroscopic collections of munitions in the third of five test series called Radiant, sponsored by the Navy TENCAP and conducted at the Naval Air Station, (NAS) Fallon, NV from the summer of 1998 to the fall of 1999 [30]. Radiant IIB was the third test in the series [28]. The following descriptions are paraphrased from Jay Orson's thesis, *Collection Of Detonation Signatures And*

Characterization Of Spectral Features [28], Robert Houser's thesis, *Survey of Military Applications for Fourier Transform Infrared (FTIR) Spectroscopy* [44], and Science Applications International Corporation's (SAIC) Test Report. [45]

Radiant IIB was a static recreation of the previous Radiant IIA test. Calibrated radiometric and optical signatures from 53 of 67 events were collected and further assessed that the many discrepancies discovered in the previous test relate to bomb delivery angle, ground penetration depth, aircraft release manner, look angle of bomb to observers line of sight, and ground surface interaction. Two different ground truth teams deployed four radiometer suites with similar spectral filters.

Radiant IIIA test consisted of 42 air-dropped explosion events over a period of three days in summer of 1999. The primary test objective was to collect munitions signatures deployed in normal operational configurations against ground targets. This was accomplished by altering the angle between collector observation and bomb impact vector. The distance to the target from the observation tower was 4825 m. Each day the scheduled events varied by aircraft heading, amount of explosive and explosive type. Ordnance weights were extra small (< 100 lbs), small (100-400 lbs), medium (400 to 600 lbs), and large (> 600 lbs) of explosive.

Radiant IIIB consisted of 23 statically detonated events over the course of two nights in fall of 1999. Three different explosive types and three different explosive amounts were used during this test. The ordnance was situated on solid ground and propped up on wooden tripods at a 45 degree elevation angle tail high. Each bomb face was pointed toward the instrumentation. The larger bombs were placed in clay craters tail high at the largest elevations possible.

A portion of Radiant IIIA and IIIB data is further analyzed in the later portion of this research. A full description of the event types, the data collection methods, and the data quality are presented in Orson's thesis [28]. Nevertheless, a few items are repeated here and later in this document to identify which portions of the data are being used. First of all, the two ordnance types are examined, called Type A and Type B in this work. Type A events are of a "small" weight and nine are dynamically dropped from a military aircraft while another nine are placed on the ground as explained above. Type B events consist of two weights, "medium" and "large:" six large are dynamically dropped, two large are statically detonated on the ground, and three medium are dynamically dropped. The field test layout is shown in Figure 4.

Iron Rose consisted of 58 rounds of M1 and A1 tank muzzle flash collected one day in June 2002 at Fallon for the purpose of establishing reproducibility. The radiometer data is reported as acceptable. The spectrometer data is in question because its field of view was overfilled. Data from an IR imager is available. [46]

The purpose of the Brilliant Flash test series is to identify methods of explosive material discrimination using remote sensors. As the principle investigator, the author lead an AFIT team (team A) along side a second team (team B) to collect signatures from these two test series using Bomem made FTIRs and various other infrared and visible instruments. Brilliant Flash I test consisted of 51 static explosive-material-only events during the summer of 2002 at Tyndall AFB Florida [47]. The detonations consisted of uncased explosive materials that were assembled with readily available components. The center of mass of the explosive materials was placed approximately one meter above

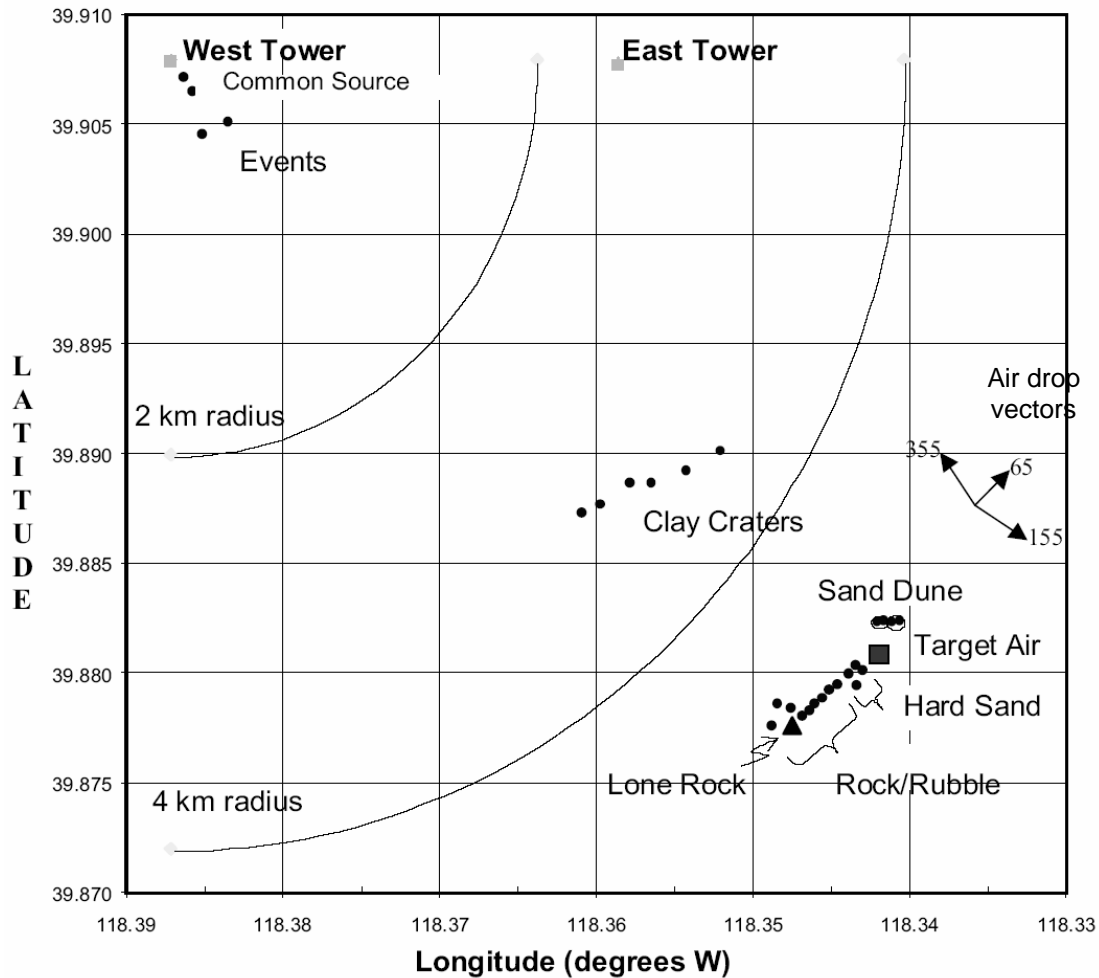


Figure 4. This graph displays the geometry of the Radiant IIIA and IIIB tests as explained in Jay Orson's thesis.[28]

ground. The types of explosive materials used were trinitrotoluene ($\text{CH}_3\text{C}_6\text{H}_2(\text{NO}_2)_3$) [48] (TNT or Type A) and two other enhanced mixtures (Types C and D) which varied in aluminum and other additives concentrations. The weights ranged from 1 to 100 pounds. Each type of explosive material at a specific weight was detonated three times. The range from the observation point to ground zero was 460 meters.

Brilliant Flash II test consisted of 44 static explosive-material-only events that were detonated at the Utah Test and Training Range (UTTR) over the period 2-13 June 2003 [49]. Again, the author led an AFIT team to obtain multi-band imagery and mid-infrared spectra. This test range is located at approximately 85 miles east of Salt Lake City, Utah. As depicted in Figure 5, the ground truth instruments were located on Diddle Knoll at 40°54.5300'N, 113°09.2767'W, and 1424 meters above sea level (using World Geodetic System 1984, WGS-84, model of the earth [50]). Ground zero was 3258 meters away at 40°55.5817'N, 113°11.1350'W and 1291 meters above sea level. The soil was dry, dusty dessert and the weather was usually clear with only a few exceptions toward the end of the test. The materials used in this test are the same as in Brilliant Flash I with the addition of two other enhanced mixtures (Types B and E). Each type of explosive material at a specific weight was detonated four times. The weights ranged from 10 to 1000 kilograms (22 to 2200 pounds).

Each of these Brilliant Flash tests required approximately six man months of effort to prepare, execute, and initially report on the test. Preparation included analysis software development, instrumentation testing and validation, and end-to-end dry-runs with all deployable equipment and personnel. The execution was approximately two and a half weeks and included coordination with explosive ordnance disposal (EOD) personnel, other instrumentation teams, and range safety. Calibrations were performed between every test shot to minimize errors in calculating absolute intensity. Likewise, cross-sensor comparisons were frequently conducted between two spectrometers and four radiometers. Finally, an initial analysis of data quality and of data interpretation is summarized with a “first look” report for the sponsoring agency.

The Chinook Winds Trials test collected performance data on various gear and equipment deployed in extreme overpressure environments. This collection was over a two week period from 3 to 13 September 2002. The team B was invited to observe and collect data. Sixteen fuel air explosives (FAE) devices were tested in the two-week period including thirteen 66-liter mixes, two 30-gallon mixes, and one much larger mix. The test team collected radiometric, spectrometric, imager, digital video and digital still photographic data from all but the first event [46].

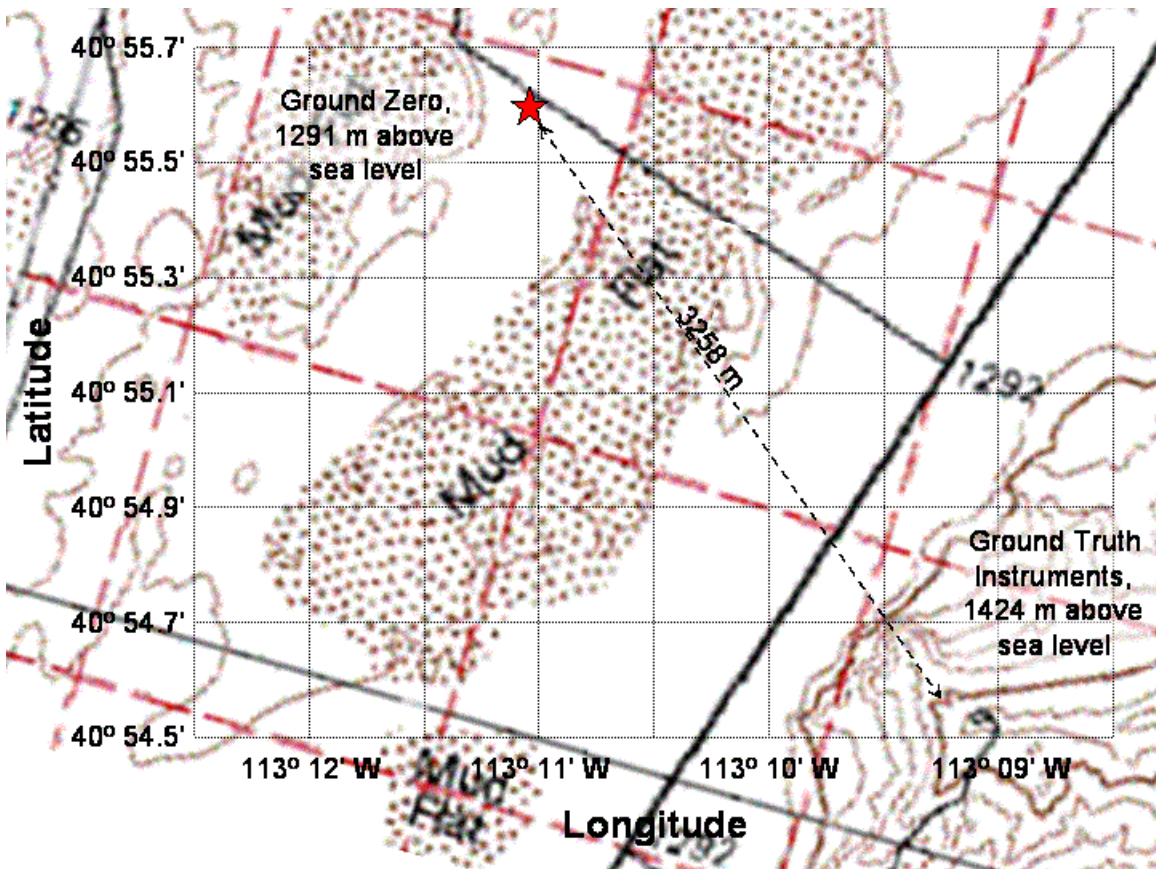


Figure 5. The test layout geometry includes ground zero indicated by the star and the instruments located at Diddle Knoll, 3258 m to the southeast. The contour lines are spaced at 20 m terrain height increments.

The Northern Lights Trials test collected performance and signature data on volumetric explosives. Twenty four volumetric explosives of various designs and sizes were also detonated over a two week period from 23 September through 4 October 2002. Unambiguous, well-calibrated spectro-radiometric data as well as test article, test layout, and meteorological data were collected throughout the test. [46]

B. Instrumentation

1. AFIT Bomem MR-154 FTIR instrument

A Bomem MR-154 Fourier Transform Infrared Spectrometer coupled to either a 75, 28, or 4.9 mrad field of view (FOV) telescope is used to record the infrared emission from fast transient events. The FTIR data is typically figured to investigate higher spectral resolution (4 cm^{-1}) at the expense of less temporal resolution (0.123 s). Two detectors, InSb and HgCdTe, covering the $1800 - 6000\text{ cm}^{-1}$ and $500 - 6000\text{ cm}^{-1}$ ranges, respectively, are used to simultaneously record interferograms from an event. Typical event signals are 15-20 times the background. The interferometer is temperature controlled at 45°C to minimize the effects of ambient temperature changes. A cold reference source is maintained at 77 K. The InSb detector typically provides a background noise signal of 5 to 50 W/Sr/cm^{-1} , about 5 times less than the HgCdTe detector. Background spectra were recorded before each event and typically exhibited a peak of 100 W/Sr/cm^{-1} at about 2000 cm^{-1} . The event intensity peaks ranged from 250 to $10000\text{ W/Sr/cm}^{-1}$.

The calibration procedure for the Bomem MR-154 FTIR instrument is exhaustively documented in the Bomem literature and several previous AFIT theses. A short explanation is given here. Calibration allows the conversion from recorded voltage

from the detectors to an absolute radiance. Three blackbodies are typically used to provide a 3-point temperature calibration. The voltage response is linearly fitted to the three calculated Planckian blackbody emission spectrum. The result is a linear response between a measured voltage and the absolute radiance, each as a function of wavenumber (frequency). The corresponding expression is

$$L^{Calibrated}(\sigma) = L_{Meas}(\sigma)K^{-1}(\sigma) - S(\sigma) \quad (9)$$

where

$L^{Calibrated}$ is the absolute spectral radiance signal ($\text{W cm}^{-2} \text{ Sr}^{-1}$),

L_{Meas} is the measured spectral voltage signal,

K is a spectral fitting term that accounts for geometry parameters (range, size of target, and field of view) and atmospheric transmission, and

S is the system stray spectral radiance.

Typically, one performs the calibration measurements with similar geometry and system settings as the event measurements. Since the range to the detonations in Brilliant Flash is too large for measuring a 1000 K blackbody for calibration, several actions are taken to compensate. The calibrations to obtain K and S values for this test are based upon a close range (50 feet) and are applied to each event creating a radiance value ($L^{Calibrated}$) appropriate for 50 feet. This radiance is then rescaled into spectral intensity $I(\sigma)$ (W/Sr/cm^{-1}) using the correct range to the event and removing the blackbody area. The scaling factor is

$$f_C = \pi \cdot r_{BB}^2 \cdot \frac{z_{event}^2}{z_{BB}^2} \quad (10)$$

where the factor, f_C , is the area of the blackbody used in the calibration, πr_{BB}^2 , multiplied by the squared ratio of the event range, z_{event} , divided by the blackbody range, z_{BB} .

Detector gain settings and layers of mesh screens are used to control the amount of photons hitting the detector to avoid saturation. The mesh screens are made of ~0.1 mm wire, spaced in ~1 mm square grids. The gain settings are in the approximate ratios of A:B:C=1:2:4. A gain setting of "B" will increase the voltage response of the detector by a factor of 2. When the event signal is intense enough to cause saturation, the gain settings are set to A and various layers of mesh screens are used as appropriate to reduce the throughput of the signal. The mesh screens are placed directly in front of the detector. The voltage responses of the meshes are measured in the field and compared to the voltage when no mesh is used. The resulting ratios are recorded in Table 7 and serve as a guide to the factor of voltage drop due to the number of mesh layers used. For example, a factor of 4 means this mesh setting reduces the incident light recorded in volts by a factor of 4. This one step in the calibration procedure may be the largest source of calibration error. For this reason, future test collections should utilize neutral density filters with known spectral responses.

Table 7. Signal response factors from using layers mesh screens.

# of Screens	MCT	InSb
2	4	
3	8	9
6		32

Calibration accuracy is evaluated by estimating the middle temperature using only the upper and lower temperatures for calibration. The calibration temperatures were 900°C, 950°C, and 1000°C. A 5% error in the calibration means the predicted middle temperature was 5% off of 950°C or $\pm 48^\circ\text{C}$. A 0.5% error equates to a 4.8°C error.

Figure 6 shows example data collected by the Bomem FTIR instrument (InSb detector) during the Brilliant Flash I test [31]. The spectra for a single time step immediately following the detonation of three similar charges are provided in Figure 7. The spectral intensity values

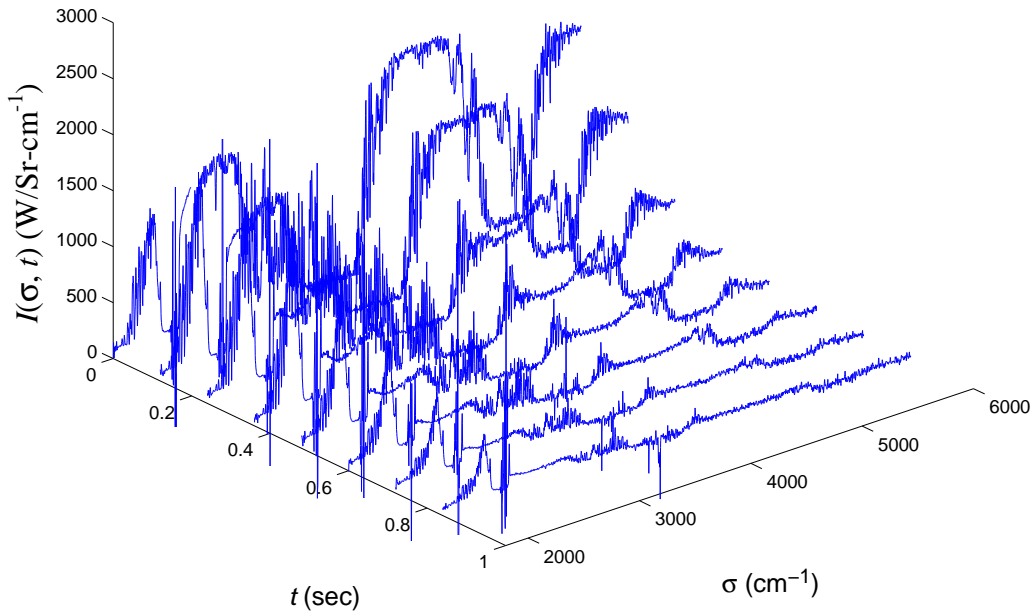


Figure 6. Observed spectral intensity I_σ as a function of time t and wavenumber σ for Brilliant Flash II Event 05, a medium type C detonation. The FTIR temporal and spectral resolutions were 0.123 s and 4 cm^{-1} .

range from approximately $1000\text{ W/Sr}\cdot\text{cm}^{-1}$ to $3000\text{ W/Sr}\cdot\text{cm}^{-1}$ with very similar spectral response. Atmospheric effects seem to be consistent across the wavenumber range and help govern the bands of interest as defined in Table 8.

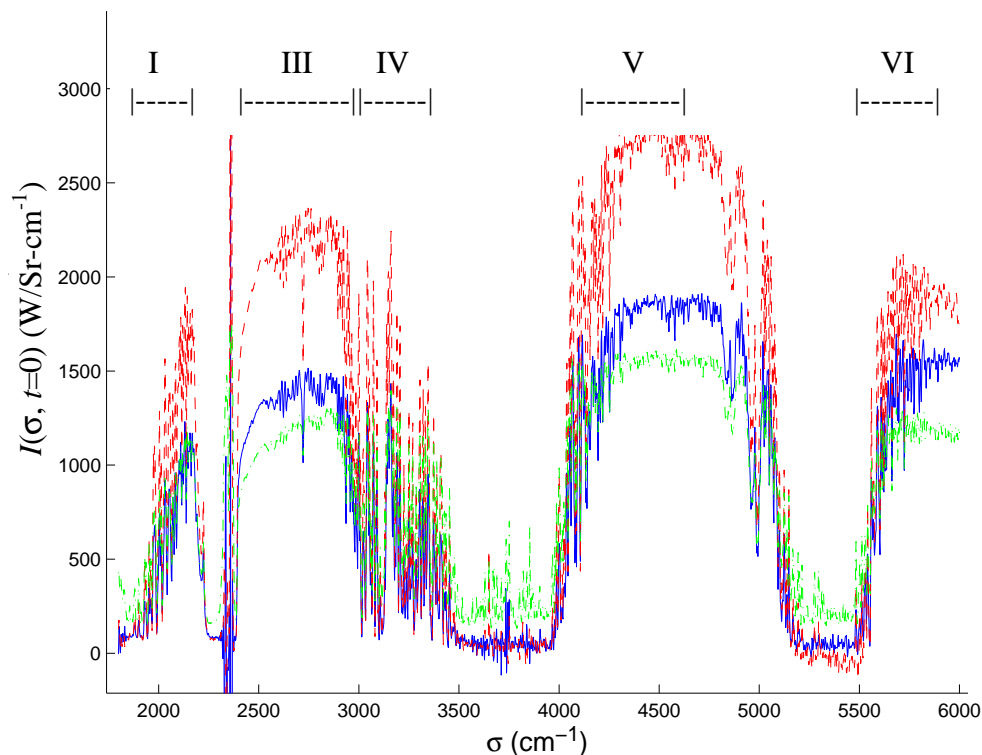


Figure 7. Three records of emissions from the detonation of type C as collected by the InSb detector. Specific bands are indicated across the top and are defined explicitly in Table 8. The spectral resolution is 4 cm^{-1} . The Brilliant Flash II events shown here, from top to bottom, are 06, 05, and 10.

Table 8. Definition of spectral bands of interest.

<i>Band</i>	σ_{start} (cm^{-1})	σ_{stop} (cm^{-1})	λ_{start} (μm)	λ_{stop} (μm)
I	2153	2245	4.455	4.645
II	2509	2581	3.875	3.985
III	2450	2800	3.57	4.08
IV	3226	3704	2.7	3.1
V	4348	4650	2.15	2.3
VI	5700	6000	1.67	1.75

A concentrated effort is made to validate the MR154 FTIR instrument data with another FTIR instrument (Team B's MR354) and a set of radiometers for the same collections. To compare the spectrometer data to the radiometer, the spectral intensity

from the spectrometers is integrated over the four radiometer bands. The radiometer bands are bands I, II, IV, and IV defined in Table 8. The radiometers are not down-sampled because the sampling rate of each of the spectrometers is sufficient to match the peak intensities. The scaling factors f_{scale} , defined in Eq. (11) below, that are required to match the peak intensities of the spectrometers to the radiometer data is given in Table 9 for each explosion event. Figure 8 shows one example of this type of comparison while Appendix K contains all the comparisons.

$$f_{Scale} = \frac{Peak_{spectrometer}}{Peak_{radiometer}} \quad (11)$$

Table 9 highlights with boxes those data that have poor temporal comparisons, *e.g.* Figure 9, and it highlights with dark background those data with very large (small) scale factors. In general, the fits overlay well, even with the large standard deviation in the scaling factors as shown in the table. The bottom row of the table shows the number of events that are within 33% of the radiometers. During Brilliant Flash II, the AFIT FTIR instrument agreed with the other FTIR and radiometers to within 33 percent in Band IV as shown in Figure 10.

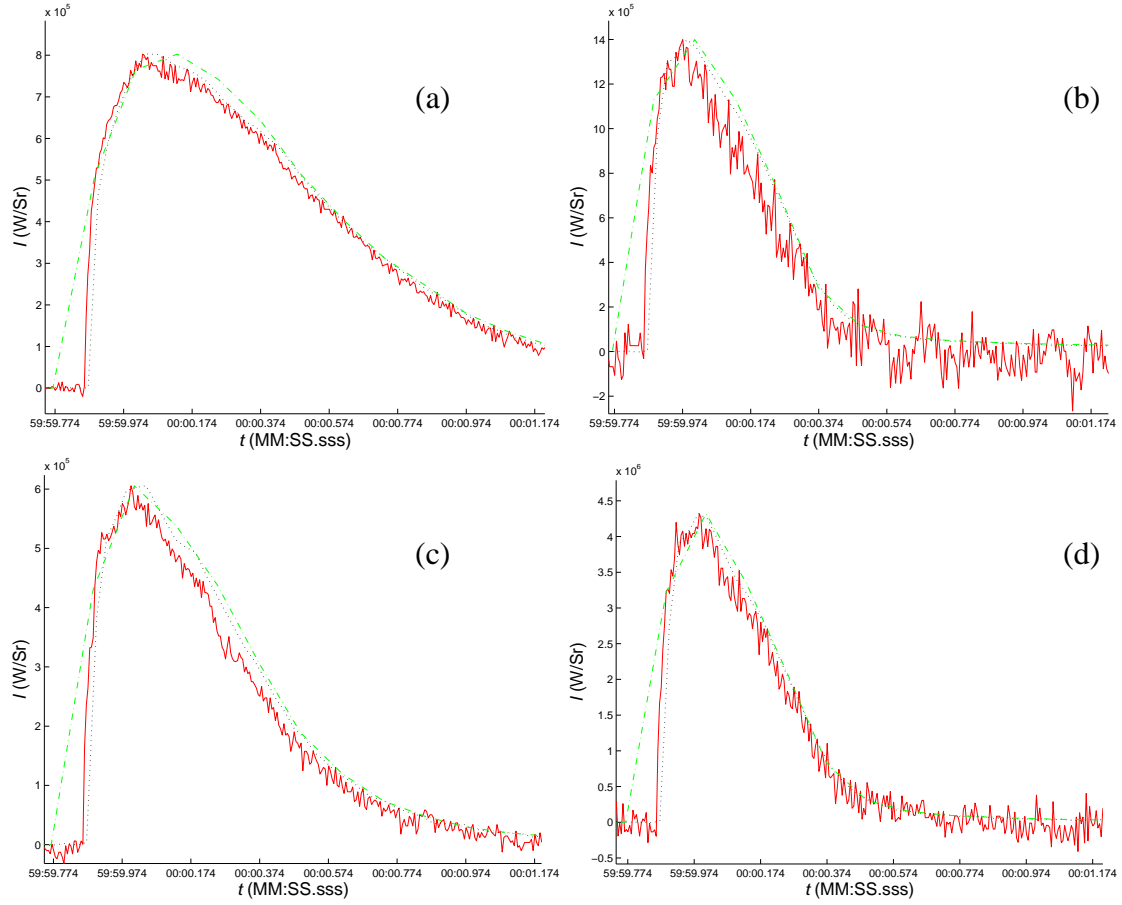


Figure 8. Comparison plots of AFIT MR154 InSb spectrometer data (dash-dot line) with the MR354 InSb spectrometer (dotted) and radiometers (close dots) for Brilliant Flash II event 31, Type A, 50 kg. Each spectrometer data is integrated over the bands, scaled to the height of the radiometer, and shifted in time if necessary to align with the radiometer. Figure (a) is from band I (4.45-4.65 μm), figure (b) is from band II (3.88-3.99 μm), figure (c) is from band IV (2.7-3.1 μm), and figure (d) is from band V (2.15-2.3 μm).

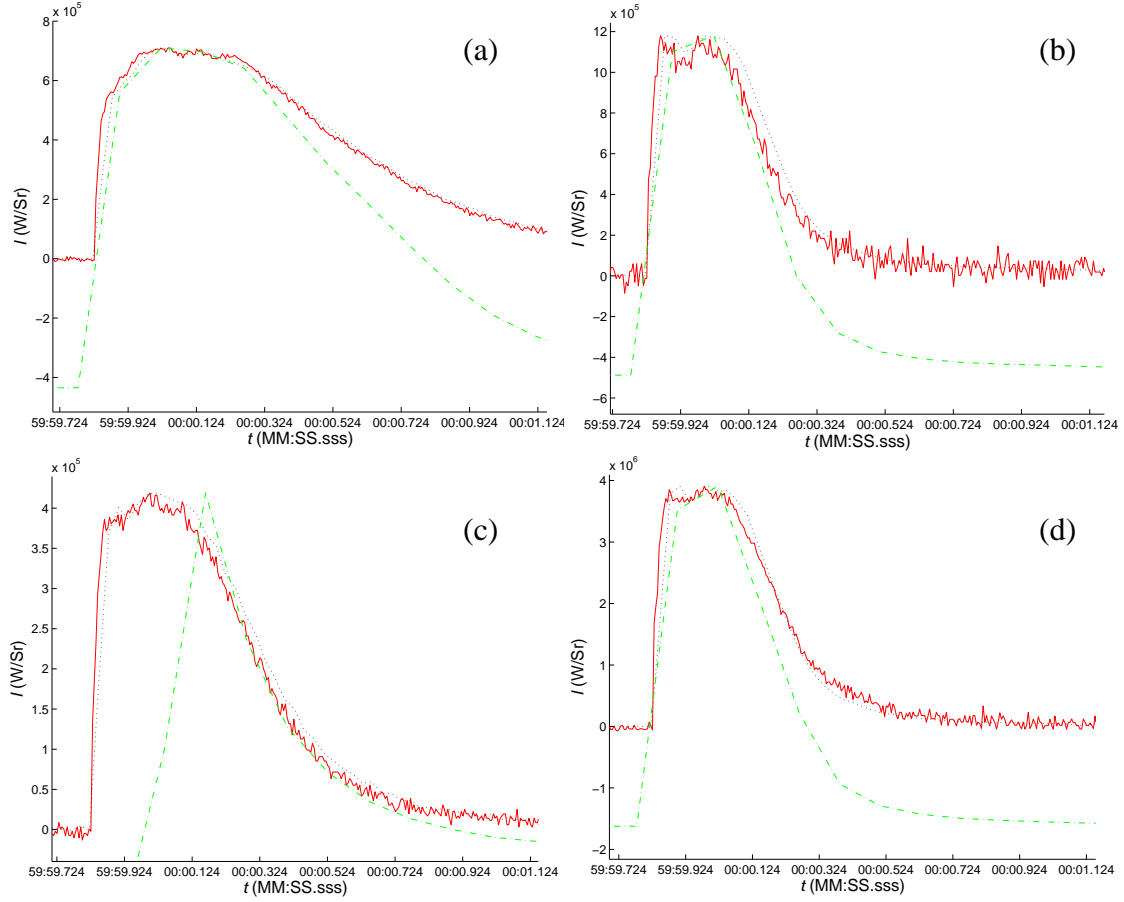


Figure 9. A second set of comparison plots of AFIT MR154 InSb spectrometer data (dash-dot line) with the MR354 InSb spectrometer (dotted) and radiometers (close dots) for Brilliant Flash II event 25, Type A, 50 kg. Each spectrometer data is integrated over the bands, scaled to the height of the radiometer, and shifted in time if necessary to align with the radiometer. Figure (a) is from band I (4.45-4.65 μm), figure (b) is from band II (3.88-3.99 μm), figure (c) is from band IV (2.7-3.1 μm), and figure (d) is from band V (2.15-2.3 μm).

Table 9. Scaling factors f_{scale} used to equate the peak intensities in specific spectral bands from the MR354 and MR154 (AFIT) InSb spectrometers to the radiometers.

Event No.	f_{scale} MR354 band IV	f_{scale} MR154 band IV	f_{scale} MR354 band II	f_{scale} MR154 band II	f_{scale} MR354 band V	f_{scale} MR154 band V	f_{scale} MR354 band I	f_{scale} MR154 band I
1	1.1622	9.4408	1.9226	6.0387	0.83921	5.5112	1.1441	1.4088
2	2.1939	5.7004	6.6754	33.3165	5.1409	24.4676	1.3627	3.9784
3	1.5678	0.79083	2.2402	0.67052	1.6675	1.0592	1.5398	0.32145
4	0.50223	1.1512	0.51647	0.45002	0.35741	0.60798	0.34243	0.25454
5	1.1889	2.0388	1.3578	2.1617	0.90527	1.4461	1.1704	2.0784
6	1.1162	1.1124	1.4943	1.4884	1.0306	1.1169	1.2411	1.4215
7	1.9094	6.3297	1.1932	4.2493	1.0233	3.491	1.7674	3.1157
8	NO	MR154	DATA					
9	NO	MR154	DATA					
10	0.92134	1.161	1.216	2.4783	0.89689	1.6634	1.0578	1.784
11	0.93792	0.7357	1.2132	0.65841	0.86644	0.72284	1.0743	0.65126
12	NO	MR354	DATA					
13	0.9386	0.919099	1.02	1.94	0.82099	1.2924	1.0176	1.1622
14	0.94572	2.5974	1.3675	7.2499	1.1739	5.52	1.0045	3.013
15	0.923	0.96969	1.5488	2.6716	1.1652	2.1508	1.0721	0.84789
16	NO	MR154	DATA					
17	1.0714	1.4233	2.0594	3.2308	1.6736	2.5074	1.0975	1.6847
18	2546.2	2886.9	8722.5	8987.5	3470.9	3636.7	911.5	1158.0
19	0.92955	0.50865	1.2735	0.35588	0.78025	0.77756	1.0469	0.20818
20	NO	MR154	DATA					
21	0.98686	0.76479	1.8382	1.2002	1.1015	0.78679	1.0867	0.83775
22	1.0787	0.82015	0.98281	0.77432	1.22	0.58966	1.0271	0.91404
23	0.77961	0.79787	0.88411	0.88857	0.63242	0.66686	0.86986	0.92449
24	NO	MR154	DATA					
25	0.85512	0.31892	0.79551	0.27086	0.77154	0.28509	0.95865	0.40109
26	0.89759	0.70837	0.78689	0.81517	0.91715	0.88553	0.98668	0.90318
27	1.1188	0.85383	0.92349	0.9178	1.0802	0.80706	1.086	1.0008
28	1.0448	0.75794	0.95355	0.71403	1.0763	0.65027	1.0785	0.80485
29	0.8549	0.74199	0.79032	0.72632	0.72458	0.67946	1.4283	1.2874
30	0.79029	0.72622	0.78557	0.73067	0.72564	0.6366	0.91511	0.93544
31	0.86957	0.78813	0.83453	0.81369	0.74837	0.68478	0.95665	0.89738
32	6.38E-06	9.85E-06	6.93E-06	1.10E-05	5.17E-06	7.86E-06	9.34E-06	1.67E-05
33	1.4928	3.9084	1.21	2.3889	4.0497	567.2614	0.04857	0.12099
34	2.0303	0.99929	3.125	0.888	1.74	0.629	1.33	0.377
35	NO	MR354	DATA					
36	0.81934	0.59939	0.87256	0.63584	0.66719	0.52567	0.86798	0.55753
37	0.84436	1.069	1.0304	1.0017	0.67128	0.66573	0.08657	0.12166
38	0.76723	0.53047	0.93506	0.691	0.64834	0.45567	12.3027	10.2611
39	0.80167	0.687	0.88608	0.94671	0.77744	0.85267	0.8114	0.6573
40	0.80587	0.57139	1.0227	0.97791	0.60548	0.57702	0.82766	0.84184
41	0.78196	0.72459	0.97557	0.90834	0.65136	0.61716	0.84063	0.81513
42	0.86712	0.67437	1.1115	0.90247	0.69134	0.55856	0.95522	0.78762
43	1.0208	0.80999	1.0768	0.88975	0.82645	0.57875	0.91795	0.85061
44	0.80712	0.66776	1.1151	0.92209	0.73969	0.57139	0.88427	0.84512
mean	1.1	1.5	1.4	1.5	1.1	1.3	1.3	1.3
std	0.4	1.9	1.0	1.6	0.9	1.3	1.9	1.8
±33%	29	22	24	19	25	13	27	16

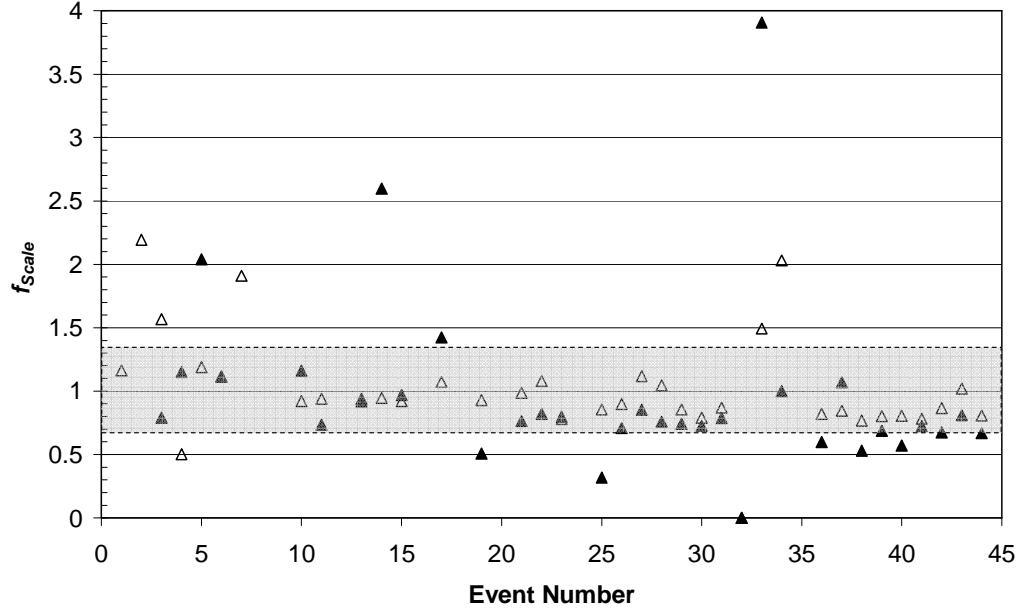


Figure 10. Scaling factor for band IV using the MR154 InSb spectrometer data (▲) and the MR354 InSb spectrometer data (Δ). The 33% lines are drawn as dotted lines with the included area shaded.

2. 3-chip CCD camera images

A Canon DM-XL1A video camera with a 16x, 200mm lens is used to acquire color motion pictures of the events at 30 Hz. The camera records the red, green, and blue images simultaneously on a three chip detection system. The camera manufacturer does not release the spectral response of the camera, thus the color bands are assumed to center around 700 nm, 540 nm, and 450 nm, respectively. The shutter speed is set sufficiently high, *e.g.* 1/1000 to 1/4000 s, to reduce the background signal to a near dark scene and to avoid saturation at multiple time frames. Post processing allows one to separate the colors and view the event image in these three broadband color regions. Figure 11 is one example of a single event frame and shows the three contributing visible bands. Figure 12 is another example of the time evolution of each color for another event.

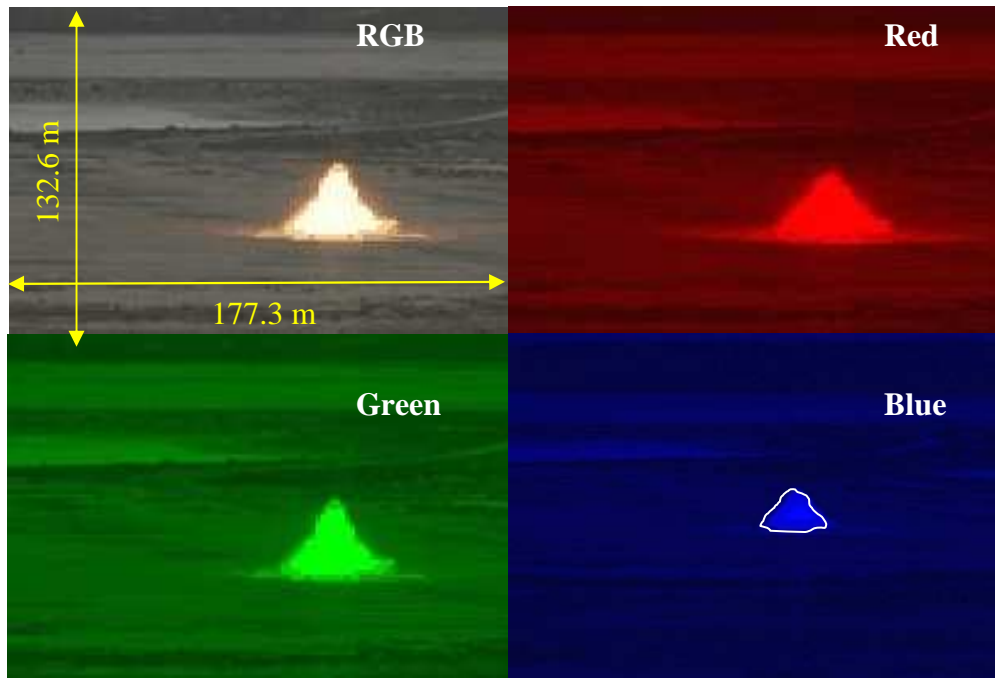


Figure 11. Each of the RGB colors is extracted through post processing from the original RGB image recorded by the Cannon 3-chip CCD. The detonation recorded in the blue band is outlined in white.

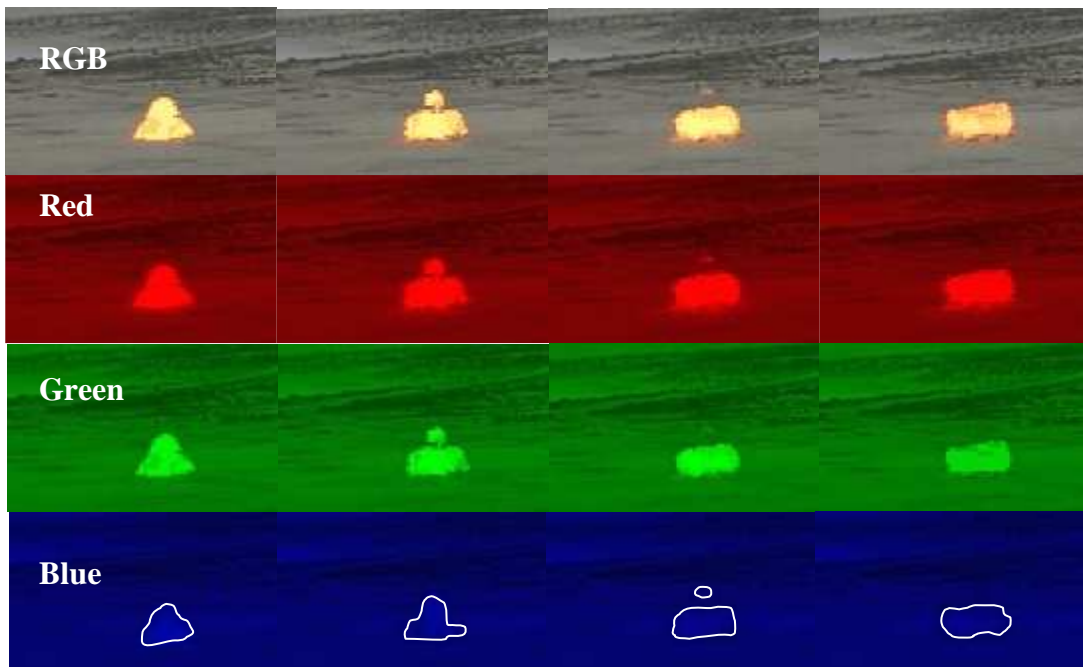


Figure 12. The first four frames of an event are shown here for each primary color and the composite RGB image. The detonation recorded in the blue band is outlined in white.

3. Near-Infrared (NIR) imagery

An Indigo Systems Alpha Near-Infrared (NIR) InGaAs Focal Plane Array (FPA) with good spectral response in the 0.6 - 1.7 μm band is used to record detonation images at a 30-Hz temporal resolution with a standard Minolta 400 mm telephoto lens ($1.36^\circ \times 1.10^\circ$) and with a 12-bit dynamic range onto a 316 x 256 pixel array. The aperture is typically set at f/11 and the exposure time is set 250 μs , both of which help reduce pixel saturation. Typical InGaAs images for the five types are shown in Figure 13. Given the range (3258 m) and lens field of view (FOV), the spatial resolution is 0.24 m x 0.24 m or an equivalent far-field pixel area of $0.060 \pm 0.004 \text{ m}^2$ which is significantly smaller than a typical fireball area (100-200 m^2). The uncertainty in the far-field area comes from the difference in the calculated and lab-measured lens FOV ($1.32^\circ \times 1.06^\circ$).

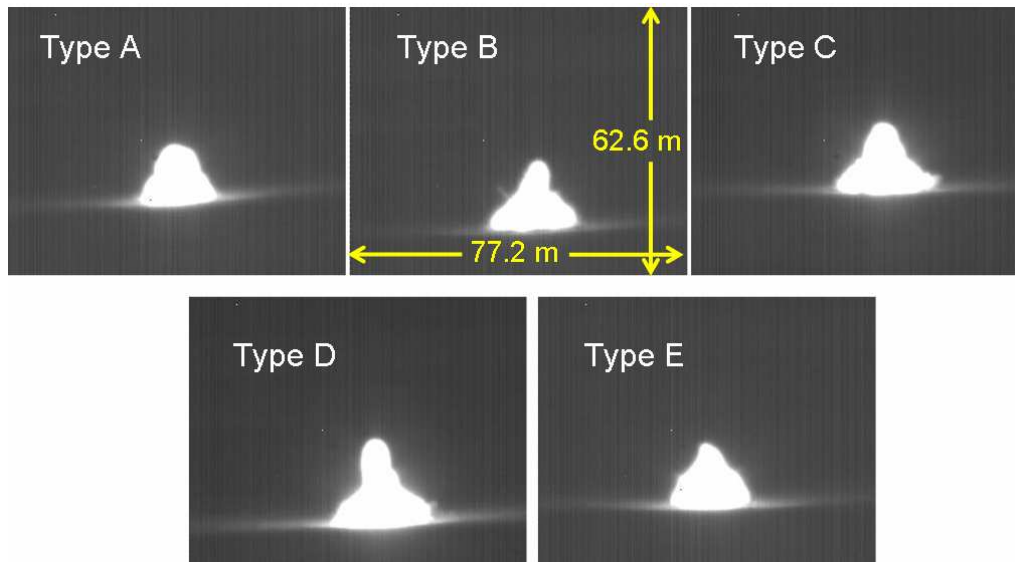


Figure 13. InGaAs camera images exhibit the relative sizes of the fireballs immediately after detonation. The images clearly show two intensity levels: one associated with the very bright fireball and the other associated with ground reflections. These images were collected during Brilliant Flash II and all represent 50-kg weights.

One method of interpreting the images is to examine the pixel intensity histograms. Such a histogram is shown in Figure 14 and graphically displays the number of pixels that record each intensity level I . The Alpha NIR camera records 12-bit intensity, ranging from 1 to 4096 digital numbers or DN. This representation of the image facilitates one to examine pixel distributions with respect to intensity. For example, Figure 14(a) illustrates that during the detonation of an event clear separation between the number of pixels having very high intensities (> 3000 DN) and those with significantly lower intensities (< 1500 DN). Figure 15 spatially identifies these relative intensities on an example fireball image. Figure 14(b) is background data collected prior to detonation and clearly shows a single distribution of pixels below 600 DN.

Both scene radiance and pixel responsivity drive the widths of histogram distributions, as demonstrated by comparing the width of high intensity pixels in Figure 14(a) inset to the width of background scene pixels in Figure 14(b) inset. The distribution about 500 DN in Figure 14(b) may indicate the distribution of pixel bias. The histogram in Figure 14(a) strongly indicates saturation, implying that the width about 3950 DN could represent the way the pixels saturate at the limit of the analog to digital conversion, i.e. the saturation effects each pixel differently. Normally, saturation effects are bad if the neighbor pixels are influenced. Yet according the histogram, the distribution of pixels associated with the very intense source is highly separated from those pixels associated with less intensity. The pixels along the edge of the fireball, as pointed out in Figure 15(b), are potentially corrupt; however, they only account for approximately 1% of the total fireball area.

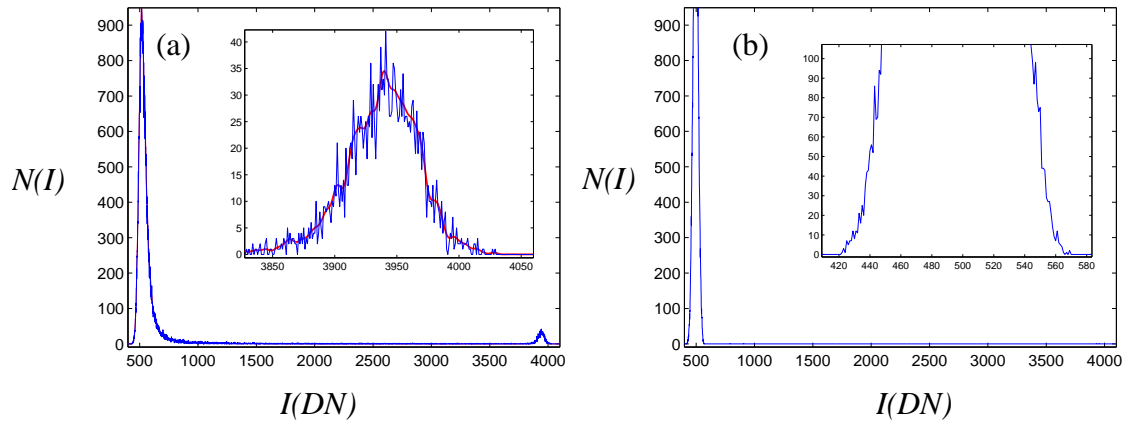


Figure 14. One representation of the range of pixel responsivity is the range of intensities I that a pixel will register for a given input source intensity. Both figures displays the number of pixels N at each registered intensity level I on a 12-bit scale. Fig. (a) represents the signal during an event frame. Its insert is a zoom of the 3550-4050 DN intensities. Fig. (b) shows the histogram for the background scene prior to detonation with 440-560 DN emphasized.

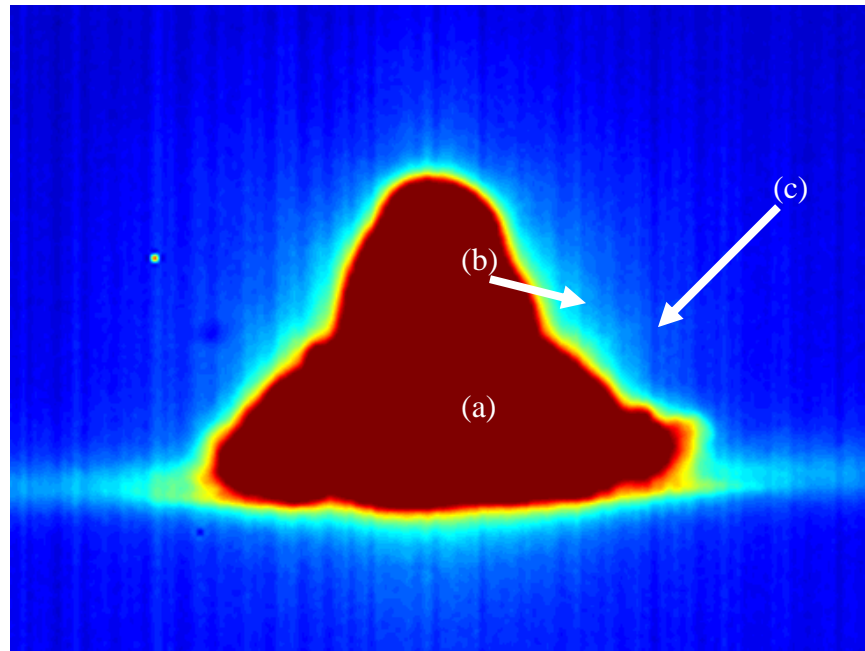


Figure 15. Relative NIR intensities of a 50-kg Type-C fireball as recorded by the Alpha Indigo camera: (a) pixels above 3000 DN, (b) pixels between 2400 and 3000 DN, (c) pixels below 2400 DN and above background illumination.

IV. Developing Discrimination Tools using Image Data

At the heart of this research lie two primary objectives: first, to develop the tools for feature extraction and pattern recognition of collected data originating from the fast transient events and two, to utilize these patterns to establish distinct and reproducible features that aid classification between two types, TNT and enhanced explosives, and that aid in understanding bomb emission phenomenology. The first goal is to identify those key features and different analysis approaches that provide discrimination between classes where each class represents a specific combination of explosive type and weight. With this goal, there are two possible approaches. One creates a model based upon first principles and then analyzes how the data matches that model. The second approach uses the data to extract key features that will aid in classification. The second approach is the focus of this research. The models that are developed in this research are not derived from first principles but are ones that capture discriminatory features in the collected data. The models, features extracted, and pattern recognition techniques to date are explained in this chapter. Additionally, the examples used in the discussion are from Brilliant Flash I and II field data of uncased explosive materials. Following the tool development, the next chapter applies these tools to spectra collected during Radiant field tests where the targets are cased munitions.

The discriminate tools are now described in this chapter and the example data is a subset of field data provided by the Alpha Indigo InGaAs near-infrared (NIR) camera and the Cannon XL1 3-chip video camera. These tools extract key features from the image data, determine feature saliency and stability, and provide figures of merit to evaluate the

data. Two variants of the technique are presented: the first assumes two explosive types at the same weight and the second examines five classes consisting of two types and three weights. With each of these tools, the NIR and 3-chip color camera data are examined independently before combining the two sources. Finally, conclusions about these tools applied without *a priori* assumptions to the field data are presented.

A. Near-Infrared Imagery Field data

A typical detonation fireball image and the corresponding pixel intensity histogram for a 50 kg Type A detonation are shown in Figure 16. The first frame represents the pre-detonation background. Note the narrow distribution at low intensity between 1200 and 1300 DN indicating a detector bias plus a nominal background. The second frame corresponds to the detonation event ($t = 0$) where the pixel illumination intensities shift above the pre-detonation intensity level. Each additional frame is delayed by 33 ms. After detonation, two significant features can be discerned: (a) a high intensity ($\text{DN} > 3500$) feature representing the intense center of the burning fireball, and (b) a low intensity ($1000 < \text{DN} < 2000$) feature representing the emission from the smoky/dusty portion of the fireball and any diffuse reflection. Both features decay to background within 300 to 550 ms. The pixels that have intensities that approach the limit of the camera's 12-bit dynamic range could be saturated at $I = 2^{12} = 4096$ DN, but the number of pixels associated with the fireball remains unchanged. The signal of interest is the high intensity distribution associated with the fireball, which has intensity characteristically greater than ten times the lower intensity associated with background illumination.

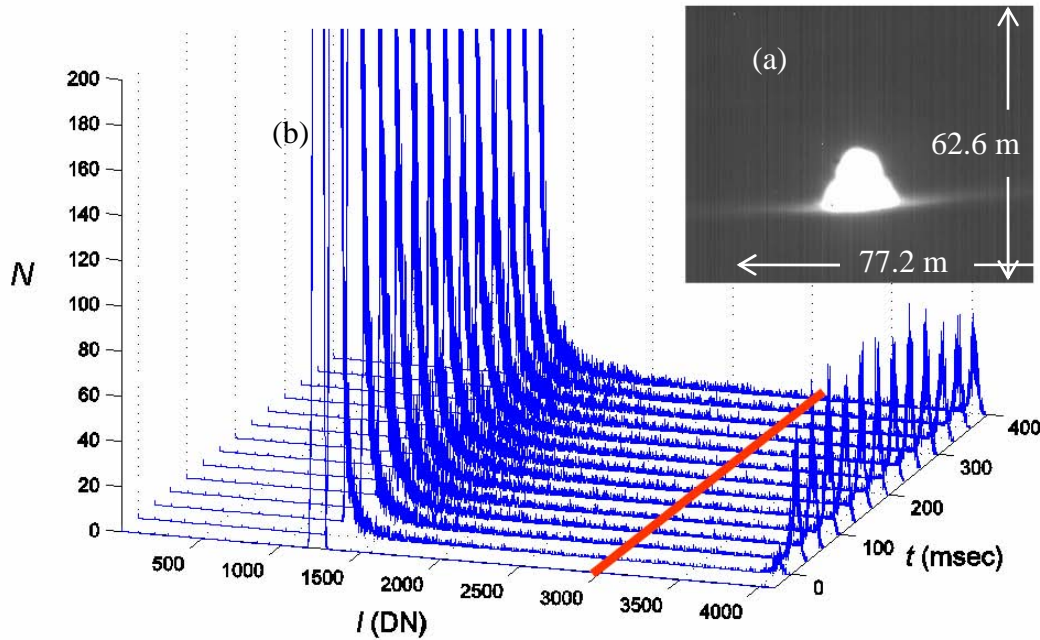


Figure 16. (a) A single image at detonation time ($t=0$) and corresponding (b) temporal evolution of the histogram for each image. Each histogram is shown as a function of the number of pixels (N), the pixel intensity I in digital numbers (DN) along the abscissa ranging from one to 4096, and the detonation time ($-33 \text{ msec} \leq t \leq 400 \text{ msec}$). The line at $I=3000 \text{ DN}$ aids in calculating fireball size. The number of pixels N at the low intensities are cut off in this figure to aid clarity between the low and high intensity features. This histogram and corresponding image is from one 50-kg Type A explosive material detonated during Brilliant Flash II.

In Figure 17(c) and (d) the histograms for Type C and D detonations consistently indicate a larger, more intense fireball initially upon detonation. They also exhibit a more intense dust cloud/diffusion reflection signature. A video of the InGaAs imagery clearly reveals re-circulation (vortices) within the intense fireball. There are usually about three vortices seen from the camera angle; each one approximately a third of the fireball size. The histogram in Figure 17(b) for the Type B charge shows a much shorter-lived fireball (approximately 167 msec) than the other types (typically greater than 400 msec).

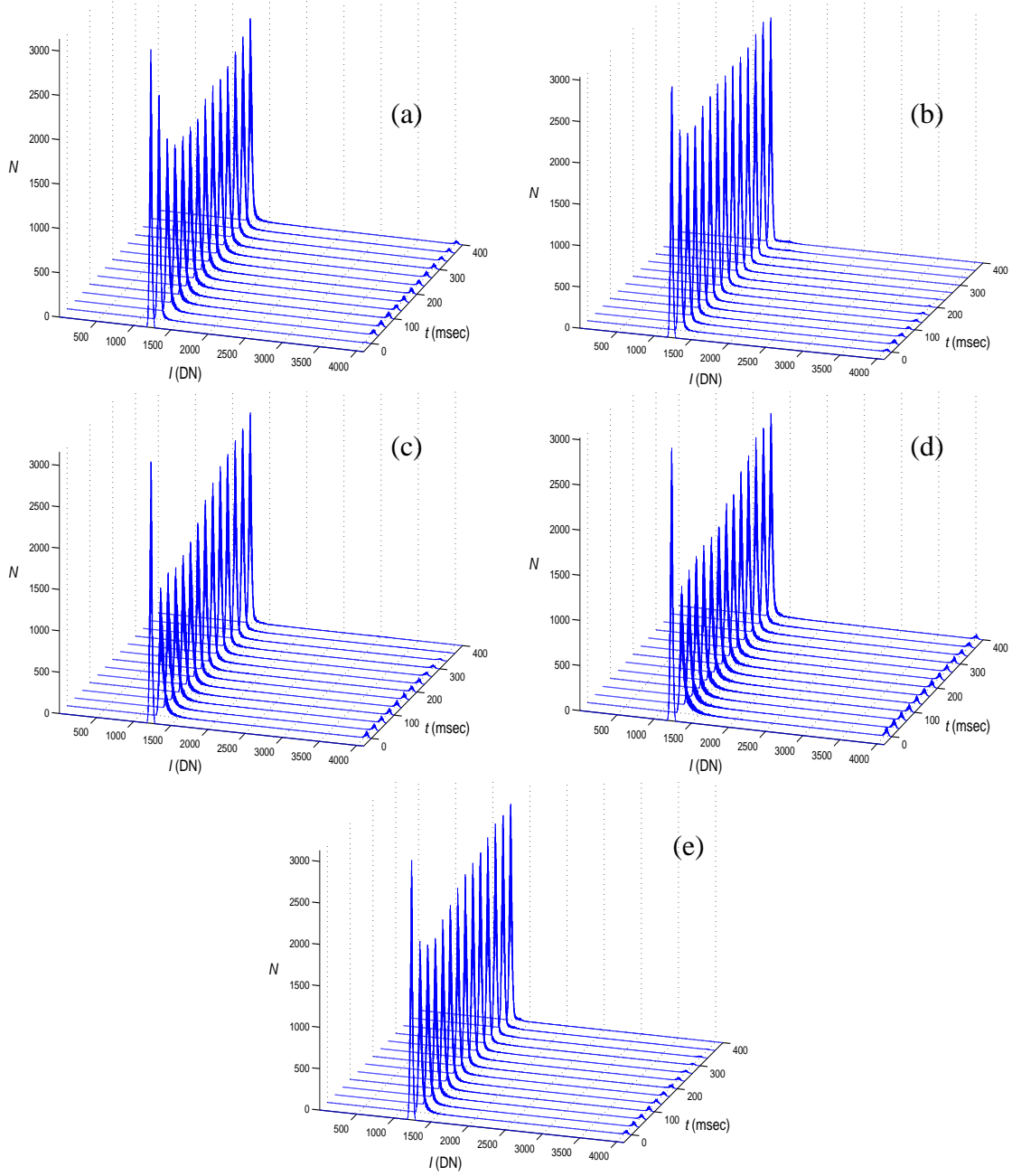


Figure 17. Histogram for the number of InGaAs pixels N illuminated at various intensities I as a function of time t for: (a) Type A, (b) Type B, (c) Type C, (d) Type D, and (e) Type E 50-kg charges. The total number of pixels in the InGaAs array is 80,896 so that a pixel count of 1000 is about 1.2% of the detector array.

The fireball size calculation exploits the large separation (typically 1800 DN) between the distributions of pixel intensities associated with the hot fireball and of those associated with the background. For instance, the fireball area is calculated by scaling the total number of pixels above a threshold value (*e.g.*, the solid line at $I = 3000$ DN in Figure 16) to the actual field of view of the collecting instrument. Using this metric, the temporal behavior of the fireball size is compared for various types of explosives. The results for the five types of 50 kg detonations (Brilliant Flash II) are provided in Figure 18. Fireball areas calculated from Brilliant Flash I data are provided in Appendix A.

The fireball area calculated in the first frame of the event could potentially be misleading depending on the event time coinciding with the camera frame timing. For example, the NIR camera collects a new image every 33 msec, however, to reduce saturation the flux of incident light onto the detector is reduced by lowering the camera exposure time, typically 250 μ sec. The uncertainty in the actual start time could be up to 33 msec.

The fireballs from event Types A, C, D, and E are consistently larger and longer-lived than Type B events. Even more pronounced are the temporal histories of the fireball area. The fireball for Type C, D, and sometimes E events exhibit a sudden initial large area not observed for the other event types. For example, the ratio of fireball area at 166 ms and 66 ms for Type B event is small (~ 0.6) and is much more for the two other detonations (~ 1 for Type A and ~ 0.9 for Type C). The outlier event in the Type D class is approximately 0.7 the size of the others. This same reduction is also seen for this event in the data simultaneously recorded by a spectrometer.

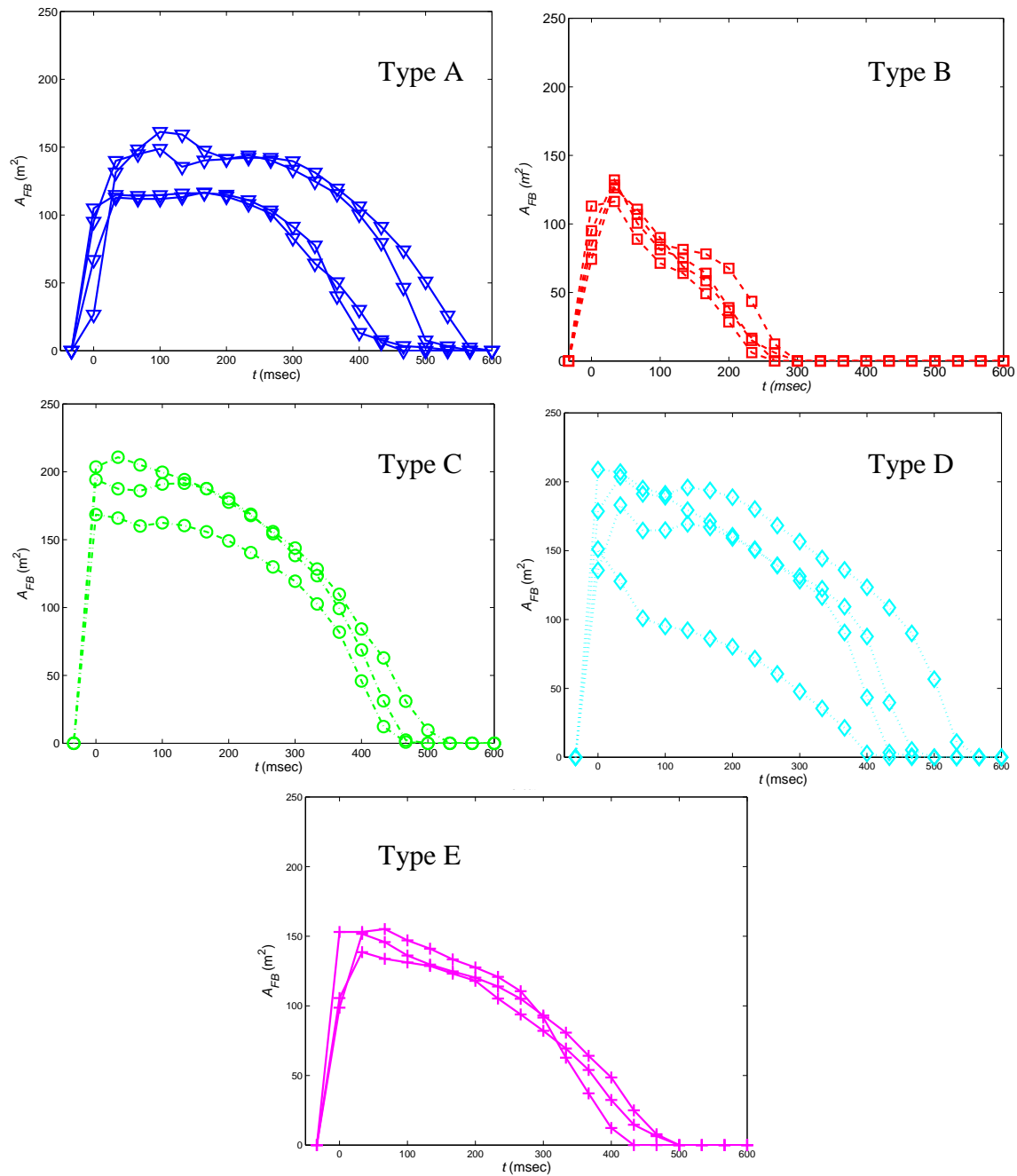


Figure 18. Reducing the image data down to the temporal behavior of the fireball area provides one method of showing reproducibility within a class and distinguishability between the classes. Pattern recognition will further remove the similarities among the curves and find the best method of discrimination. The five types shown in this figure are 50-kg weights from the Brilliant Flash II test. Type A is TNT.

These fireball areas not only show promise at distinguishing explosive types, but also demonstrate reproducibility. Notice that within each type of explosive, the fireball areas overlay each other within 15 to 30 percent. The only exception is already identified as a Type D event.

B. Feature extraction

To fully utilize pattern recognition tools, these fireball areas are further reduced to a set of features that capture much of the fireball area information. In essence, the collected image data is reduced to a set of simple features. There are numerous ways to extract features from the area curves. The best begins with parameters that represent a phenomenological-based model. Without this description of the fireball emission, a pragmatic approach obtains simple features from the derived area. The first seven such features are basic descriptors of the area curve, *e.g.* peak values, etc., while an additional set of seven features are extracted during the conversion of the area curve into a probability density function with derivable moments.

Using Figure 19(a) as an example, the first set of features include the most probable time and area (t_{mp} , A_{mp}); the median time, area, and respective standard deviations (t_{median} , A_{median} , σ_{t_median} , σ_{A_median}); and the integrated fireball area during the detonation time Δt ,

$$\underline{A} = \langle A(t) \rangle \Delta t = \int_{t_{event}}^{t_{event} + \Delta t} A_{FB}(t) dt \quad (12)$$

where $\langle A(t) \rangle$ is the time average of the fireball size. The second set of features involves fitting the area curve to a simple quadratic, $f(t) = c_1 t^2 + c_2 t + c_3$, and converting the

resulting residuals ($\text{data}(t) - f(t)$) as shown in Figure 19(b) to a probability density function ($P(t)$) by normalizing the residual between the quadratic and the area data points, such that the minimum occurs at zero and the area under the curve is unity:

$$P(t)|_{\min} = 0, \text{ and}$$

$$\int_{t_{event}}^{t_{event} + \Delta t} P(t) dt = 1, \quad (13)$$

where Δt represents the duration of the fireball. A simple quadratic fit from the most probable area A_{mp} to the last point above background does not represent a physical system. Thus the pragmatic approach only aids in finding simple features that may help in discrimination. These three fit parameters (c_1, c_2, c_3) and the first four moments of the PDF ($\mu_1, \mu_2, \mu_3, \mu_4$) are the remaining seven features. The first four moments are:

$$\mu_1 = \int t \cdot P(t) dt, \quad (14)$$

$$\mu_2 = \int (t - \mu_1)^2 \cdot P(t) dt, \quad (15)$$

$$\mu_3 = \frac{1}{\mu_2^{3/2}} \int (t - \mu_1)^3 \cdot P(t) dt, \text{ and} \quad (16)$$

$$\mu_4 = \frac{1}{\mu_2^2} \int (t - \mu_1)^4 \cdot P(t) dt, \quad (17)$$

where in each case, the theoretical integration limits are for all time, yet the practical limits with non-zero $P(t)$ are t_{event} to $t_{event} + \Delta t$. All the feature values for imagery are provided in Appendix B.

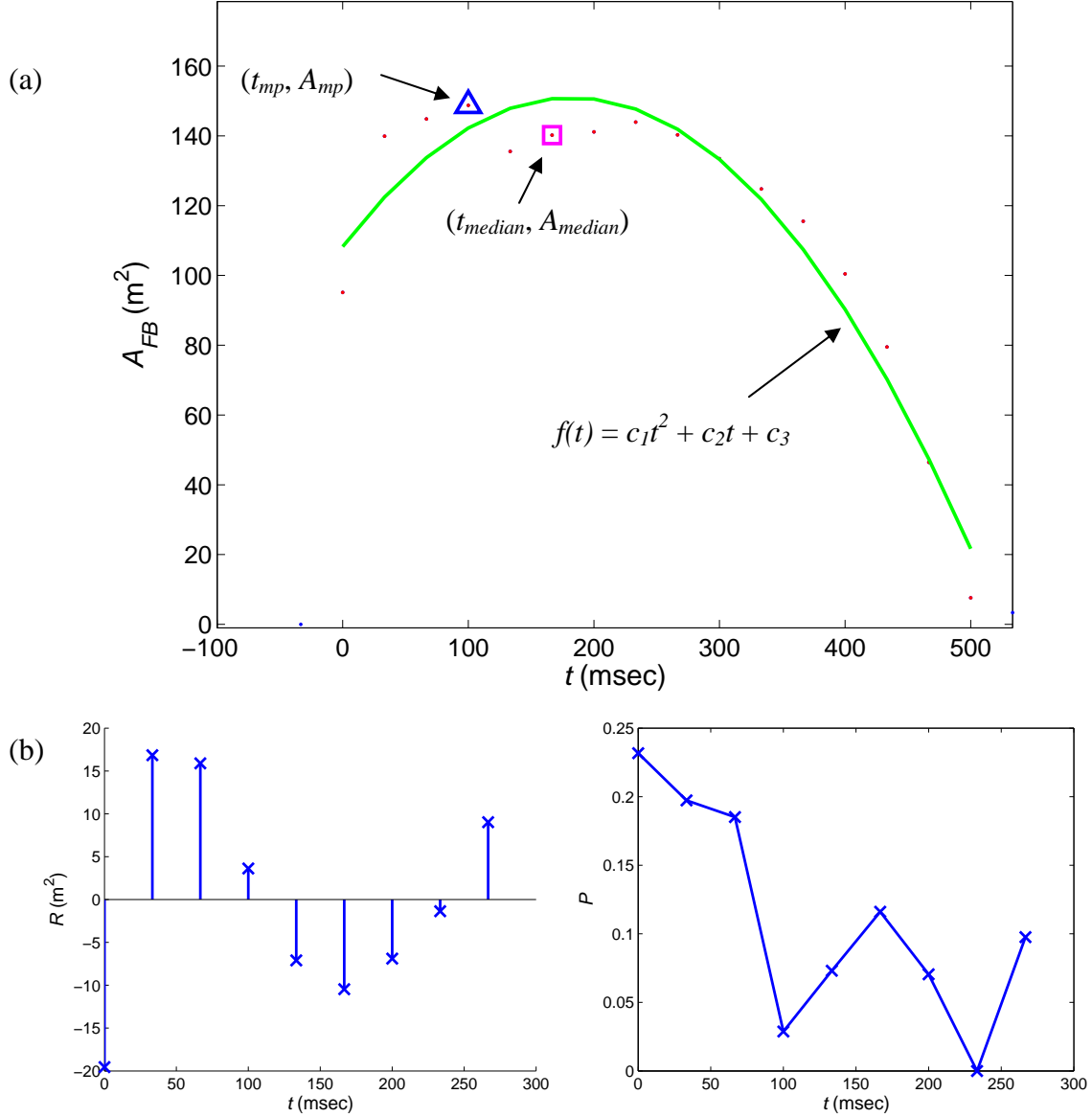


Figure 19. The extracted features from the fireball area A_{FB} curves include simple observations of the area curve (figure a) and calculated moments of a probability density P derived from the residuals R between the data and a quadratic fit f of the data (figure b). Pattern recognition techniques help prioritize which features are the most important in discriminating among the various types of explosives.

C. Fisher discrimination, Feature saliency and stability measures of merit

After feature extraction, the original $M \times N \times \text{frames}$ pixel image is reduced to fourteen features. Not all of these features will aid in classification, and of those that do,

only a few of the most important features are needed. Various pattern recognition techniques are now employed to (1) determine the usefulness of imagery data for classification, (2) determine feature saliency (the ranking of features that best discriminate), (3) identify the minimum number of features needed to accurately classify among the various types of explosives, and (4) show that these features produce stable results in classification. Stability is explicitly defined in a later section, but in general it refers to those features that consistently give (proven through robust testing) the best discrimination with the least amount of variation in class-conditional probability densities.

The level of difficulty of this problem is exacerbated by a limited data set for each type and weight of explosive. For example, the combined number of events between Brilliant Flash I and Brilliant Flash II is thirty nine. Of those, the largest weight class is 50 kg, consisting of twenty seven events, ten Type A and seventeen enhanced novel explosives (ENE). For this reason, the problem is recast into two potentially more achievable objectives that pattern recognition techniques can exploit. The first objective is to solve the classification problem with only two classes: TNT and all ENE, all at 50 kg weights. The five classes for the second objective are TNT-10kg, TNT-50kg, TNT-100kg, ENE-50kg, and ENE-100kg.

1. Two-class problem

Beginning with the two-class problem, the desired features are those that best distinguish the two classes while preserving individual class grouping. One pattern recognition approach to accomplish this objective is Fisher linear discrimination. While the mathematics is described in [51:117-124] and [52:105-109], a simpler explanation

begins with a picture. Suppose the data can be represented by two features, t_{mp} and σ_{τ_median} , and the scatter plot of the data values shown in Figure 20.

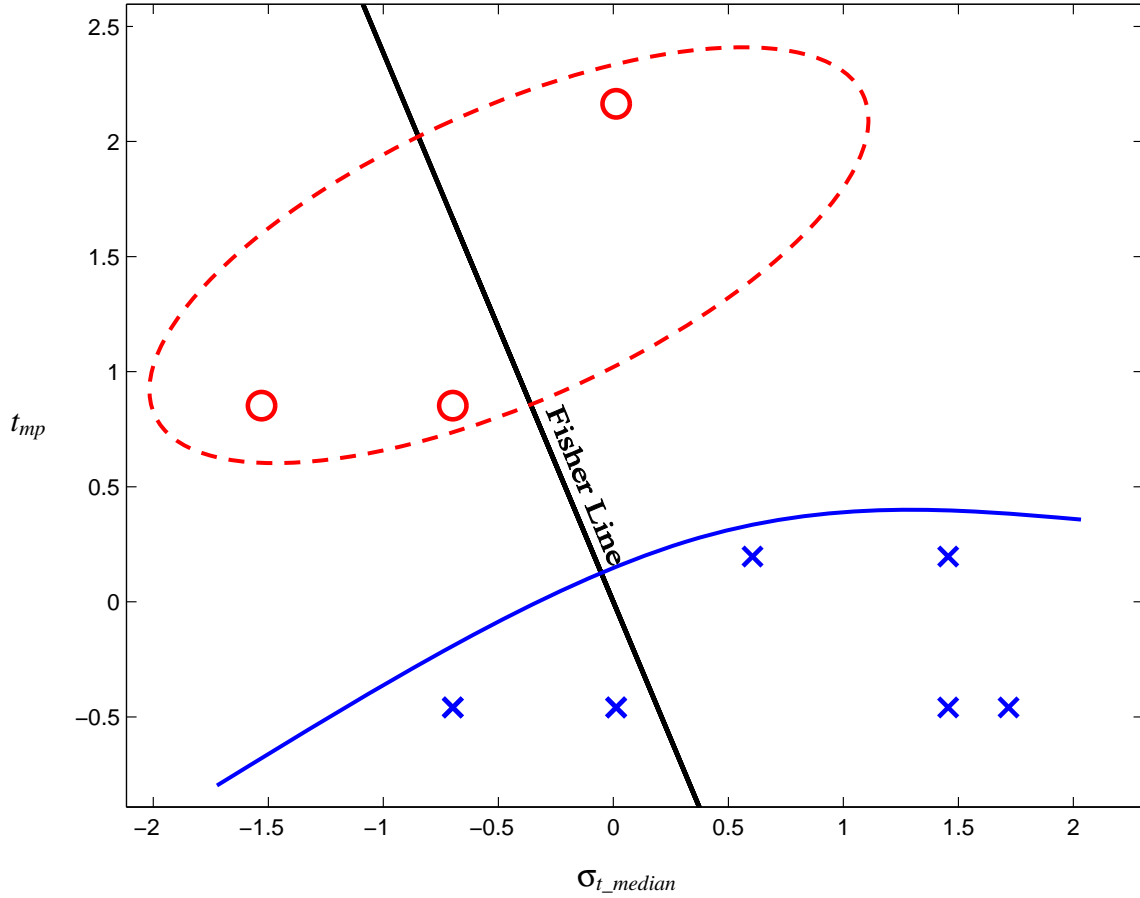


Figure 20. A scatter plot of Brilliant Flash II data represented by two features, t_{mp} and σ_{t_median} , shows individual class clusters (O = TNT, X = ENE) and an appropriate Fisher discrimination line (solid black line).

The Fisher discrimination technique identifies the vector in the feature space that maximizes the differences in the class means and minimizes the class variances when the data is perpendicularly projected onto a line (Fisher line) defined by that vector. Suppose that for class i the data projected onto the Fisher line is represented by the vector \underline{x}_i . Then

one mathematical representation of a ratio (called a Fisher ratio), when maximized, defines the Fisher line as

$$FR = \frac{\frac{1}{D} \sum_{i \neq j} (\underline{x}_i - \underline{x}_j)^2}{\frac{1}{C} \sum_i \sigma_i^2}, \quad (18)$$

where the average of the square of the class means differences $(\underline{x}_i - \underline{x}_j)$ is the numerator and the average of the class variances is the denominator. Here, D is the number of class mean differences and C is number of classes which have variance σ_i^2 .

The Fisher line is found either by a search method, an analytic method, or a least-squares method [51: 240-242]. The search method is a global minimization challenge and is not adequate for the limited data-set under the current investigation. For the two-class problem, the analytic method is identical to the least-squares method except that the latter requires less computation time [51: 240-242].

The least-squares method treats the problem as a set of linear equations whose solution yields the Fisher line vector. For example, let each row of $\underline{\mathbf{X}}$ represent an event (N events) and each column represent a feature value (M features), excluding the first column of ones ($N \times M+1$ matrix). Suppose there are N_1 events belonging to class 1 and N_2 events belonging to class 2, with a total number of events $N = N_1 + N_2$. Let each element in the target $\underline{\mathbf{b}}$ have a target value that is either N/N_1 or $-N/N_2$ for class 1 or class 2, respectively. Then the linear equation to solve for the Fisher vector $\underline{\mathbf{a}}$ is

$$[\underline{\mathbf{1}} \ \underline{\mathbf{X}}] \underline{\mathbf{a}} = \underline{\mathbf{b}} \quad (19)$$

$$\begin{pmatrix} 1 & x_{11} & x_{12} & \cdots & x_{1M} \\ 1 & x_{21} & x_{22} & \cdots & x_{2M} \\ \vdots & \vdots & \vdots & & \vdots \\ \vdots & \vdots & \vdots & & \vdots \\ 1 & x_{N1} & x_{N2} & \cdots & x_{NM} \end{pmatrix} \begin{pmatrix} w_0 \\ a_1 \\ \vdots \\ a_M \end{pmatrix} = \begin{pmatrix} b_1 \\ b_2 \\ \vdots \\ b_N \end{pmatrix}, \quad (20)$$

where a_1 to a_M defines the Fisher line $\underline{\mathbf{a}}$ with a threshold weight w_0 associated with the target values in $\underline{\mathbf{b}}$. This equation has a solution

$$\underline{\mathbf{a}} = \underline{\mathbf{Y}}^{-1} \underline{\mathbf{b}} \quad (21)$$

when $\underline{\mathbf{Y}}$ is nonsingular, or

$$\underline{\mathbf{a}} = (\underline{\mathbf{Y}}^t \underline{\mathbf{Y}})^{-1} \underline{\mathbf{Y}}^t \underline{\mathbf{b}} \quad (22)$$

when $\underline{\mathbf{Y}}$ is overdetermined. The solution $\underline{\mathbf{a}}$ is a $(M+1 \times 1)$ vector, and $\underline{\mathbf{a}}/|\underline{\mathbf{a}}|$ represents relative importance among the M features. A new event vector $\underline{\mathbf{x}}$ ($1 \times M$) belongs to class 1 if the inner product $[1 \ \underline{\mathbf{x}}] \underline{\mathbf{a}}$ is closer to N/N_1 ; it belongs to class 2 if the inner product is closer to $-N/N_2$.

2. *Class-conditional probability densities*

Once the Fisher line with the highest Fisher ratio is determined, probability density functions for each class are calculated along the Fisher line using kernel (or Parzen window) density estimation [52: 53-55]. The procedure begins by projecting each data point onto the Fisher line and determining the class means and standard deviations. A Gaussian distribution with a width equal to the class standard deviation is centered at each data point in the class. The Gaussian distributions for all the points in a class are summed and divided by the number of points in the class to ensure that the total area

under the distribution curve is unity. The result is a class-conditional probability density function, $p(x/c_i)$, e.g. the thick lines in Figure 21, defining the probability of an event having a value x given it is in class c_i . Once the correct Fisher line is determined, then any subsequent data can be projected onto this line and classified according to the Bayes' decision rule for minimizing the probability of error.

Bayesian decision theory provides the guidelines used to classify an event. Duda, *et al.* explain this theory in general [51: 20-23], but an explanation using the current example will help solidify the concept. Let each class be, $c_1 = \text{ENE}$ and $c_2 = \text{TNT}$ with equal *a priori* probabilities (or priors P) where their sum is one: $P(c_1) + P(c_2) = 1$. Since there is an equal chance that the next event is either class, then $P(c_i) = 1/2$. However the probability predicting the next event is best described using Bayes' formula,

$$P(c_i | x) = \frac{p(x | c_i)P(c_i)}{p(x)}, \quad (23)$$

where the *a posteriori* probability $P(c_i/x)$ (or posterior) is the probability that an event falling along the Fisher line at x is in class c_i , for example, the thin lines in Figure 21. The posterior is directly proportional to $p(x/c_i)$, the *likelihood* of c_i with respect to x (or the class-conditional probability density functions described earlier) and the *a priori*, $P(c_i)$. The posterior is also inversely proportional to the *evidence* or scaling factor $p(x)$ that ensures $P(c_i/x)$ sum to one. Thus for the two-class problem with priors both equaling $1/2$, the evidence is

$$p(x) = \frac{p(x | c_1) + p(x | c_2)}{2}. \quad (24)$$

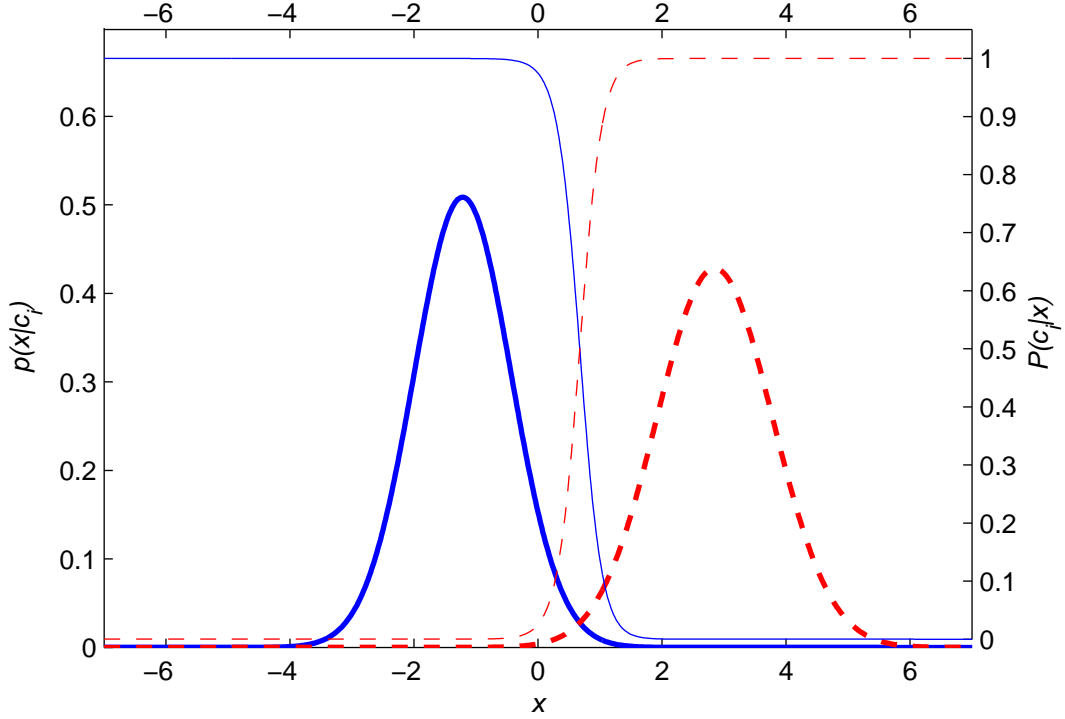


Figure 21. Class-conditional probability density functions, $p(x/c_i)$, (left ordinate, thick lines) and posterior probabilities, $P(c_i/x)$, (right ordinate, thin lines) for each class c_i (TNT dashed, ENE solid) are calculated along the Fisher line x using two features: t_{mp} and σ_{t_median} . The $p(x/c_i)$ are normalized such that the area under each curve is 1.0. The posterior probabilities represent the total probability that an event with a certain value along the Fisher line is in one of the two classes, thus at every point along the Fisher line the posteriors sum to one. For a Fisher line value $x = 1.5$, the probability the event is ENE is roughly 0.1, and that it is TNT is 0.9.

Knowing the posterior, one applies Bayes' decision rule for minimizing the probable error to generate appropriate classification and associated errors:

$$\text{Decide } c_1 \text{ if } P(c_1/x) > P(c_2/x); \text{ otherwise decide } c_2, \quad (25)$$

and where the probability of error is

$$P(\text{error}/x) = \min[P(c_1/x), P(c_2/x)]. \quad (26)$$

In addition to the Fisher ratio described earlier, another standard metric to capture the goodness of classification is area under the receiver operating characteristic or ROC curve. While the Fisher ratio captures the means and variances of the class-conditional probability densities, the ROC includes integration of these density functions. Thus the ROC captures probabilities of error in classification and the overall behavior of each *likelihood*. By definition, a ROC curve, as shown in Figure 22(b), consists of the

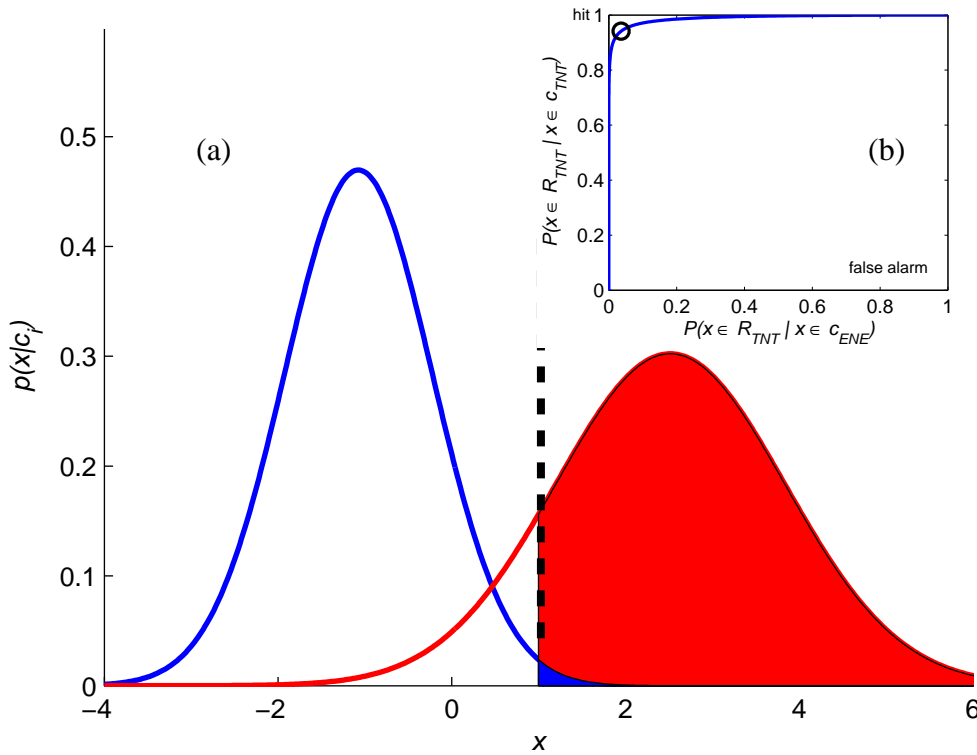


Figure 22. Figure (a) shows class-conditional likelihoods where the shaded areas represent the probability of a hit (red/light gray area) and the probability of false alarm (blue/dark gray area) as a function of decision threshold along x . The resulting receiver operating characteristic curve in figure (b) shows the ordinate as the probability of hit, $P(x \in R_{TNT} | x \in c_{TNT})$, and the abscissa as the probability of false alarm, $P(x \in R_{TNT} | x \in c_{ENE})$. This example is generated using the single feature t_{mp} and shows that the likelihoods cross at $x \sim 0.5$ and $x \ll -6$.

probability of false alarm (calling an event TNT when it is actually an ENE) along the abscissa and the probability of hit (accurately calling an event TNT) along the ordinate.

The probability of a hit is

$$\begin{aligned}
 P_{hit}(x^*) &= P(x > x^* | x \in c_1) \\
 &= P(x \in R_1 | x \in c_1) \\
 &= \int_{R_1} p(x | c_1) dx,
 \end{aligned} \tag{27}$$

where R_1 is defined as all x such that $P(c_1|x) > P(c_2|x)$ as shown by the shaded areas in Figure 22(a), and the probability of a false alarm is defined as

$$\begin{aligned}
 P_{false\ alarm}(x^*) &= P(x > x^* | x \in c_2) \\
 &= P(x \in R_1 | x \in c_2) \\
 &= \int_{R_1} p(x | c_2) dx.
 \end{aligned} \tag{28}$$

3. *Validation with leave-one-out and determining feature saliency*

One can use either the Fisher ratio or the total area under the receiver operating characteristic or ROC curve (A_{ROC}) and a leave-one-out process to determine the best features and their saliency. The results are nearly the same with the Fisher ratio and the A_{ROC} . The leave-one-out process is a validation step in which a single data point (an explosion event) is eliminated from the data (all the explosion events) before calculating the Fisher line, the Fisher ratio, the classification boundary, and the ROC. This left-out data point is then used to validate the classification boundary by projecting it onto the Fisher line and comparing its classification with its actual class. The percent of correctly

classified left-out data points is tracked along with the average of the Fisher ratios and A_{ROCS} .

The leave-one-out process is a useful tool in determining the best features to use in classification. When the leave-one-out process is applied to a set of features, then each feature set is sorted based upon importance. Importance is measured a variety of ways. Some metrics available to sort the features include percent correctly classified, Fisher ratio, area under the ROC curve, probability of total error, and probability of error in a classification. The standard metrics are the Fisher ratio and the A_{ROC} . Again, the results using the current data set are the same whether the Fisher ratio or A_{ROC} is used. There are two ways to apply this knowledge. The first is to iterate through every combination of features starting with all possible one combinations (*e.g.* 14) and going through all possible 14 features. This approach does not retain information about the previous iteration, but it does provide the best 1-, 2-, etc. feature combination sets for classification. The resulting Fisher ratios for every combination of features are provided in Figure 23, where the feature combinations with the highest Fisher ratio are labeled and marked with an “X”.

The second approach with the leave-one-out is the forward-back approach. During the forward portion of this approach, one finds the best single feature; fixes it, then finds the next best feature, then the next, and so forth until a final set of rank ordered features is determined. Figure 24 shows the result of this method when applied to the 14 features extracted from the near infrared camera. In Figure (a), the Fisher ratio makes a significant improvement from ~10 to ~30 when the second feature is added; however, more features do not significantly contribute to improving the Fisher ratio until six or ten

features are used. The use of this many features is addressed later with regard to stability. Since the A_{ROC} and probability of correct classification is tracked for each feature set, then one can observe the effect on discrimination by adding additional features. This example clearly shows in figure (b) that within its uncertainty the A_{ROC} does not significantly improve by adding additional features. The backward portion of a forward-back approach is similar except one starts with all fourteen features and eliminates the single worst feature, one at a time. The results of this approach are given in Figure 25.

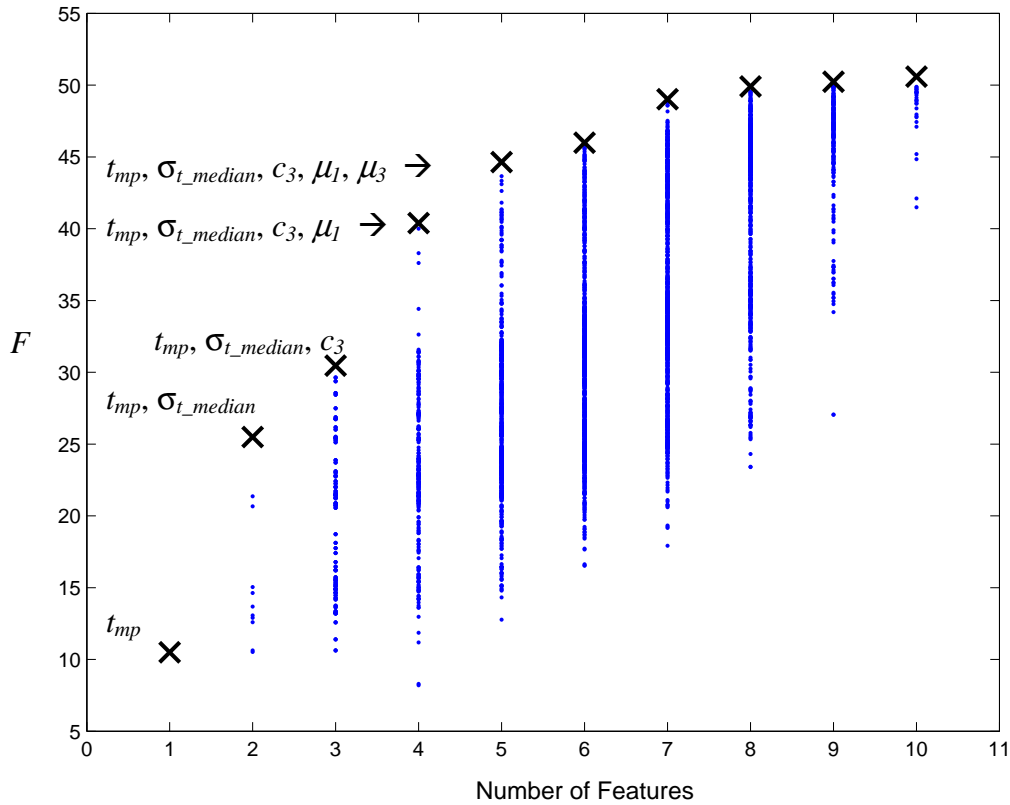


Figure 23. Examining every feature combination from one feature to all ten feature combinations provides one quantitative method to determine how many features are necessary for classification. The "X" data points represent the N-feature combination with the highest Fisher ratio, F . The remaining dots represent all the other N-feature combinations. The 11 through 14 feature combinations are not shown because they did not satisfy the 100% correctly classified criteria.

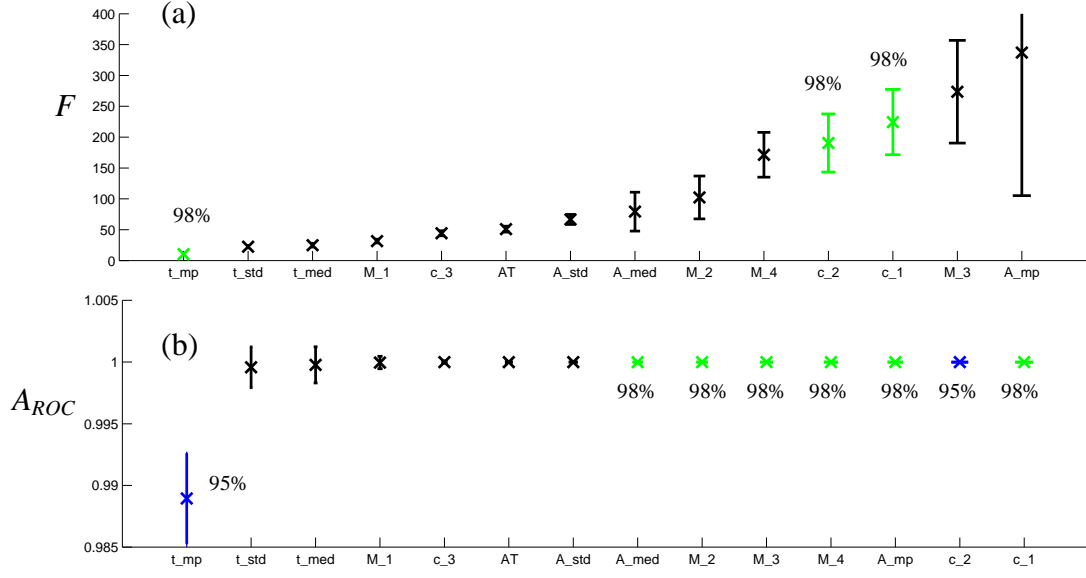


Figure 24. Feature saliency is a product of leave-one-out and finding the best features with the highest Fisher ratio F (Fig. a) or area under the receiver operating characteristic (ROC) curve A_{ROC} (Fig. b). Once the single best feature is determined, it is fixed while finding the next best feature. The percent of iterations of the leave-one-out process that correctly classified the left-out event into one of the two possible classes is indicated, except for those that are 100%. The error bars represent the standard deviation of the mean F and mean A_{ROC} for each feature combination.

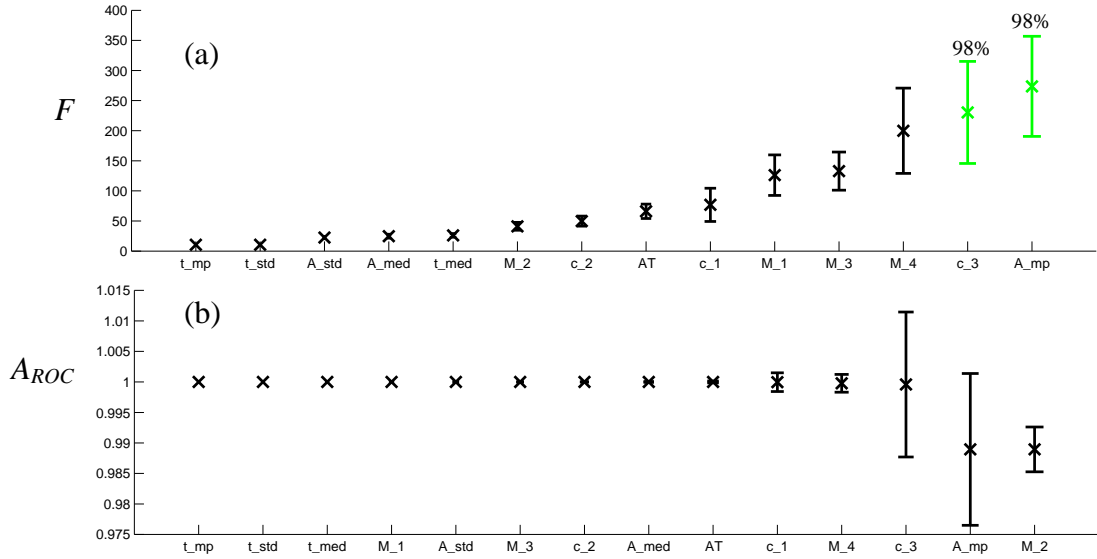


Figure 25. Similar to Figure 24, Feature saliency is a product of leave-one-out and finding the best features with the highest Fisher ratio F (Fig. a) or highest A_{ROC} (Fig. b), except this time features are eliminated down from 14 to 1. In this example, A_{mp} was the first feature to be eliminated.

One measure of confidence in the selection of the best features is a strong correlation between the three approaches. This however is not possible with the area derived feature set because many of the features are not independent of one another. For this reason, once the number of features exceeds five or six, the improvement in Fisher ratios and A_{ROC} s decline and the stability worsens (discussed next). Despite this handicap, the following findings are clear: (1) the first four “best” features in Figure 24 agree with the 1-, 2-, 3-, and 4-feature combinations with the highest Fisher ratio (Figure 23), (2) the best single feature t_{mp} agrees in all three approaches, and (3) the Fisher ratio and A_{ROC} stop improving significantly after two features.

4. *Stability of class-conditional probability densities*

In addition to the Fisher ratio, another metric to track is the stability of the class-conditional probability densities for each iteration of the leave-one-out process. In terms of stability, each pair of $p(x/c_i)$ should remain nearly constant during validation. For example, Figure 21 actually shows the average class-*likelihoods* of all the iterations in the leave-one-out process when three features are examined. Each individual class-*likelihood* for the same examination is shown in Figure 26. The vertical lines in this figure are the “left-out” events projected onto x and dashed according to the classification rules. For example, any dashed vertical lines less than $x = 1$ would be incorrectly classified into the class shown with the solid lines. In this example, all the left-out events are classified 100% correctly. The average $p(x/c_i)$ is a Gaussian with its center and variance equal to the mean center and mean variance of all the densities generated by each leave-one-out training set. Two measures for stability are the standard deviation of the center values and the standard deviation of the peak values for each individual $p(x/c_i)$.

As the standard deviations for a given feature set increase, the stability decreases. For example, the results from the all-feature combinations approach and the forward-best features approach are given in Figure 27 and Figure 28, respectively. They are similar in that the stability decreases as the number of features increases. Even though the absolute values change only slightly, the results using the “best” features provide some insight. The $\sigma_{centers}$ suggests that the two features $\{ t_{mp}, \sigma_{t_median} \}$ are more stable than a t_{mp} alone or even the first three feature combinations. On a similar note, σ_{peaks} suggests that the first two features provide the best stability and the stability worsens as more features are included.

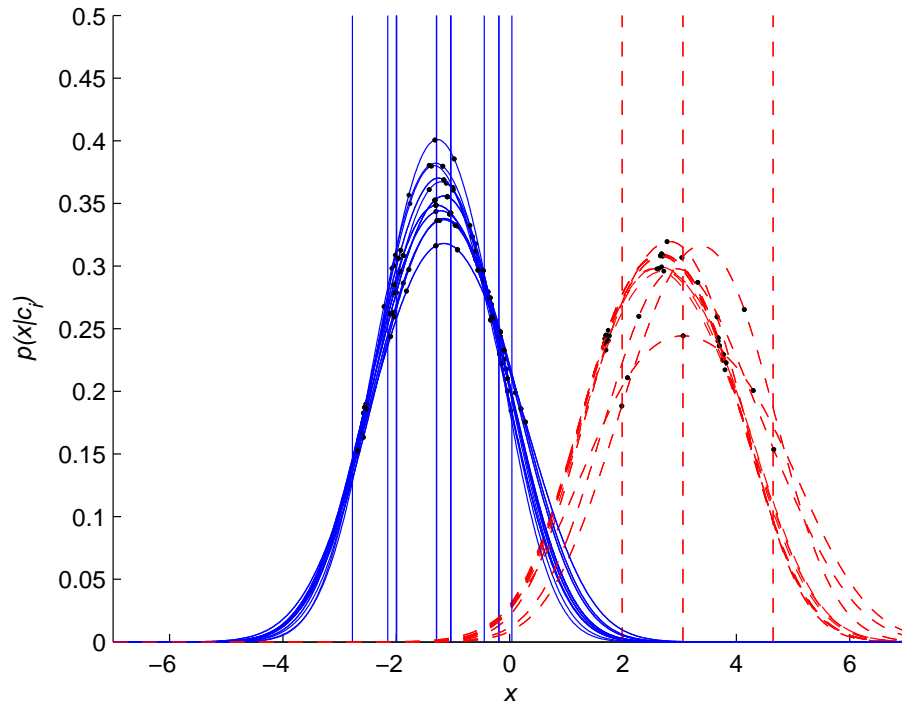


Figure 26. Class-conditional probability density functions, $p(x/c_i)$, show the probability density of measuring a particular Fisher line value x given the event is in one of two classes, $c_1 = \text{ENE}$ (—) and $c_2 = \text{TNT}$ (- - -). This Fisher line is determined by maximizing the Fisher ratio using two features: t_{mp} and σ_{t_median} . The densities are normalized, thus the area under each curve is unity. The dots (\cdot) are events used in training.

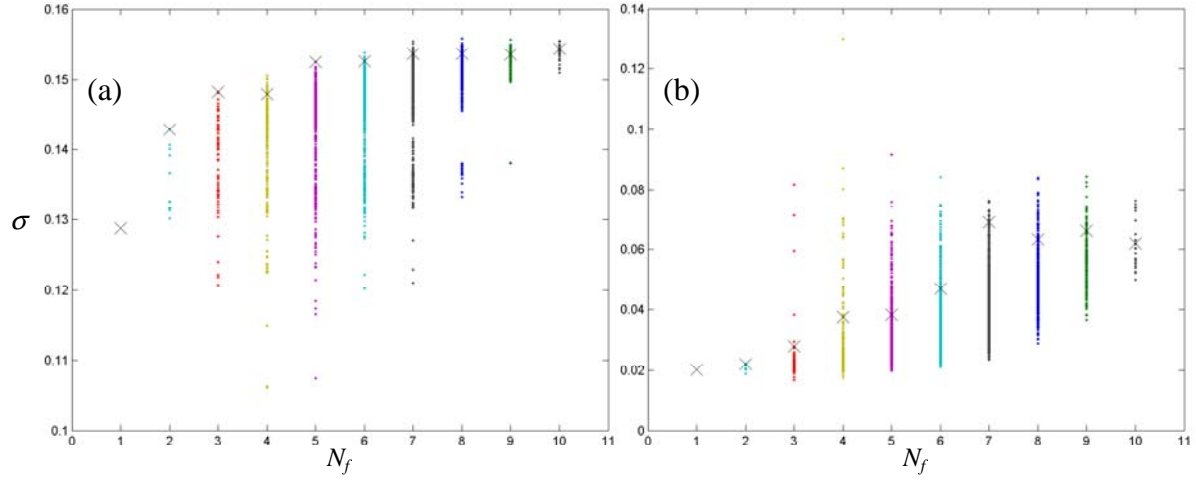


Figure 27. The mean standard deviation of (a) the peak centers, $\sigma_{centers}$, and (b) the peak values, σ_{peaks} , from each pair of individual $p(x/c_i)$ and from each leave-one-out iteration is a useful metric to quantify $p(x/c_i)$ stability as a function of number of features. The number of features N_f is indicated on the abscissa and the data points represent each combination of N-features. The "X" data points represent the N-feature combination with the highest Fisher ratio. Notice, as the number of features increase the stability decreases or σ 's increases.

Combining the stability and Fisher ratio metrics, one possible conclusion is to use the most probable time and the standard deviation of the median time as the two features for classifying between TNT and ENE at the 50-kg weight. The corresponding average and individual class-conditional probability densities (or *likelihoods*) are provided in Figure 21 and Figure 26, respectively. The corresponding two-dimensional feature set scatter plot is given in Figure 20. For reference, the densities for the set $\{ t_{mp}, \sigma_{t_median}, t_{median} \}$ are shown in Figure 29 and for the single t_{mp} feature are provided in Figure 30.

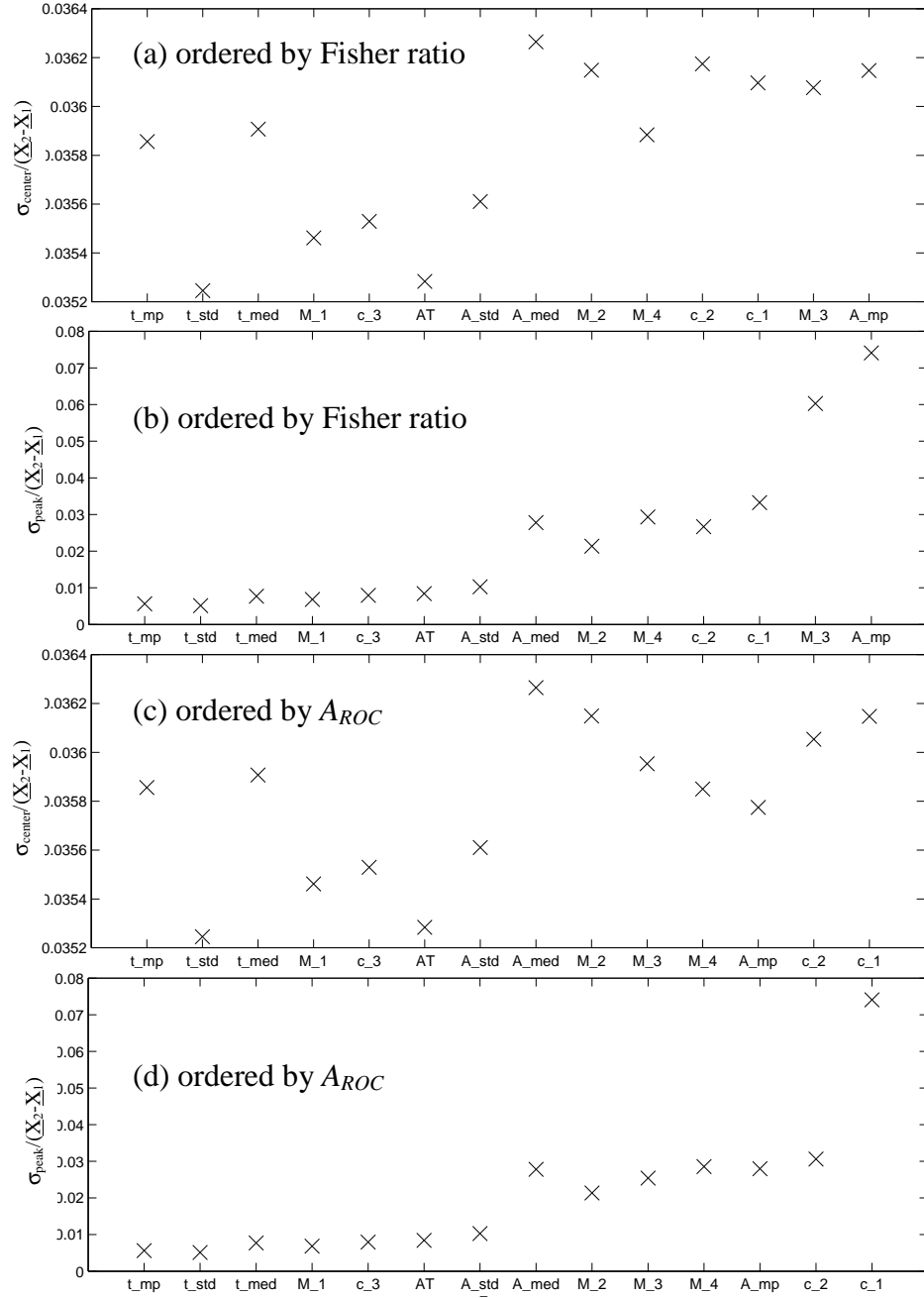


Figure 28. Similar to Figure 27, the center (a, c) and peak (b, d) standard deviations of the *likelihoods* are calculated for each feature combination derived from the "best" features shown in Figure 24. The standard deviations are normalized by the separation between the class-conditional densities. The colors are described in Figure 24's caption.

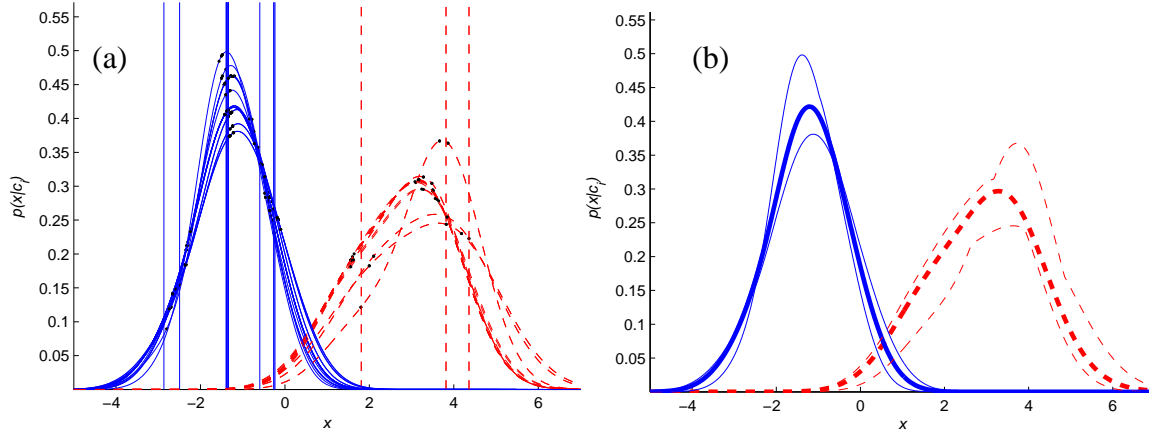


Figure 29. Class-conditional probability density functions, $p(x/c_i)$ or *likelihoods*, for the three-feature set $\{t_{mp}, \sigma_{t_median}, t_{median}\}$ show the probability density of measuring a particular Fisher line value x given the event is in one of two classes, $c_1 = \text{ENE}$ and $c_2 = \text{TNT}$. This Fisher line is determined by maximizing the Fisher ratio using the three features. The density functions are normalized, and thus the area under each curve is 1.0. Figure (a) has each $p(x/c_i)$ from the leave-one-out process where the vertical lines are the “left-out” events projected onto x and colored according to the classification rules. Figure (b) contains the average $p(x/c_i)$ along with confidence intervals.

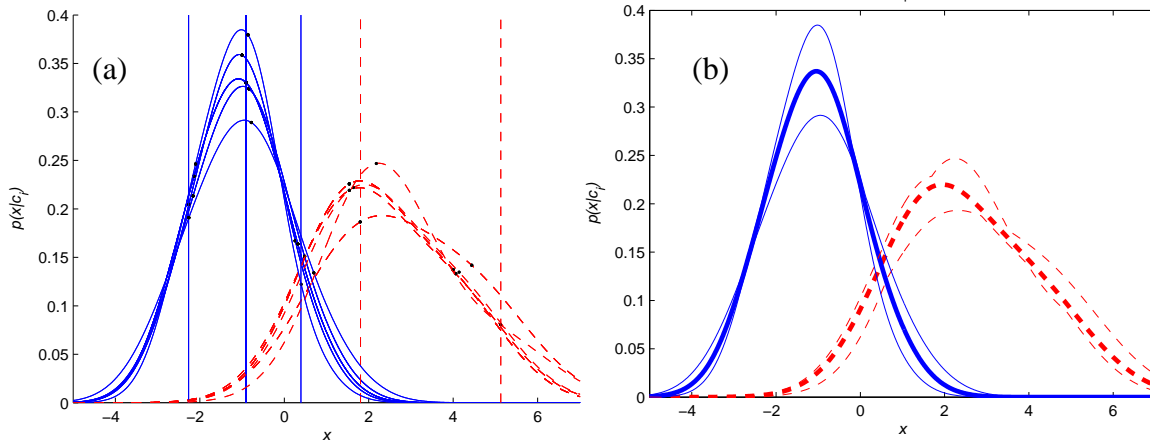


Figure 30. Same as Figure 29 except the features set is a single feature: t_{mp} .

D. Testing

The discussion and analysis to this point exploit only near-infrared imagery from Brilliant Flash II which suggests that the following two features are recommended to achieve the objective of stable classification: the most probable time and the standard deviation of the median time. Before examining the three-chip color images for key features (Section IV-0), two scenarios are now employed to test the near-infrared features' classification performance. The first uses the Brilliant Flash II data as the training and validation data and the Brilliant Flash I data as the test data. The second scenario combines both the test series, selects a random five events as the test data and uses the remaining events as the training set. At least four additional random choices or test cases are examined. Repeatedly choosing a random set for testing is called "bootstrapping." [51: 474] The five outcomes of the bootstrapping test provide insight into the most important features independent of test data. These features are further examined during robust testing (Section IV-G).

1. *Testing with Brilliant Flash I data*

Using Brilliant Flash I as a test case to evaluate the class-conditional probability densities derived in the previous section yields a 82% accuracy in classification when using the single feature $\{ t_{mp} \}$, 64% for $\{ t_{mp}, \sigma_{t_median} \}$, and 27% for $\{ t_{mp}, \sigma_{t_median}, \sigma_{A_median} \}$. The two-feature set doubles the Fisher ratio and increases the area under the ROC curve (A_{ROC}) to one. Even with these improvements, the percent of the Brilliant Flash I events that are correctly classified decreases to 64%. Additional features provide little or no improvement in the Fisher ratio or the A_{ROC} as shown in Table 10 and Figure 31. The class-conditional probabilities and posteriors for the sets

$\{t_{mp}\}$ and $\{t_{mp}, \sigma_{t_median}\}$ given in Figure 32 show increased class separation and *likelihood* stability using two features for discrimination.

Table 10. Record of test results where Brilliant Flash II data is the training data and Brilliant Flash I is the testing data. FR is the Fisher ratio. A_{ROC} is the area under the receiver operating characteristic curve. σ is the standard deviation.

Training Set	Testing Set	Best 5 Forward Features	FR	σ_{FR}	A_{ROC}	$\sigma_{A_{ROC}}$	% Correct	Best 5 Backward Features
Brilliant Flash II	Brilliant Flash I	t_{mp}	12	0.9	0.992	0.004	82	σ_{t_median}
		σ_{t_median}	33	7	1	0.001	64	A_{median}
		σ_{A_median}	59	33	1	<0.001	27	c_2
		c_2	79	40	1	<0.001	45	μ_1
		A_{median}	96	37	1	<0.001	73	μ_4
		t_{median}	211	98	1	<0.001		t_{mp}
		\underline{A}	612	123	1	<0.001		t_{median}
		c_3	882	436	1	<0.001		c_3
		μ_2	*	*	1	<0.001		\underline{A}
		μ_4	*	*	1	<0.001		μ_2
		A_{mp}	*	*	1	<0.001		A_{mp}
		c_1	*	*	1	0.2		μ_3
		μ_3	*	*	1	0.002		c_1
		μ_1	*	*	1	0.002		
								σ_{A_median}

It is important to remember that these features are parametric and not physical. Many of them could be represented by linear (or possibly non-linear) combinations of other features. These tools, even with the small amount of test data, provide a mechanism to determine those few features that provide the best classification. Specifically, the drop in the testing performance may be analogous to adding additional features to a curve fitting problem: the more terms you add, the better the fit goes through the data, yet the prediction performance potentially declines.

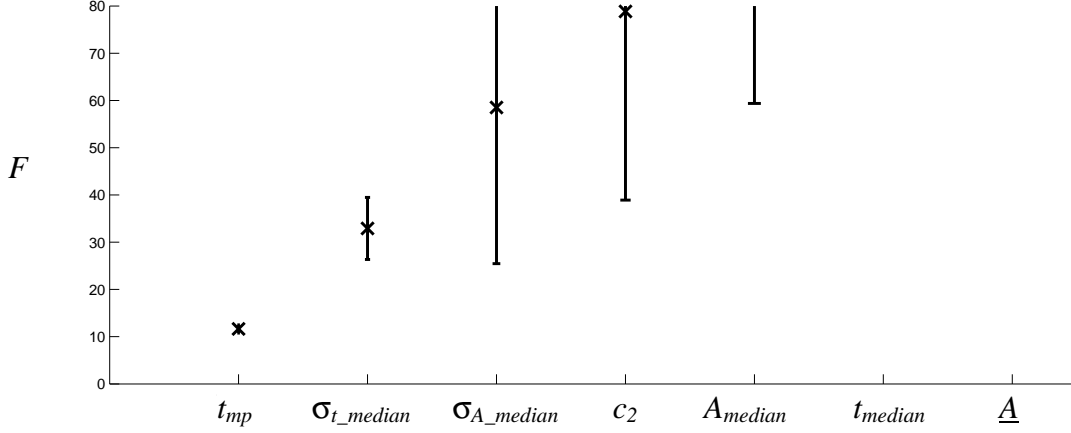


Figure 31. Resulting feature saliency measured by the Fisher ratio when using all of Brilliant Flash II data for training and all of Brilliant Flash I for testing. The colors are described in the caption for Figure 24.

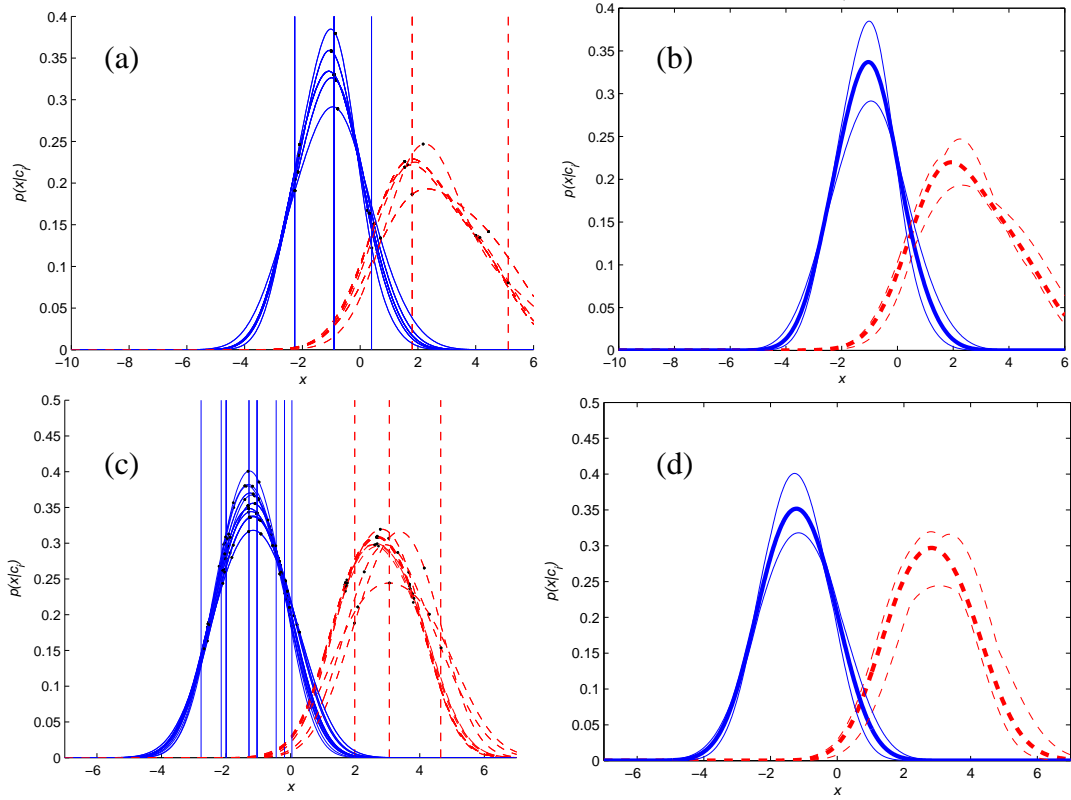


Figure 32. Class-conditional *likelihoods* $p(x/c_i)$ resulting from the feature sets $\{t_{mp}\}$ (Figs. a and b) and $\{t_{mp}, \sigma_{t_median}\}$ (Figs. c and d) using Brilliant Flash II data for training and Brilliant Flash I data for testing. Figures (a) and (c) contain the individual *likelihoods* generated during training and validation using leave-one-out. Figures (b) and (d) contain the average of the training *likelihoods* with confidence intervals. Solid = ENE; dashed = TNT.

2. *Bootstrapping with combined Brilliant Flash tests*

Combining Brilliant Flash I and Brilliant Flash II data gives 26 50-kg events from which the “bootstrap” method is applied. The bootstrap data consists of 21 random events for training and validation purposes and of 5 random events for testing. Using the 21 training events, the forward-back and leave-one-out techniques are employed to determine feature saliency and appropriate class-conditional probability density functions and posteriors. Each test event is classified according to the class-conditional posteriors generated by the training data for the best single feature, the best two-feature combination, and so forth, up to the best five-feature combination.

The results of five independent test scenarios are provided in Table 11 for the best features ranked by the area under the ROC (A_{ROC}) curve. Identical results are obtained when the best features are ranked by the Fisher ratio. Overall, the Fisher ratios and A_{ROCs} are much worse than when only the Brilliant Flash I data was the test case; however, the performance of the test cases are significantly better, *e.g.* 80% to 100% correct versus 82% down to 27% in the previous test scenario. Nevertheless, the bootstrap results suggest that the t_{mp} feature provides the needed stability along with adequate classification capability as visually represented in Figure 33.

With only a slight degrade (1 in 5) in classification stability between test cases, the two-feature set $\{t_{mp}, \mu_3\}$ provides a marginal improvement in classification shown by the Fisher ratio increase of about one and by the class-conditional probability densities in Figure 34. This figure also contains the two dimensional scatter plot of the events as a function of μ_3 vs t_{mp} . The shallow Fisher line slope is another indication that t_{mp} alone may be sufficient to classify the two classes.

Table 11. Selecting a random set of five events from two test series, Brilliant Flash I and Brilliant Flash II, as the test set and using the remaining events for training and validation yields the following results in the percent of the test set that was classified correctly (last column) based upon a feature set sorted by the best area under the receiver operating characteristic curve (A_{ROC}). t_{mp} is consistently the “best” feature derived from the forward-back routine. FR is the Fisher ratio. σ is the standard deviation.

Random Choice	Test Types	Test Series	Test Event No.	Best 5 Forward Features	FR	σ_{FR}	A_{ROC}	$\sigma_{A_{ROC}}$	% Correct
1	TYPED	BFI	29	t_{mp}	2.0	0.4	0.84	0.02	100
	TNT	BFII	24	μ_3	3.2	0.5	0.90	0.02	100
	TYPEB	BFII	13	c_2	5.9	0.9	0.96	0.02	80
	TYPEB	BFII	15	A_{mp}	6.9	0.9	0.97	0.01	100
	TYPEB	BFII	12	A_{median}	11	2	0.99	0.01	80
2	TNT	BFII	43	t_{mp}	1.0	0.4	0.76	0.03	100
	TNT	BFII	30	μ_3	1.9	0.4	0.83	0.02	100
	TYPED	BFII	18	c_1	2.6	0.6	0.87	0.02	100
	TNT	BFII	39	t_{median}	3.3	0.5	0.90	0.02	100
	TNT	BFI	23	A_{mp}	4.1	0.6	0.92	0.02	100
3	TYPEC	BFI	2	t_{mp}	3.1	0.9	0.89	0.03	80
	TNT	BFII	43	c_1	8	1	0.98	0.01	60
	TYPEB	BFII	12	μ_3	10	1	0.988	0.009	60
	TNT	BFI	25	\underline{A}	14	2	0.996	0.007	60
	TYPED	BFI	18	μ_4	15	3	0.997	0.007	60
4	TYPED	BFI	19	t_{mp}	1.4	0.4	0.79	0.03	100
	TNT	BFII	39	μ_3	2.7	0.4	0.88	0.02	80
	TYPEC	BFII	8	c_1	3.2	0.6	0.90	0.02	100
	TNT	BFII	24	\underline{A}	4.0	0.7	0.92	0.02	100
	TNT	BFI	31	t_{median}	4.1	0.7	0.92	0.02	100
5	TNT	BFI	23	t_{mp}	2.2	0.5	0.85	0.02	100
	TYPEC	BFII	8	μ_3	3.7	0.5	0.91	0.02	80
	TYPEC	BFII	9	$\sigma_{t_{median}}$	4.7	0.7	0.94	0.02	80
	TYPED	BFI	19	c_1	5.3	0.9	0.95	0.02	100
	TYPED	BFI	30	A_{mp}	6	1	0.95	0.02	100

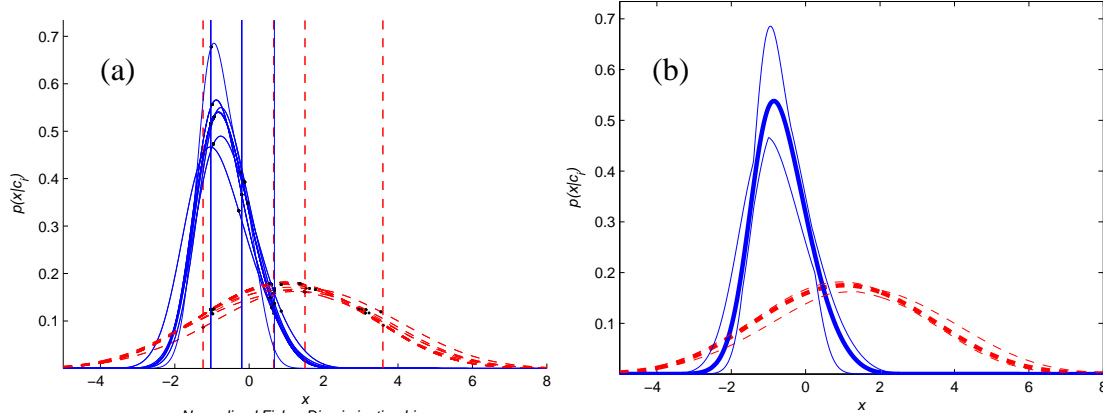


Figure 33. Class-conditional *likelihoods* $p(x/c_i)$ resulting from the feature set $\{t_{mp}\}$ using the first bootstrap data indicated in the first row of Table 11. Figure (a) contains the individual *likelihoods* generated during training and validation using leave-one-out. Figure (b) contains the average of the training *likelihoods* and the confidence intervals. Solid = ENE; dashed = TNT.

The bootstrap results also provide some guidance as to which features are consistently ranked high in discriminator importance—irregardless if they are necessary for classification. These results suggest that one feature saliency list may be $\{t_{mp}, \mu_3, c_1, A_{mp}\}$. Forcing this feature list on all the combined Brilliant Flash I and II data results in around 85% classification performance as shown in Figure 35 where the measures of merit are again the Fisher ratio and the A_{ROC} .

E. Applying discrimination tools to Cannon 3-chip color images

The tools described in the previous section are now employed to examine the images from a Cannon XL1 3-chip camera which simultaneously recorded the same events as the NIR camera above. The next section explores the combined features sets from both cameras. At 30 Hz, the Cannon camera records the images onto three sections of the CCD, one for each primary color (RGB). During post processing, these colors are independently extracted to obtain RGB images as a function of time from which features

are extracted. Like the NIR image processing, the histogram for each color image is exploited to generate an appropriate area as a function of time, each of which is displayed in Figure 36 (for Brilliant Flash II series) and Figure 37 (for Brilliant Flash I series).

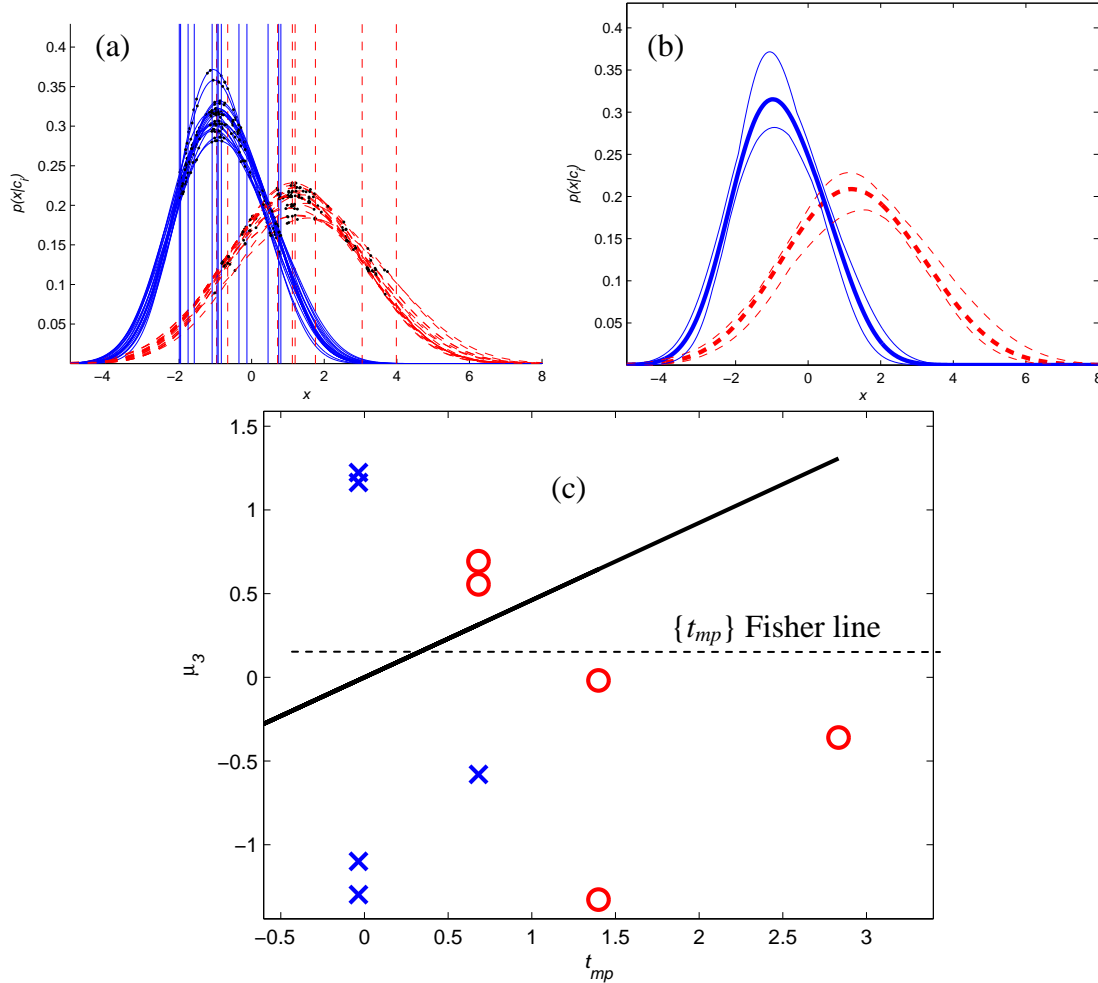


Figure 34. Class-conditional *likelihoods* $p(x/c_i)$ resulting from the feature set $\{t_{mp}, \mu_3\}$ using the first bootstrap data indicated in the first row of Table 11. Figure (a) contains the individual *likelihoods* generated during training and validation using leave-one-out. Figure (b) contains the average of the training *likelihoods* and the confidence intervals. Figure (c) displays the events features on a two dimensional scatter plot. Solid (X) = ENE; dashed (O) = TNT.

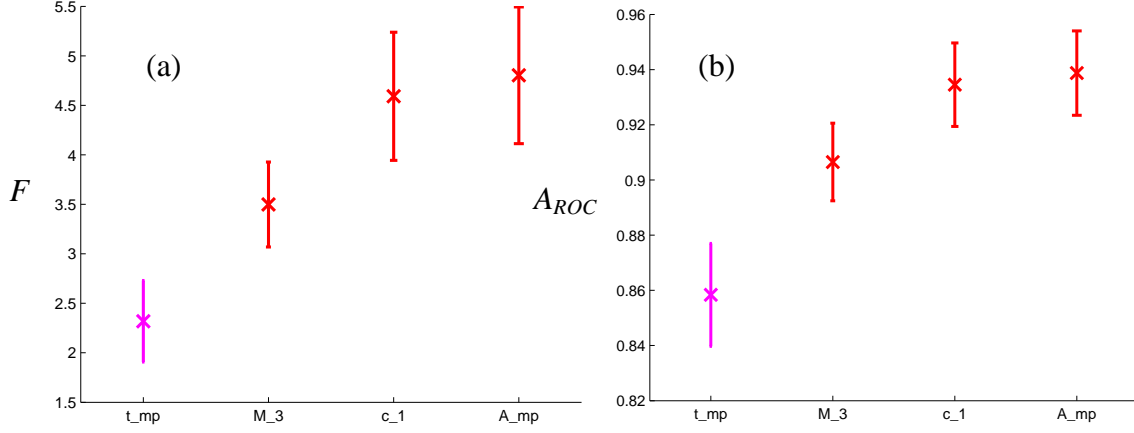


Figure 35. A subjective evaluation of the five test cases' results using A_{ROC} suggests the best features shown in this figure. Using this set and order of features, each test case is evaluated and the resulting (a) Fisher ratio and (b) A_{ROC} are displayed here as a function of the feature set. Each feature set beyond t_{mp} alone has less than 22 out of the 26 events (<85%) classified correctly during the leave-one-out. Using only t_{mp} , 23 of the 26 events (88%) are classified correctly.

In both series, the area in the blue band is shorter lived and smaller than the other colors. Type A is reproducible within 10-12% in the red and green bands; whereas the area in the blue band for Type A varies up to 67%. With exception to a few outliers, Type B is reproducible within 25-50% and Type C is reproducible within 7-15% across each color band. Type D is reproducible within 17-30%. In general, the areas for each color band originating from the Brilliant Flash I test series are less reproducible, *e.g.* 22% to 90% in variations. While Type D shows most reproducible in Brilliant Flash II tests, it is the least reproducible in Brilliant Flash I.

Two test scenarios are now employed with two defined classes: Type A as TNT and Types B through D as ENE. The first test uses the Brilliant Flash II data as the training and validation data and the Brilliant Flash I data as the test data. The second test

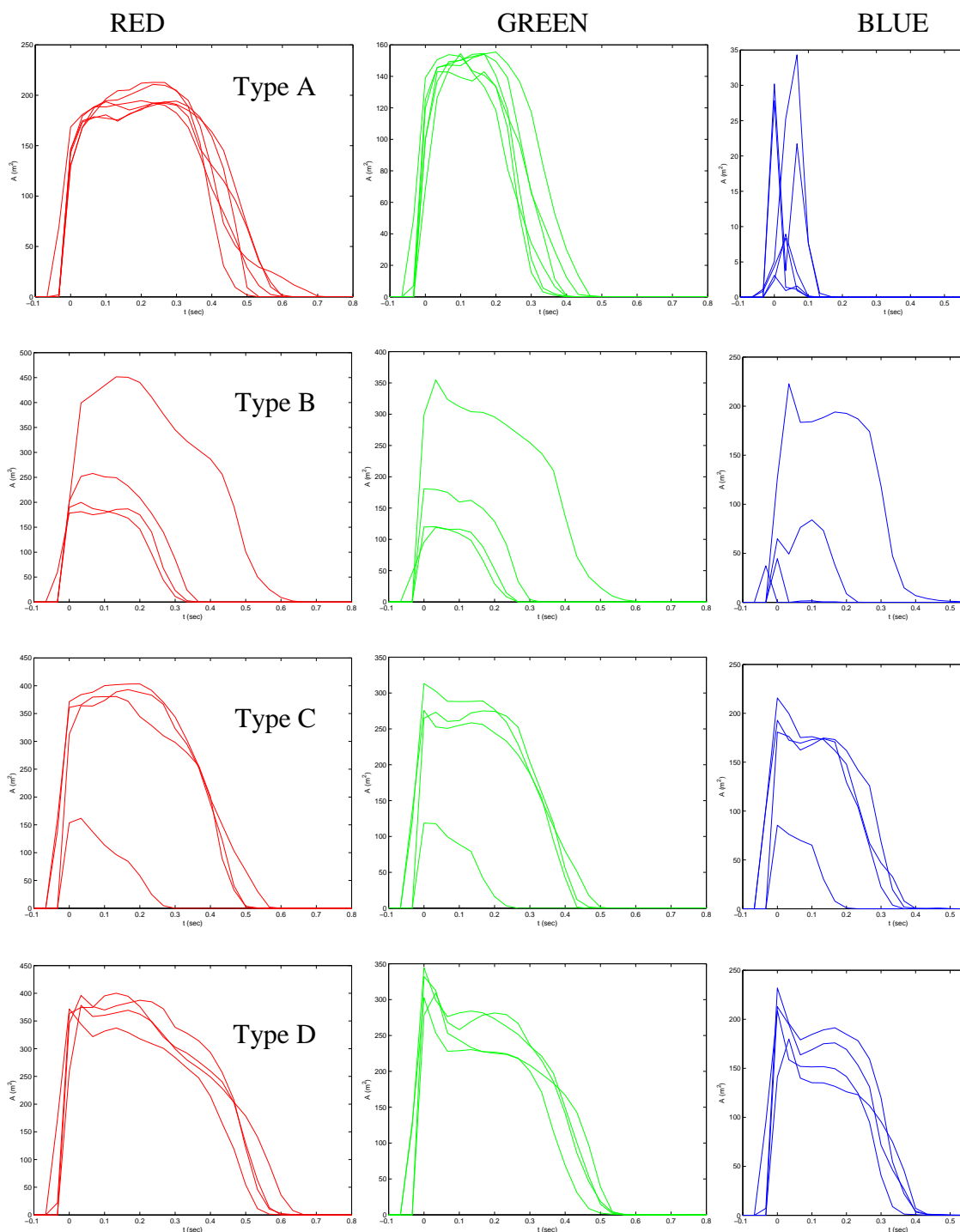


Figure 36. The 3-chip color area plots shown here aid in feature extraction and provide an overview of their potential to distinguish TNT from the enhanced explosives detonated in the Brilliant Flash II. The two-class discrimination problem groups Types B through D into one class called ENE.

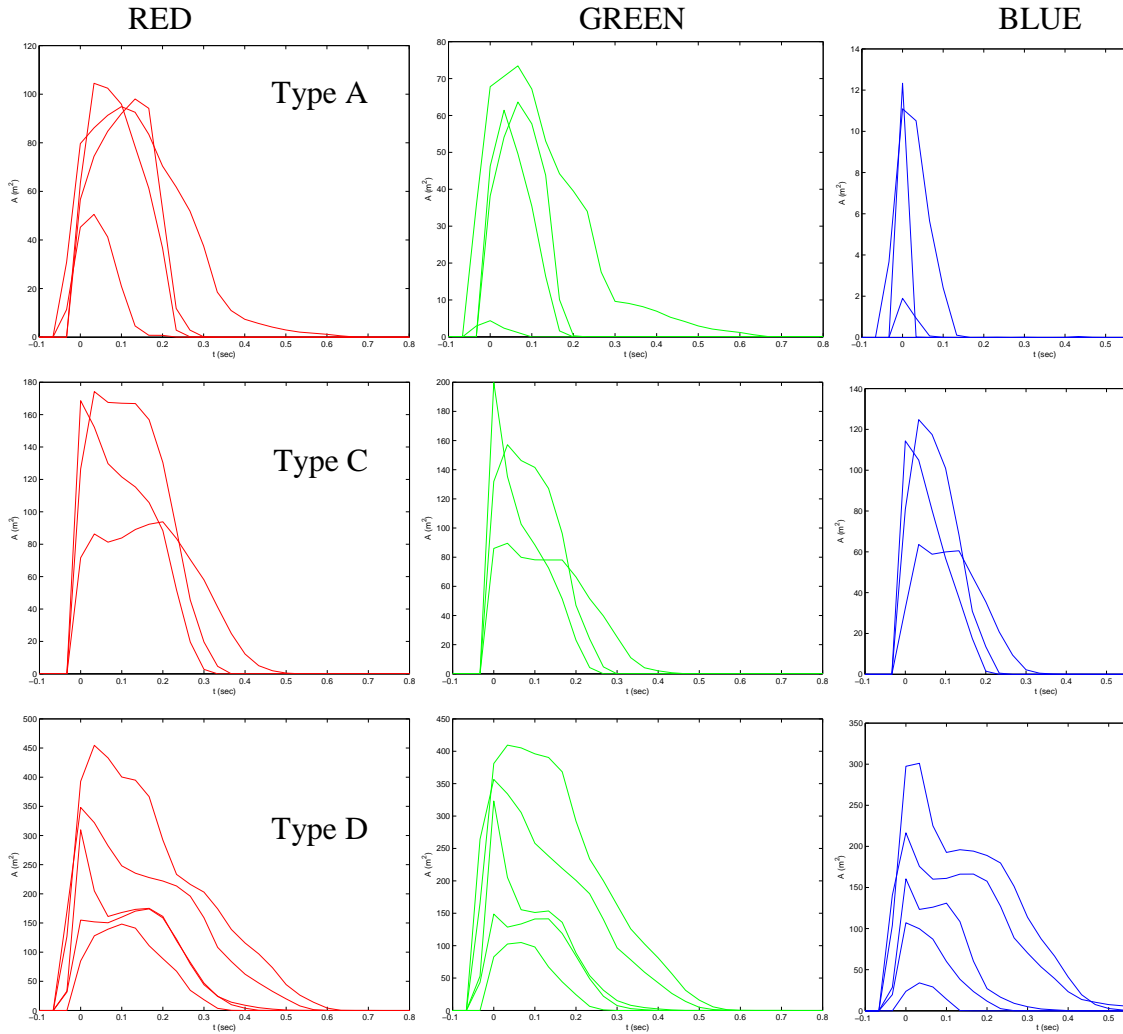


Figure 37. The 3-chip color area plots shown here aid in feature extraction and provide an overview of their potential to distinguish TNT (Type A) from the enhanced explosives (Types C and D) detonated in the Brilliant Flash I series. Type B was not tested in Brilliant Flash I.

scenario is bootstrapping which combines both test series, selects a random five events as the test data and uses the remaining events for training. Five test cases are examined.

1. Testing with Brilliant Flash I data

Using only the events common to both the NIR and 3-chip recorded events, Brilliant Flash II 3-chip data is used for training and Brilliant Flash I 3-chip data is used for

testing. The resulting percent of correctly classified test data along with the classification statistics of Fisher ratio and A_{ROC} are presented in Table 12. These results show less

Table 12. Record of Cannon 3-chip data test results where Brilliant Flash II data is the training data and Brilliant Flash I is the testing data. Feature saliency is found by ranking with the Fisher ratio (FR). A_{ROC} is the area under the receiver operating characteristic curve. σ is the standard deviation. The RGB is in parentheses.

Training Set	Testing Set	Best 5 Forward Features	FR	σ_{FR}	A_{ROC}	$\sigma_{A_{ROC}}$	% Correct
Brilliant Flash II	Brilliant Flash I	$A_{mp}(B)$	6	1	0.95	0.02	91
		$t_{median}(R)$	47	6	1	8E-5	64
		$\mu_3(B)$	97	13	1	4E-8	82
		$\mu_4(B)$	167	27	1	2E-12	82
		$t_{median}(B)$	283	78	1	7E-16	82

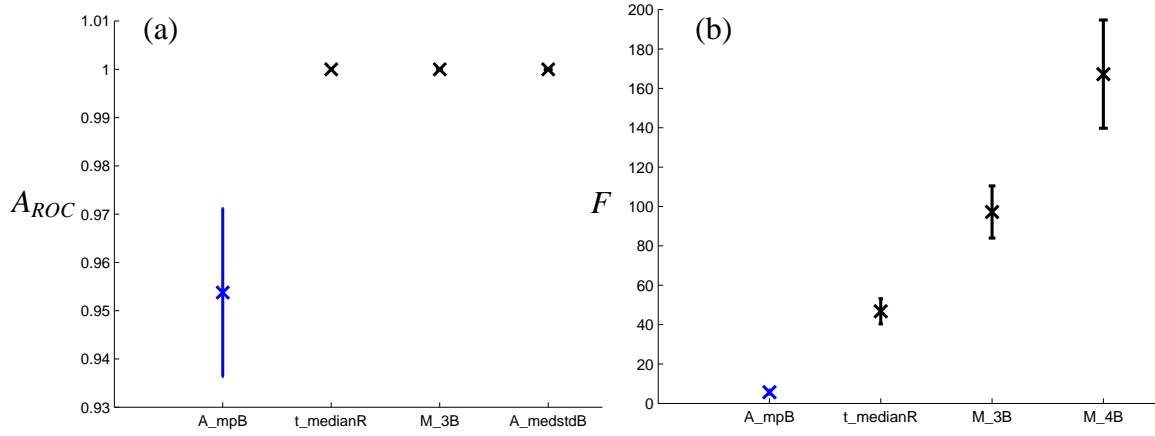


Figure 38. The best features, ranked by their (a) A_{ROC} or (b) Fisher ratio F , are generated for the 3-chip images. Once a feature is determined as best, it is fixed before finding the next best feature. The data points represent the mean and standard deviation from the leave-one-out process.

classified correctly events from the test set as additional features are included into the discrimination model despite an increase in class separation and clustering as quantified

by the Fisher ratio and A_{ROC} . As Figure 38 shows, the A_{ROC} stops improving after two features and the Fisher ratio has significantly improved. While adding a third feature improves the Fisher ratio, it marginally improves the ROC performance. With regards to the stability of the class-conditional densities represented in Figure 39, more features cause the density center stability to decline. Likewise, only two features are necessary to maximize the density peak stability. These effects are directly observed in the actual densities, *e.g.*, the densities derived from the first two feature sets are given in Figure 40.

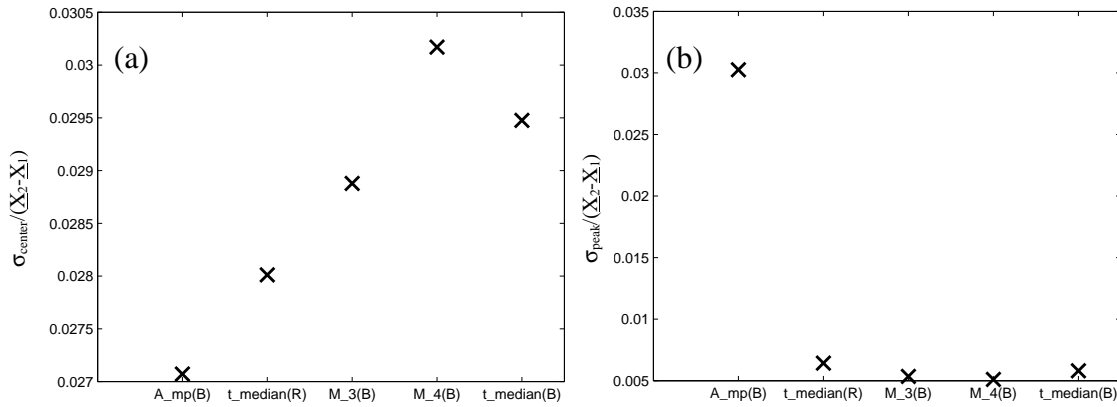


Figure 39. The mean standard deviation of the peak (a) centers, $\sigma_{centers}$, and (b) the values, σ_{peaks} , from each pair of $p(x/c_i)$ and from each leave-one-out iteration quantifies $p(x/c_i)$ stability as a function of number of features.

2. Bootstrapping with combined Brilliant Flash tests

Combining Brilliant Flash I and Brilliant Flash II data gives 26, 50-kg events from which “bootstrap” data is generated. The bootstrap data consists of 21 random events for training and validation purposes and of 5 random events for testing. With 26 total events, there are 65,780 possible permutations to select 5 random events for testing. Using the 21 training events, the forward-back and leave-one-out techniques are

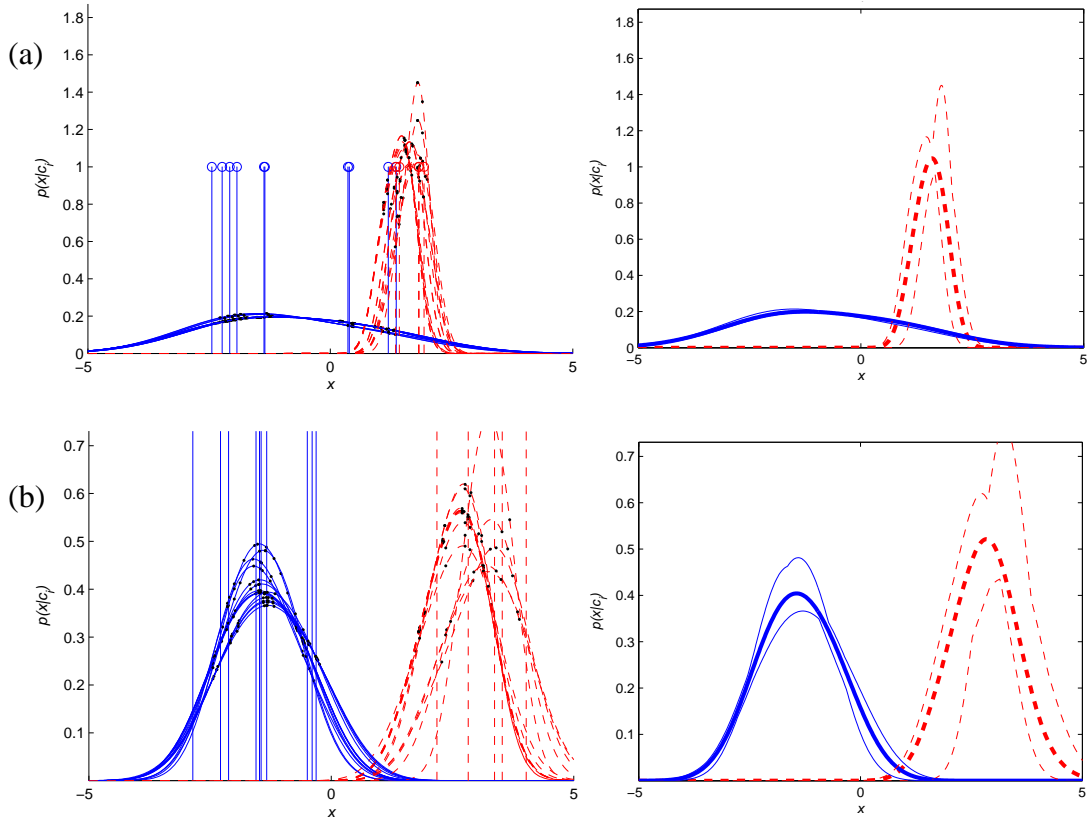


Figure 40. Class-conditional *likelihoods* $p(x/c_i)$ resulting from the feature sets (a) $\{Amp(B)\}$ and (b) $\{Amp(B), t_{median}(R)\}$ using the Brilliant Flash II series as the training set. The left column contains the individual results from the leave-one-out; the right column is the average *likelihoods* and corresponding confidence intervals. The solid lines are ENE; the dashed lines are TNT.

employed to determine feature saliency and appropriate class-conditional probability density functions and posteriors. Each test event is classified according to the class-conditional posteriors generated by the training data for the best single feature, the best two-feature combination, and so forth, up to the best five-feature combination. The results of five independent test scenarios are provided in Table 13 for the best features ranked by the Fisher ratio. The results for the best features ranked by the area under the receiver operating characteristic curve (A_{ROC}) are nearly identical. Overall, the Fisher

ratios, A_{ROC} s, and performance show little or no improvement over the previous case where only the Brilliant Flash I data was the test case. Additionally, the bootstrap results suggest that no single feature or set of features provides the needed stability and classification capability to distinguish TNT from ENE when using only the 3-chip color images.

Table 13. Record of Cannon 3-chip data bootstrapping test results where Brilliant Flash I and II data are combined and a random set of five events are chosen to be test data. The best features are sorted by their Fisher ratio. FR is the Fisher ratio. A_{ROC} is the area under the receiver operating characteristic curve. σ is the standard deviation.

Random Choice	Test Types	Test Series	Test Event No.	Best 5 Forward Features	FR	σ_{FR}	A_{ROC}	$\sigma_{A_{ROC}}$	% Correct
1	TYPED	BFI	29	$\sigma_{A_median}(B)$	10	2	0.988	0.010	60
	TNT	BFII	24	$\sigma_{A_median}(G)$	15	4	0.997	0.008	40
	TYPEB	BFII	13	$t_{mp}(B)$	24	8	1.000	0.004	60
	TYPEB	BFII	15	$\mu_2(B)$	27	11	1.000	0.003	60
	TYPEB	BFII	12	$\mu_2(R)$	34	14	1.000	0.002	60
2	TNT	BFII	43	$A_{mp}(B)$	5.6	0.5	0.953	0.010	60
	TNT	BFII	30	$\underline{A}(B)$	12	1	0.993	0.005	60
	TYPED	BFII	18	$\mu_2(B)$	21	2	0.999	0.003	60
	TNT	BFII	39	$c_2(B)$	29	4	1.000	0.001	60
	TNT	BFI	23	$\mu_1(G)$	36	10	1.000	0.001	60
3	TYPEC	BFI	2	$c_3(B)$	6.6	0.6	0.964	0.010	60
	TNT	BFII	43	$\underline{A}(B)$	11	1	0.991	0.008	60
	TYPEB	BFII	12	$A_{mp}(B)$	15	2	0.997	0.006	60
	TNT	BFI	25	$\mu_2(B)$	18	5	0.998	0.007	80
	TYPED	BFI	18	$c_1(B)$	25	11	1.000	0.005	80
4	TYPED	BFI	19	$A_{mp}(B)$	5.5	0.5	0.951	0.010	100
	TNT	BFII	39	$\underline{A}(B)$	11	1	0.990	0.008	80
	TYPEC	BFII	8	$t_{mp}(G)$	14	2	0.996	0.005	80
	TNT	BFII	24	$\mu_2(G)$	22	5	0.999	0.004	80
	TNT	BFI	31	$c_2(B)$	26	11	1.000	0.005	60
5	TNT	BFI	23	$A_{mp}(B)$	5.8	0.5	0.96	0.01	80
	TYPEC	BFII	8	$\underline{A}(B)$	11	1	0.990	0.008	80
	TYPEC	BFII	9	$t_{mp}(G)$	18	2	0.999	0.004	60
	TYPED	BFI	19	$\mu_2(G)$	36	4	1.0000	0.0003	60
	TYPED	BFI	30	$c_2(B)$	50	7	1.0000	0.0001	60

Using the results of the five test cases, a subjective choice of best features could be $\{ A_{mp}(B), \underline{A}(B), \mu_2(B), t_{mp}(G) \}$. Fixing this order and computing the Fisher ratio and the A_{ROC} for each one-, two-, ... feature combination yields the results shown in Figure 41. Here, the A_{ROC} stops improving after adding $\underline{A}(B)$ while the FR continues to improve

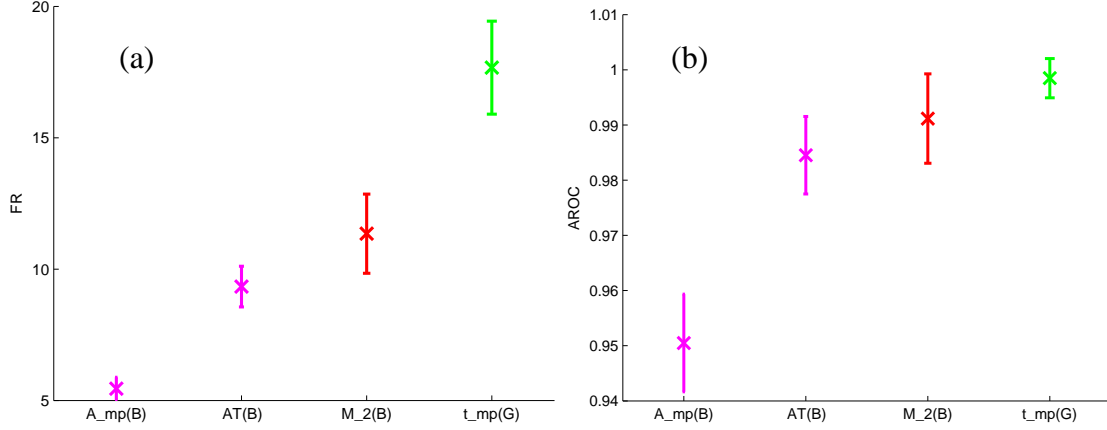


Figure 41. A subjective evaluation of the five test cases' results using the 3-chip data suggests the best features shown in this figure. Using this set and order of features, each test case is evaluated and the resulting (a) Fisher ratio and (b) A_{ROC} are displayed here as a function of the feature set.

as more features are added. With regard to stability, the optimum set is possibly

$\{ A_{mp}(B), \underline{A}(B) \}$ according to Figure 42 and Figure 43. Overall, an improvement in

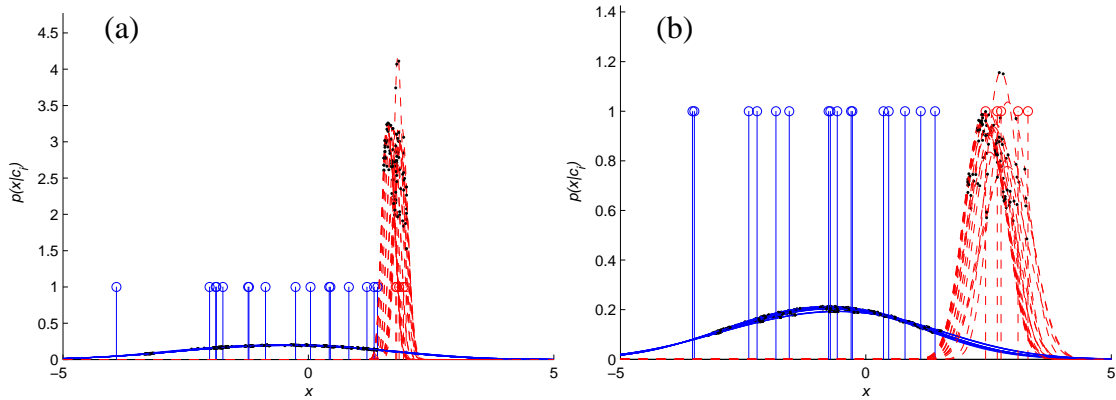


Figure 42. Class-conditional *likelihoods* $p(x/c_i)$ resulting from the feature sets (a) $\{ A_{mp}(B) \}$ and (b) $\{ A_{mp}(B), \underline{A}(B) \}$ using the second bootstrap result in Table 13. Each density is a result from the leave-one-out.

classification is achieved by utilizing the blue band image data. Possibly the best visible features which help in discrimination are from the blue band where the maximum fireball area and the area integrated over time is unique for ENE and TNT. Recall that TNT is observed to have a short duration and a small intensity in this band (refer to Figure 36 and Figure 37 for the area plots).

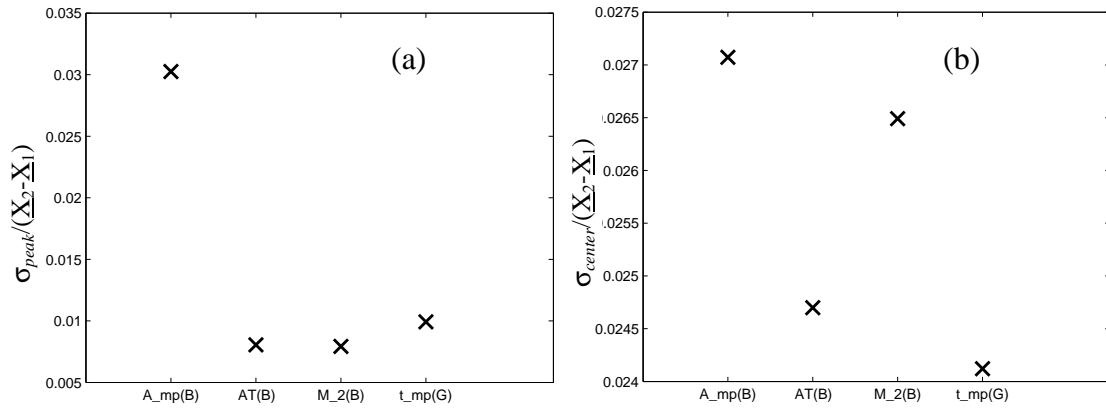


Figure 43. The mean standard deviation of (a) the peak centers, $\sigma_{centers}$, and (b) the peak values, σ_{peaks} , from each pair of individual $p(x/c_i)$ and from each leave-one-out iteration quantifies $p(x/c_i)$ stability as a function of number of features.

F. Applying discrimination tools to combined NIR and 3-chip images

Combining the NIR and the 3-chip color images into one data set gives 14 features for each of the four color bands (56 total features). The results of the two types of tests, (1) train with Brilliant Flash II and test with Brilliant Flash I and (2) bootstrapping with five test cases, are provided in Table 14 where the best features are sorted by the Fisher ratio. The results where the best features are sorted by the area under the receiver operating characteristic curve are almost identical to the Fisher ratio results, thus are not repeated in another table. The findings here suggest that more features

Table 14. Test results of combining NIR and Cannon 3-chip data for (1) Brilliant Flash (BF) II training and BF I testing and (2) combined BF I and BF II data with a random set of five test events. The best features are sorted by their Fisher ratio (FR), followed by the A_{ROC} . σ is the standard deviation. The RGB is in parentheses. No RGB letters signifies a NIR feature.

Random Choice	Test Types	Test Series	Test Event No.	Best 5 Forward Features	FR	σ_{FR}	A_{ROC}	$\sigma_{A_{ROC}}$	% Correct
NA		All BFI		t_{mp}	12	1	0.992	5E-03	82
				σ_{t_medstd}	33	7	1.000	8E-04	64
				$A_{mp}(B)$	90	29	1.000	3E-07	64
				$A_{mp}(G)$	211	66	1.000	5E-15	64
				t_{median}	1666	148	1.000	1E-15	64
1	TYPED	BFI	29	$\sigma_{A_medstd}(B)$	10	2	0.988	0.010	60
	TNT	BFII	24	$\sigma_{A_medstd}(G)$	15	4	0.997	0.008	40
	TYPEB	BFII	13	$t_{mp}(B)$	24	8	1.000	0.004	60
	TYPEB	BFII	15	t_{mp}	32	7	1.000	0.001	60
	TYPEB	BFII	12	$\sigma_{t_medstd}(B)$	40	18	1.000	0.0007	60
2	TNT	BFII	43	$A_{mp}(B)$	5.6	0.5	0.953	0.010	60
	TNT	BFII	30	$\underline{A}(B)$	12	1	0.993	0.005	60
	TYPED	BFII	18	$\mu_2(B)$	21	2	0.999	0.003	60
	TNT	BFII	39	$c_2(B)$	29	4	1.000	0.001	60
	TNT	BFI	23	$\mu_1(G)$	36	10	1.000	0.001	60
3	TYPEC	BFI	2	$c_3(B)$	6.6	0.6	0.964	0.010	60
	TNT	BFII	43	$\underline{A}(B)$	11	1	0.991	0.008	60
	TYPEB	BFII	12	$A_{mp}(B)$	15	2	0.997	0.006	60
	TNT	BFI	25	t_{mp}	21	2	0.999	0.003	80
	TYPED	BFI	18	$t_{median}(B)$	52	7	1.000	0.00006	60
4	TYPED	BFI	19	$A_{mp}(B)$	5.5	0.5	0.951	0.010	100
	TNT	BFII	39	$\underline{A}(B)$	11	1	0.990	0.008	80
	TYPEC	BFII	8	$t_{mp}(G)$	14	2	0.996	0.005	80
	TNT	BFII	24	$\mu_2(G)$	22	5	0.999	0.004	80
	TNT	BFI	31	$c_2(B)$	26	11	1.000	0.005	60
5	TNT	BFI	23	$A_{mp}(B)$	5.8	0.5	0.96	0.01	80
	TYPEC	BFII	8	$\underline{A}(B)$	11	1	0.990	0.008	80
	TYPEC	BFII	9	$t_{mp}(G)$	18	2	0.999	0.004	60
	TYPED	BFI	19	$\mu_2(G)$	36	4	1.0000	0.0003	60
	TYPED	BFI	30	$c_2(B)$	50	7	1.0000	0.0001	60

actually degrade the stability of the feature saliency. While a few 3-chip features provide higher Fisher ratios than the NIR feature t_{mp} , these color features are inconsistently

ranked according to their Fisher ratio and their A_{ROC} . Nevertheless, the pair of features, $A_{mp}(B)$ and $\underline{A}(B)$ show up most frequently.

G. Committee of classifiers for robust testing two-class discrimination

At this point, feature saliency and stability has been examined using features extracted from near-infrared images, from RGB color images, and from the combination of NIR and RGB images which provide four color images. Before conclusions are drawn based upon limited testing it is important to robustly test the findings. The approach for robust testing utilizes Bishop's committee of networks [52: 364-365] approach, but in this problem it is more appropriately called a committee of classifiers. The motivation to use a committee is to overcome the drawbacks of isolated pattern recognition on subsets of the data. The previous results from the NIR and 3-chip color features show that the feature saliency depends on the training set used, *e.g.* Brilliant Flash II or one of many test sets in the bootstrap method. A common practice is to select the training set and spectral bands that have the best performance on the independent test set. As Bishop points out, two drawbacks of this approach are the loss of information gained with other training sets and the noise in the data being ignored such that the best performance with a training set might not have the best performance on a new set of test data.

Using a committee of classifiers approach to robust testing, one first selects a list of features based upon the results from individual tests using the NIR, 3-chip, and combined NIR/3-chip data. This selection process is the first committee. Based upon the results in the previous sections and constrained by stability in feature saliency and probability density functions, the features that are potentially the best in distinguishing between TNT and ENE at the 50-kg weight include t_{mp} , σ_{t_medstd} , $A_{mp}(B)$, $\underline{A}(B)$, and

$t_{median}(R)$. Once a set of features is selected, then the second committee robustly tests each feature and where appropriate, combinations of multiple features. Since the previous results imply that stability degrades as more features are added, then the robust test combinations are currently limited to two feature combinations. The robust test method used in this analysis is based upon a bootstrap approach. For example, suppose there are 40 events, then there are 658,008 possible ways to create a test set using five of those events. The robust test randomly chooses 1,000 of these test sets and corresponding training sets and computes the average probability densities from all 1,000 training sets. The resulting densities statistically represent all 658,008 possible permutations with representative means and variances.

The last step is to report the classification performance as a percentage of the 40 events that are classified correctly using these average densities. These percentages are reported in the following tables, where each one represents the results of applying the discrimination tools to weights 50-kg, 100-kg, and all weights 10 to 100 kg.

Table 15. Percentages of the 50-kg events that are correctly classified using a selected set of feature(s). The diagonal values represent single feature discrimination and the off-diagonal values represent two-feature discrimination between types.

50kg	t_{mp}	$A_{mp}(B)$	$\underline{A}(B)$	$t_{median}(R)$	$\sigma_{t_{median}}$
t_{mp}	89%	85%	85%	93%	89%
$A_{mp}(B)$	85%	93%	93%	85%	100%
$\underline{A}(B)$	85%	93%	89%	78%	89%
$t_{median}(R)$	93%	85%	78%	67%	67%
$\sigma_{t_{median}}$	89%	100%	89%	67%	74%

Table 16. Percentages of the 100-kg events that are correctly classified using a selected set of feature(s). The diagonal values represent single feature discrimination and the off-diagonal values represent two-feature discrimination between types.

100kg	t_{mp}	$A_{mp}(B)$	$\underline{A}(B)$	$t_{median}(R)$	σ_{t_median}
t_{mp}	89%	100%	100%	100%	100%
$A_{mp}(B)$	100%	89%	89%	100%	100%
$\underline{A}(B)$	100%	89%	89%	100%	100%
$t_{median}(R)$	100%	100%	100%	100%	100%
σ_{t_median}	100%	100%	100%	100%	67%

Table 17. Percentages of the weight independent events that are correctly classified using a selected set of feature(s). The diagonal values represent single feature discrimination and the off-diagonal values represent two-feature discrimination between types.

10,50,100 kg	t_{mp}	$A_{mp}(B)$	$\underline{A}(B)$	$t_{median}(R)$	σ_{t_median}
t_{mp}	87%	87%	87%	90%	87%
$A_{mp}(B)$	87%	79%	85%	82%	85%
$\underline{A}(B)$	87%	85%	79%	82%	85%
$t_{median}(R)$	90%	82%	82%	62%	54%
σ_{t_median}	87%	85%	85%	54%	59%

Due to the small numbers of 10-kg and 100-kg events, only a leave-one-out process is used to generate those respective percentages. The feature pair, $A_{mp}(B)$ and σ_{t_medstd} (NIR), is 100% accurate in predicting an event as either TNT or ENE at *a priori* weight of 50 kg; however, a single feature performs almost as well. For example, t_{mp} , $A_{mp}(B)$ and \underline{A} all perform at approximately 90% accuracy if the weight is known *a priori* to be 50 kg. The time to the peak of the fireball area in the near-infrared provides a Fisher ratio $F = 2.9 \pm 0.3$, represented by the separation in the class-conditional Posteriors and densities calculated during the robust testing (Figure 44). Even though the reported performance is sufficiently high, the range of densities from the 997 test scenarios clearly shows a region of high uncertainty in the range of -1.5 to 0 along the abscissa. Upon

examining the 4,985 test scenarios, only 87% or 4,346 provided correct classification.

This feature is also the single best discriminator when weight is unknown (Figure 45):

87% accuracy, $F = 2.5 \pm 0.1$, and 87% of 5,000 classified correctly.

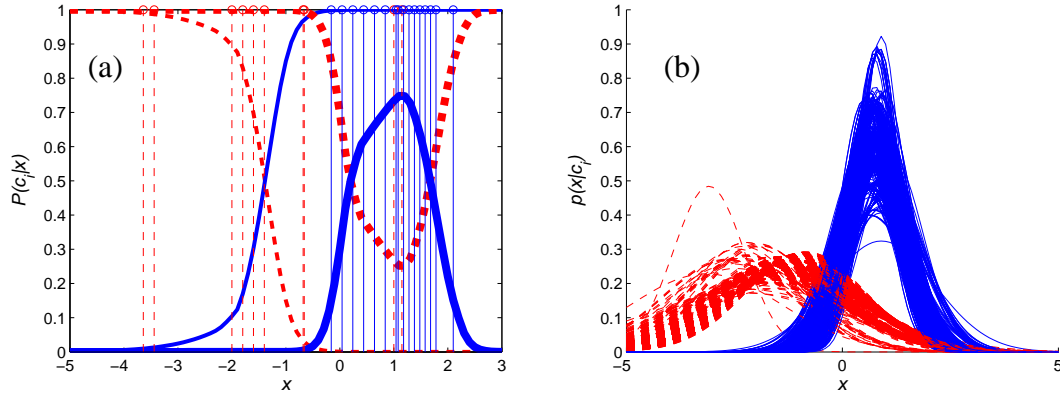


Figure 44. (a) The range of possible class-conditional posteriors as a result of 997 tests and (b) the 997 class-conditional probability densities from robust testing for the feature t_{mp} which provides an 89% accurate prediction of events as either ENE or TNT when weight is known to be 50 kg. The Fisher ratio is 2.9 ± 0.3 for the average densities. The vertical lines represent locations along the Fisher line, x , for each test event. Solid = ENE; dashed = TNT.

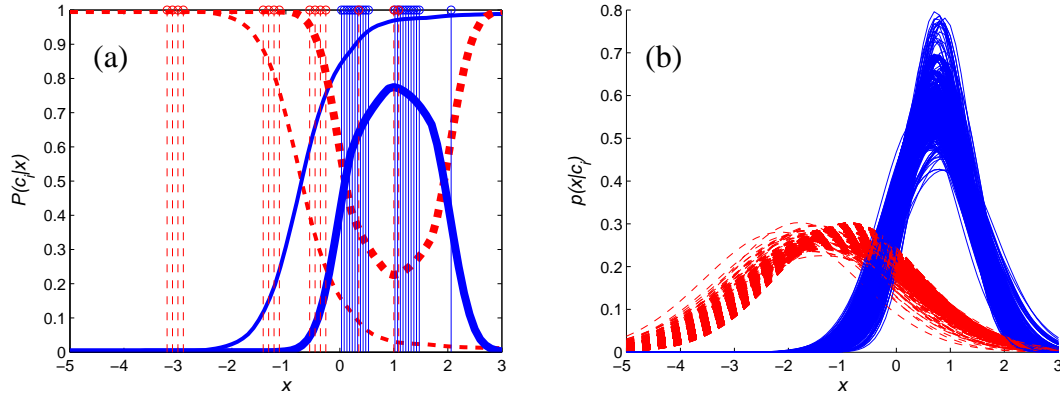


Figure 45. (a) The range of possible class-conditional posteriors as a result of 997 tests and (b) the 997 class-conditional probability densities from robust testing for the feature t_{mp} which provides an 87% accurate prediction of events as either ENE or TNT when weight is unknown. The Fisher ratio is 2.5 ± 0.1 for the average class-conditional densities. The vertical lines represent locations along the Fisher line, x , for each test event. Solid = ENE; dashed = TNT.

The single best feature from the 3-band visible imagery is the maximum area in the blue band, A_{mp} , of $10 - 60 \text{ m}^2$ for TNT and $40 - 280 \text{ m}^2$ for ENE. This feature provides 93% correct classification using the average densities from the test results (91% of 4,985) and $F = 5.4 \pm 0.2$ for the 50 kg case (Figure 46). Similarly as shown in Figure 47 for the unspecified weights case, this feature provides 79% correct classification using the average densities from the test results (80% of 5,000 test cases) and $F = 4.4 \pm 0.1$. Combining the time to peak size in the near IR and maximum area in the blue does not significantly improve the classification performance.

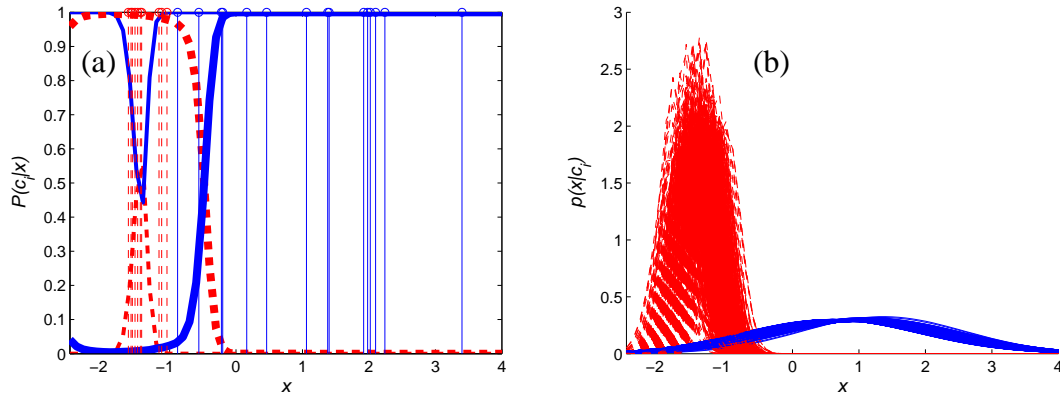


Figure 46. (a) The range of possible class-conditional posteriors as a result of 997 tests and (b) the 997 class-conditional probability densities from robust testing for the feature $A_{mp}(B)$ which provides an 93% accurate prediction of events (ENE or TNT) when weight is known to be 50 kg. The Fisher ratio is 5.4 ± 0.2 for the average class-conditional densities. The vertical lines represent locations along the Fisher line, x , for each test event. Solid = ENE; dashed = TNT.

H. Multiple-class discrimination

The previous sections address only one weight (50 kg) collected during the Brilliant Flash tests; however, the test series collected image data from various weights of

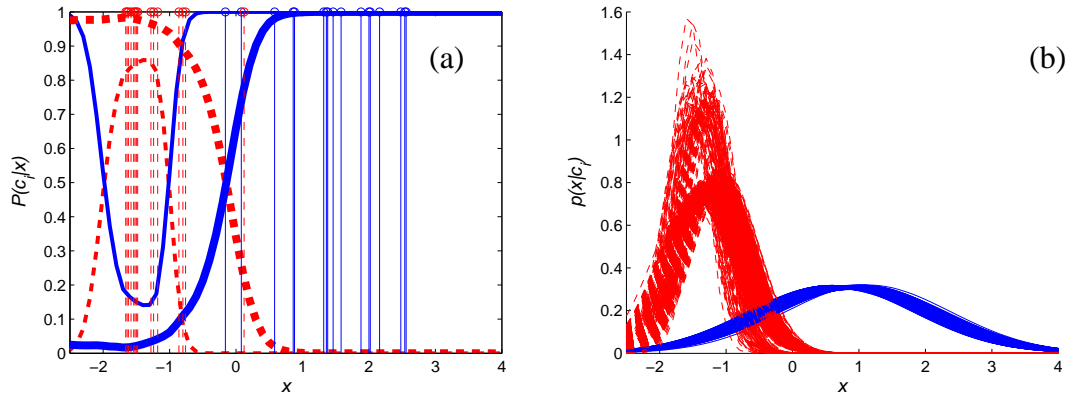


Figure 47. (a) The range of possible class-conditional posteriors as a result of 997 tests and (b) the 997 class-conditional probability densities from robust testing for the feature $A_{mp}(B)$ which provides an 79% accurate prediction of events (ENE or TNT) when weight is unknown. The Fisher ratio is 4.4 ± 0.1 for the average class-conditional densities. The vertical lines represent locations along the Fisher line, x , for each test event. Solid = ENE; dashed = TNT.

TNT and ENE explosives. Enough repetitions of five types allow an application of a multi-class Fisher discrimination technique: $\{TNT_{10}, TNT_{50}, TNT_{100}, ENE_{50}, ENE_{100}\}$ where the numbers represent the weight in kilograms. This subsection explains the theory of multiple-class Fisher discrimination, presents the fireball area data of the five candidate classes, identifies potential scaling relationships of the features and their use in classification, reports the feature saliency results of using a five-class discriminator tool to examine the two test scenarios discussed earlier, and finally presents the results of a committee of classifiers approach to solving the five-class problem.

The five-class discrimination tools first use all Brilliant Flash II for training and Brilliant Flash I for testing. Since Brilliant Flash I only contains 50 kg weights, this series alone cannot be used for training. Each field camera data is examined

independently before combining them to make a four color set of features. Following this test analysis, the bootstrap testing approach is applied to obtain additional results.

1. Theory

A more general discrimination approach beyond the two-class problem allows for multiple classes from which to derive class-conditional probability densities and posteriors. The generalized multiple discriminate (or Fisher) analysis is well documented in various sources [51: 121-124] [52: 110-112] [53]. Similar to the two class problem, Fisher Linear Discriminant defines a Fisher ratio which uses a projection matrix $\underline{\mathbf{W}}$ to reshape the scatter of data to maximize class separability and minimize within-class variability.

Suppose the features are described in the matrix $\underline{\mathbf{X}}$ of N column vectors (one for each event) and M rows for each feature, *e.g.* $M = 14$. The mean of each feature for all events is recorded in a $M \times 1$ vector $\underline{\mu}$, with elements

$$\mu_j = \frac{1}{N} \sum_{i=1}^N x_{ji} . \quad (29)$$

If there are K classes $\{C_1, C_2, \dots, C_K\}$, the mean of each feature for all events in one class is

$$\bar{\mu}_k = \frac{1}{N_k} \sum_{\vec{x}_i \in C_k} \vec{x}_i , \quad (30)$$

where the vector of features for the i^{th} event is $\underline{\mathbf{x}}_i$. The between-class scatter matrix is

$$S_{\underline{\underline{B}}} = \sum_{k=1}^K N_k (\bar{\mu}_k - \bar{\mu})(\bar{\mu}_k - \bar{\mu})^T, \quad (31)$$

and the within-class scatter matrix is

$$S_{\underline{\underline{W}}} = \sum_{k=1}^K \sum_{\vec{x}_i \in C_k} (\vec{x}_i - \bar{\mu}_k)(\vec{x}_i - \bar{\mu}_k)^T. \quad (32)$$

The equivalent Fisher ratio, now a transformation matrix, that repositions the data to be most separable is the matrix $\underline{\underline{W}}$ that maximizes

$$J(\underline{\underline{W}}) = \frac{|\underline{\underline{W}}^T S_{\underline{\underline{B}}} \underline{\underline{W}}|}{|\underline{\underline{W}}^T S_{\underline{\underline{W}}} \underline{\underline{W}}|}. \quad (33)$$

According to the references cited earlier, the method of finding the correct $\underline{\underline{W}}$ is relatively simple: the columns of the $\underline{\underline{W}}$ which maximizes $J(\underline{\underline{W}})$ are the generalized eigenvectors that correspond to the largest eigenvalues in

$$S_{\underline{\underline{B}}} \vec{w}_i = \lambda_i S_{\underline{\underline{W}}} \vec{w}_i. \quad (34)$$

After determining the correct vector which maximize the Fisher ratio $J(\underline{\underline{W}})$, each event record is projected onto a line defined by this vector. The corresponding class-conditional probability densities and posteriors aid in quantifying feature saliency and stability as they did in the two-class problem discussed earlier. An example five class problem using Brilliant Flash I and II is now examined.

2. Data

The Brilliant Flash test series collected image data from various weights of TNT and ENE explosives. Enough repetitions of these five types allow an application of the multi-class Fisher discrimination technique: $\{\text{TNT}_{10}, \text{TNT}_{50}, \text{TNT}_{100}, \text{ENE}_{50}, \text{ENE}_{100}\}$ where the numbers represent the weight in kilograms. The extracted areas from each of these types are provided in Figure 48 (Brilliant Flash I), Figure 49 (Brilliant Flash II ENE), and Figure 50 (Brilliant Flash II TNT). An initial look at these areas suggests that the time and height of the peak area should be a good feature for discrimination.

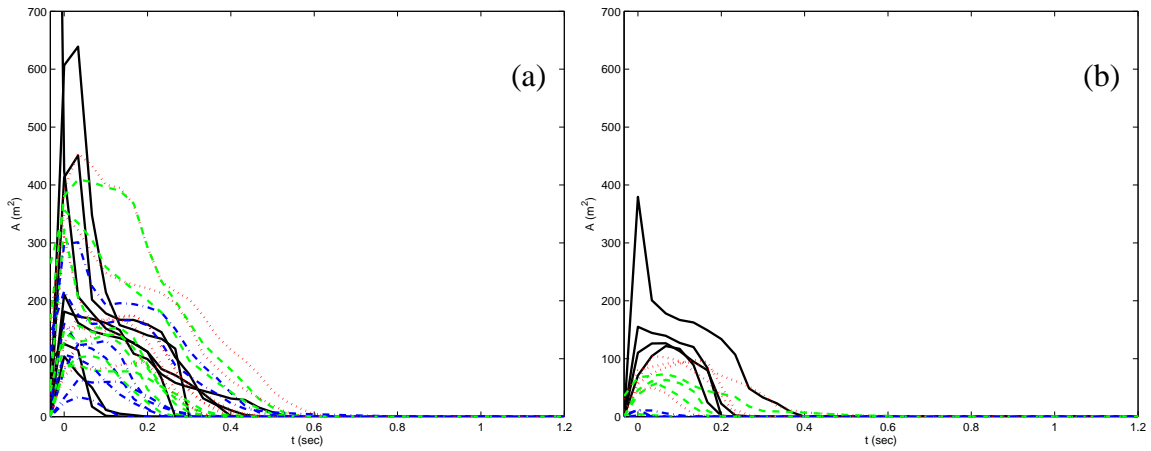


Figure 48. The extracted areas for each color, derived from Brilliant Flash I are shown here as a function of time: (a) ENE-50kg, (b) TNT-50kg. The NIR derived areas are the solid black lines; the RGB derived areas are dotted, dashed, and dash-dot, respectively.

3. Scaling laws

Before applying the extracted features (14×4 colors = 56) to the discrimination tools, a pragmatic look at the feature values as a function of weight and type provides some insights into the discrimination challenge. These representations are often called

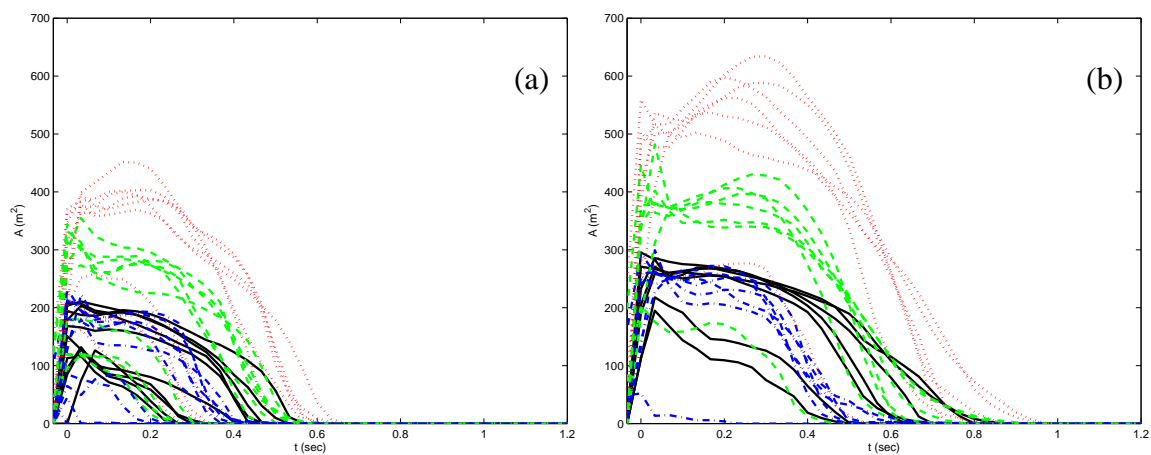


Figure 49. The extracted areas for each color, derived from Brilliant Flash II are shown here as a function of time: (a) ENE-50kg, (b) ENE-100kg. The NIR derived areas are the solid black lines; the RGB derived areas are dotted, dashed, and dash-dot, respectively.

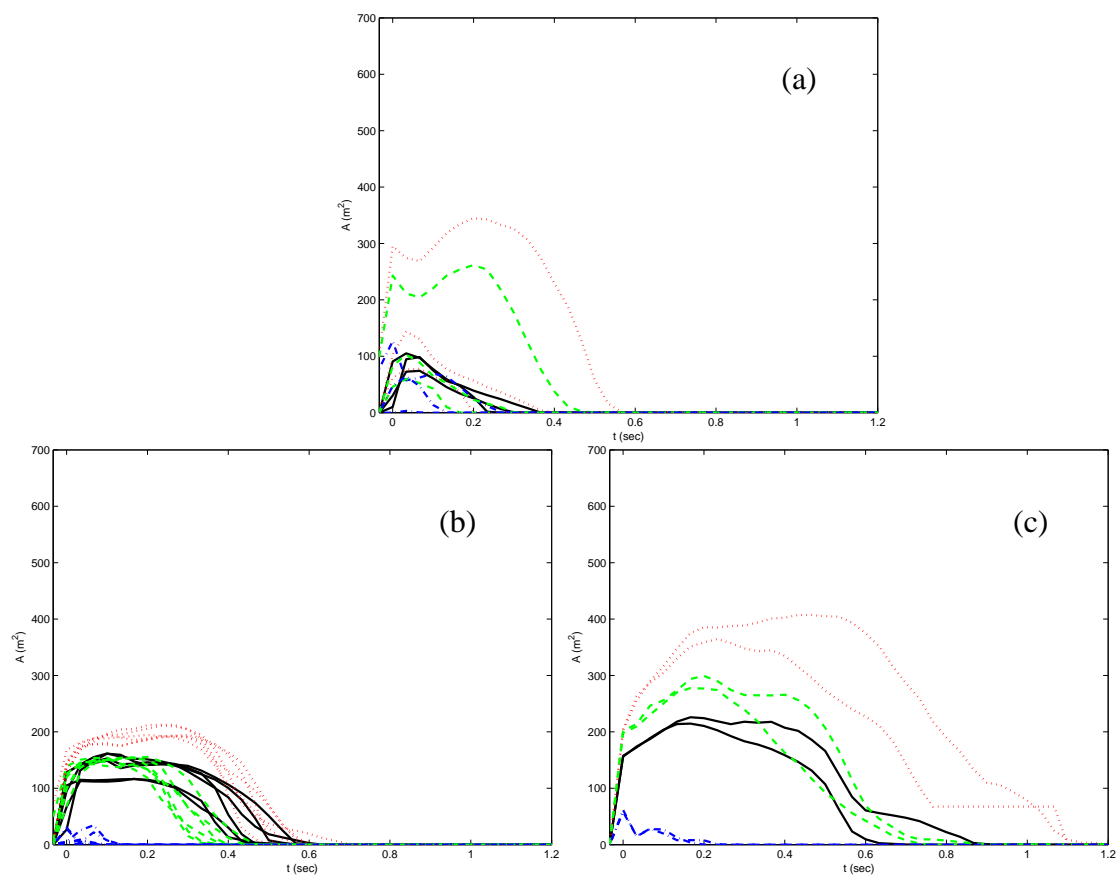


Figure 50. The extracted areas for each color, derived from Brilliant Flash II are shown here as a function of time: (a) TNT-10kg, (b) TNT-50kg, and (c) TNT-100kg. The NIR derived areas are the solid black lines; the RGB derived areas are dotted, dashed, and dash-dot, respectively.

scaling laws. From examining the fourteen near-infrared features, four stand out with strong weight and type dependence. As shown in Figure 51, these features are the time to peak area (t_{mp}), the value of the area curve integrated over the detonation time (\underline{A}), the median time (t_{median}), and the standard deviation of the median time ($\sigma_{t_{median}}$). The data points represent the mean of that type and weight and the error bars are the corresponding standards of deviation.

On the average, the time to peak values for the TNT is quite different than those of the ENE, which is consistent with the findings earlier in the 50-kg two-class problem. For this feature, both the slope with regard to weight and the absolute values at each weight are different. Potentially the strongest indicator of weight, independent of type, is the area curve integrated over the detonation time. Regardless of the type, the weights are scalable with an \underline{A} to weight W slope between 1083 and 1323 $\text{m}^2\text{-msec-kg}^{-1}$. The median time and its standard deviation also provide good indicators of weight if the type is known *a priori*. A committee of classifiers approach is later discussed in this chapter and uses one feature to determine weight before using a second feature to determine type. For example, the scaling laws suggest using the \underline{A} to determine weight before using t_{mp} to distinguish type.

The presented scaling laws are useful in capturing predicted behavior of certain features as they scale with weight. For example, suppose a new event is recorded and the integrated area over the detonation time was $8 \times 10^4 \text{ m}^2\text{-msec}$. Then according to the scaling relationship in Figure 51, the event's weight is 80 kg. However, the prediction uncertainty needs to be addressed. To answer this, the scaling law figures are redrawn to

capture the spread in the data X and the errors σ_f in the least squares best fit lines f as defined in Eq(35) and adapted from Bishop[52: 399-401]:

$$\sigma_{f_{ki}}^2 = B_k + \frac{1}{N_k} B_k + E_{ki} \quad (35)$$

where the value of the least square fit line for class k having N_k events and weight W_i is f_{ki} , and the weighted variance between the least squares line and the average data point for class k and weight W_i is

$$E_{ki} = \frac{B_k}{N_k C_{ki}} (f_{ki} - \text{Avg}(\underline{X}_{ki}))^2, \quad (36)$$

and the data points for class k and W_i are captured in the vector \underline{X}_{ki} such that the average for N_{ki} events is

$$\text{Avg}(\underline{X}_{ki}) = \frac{1}{N_{ki}} \sum_{j=1}^{N_{ki}} X_{kij}. \quad (37)$$

The variance in the difference between the data and the least squares line is

$$B_k = \frac{1}{N_k - 1} \sum_{j=1}^{N_k} (A_{ki} - \text{Avg}(\underline{A}_k))^2, \quad (38)$$

where the difference between each data record in a specific class and at a specific weight is $A_{ki} = \underline{X}_{ki} - f_{ki}$, which are elements of the vector, $\underline{A}_k = [A_{k1} \quad A_{k2} \quad \cdots \quad A_{kN_k}]$, with average

$$Avg(\underline{A}_k) = \frac{1}{N_k} \sum_{i=1}^{N_k} A_{ki}. \quad (39)$$

The last term C_{ki} is the variance of the individual data points in class k and weight W_i ,

$$C_{ki} = \frac{1}{N_{ki} - 1} \sum_{j=1}^{N_{ki}} (X_{kij} - Avg(\underline{X}_{ki}))^2 \quad (40)$$

Using the \underline{A} relationship in Figure 52, the correct answer to this example should now be 80 ± 30 kg. In another example, suppose the weight is known to be 80 kg and the type is unknown. According to the scaling relationship, if t_{mp} is between 0 and 50 msec, the event could be an enhanced explosive; other wise, a t_{mp} value between 20 and 225 msec might indicate a TNT explosive. Clearly, the scaling laws do not give a definitive answer, but they do provide an alternate view of the data that helps explain the level of classification difficulty with a limited data set and that may aid others in understanding the physics of the emissions from a detonation. All the scaling relationships for both the near-infrared and the 3-chip color features are provided in Appendices G and H.

4. Results

Consistent with the two class discrimination discussion earlier, two test scenarios are examined before applying the results to the robust committee analysis (Section IV-I). The first test uses all of Brilliant Flash II data for training and then tests the resulting class-conditional posteriors with the events from Brilliant Flash I test series, which consists of only 50-kg explosions. Table 18 contains the test results when the 5-class discrimination technique is applied to the NIR, 3-chip, and the combined NIR/3-chip data. The best five forward features for the NIR and NIR/3-chip combination

consistently show that the time to the peak area, t_{mp} , is again the best feature for discrimination. This is also true for the best five backward features using the NIR only data. Recall from previous discussion that t_{mp} provides adequate two-class discrimination between TNT and ENE of the same 50-kg weight.

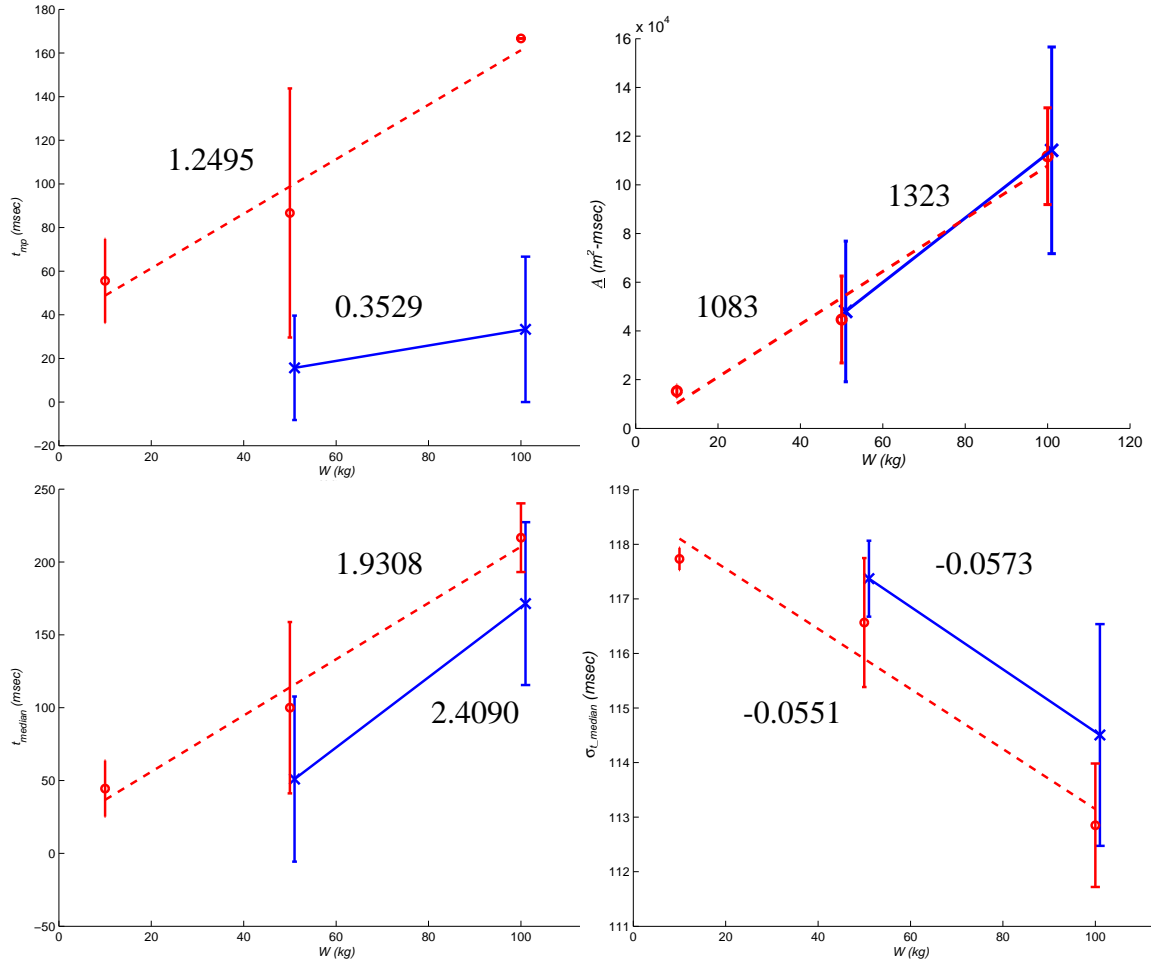


Figure 51. Four of the features extracted from the area curve derived from the NIR images possibly provide scaling law relationships. The data points and error bars are the mean and standard deviation of each feature for each weight and type (solid line for ENE, dashed line for TNT). The slopes of each line are indicated next to each line.

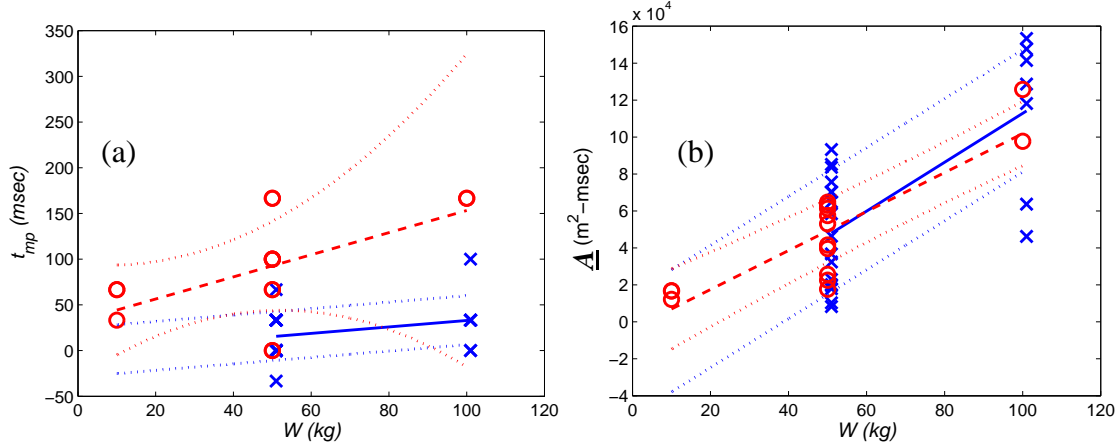


Figure 52. The most probable time (a) and the integrated area over the detonation time (b) features extracted from the fireball area derived from the NIR images demonstrate scaling as a function of weight and type relationships. These representations help visualize the spread in the data and the uncertainty in the slopes (dotted lines). X=ENE; O=TNT.

Table 18. Record of 5-class IR data test results where Brilliant Flash II data is the training data and Brilliant Flash I is the testing data. Feature saliency is found by ranking with the Fisher ratio (FR). σ is the standard deviation. The RGB is in parentheses. No RGB letters signifies a NIR feature.

Camera	Training Set	Testing Set	Best 5 Forward Features	FR	σ_{FR}	% Correct	Best 5 Backward Features	FR	σ_{FR}
NIR	Brilliant Flash II	Brilliant Flash I	t_{mp}	12	1	55	t_{mp}	12	1
			A_{mp}	24	2	27	t_{std}	12	1
			A_{median}	29	2	27	μ_2	20	1
			μ_2	32	2	27	μ_1	26	2
			t_{std}	34	3	18	μ_3	40	4
3-chip	Brilliant Flash II	Brilliant Flash I	$\sigma_{t_{median}}(R)$	11	5	0	NA	NA	NA
			$\sigma_{t_{median}}(G)$	28	4	64			
			$c_2(G)$	40	7	64			
			$t_{mp}(R)$	69	9	64			
			$\mu_1(B)$	83	10	64			
NIR & 3-chip	Brilliant Flash II	Brilliant Flash I	t_{mp}	12	1	55	NA	NA	NA
			A_{mp}	24	2	27			
			$c_3(B)$	45	5	9			
			$c_3(G)$	132	17	18			
			$t_{median}(R)$	206	21	18			

The resulting class-conditional probability posteriors, densities, and test results when using the single feature t_{mp} are represented in Figure 53. One interesting finding is the reduction in the number of test events that are correctly classified. This again is seen

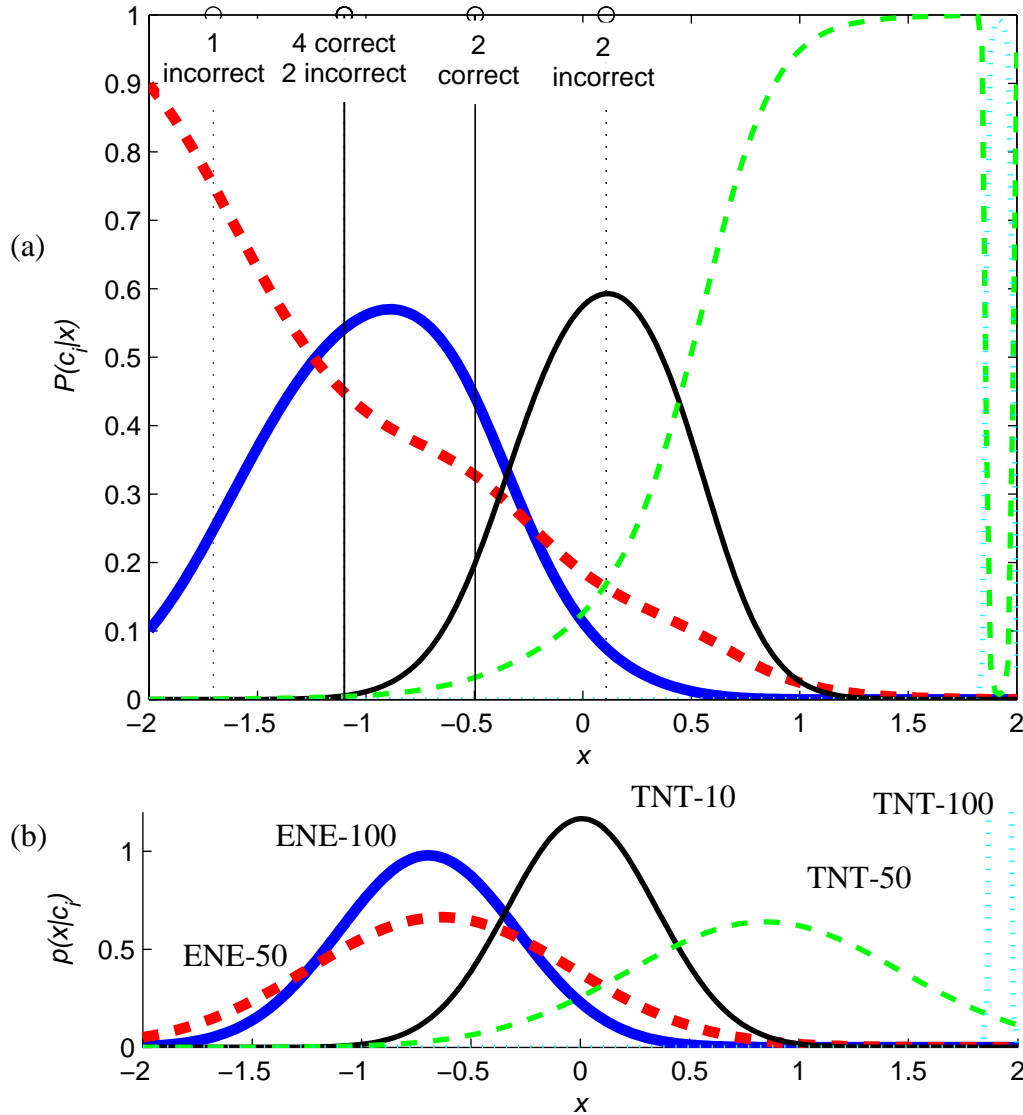


Figure 53. (a) Class-conditional posteriors and (b) class-conditional probability densities for the five classes with vertical lines drawn for each of the eleven test cases projected onto the single feature t_{mp} normalized to zero mean and unit variance. A solid (dotted) vertical line indicates a correct (incorrect) classification of the test event. The five types are ENE-50kg (thick dashed), ENE-100kg (thick solid), TNT-10kg (solid), TNT-50kg (dashed), and TNT-100kg (dotted).

in the two-class problem. For the NIR data applied to the five class problem, this percentage drops from 55% to 18% for the first five features. It is important to remember that these features are parametric and not physical. Many of them could be represented by linear (or possibly non-linear) combinations of other features. Thus only a few features are needed. These tools, even with the small amount of test data, provide a mechanism to determine those few features that provide the best classification. Specifically, the drop in the testing performance may be analogous to adding additional features to a curve fitting problem: the more terms you add, the better the fit goes through the data, yet the prediction performance potentially declines. Similar results are seen with the 3-chip data and the combined NIR/3-chip data whose individual probability densities are given in Figure 54.

The stability of the class-conditional probability densities is represented by the normalized standard deviation of the density peaks and the density center locations:

$$\overline{\sigma_{param}} = \sigma_{param} \cdot \left(\sum_{i=1}^{N-1} \sum_{j=i+1}^N (X_i - X_j)^2 \right)^{-1/2} \binom{N}{2}, \quad (41)$$

where *param* is either the *peak* or *center* of the Gaussian distribution, the normalization is the root mean of the squared differences of class positions, and the number of 2-class pairs defined by the binomial coefficient for N classes

$$\binom{N}{2} = \frac{N!}{2!(N-2)!}. \quad (42)$$

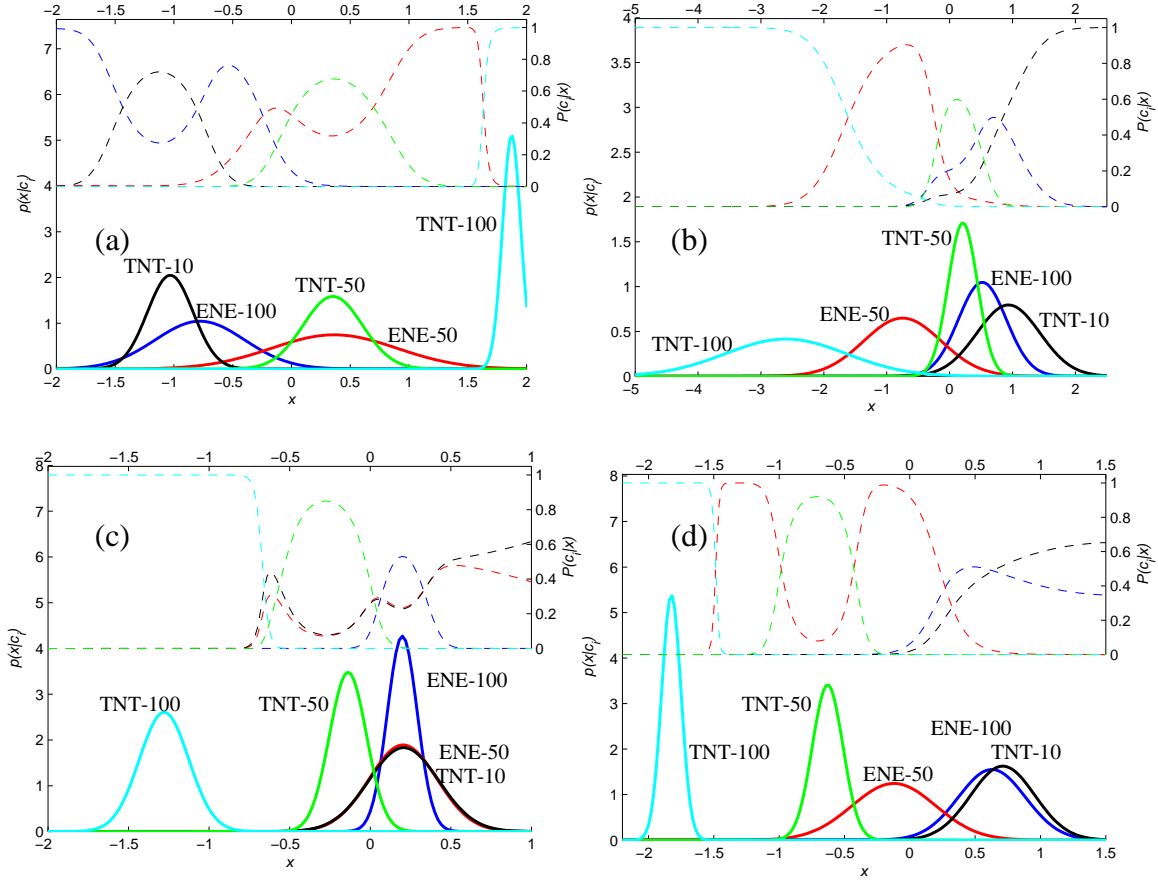


Figure 54. The class-conditional probability densities (lower halves) and posteriors (upper halves) are given for a few of the top features from each camera data set. Figure (a) is the result from using the two features, t_{mp} and A_{mp} . Figures (b) and (c) show the results from using the 3-chip camera: (b) a single feature, $\sigma_{t_median}(R)$ and (c) two features, $\sigma_{t_median}(R)$ and $\sigma_{t_median}(G)$. Figure (d) shows the top three features as a result of combining the NIR and 3-chip camera data, $\{t_{mp}, A_{mp}, c_3(B)\}$.

A plot of each of these stability measures for each data set is provided in Figure 55. Each of these representations suggests that no more than one or at most two features can be used before stability significantly degrades.

The second test is the bootstrap approach where Brilliant Flash I and Brilliant Flash II test data are combined and a random set of five is chosen to be the test events. The remaining events are used for training and validation. With bootstrapping, multiple

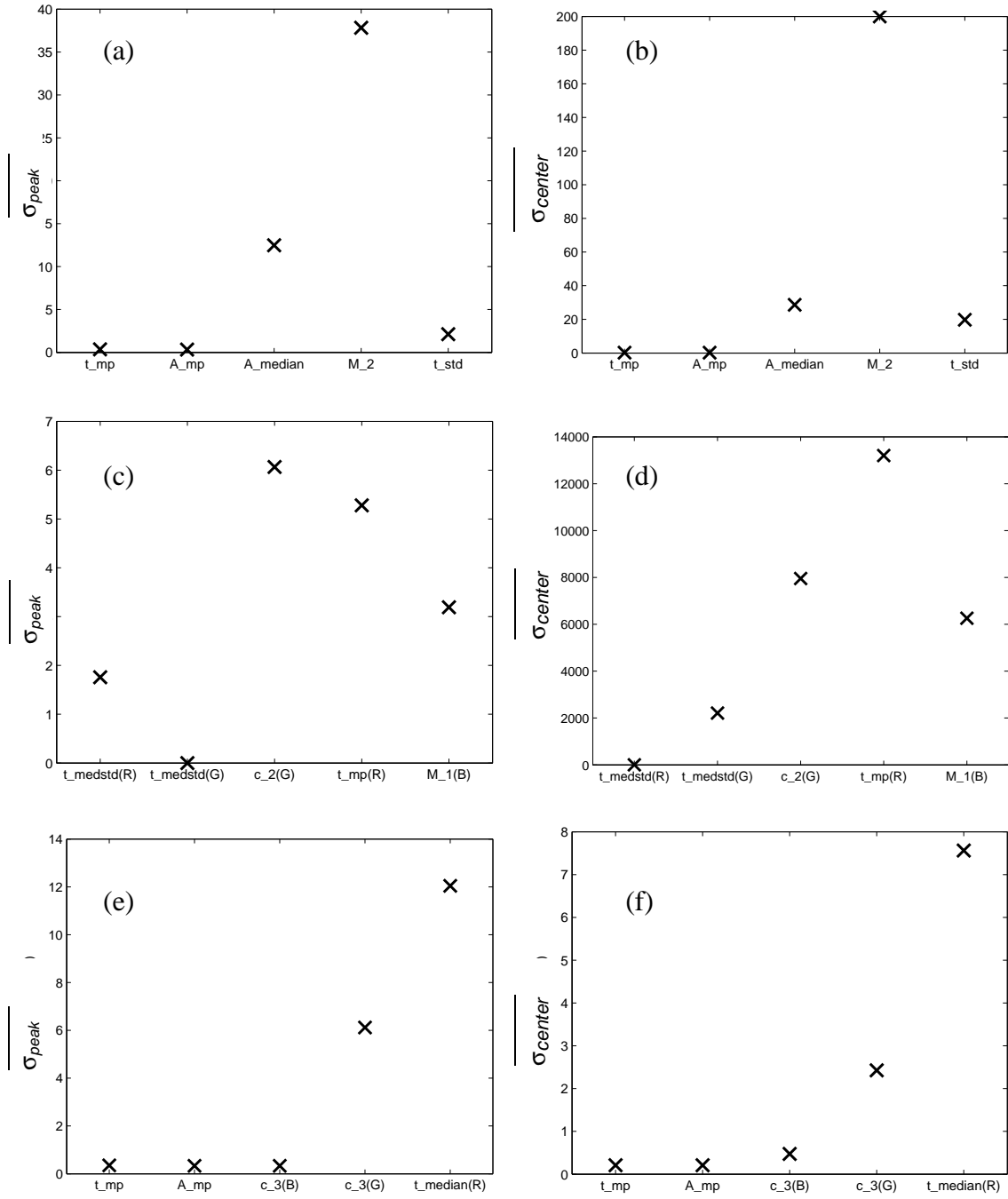


Figure 55. Stability of the class-conditional probability densities are quantified by the standard deviations of the density peaks (a, c, e) and centers (b, d, f) and is a function of the feature saliency defined by the test results. (a,b) utilize only NIR data, (c,d) use only 3-chip color data, and (e,f) combines the two sources.

random choices, thus multiple test cases are examined. The results of applying bootstrapping to the five-class problem are provided in Table 19. This table identifies the test events chosen, the resulting best five features with Fisher ratios and testing

Table 19. Record of 5-class data bootstrapping test results where Brilliant Flash I and II data are combined and a random set of five events are chosen to be test data. The best features are sorted by their Fisher ratio. FR is the Fisher ratio. σ is the standard deviation. The RGB is in parentheses. No RGB letters signifies a NIR feature.

#	Test Types	Test Series	Test Wt	Test Ev. No.	Best 5 NIR Features	FR	%	Best 5 3-Chip Features	FR	%	Best 5 Comb. Features	FR	%
1	TYPEB	BFII	50	13	t_{std}	6.3	0	\underline{A} (R)	7	40	\underline{A} (R)	7	40
	TYPEC	BFII	50	5	μ_2	8	20	A_{mp} (B)	13	60	A_{mp} (B)	13	60
	TNT	BFII	50	31	t_{mp}	12	60	t_{mp} (R)	20	60	t_{mp} (R)	20	60
	TYPED	BFII	50	12	μ_4	14	60	A_{medstd} (G)	24	40	A_{medstd} (G)	24	40
	TYPEC	BFI	50	2	c_1	17	60	A_{mp} (R)	30	60	A_{mp} (R)	30	60
2	TYPEC	BFII	100	30	t_{mp}	6.9	60	t_{median} (R)	7	80	t_{mp}	7	60
	TYPEB	BFII	50	13	t_{std}	9.0	80	A_{mp} (B)	12	40	t_{mp} (B)	14	20
	TYPED	BFII	50	12	μ_2	13	60	c_2 (G)	15	20	c_3 (R)	20	40
	TYPEB	BFII	50	17	μ_4	14	60	A_{medstd} (R)	20	40	\underline{A}	27	20
	TNT	BFII	50	44	μ_1	17	80	t_{medstd} (R)	25	40	t_{medstd} (R)	30	0
3	TNT	BFI	50	24	t_{mp}	7.7	0	t_{median} (R)	7	60	t_{mp}	8	0
	TYPEC	BFI	50	3	\underline{A}	11.1	20	A_{mp} (B)	18	20	A_{mp} (B)	13	20
	TNT	BFI	50	31	μ_4	15	20	c_2 (G)	23	20	\underline{A} (G)	23	40
	TYPED	BFI	50	19	μ_2	18	0	A_{medstd} (G)	28	20	t_{medstd} (B)	31	20
	TYPEB	BFII	50	13	t_{std}	21.1	20	μ_3 (B)	34	20	c_1 (G)	43	40
4	TNT	BFII	10	15	t_{mp}	6.5	60	\underline{A} (B)	6	40	t_{mp}	6	60
	TYPED	BFII	50	12	\underline{A}	9.0	20	t_{median} (R)	11	40	t_{mp} (B)	12	0
	TNT	BFI	50	31	μ_3	10.6	40	c_1 (G)	17	20	t_{medstd} (R)	17	20
	TYPED	BFI	50	18	c_1	12.0	80	μ_4 (B)	21	20	t_{medstd} (G)	23	60
	TYPED	BFI	50	19	μ_2	13.3	80	A_{median} (G)	30	20	t_{median} (R)	38	60
5	TNT	BFII	50	31	t_{mp}	8.3	40	t_{median} (R)	5	60	t_{mp}	8	40
	TYPED	BFII	50	19	\underline{A}	10	40	A_{median} (B)	11	60	t_{medstd} (R)	12	40
	TNT	BFII	10	15	c_1	11	40	c_1 (G)	15	60	μ_1	16	60
	TYPEC	BFII	100	23	μ_4	14	20	μ_1 (R)	21	40	μ_2	26	20
	TYPED	BFII	100	38	μ_2	15	20	μ_3 (B)	25	40	t_{mp} (B)	37	40

performance for each bootstrap iteration and for each data set used, *e.g.* NIR only, 3-chip only, or combined NIR and 3-chip. This table is not an end in itself but a means to

determine which features are consistently important in the discrimination problem. The NIR results again suggest that the time to the peak of fireball area is an important feature. The resulting probability densities (Figure 56) suggest t_{mp} provides some discrimination among four classes: ENE, TNT-10, TNT-50, and TNT-100.

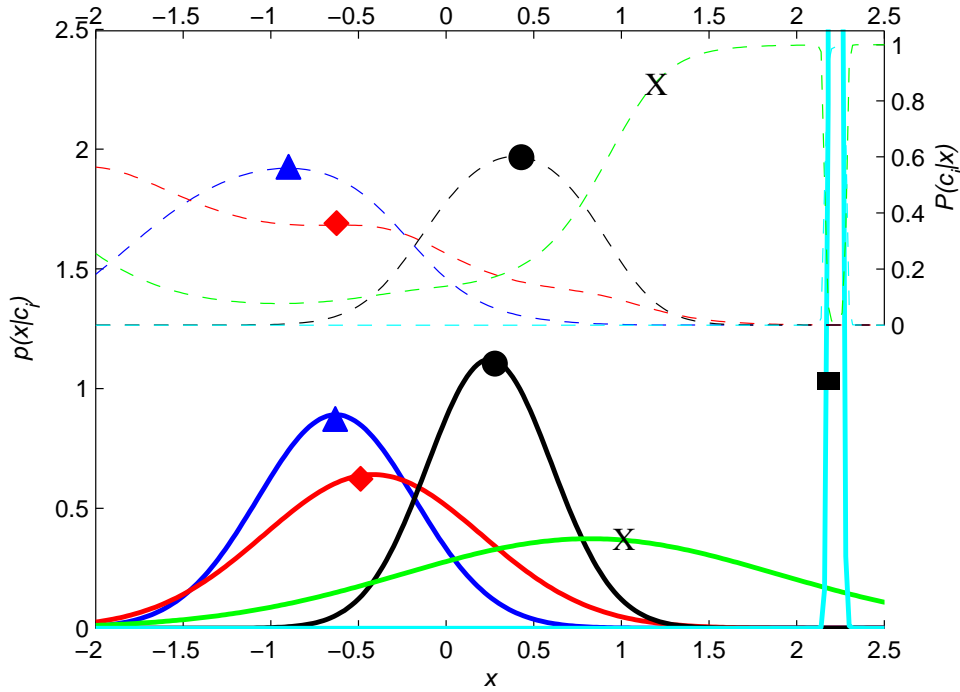


Figure 56. Data projected onto the single feature, t_{mp} , best separates the five classes. The posteriors $[P(c_i/x)]$ (dashed lines) give a correct classification probability range between 30 to 100%. \blacktriangle =ENE-50kg, \blacklozenge =ENE-100kg, \bullet =TNT-10kg, X=TNT-50kg, \blacksquare =TNT-100kg.

According to the bootstrap results, a second feature to combine with t_{mp} is the integrated area over the detonation time, \underline{A} ; however, all the probability densities overlap sufficiently enough to prevent this feature from aiding in the discrimination. The higher Fisher ratio is attributed to smaller class variances. Other possibly important NIR features from the bootstrap results include μ_2 and c_1 as shown in the feature saliency plot

of Figure 57; yet neither of these features significantly improves the Fisher ratio or the probability densities class separation.

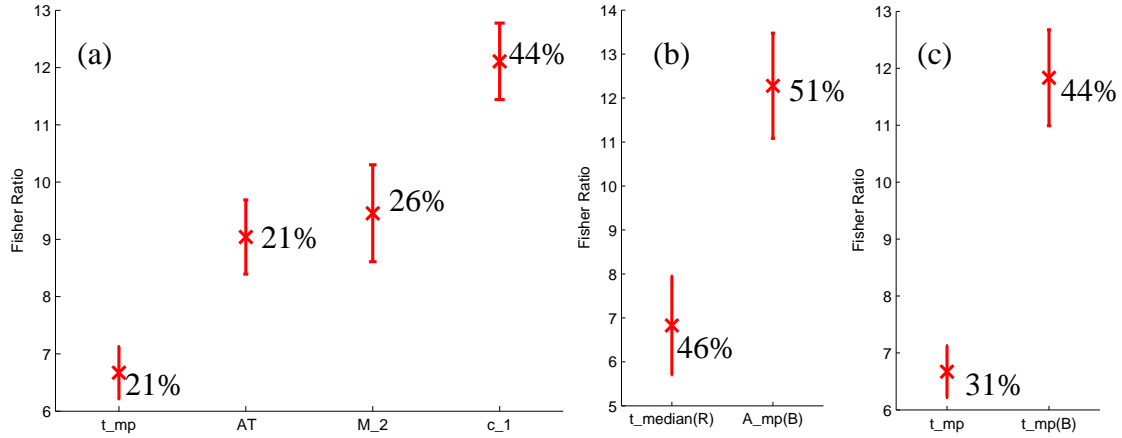


Figure 57. Using the NIR only bootstrap results as a guide, one possible feature saliency shown in (a) is the t_{mp} , A , μ_2 , and c_1 . The Fisher ratios calculated here come from the leave-one-out using all the data. The 3-chip color results and the combined NIR and 3-chip color results are displayed in (b) and (c), respectively. The percent of the left out test events that are correctly classified labels each data point. Different training sets cause variation in t_{mp} values.

Figure 57 (b) and (c) also shows the Fisher ratio results when choosing the top features from the 3-chip data analysis and the combined NIR/3-chip data analysis, respectively. The top two 3-chip features are $t_{median}(R)$ and $A_{mp}(B)$. The median time in the red wavelength band provides slight separation for all five classes, but as shown in Figure 58(a), it does provide better classification if there are only four classes, leaving out TNT-10 or TNT-50. The peak in the blue area $A_{mp}(B)$ does not significantly improve the $t_{median}(R)$ results. Likewise from the combined NIR/3-chip results, a second top feature is the time to the peak blue fireball area $t_{mp}(B)$, yet as shown in Figure 58(b), this second feature does not significantly improve class separation over that achieved by the time to

the NIR peak area. An interesting finding is the best NIR feature t_{mp} and the best Color feature $t_{median}(R)$, when combined, actually degrade the Fisher ratio and do not improve the class-conditional probability densities derived from the best Color feature. This suggests that these two features contain nearly the same information about the fireball. Also, the best Color feature provides slightly better classification of all five types than the best NIR feature.

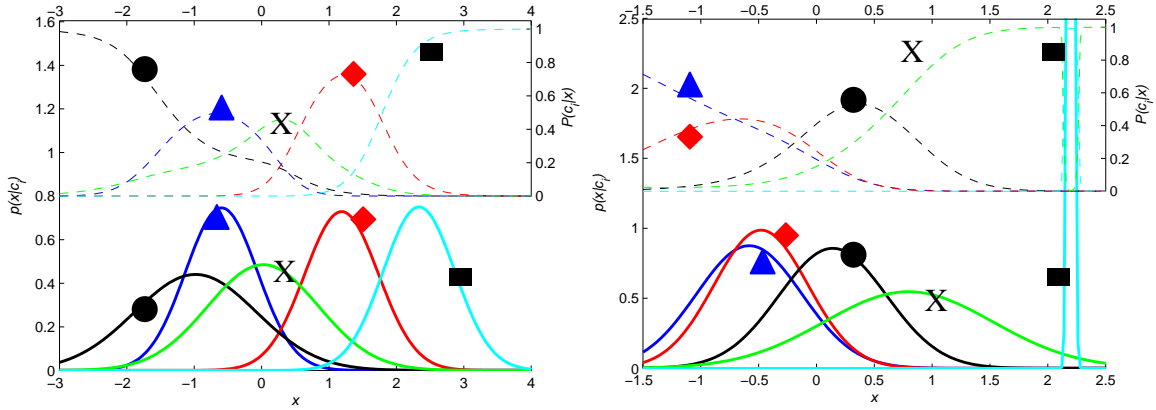


Figure 58. Using the 3-chip camera data (Figure a) and the combined NIR/3-chip data (Figure b), the class-conditional probability densities (lower halves) and posteriors (upper halves) are given for a (a) $t_{median}(R)$ and (b) feature set $\{t_{mp}, t_{mp}(B)\}$. \blacktriangle =ENE-50kg, \blacklozenge =ENE-100kg, \bullet =TNT-10kg, \times =TNT-50kg, \blacksquare =TNT-100kg.

I. Committee of classifiers for robust testing five-class discrimination

The committee of classifiers approach is again utilized to robustly test the features that indicate high Fisher ratio and high stability at classifying the five classes as determined by the two test scenarios and scaling relationships. Since the number of 100 kg events is limited, then the robust test is simply a leave-one-out test. Each time an event is used as a test case, the training produces five class-conditional probability

densities. After all the test cases are exhausted, an average of all the class-conditional densities is used to evaluate each event to determine the percent of those events that are correctly classified. The features chosen for testing are top one or two features from each of the previous test cases on the five-class problem. In addition to these features, those from the two-class problem are also tested. Lastly, the scaling relationships shown in Figure 59 suggest that the integrated area over the detonation time and the median time in the green band are possible discriminates of weight, independent of type. A test of these

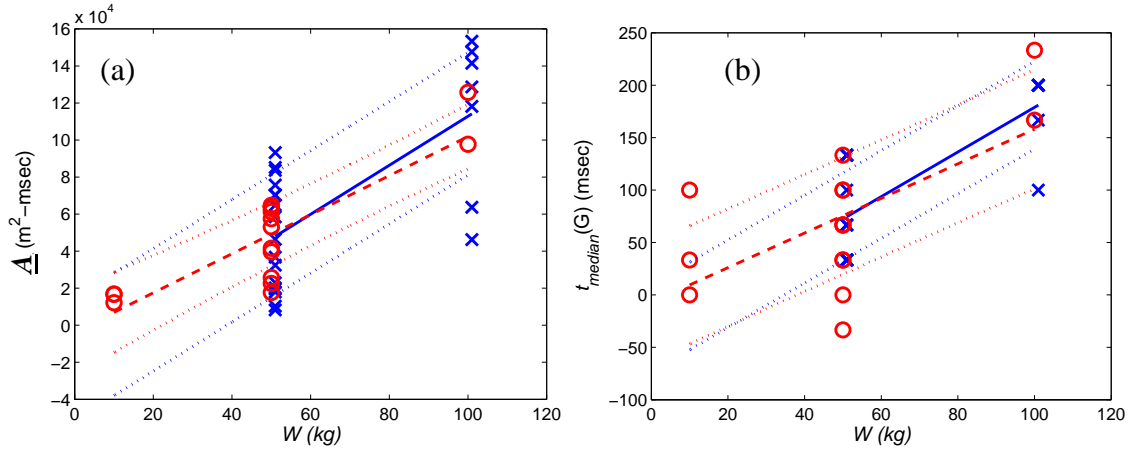


Figure 59. Possible scaling laws for the Brilliant Flash types are represented by (a) the integrated near-infrared area over the detonation time \underline{A} and (b) the median time t_{median} (G) in the green color band. X = ENE events; O = TNT events.

two features' performance on predicting weight independent of type yields 74% accuracy for \underline{A} while t_{median} (G) yields 51%. Their combined effect yields 67% accuracy. The results of applying all the before mentioned features to the five-class discrimination are provided in following table:

Table 20. The percent of events that are correctly classified when using an average of the class-conditional probability densities are presented for the five-class discrimination problem. The values along the diagonal are the percentage of correct classifications when only one feature is used to classify the five types. The off-diagonal elements are the percentages of correct classification when two features are utilized.

5-class	t_{mp}	$A_{mp}(B)$	$A(B)$	$t_{median}(R)$	t_{medstd}	A	A_{mp}
t_{mp}	59%	74%	74%	51%	51%	23%	54%
$A_{mp}(B)$	74%	54%	59%	59%	15%	54%	59%
$A(B)$	74%	59%	67%	56%	38%	62%	62%
$t_{median}(R)$	51%	59%	56%	64%	62%	36%	64%
t_{medstd}	51%	15%	38%	62%	28%	46%	33%
A	23%	54%	62%	36%	46%	46%	51%
A_{mp}	54%	59%	62%	64%	33%	51%	56%

Consistent with the two-class results, t_{mp} is likely a key feature in discriminating the five classes. The 59% performance and $F = 6.7 \pm 0.5$ is reflected in the test results and class-conditional probability densities shown in Figure 60. The results based upon

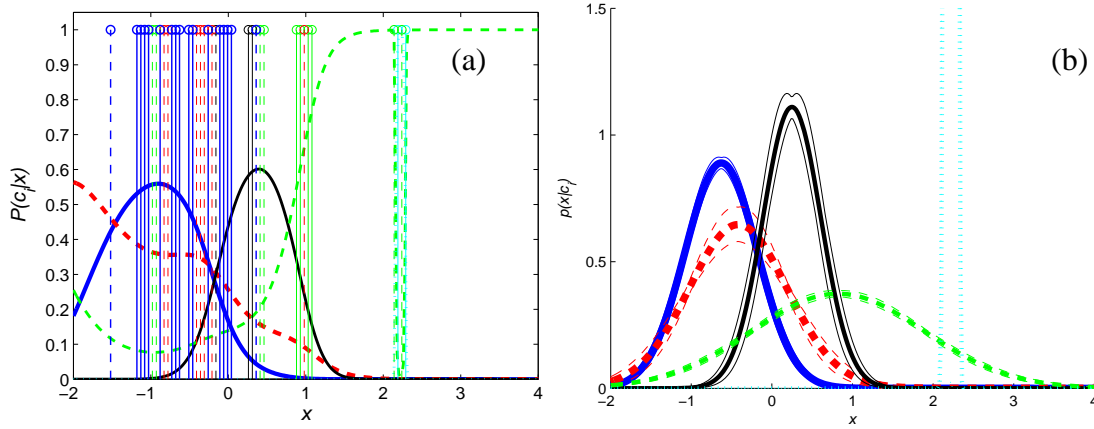


Figure 60. (a) Class-conditional posteriors and (b) class-conditional probability densities with a Fisher ratio of 6.7 ± 0.5 for the five classes with vertical lines drawn for test cases projected onto the single feature t_{mp} normalized to zero mean and unit variance. A solid (dotted) vertical line indicates a correct (incorrect) classification of the test event. The five types are ENE-50kg (thick solid), ENE-100kg (thick dashed), TNT-10kg (thin), TNT-50kg (thin dashed), and TNT-100kg (thin dotted).

$A_{mp}(B)$ shown in Figure 61, on the other hand, decreases the chance of correct classification to 54% with a $F = 4.6 \pm 0.9$. The combined effect of these two features (Figure 62) significantly raises the confidence to 74% and Fisher ratio to 11 ± 1 . As a corollary, $\underline{A}(B)$ has similar performance as $A_{mp}(B)$.

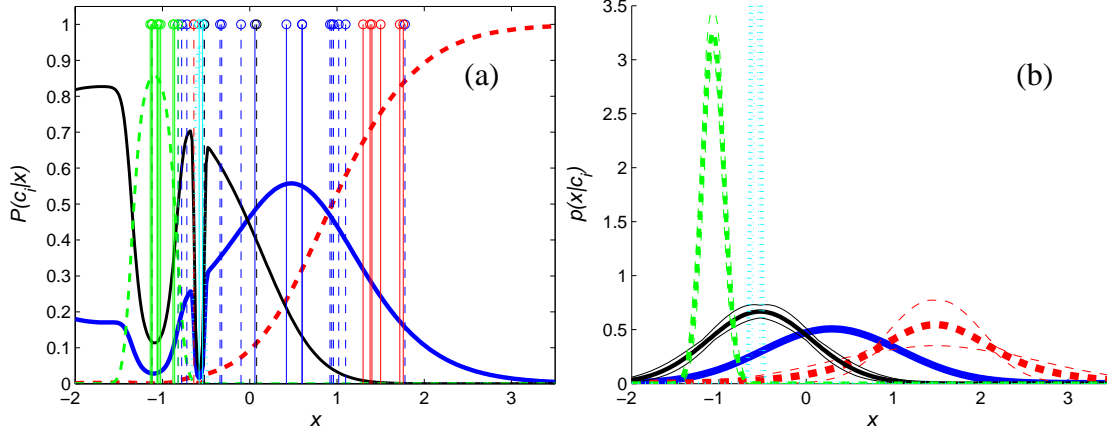


Figure 61. (a) Class-conditional posteriors and (b) class-conditional probability densities with a Fisher ratio of 4.6 ± 0.9 for the five classes with vertical lines (solid=correct, dashed=incorrect) drawn for test cases projected onto the single feature, $A_{mp}(B)$, normalized to zero mean and unit variance. The five types are ENE-50kg (thick solid), ENE-100kg (thick dashed), TNT-10kg (thin), TNT-50kg (thin dashed), and TNT-100kg (thin dotted).

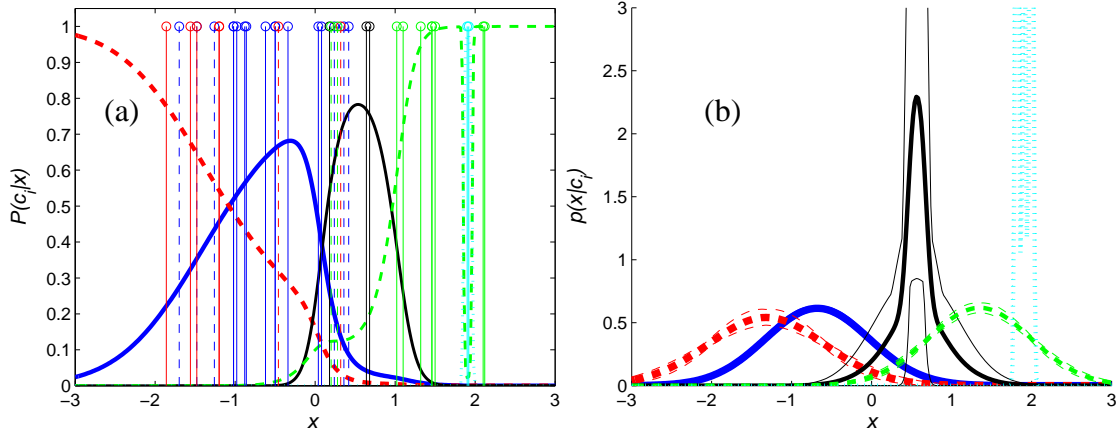


Figure 62. (a) Class-conditional posteriors and (b) class-conditional probability densities with a Fisher ratio of 11 ± 1 for the five classes with vertical lines (solid=correct, dashed=incorrect) drawn for test cases projected onto the two-feature set $\{t_{mp}, A_{mp}(B)\}$ normalized to zero mean and unit variance. The five types are ENE-50kg (thick solid), ENE-100kg (thick dashed), TNT-10kg (thin), TNT-50kg (thin dashed), and TNT-100kg (thin dotted).

J. Conclusions to discrimination tools development and imagery analysis

This chapter focused on one possible method of employing pattern recognition techniques to discriminate uncased explosives using features derived from imagery. The bomb detonation images are reduced to fireball areas which, for the first time, demonstrate that these types of explosives are reproducible. The pattern recognition tools, confirmed by scaling relationships, then quantify and rank the classification ability of various characteristic features of the fireball areas.

In general, as the number of features used to classify an event increase, the class-conditional probability densities become less stable and the resulting cross-validation returns a lower percentage of events that are correctly classified. Whether one uses a near-infrared InGaAs camera or a 3-chip color camera, one or two features provide sufficient ability to classify an explosive.

Three *a priori* conditions are examined for each type of camera and the combination of the two: (1) all events weigh 50 kg and are either TNT or ENE, (2) the weight is unknown and the type is either TNT or ENE, and (3) neither the weight nor the type is known. Overall, the features related to the peak of the fireball provide the best classification. For example, the time to fireball peak in the near-infrared (t_{mp}) is the best discriminator for each of the three *a priori* conditions. This feature correctly discriminates between TNT and ENE about 90% of the time, whether weight is known or not. The associated class-conditional probability densities separate the two classes with a Fisher ratio of 2.9 and an area under the receiver operating characteristic, A_{ROC} , of 0.992. Also, t_{mp} achieves approximately 60% success rate at discerning both weight and type.

Similarly in the blue band, the maximum fireball size ($A_{mp}(B)$) can tell a TNT event from an ENE event approximately 93% of the time when weight is 50-kg; otherwise, this feature is 79% accurate when weight is unknown. The better performance is indicative of the corresponding larger Fisher ratio of 5.4. The fireball area, integrated over the detonation time ($\underline{A}(B)$), is the best single color feature in discriminating both type and weight at a 67% success rate.

Linear combinations of two features improve classification. For example, combining $A_{mp}(B)$ with σ_{t_median} from the near-infrared will maximize (100%) the ability to classify an event as TNT or ENE if weight is known to be 50 kg. Likewise, t_{mp} and $\underline{A}(B)$ increase the accuracy from 59% using t_{mp} alone to 74% in the five class problem of distinguishing both explosion type (TNT or ENE) and weight (10, 50, or 100 kg).

A committee of classifiers breaks the unknown weight and type problem into two potentially solvable parts or committees. The first committee uses a feature to determine weight followed by the second committee which determines type from a second feature. Two of the extracted features scale with weight with varying amounts of error: the integrated near-infrared area over the detonation time \underline{A} , which has a 74% accuracy in predicting the three weights of 10 kg, 50 kg, and 100 kg, and the median time in the green color band $t_{median}(G)$, which has a 51% prediction accuracy. If a feature predicts weight accurately, then a second feature could determine the type as TNT or ENE. For example, if the weight is 50 kg then $A_{mp}(B)$ and σ_{t_median} could be used to determine the type. Unless additional reproducible data is acquired to improve weight prediction performance, then estimating both type and weight from $\underline{A}(B)$ alone yields similar accuracy.

V. Fisher discrimination of Radiant explosives

The previous chapter introduced a pattern recognition approach to classifying events and applied it to image data collected on uncased explosive materials. The spectra from these detonations were simultaneously collected and introduce very distinct spectral profiles from cased munitions detonation spectra as shown in Figure 63. Specifically, the cased munitions generate emission spectra similar to a blackbody attenuated by the atmosphere; on the other hand, uncased explosives under investigation are very non-Planckian as demonstrated with extra emissions and absorption spectral regions. Since a simple model to describe the uncased detonation spectra does not exist and is beyond the scope of the current work, the discrimination tools and approach developed in the previous chapter are now applied to spectra collected from the uncased munitions during Radiant field tests 3A and 3B. This chapter is begins with

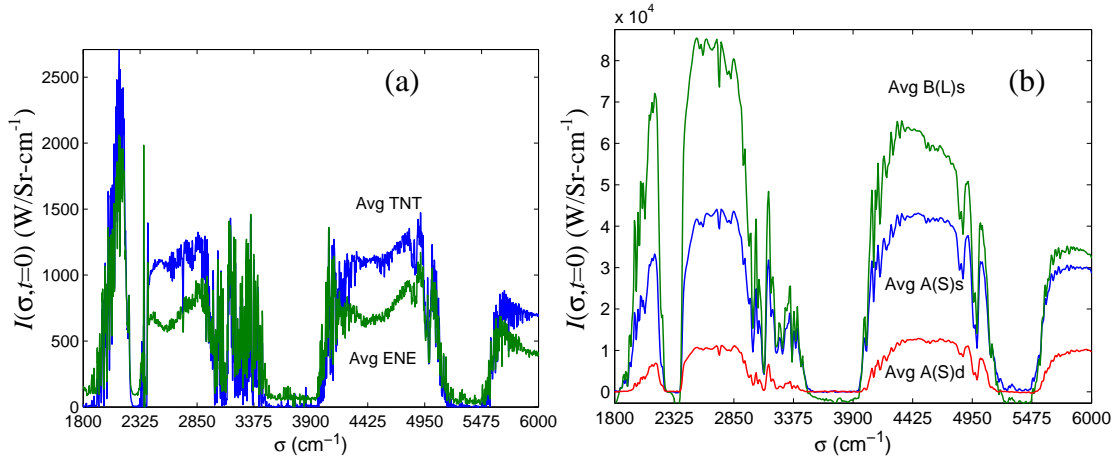


Figure 63. Spectral comparisons of various classes of munitions show that (a) uncased explosives contain strong emissions and absorption regions not characteristic of graybody emission and (b) the cased ordnances look much like a graybody attenuated by the atmosphere.

an introduction to the Radiant test series data followed by a short description of a referenced spectral fitting model. The discrimination tools are then applied to the fit parameters to establish feature saliency and classification ability.

A. Radiant test series

The Radiant test series collected spectral data from a variety of weapon munitions, which are grouped within five types: Type A Small static and dynamic (Table 21), Type B Large static and dynamic (Table 22), and Type B Medium dynamic (Table 23). Within these tables, the first letter is the type of ordnance (A or B); the second is the weight (S, M, or L); and the third is the method of delivery (d for dynamically air-dropped or s for a static detonation on the ground). An AFIT thesis by Jay Orson [28] contains a complete description of the test setup.

Typical spectral data is dependent on both the frequency (or wavenumber σ) and duration of the emission as shown in Figure 64 below. Atmospheric absorption regions cause the drop out in the data at various wavenumbers, *e.g.*, between 3000 and 4000 cm^{-1} . See Figure 2 on page 11 for more details on the atmospheric transmission properties. The intensity at longer wavelengths (shorter wavenumbers) is longer lived than the shorter wavelengths, which is consistent with a cooling blackbody emitter. At a moment in time, as seen in Figure 65, the intensity resembles the Planckian radiation law multiplied by an appropriate atmospheric transmission function, which is the fundamental aspect of the spectral model described in the next section. At a fixed wavenumber, the intensity exhibits two common profiles: one that decays like a single exponential and another that decays like a triple exponential as seen in the two examples in Figure 66.

Table 21. Type A Small (InSb, 16 cm^{-1}) event list.

Event ID	Type	Angle	Test
e214_03b	A (S)d	155°Perpendicular	RB3A
e214_04b	A (S)d	155°Perpendicular	RB3A
e214_05b	A (S)d	155°Perpendicular	RB3A
e214_06b	A (S)d	155°Perpendicular	RB3A
e214_07b	A (S)d	155°Perpendicular	RB3A
e215_22b	A (S)d	335°Toward	RB3A
e216_30b	A (S)d	65°Away	RB3A
e216_32b	A (S)d	65°Away	RB3A
e216_33b	A (S)d	65°Away	RB3A
e298_04b	A (S)s	45°Tower	RB3B
e298_05b	A (S)s	45°Tower	RB3B
e298_06b	A (S)s	45°Tower	RB3B
e298_07b	A (S)s	45°Tower	RB3B
e298_08b	A (S)s	45°Tower	RB3B
e298_10b	A (S)s	45°Tower	RB3B
e301_12b	A (S)s	45°Tower	RB3B
e301_18b	A (S)s	45°Tower	RB3B
e301_21b	A (S)s	45°Tower	RB3B

Table 22. Type B Large (InSb, 16 cm^{-1}) event list.

Event ID	Type	Angle	Test
e214_10b	B (L)d	155°Perpendicular	RB3A
e214_13b	B (L)d	155°Perpendicular	RB3A
e215_18b	B (L)d	335°Toward	RB3A
e215_20b	B (L)d	335°Toward	RB3A
e215_21b	B (L)d	335°Toward	RB3A
e216_43b	B (L)d	65°Away	RB3A
e301_15b	B (L)s	30°Elevation	RB3B
e301_16b	B (L)s	10°Elevation	RB3B

Table 23. Type B Medium (InSb, 16 cm^{-1}) event list.

Event ID	Type	Angle	Test
e214_14b	B (M)d	155°Perpendicular	RB3A
e214_15b	B (M)d	155°Perpendicular	RB3A
e216_39b	B (M)d	65°Away	RB3A

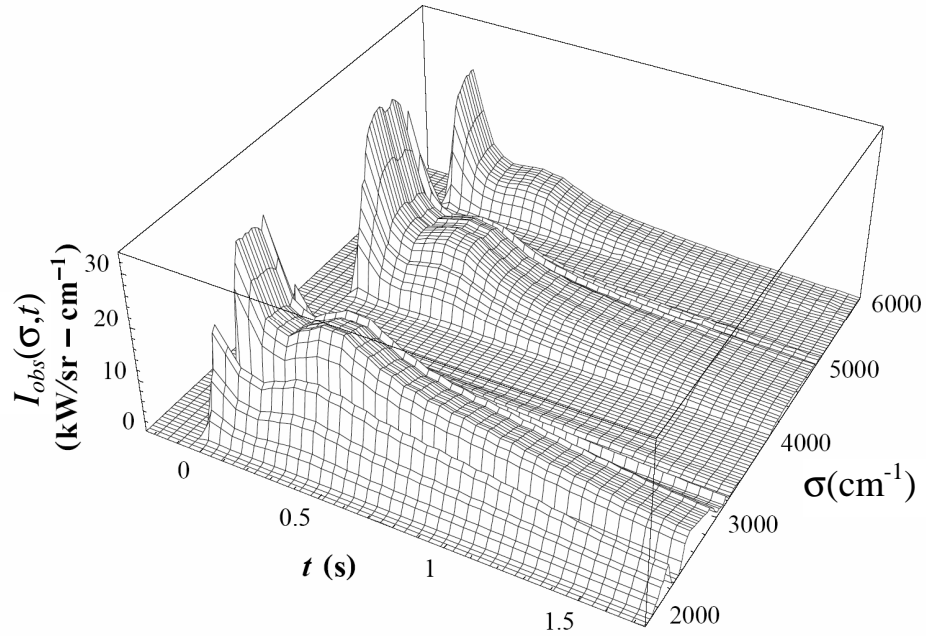


Figure 64. Typical Radiant spectral data is observed intensity I_{obs} as a function of frequency σ (cm^{-1}) and time t . The data shown here is downsampled to simplify the view.

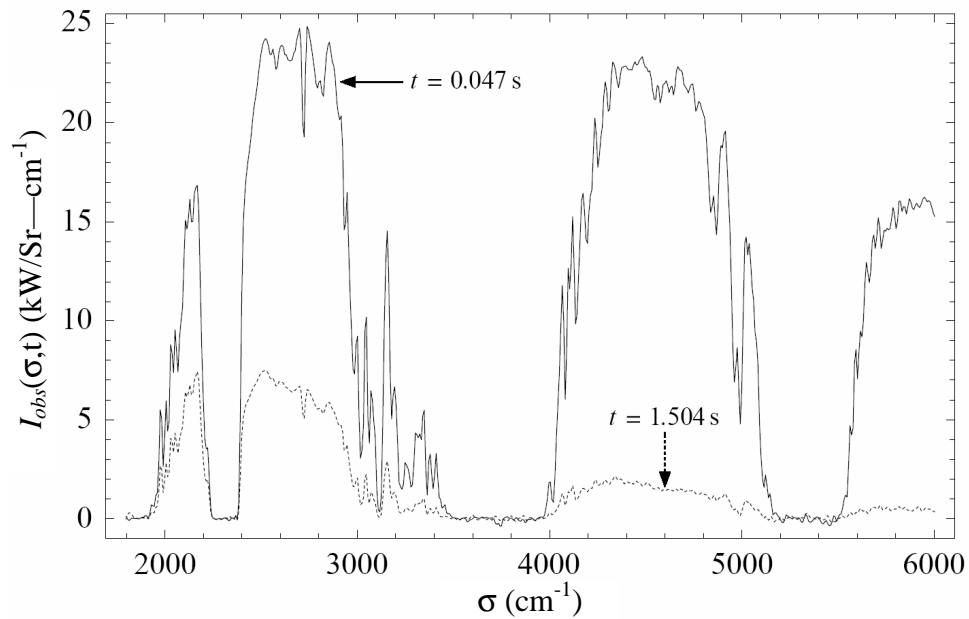


Figure 65. Radiant spectra from two time steps exhibits Planckian radiation law characteristics for when the atmospheric transmission is accounted.

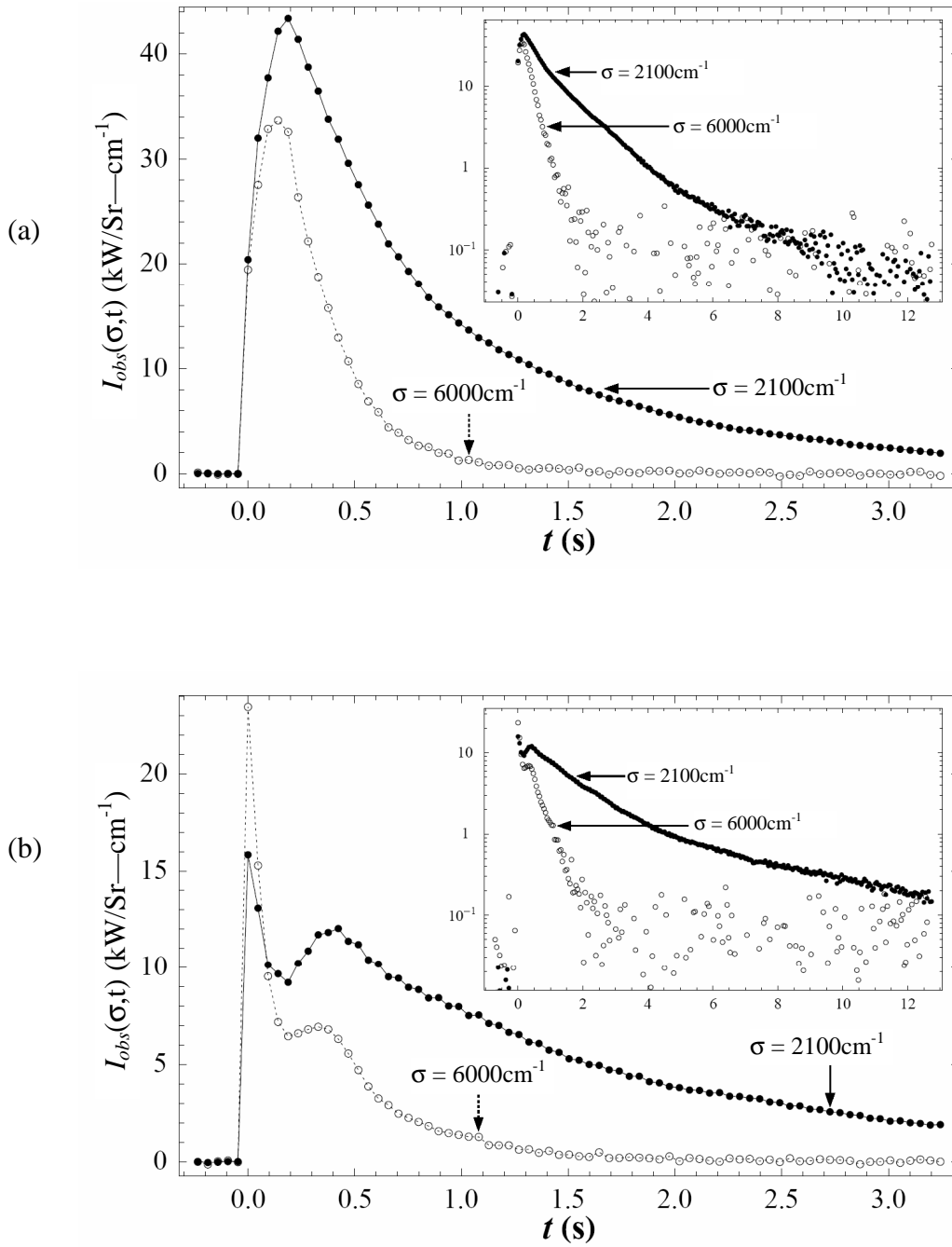


Figure 66. Temporal profiles of two types of emissions from Radiant test. Figure (a) shows an emission with a single exponential decay behavior, while Figure (b) exhibits a triple exponential decay.

B. Basic spectral model description

Current research by Ph.D. candidate, Mr. Kevin Gross, at the Air Force Institute of Technology [54] demonstrates the possibility of distinguishing explosive types by the features derived from a fit of the spectral data to the Planckian radiation law:

$$I(\sigma, T(t)) = A\varepsilon(t) \cdot L_{BB}(\sigma, T(t)) = A\varepsilon(t) \frac{2hc^2\sigma^3}{\exp(hc\sigma/k_B T(t)) - 1}. \quad (43)$$

Since the event intensities for these events is greater than 20,000 times the background, the background radiance contribution is ignored. The fit parameters in Eq.(43) include the temperature as a function of time $T(t)$, the area-emissivity product as a function of time $A\varepsilon(t)$ or $A(t)$ for short, and the fit residual as a function of time $\Delta I(t)$. This type of fit is made possible because of the Planckian nature of the spectral data and a unique method to describe the current state of the atmosphere. The atmospheric model, in most simple terms, uses distinct features of the various absorbers (*e.g.*, H₂O, CO₂, CH₄, N₂O, and N₂ continuum), to correct a generic MODTRAN transmission description. An example form [37] which displays these corrections is provided in Figure 67. An example residual to the fit data is shown in Figure 68. Pronounced residuals above background, *e.g.* $\Delta I_0 = 4$ - 8 kW/Srcm^{-1} , are consistently observed for the Radiant data in the 1950 to 2250 cm^{-1} region. Thus, in addition to the area-emissivity $A(t)$ and temperature $T(t)$ derived from the Planck fit, the integrated residual as a function of time in this region $\Delta I(t)$ provides a third extracted parameter. These three parameters now represent the data set seen in Figure 64. Each of the three parameter values for each event in the Radiant test series is plotted in Figure 69 through Figure 71.

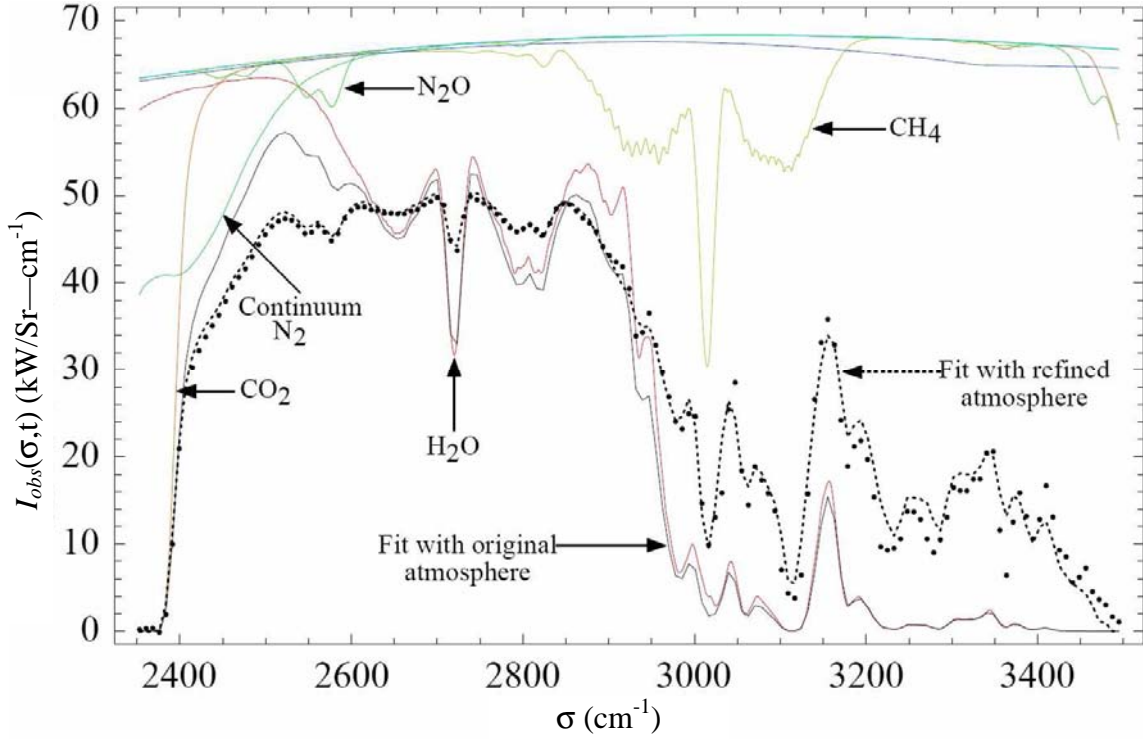


Figure 67. Atmospheric correction involves systematically adjusting atmospheric absorption species' concentrations to match the absorption features seen in the data.

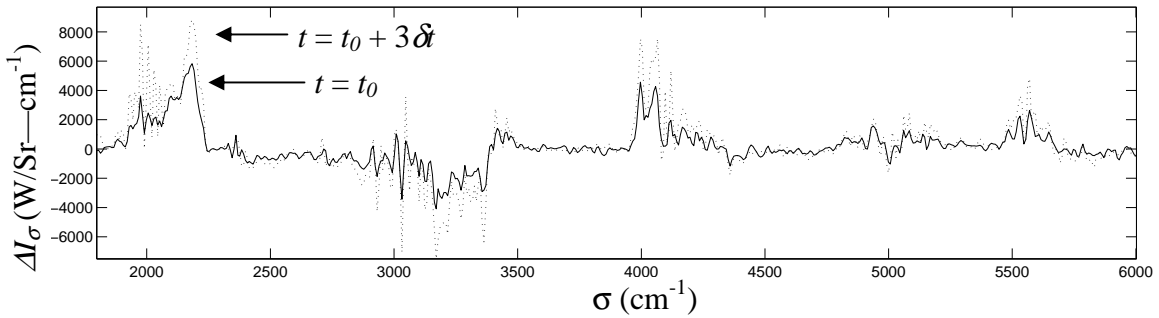


Figure 68. Spectral residuals between the data and the Planckian fit for a Radiant event show a growth in the 1950-2250 cm^{-1} region. The two residuals shown here are calculated at detonation time, t_0 and three time steps later $3\delta t = 0.147\text{s}$.

The least distinguishing Planck radiation parameter is the temperature as a function of time from detonation $T(t)$. Each of the types shown in Figure 70 and Figure

72(b) all exhibit an exponential decay in temperature. One possible discriminator is the rate at which these temperatures cool down to ambient. The area-emissivity product $\epsilon A(t)$ on the other hand shows some potential for discriminating a few of the types shown in Figure 69 and Figure 72(a). This area is different than the area from the imagery as discussed in the last chapter. The product of the area and emissivity is a mid-IR feature that combines the effect of a fireball growing and cooling in time and the emissive properties of a graybody fireball. These differences may be beneficial in distinguishing between the Radiant explosive types. First of all, $A(t)$ reaches a higher first maximum in the A(S)s events than it does in the A(S)d events. A strong positive slope toward this first maximum is also consistent with A(S)s events; where as, a negative slope toward a minimum is representative of B(L)s events. Additionally, the areas continue to grow at a faster rate in the static events. Lastly, if one excludes the outlier B(L)d event, there seems to be no obvious differences between the dynamic events.

Possibly the strongest discriminator lies in the integrated residual between 1950 and 2250 cm^{-1} . (A short-hand notation of ΔI is used in replace of $\Delta I/\tau$ (1950-2250 cm^{-1}).) The represented data in Figure 71 and Figure 72(c) shows that most of the static events have a peak ΔI greater than $3 \times 10^6 \text{ kW/Sr}$. Within the static events, the initial Δt_0 and the ratio of the this value to the peak Δt_{mp} is smaller for the Type A small (A(S)) events than they are for the Type B large (B(L)) events. Lastly, the shapes of the static events are more reproducible, resembling either a double exponential for A(S)s events or a single exponential decay for the B(L)s events.

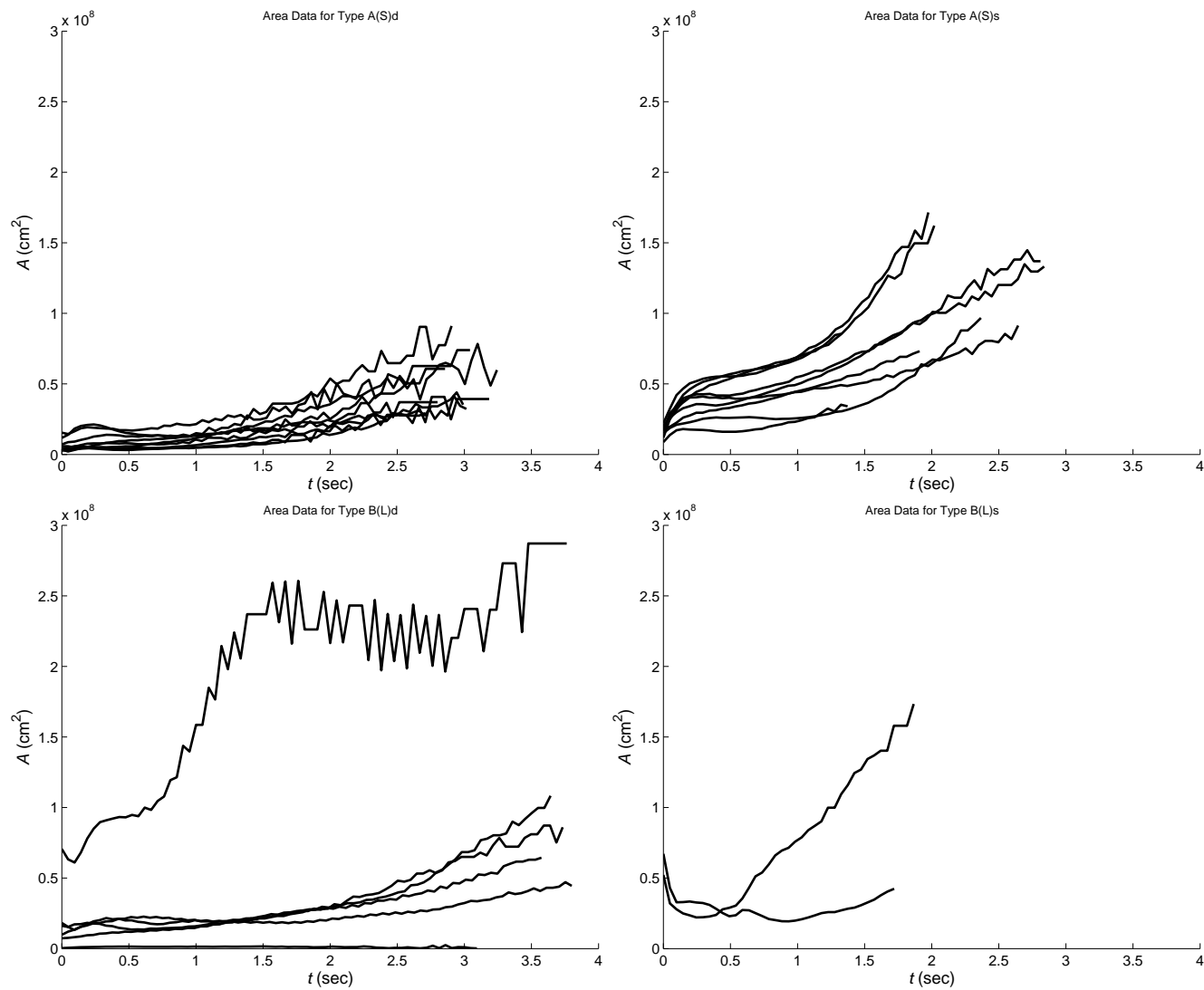


Figure 69. Radiant area-emissivity products A as a function of time t , as derived from the Planckian fits.

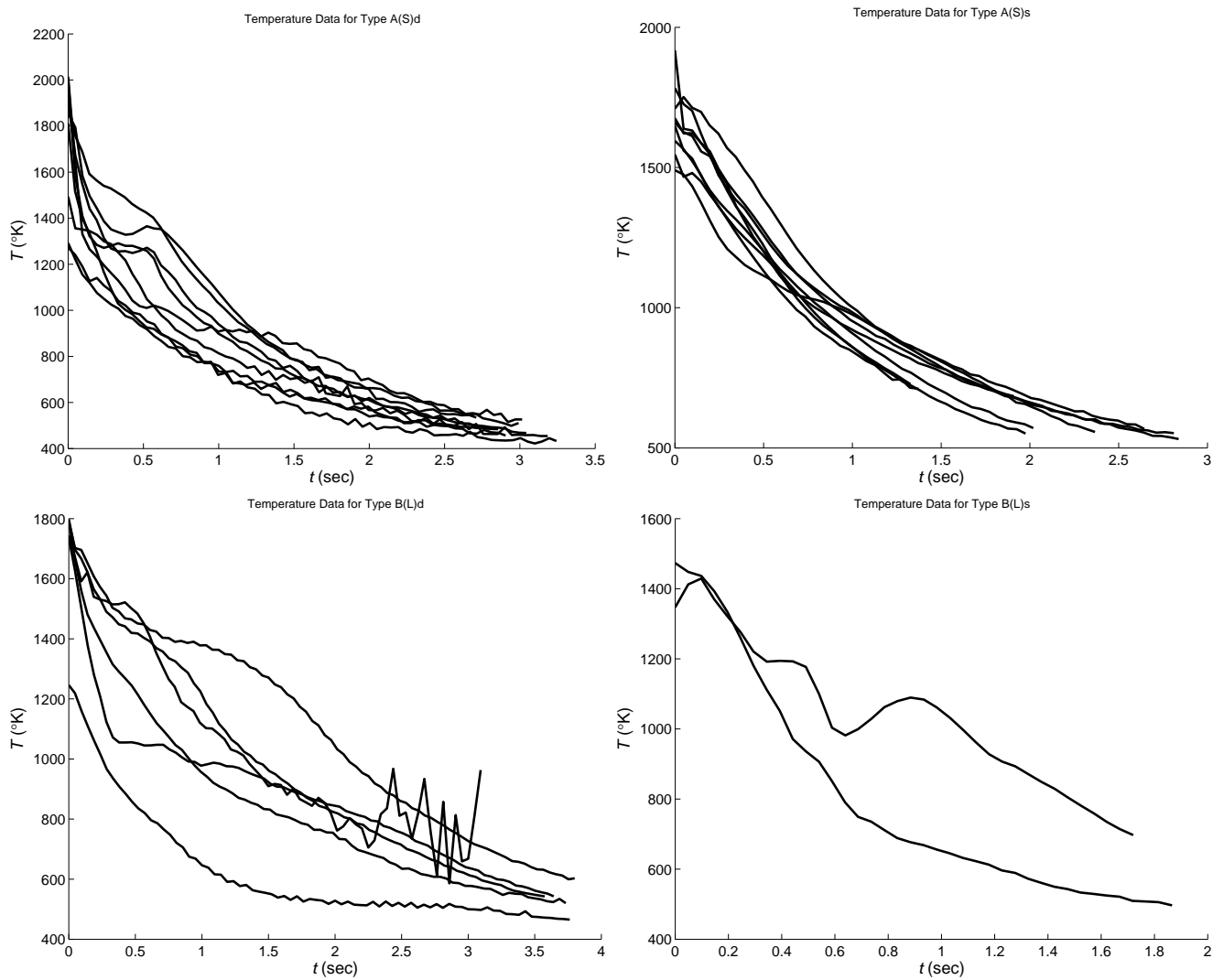


Figure 70. Radiant temperatures T as a function of time t , as derived from the Planckian fits.

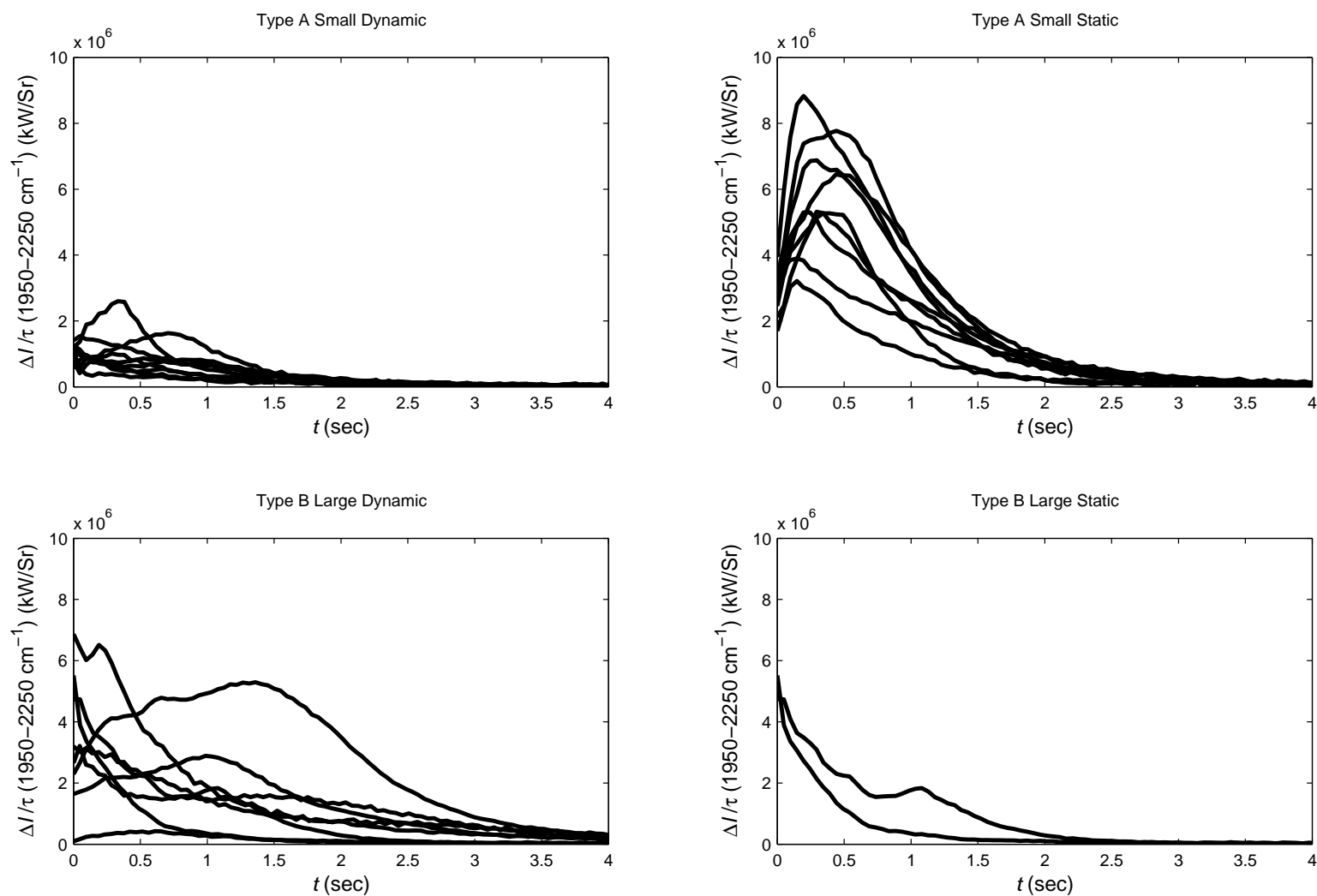


Figure 71. Radiant integrated residuals ΔI ($1950\text{--}2250\text{cm}^{-1}$) divided by the atmospheric transmission function τ as a function of time t , as derived from the Planckian fits.

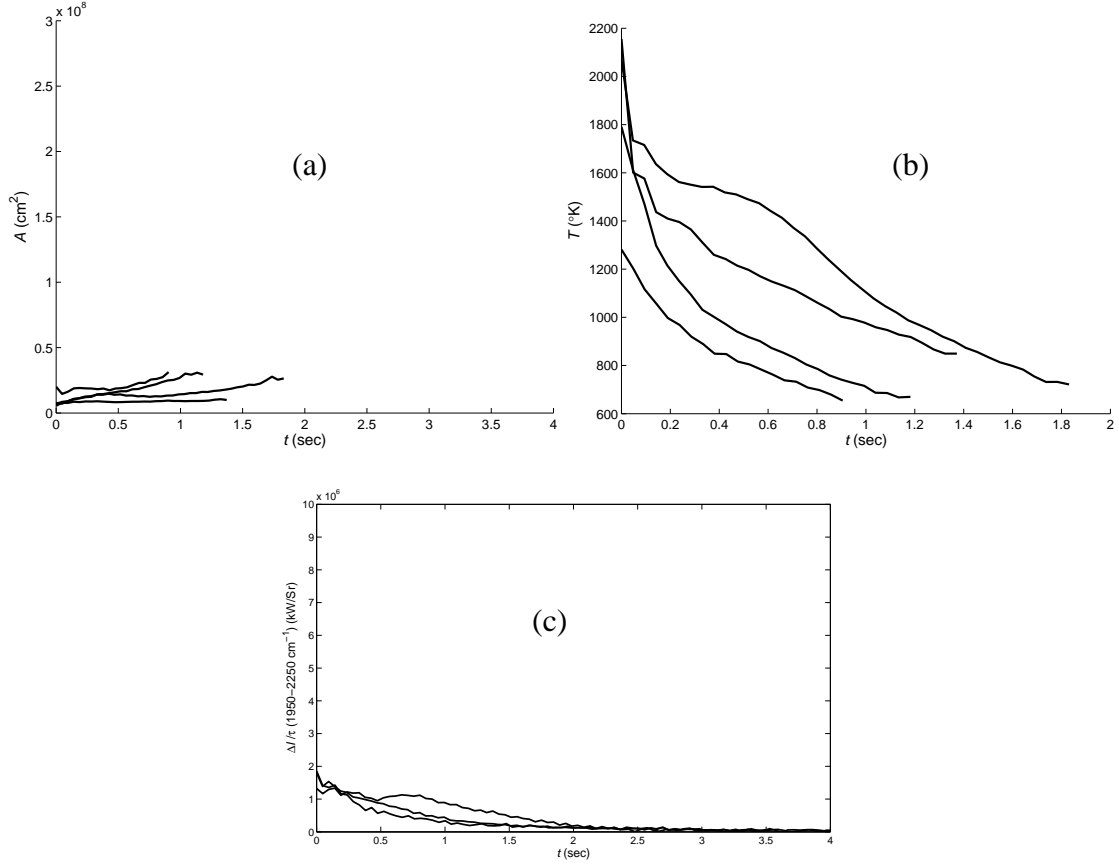


Figure 72. Planckian fit parameters for Radiant events of type B, medium weight, and dynamically dropped. Figures (a), (b), and (c) are the area-emissivity, temperature, and residual properties, respectively.

C. Feature extraction

The temporal behaviors of the Planckian fit parameters identified above aid in determining features that capture the differences and similarities among the various data types. This list of features is fed into the discrimination tools developed in the last chapter to produce probabilistic capabilities to distinguish among the Radiant event types.

The features that capture the $T(t)$ are the fit values to an exponential decaying function that begins at a high temperature T_H and decays at the rate Γ to a low temperature T_L :

$$T(t) = (T_H - T_L) \cdot \exp(-\Gamma \cdot t) + T_L. \quad (44)$$

The area-emissivity product $A(t)$ is captured by a more complicate model that includes terms to model the initial rise, the plateau, and final rise in the tail:

$$A(t) = A \cdot S(t | s) \cdot \exp(-k_a t) + B \cdot (1 - \exp(-k_b t)) + C \cdot H(t_0) \cdot (t - t_0), \quad (45)$$

where A and B are amplitudes; k_a and k_b are rates of decay; $H(t_0)$ is the heavy-side function turning on a linear term, $C(t - t_0)$, as needed; and $S(s)$ is a switching function that monotonically and smoothly increases from 0 to 1 and controls the rate at which the first term “turns-on:”

$$S(t | s) = \frac{1}{1 + \exp(-st + \alpha)}, \quad (46)$$

where α is a fixed constant, $\alpha = 3.42174$. This single model for the area-emissivity product captures the range in the $A(t)$ behavior as shown by a few examples in Figure 73.

The last set of features is derived from the residual information ΔI which is the residual between the data and the Planckian fit, integrated from 1950 to 2250 cm^{-1} which is speculated by Mr. Gross to be the spectral region associated with burning of hot CO_2 . The inconsistent temporal behaviors of ΔI lead to no simple single model to describe all the data. Thus direct values, such as the ones mentioned before, are extracted from the data and used as features. These features as well as a general description of all the features mentioned for the Radiant data is presented in Table 24.

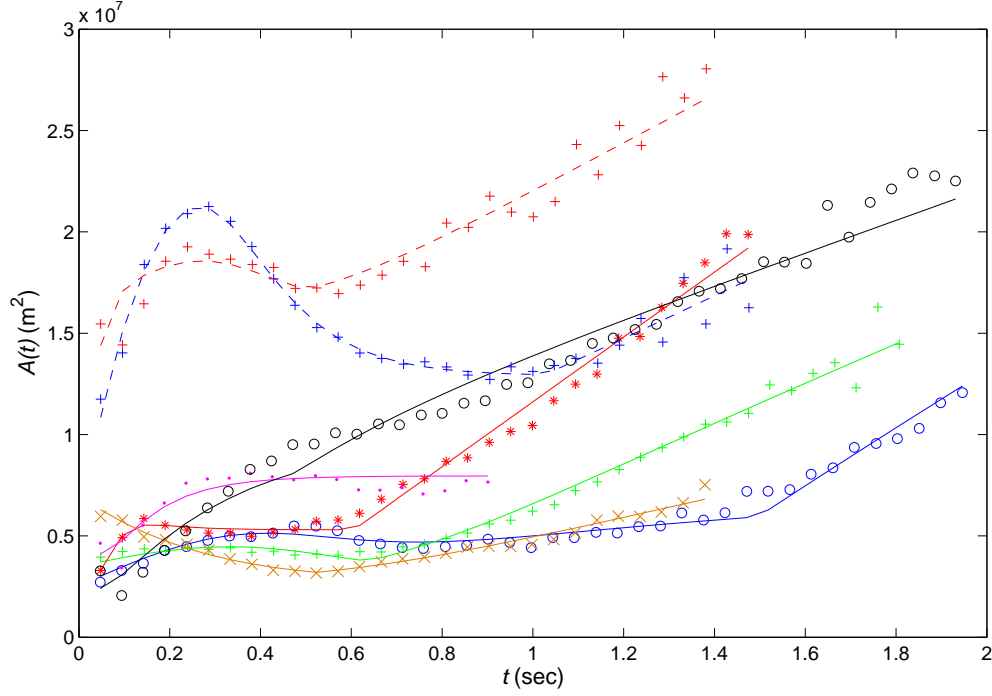


Figure 73. These fits to example area data show that Eq.(45) models the range of possible $A(t)$ behavior.

D. Scaling relationships of the extracted spectral features

The values of each of the features described above are examined for possible scaling relationships. Appendix I contains each feature plotted as a function of size (small, medium, and large given fictitious values of 10, 50, and 100 kg) and type (x for static events and o for dynamic events). Of the 23 features, five show promised ability to distinguish either type or weight and are shown in Figure 74. $\Delta I_{mp}/\tau$ separates most of the static events from the dynamic events independent of weight. For the Type A small, $A(S)$, both T_L and A_{t0} separate most of the static and dynamics events. Within the static events, $\Delta I_0/\tau$ and $R_{mp/0}$ both show promise in distinguishing weight.

Table 24. Features and their descriptions used for discriminating spectral data.

Symbol	Unit	Description
T_H	(K)	High temperature for $T(t)$
T_L	(K)	Low temperature for $T(t)$
Γ	(s ⁻¹)	Exponential decay rate for $T(t)$
σ_{TH}	(%)	Error in T_H
σ_{TL}	(%)	Error in T_L
σ_Γ	(%)	Error in Γ
A_A	(cm ²)	Amplitude of first term in $\varepsilon A(t)$
A_Switch	(unitless)	Switching value to control the turn-on of the second term in $\varepsilon A(t)$
A_k _a	(s ⁻¹)	Exponential decay rate for the first term in $\varepsilon A(t)$
A_B	(cm ²)	Amplitude of the second term in $\varepsilon A(t)$
A_k _b	(s ⁻¹)	Exponential decay rate for the second term in $\varepsilon A(t)$
A_C	(cm ²)	Amplitude of the third term in $\varepsilon A(t)$
A_t ₀	(s)	Time to turn on linear term in $\varepsilon A(t)$
CO_I _{mp}	(W/Sr)	Peak of $\Delta I(t)$, also ΔI_{mp}
CO_t _{mp}	(sec)	Time at ΔI_{mp}
CO_I ₀	(W/Sr)	$\Delta I(t)$ at detonation time, also ΔI_0
CO_t ₂	(sec)	Time nearest to 2 seconds
CO_I ₂	(W/Sr)	ΔI at $t = 2$ seconds, also ΔI_2
CO_t _{0.5}	(sec)	Time nearest to 1/2 second
CO_I _{0.5}	(W/Sr)	ΔI at $t = 1/2$ second, also $\Delta I_{0.5}$
CO_R _{I2/10}	(unitless)	$\Delta I_2 / \Delta I_0$
CO_R _{2/0.5}	(unitless)	$\Delta I_2 / \Delta I_{0.5}$
CO_R _{mp/0}	(unitless)	$\Delta I_{mp} / \Delta I_0$

E. Committee of classifiers to discriminate Radiant events

The committee of classifiers approach to discriminating the Radiant events using the spectral data uses the observations made earlier to identify candidate features that may aide in classification followed by a robust test to determine the accuracy in class predictions. These candidate features are the five shown in Figure 74 and accuracy results from robustly testing are given in Table 25. For each feature or combination of features, the robust test examines 1000 possible cases where each case uses a different set

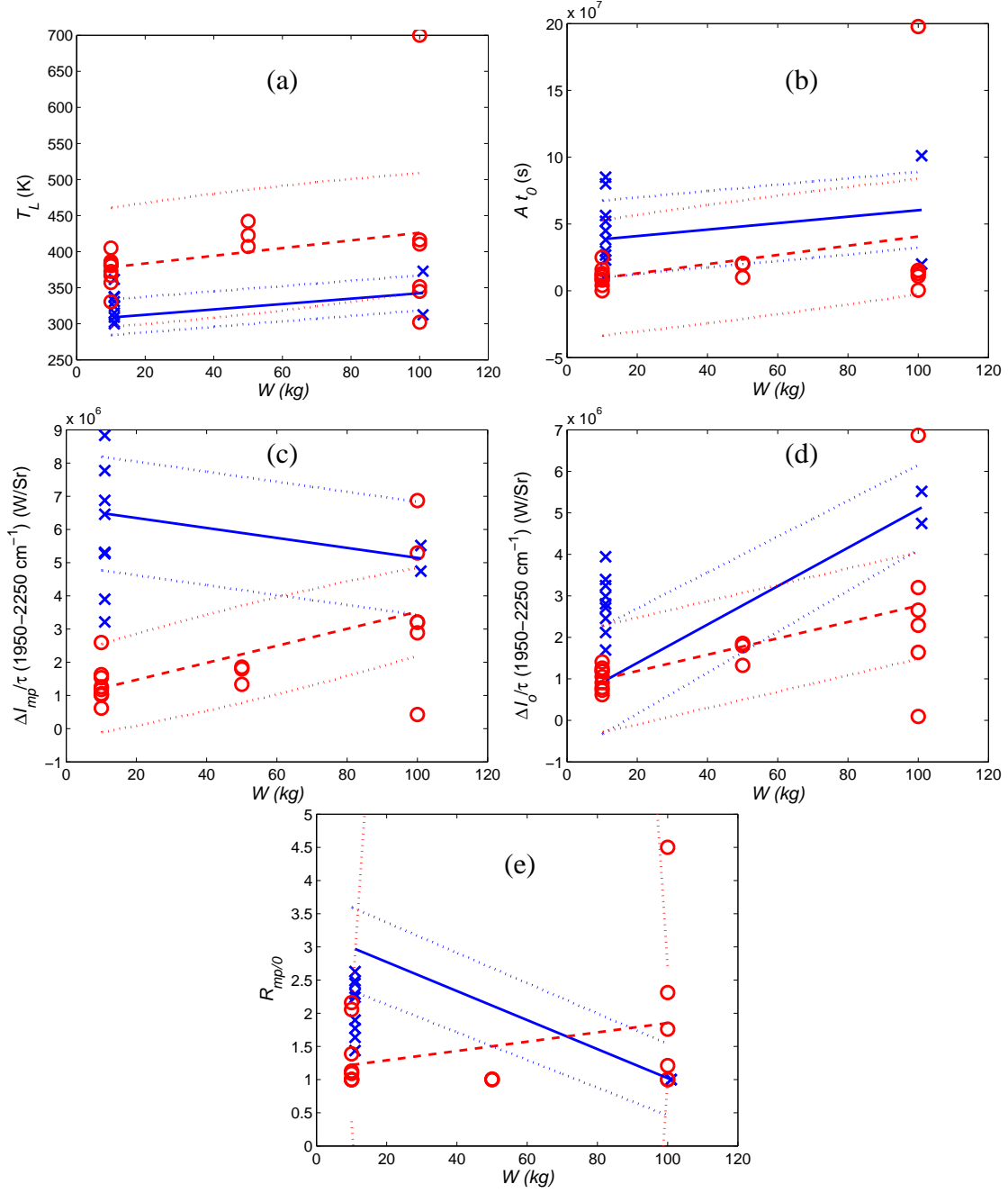


Figure 74. Five features extracted from the spectra that exhibit classification potential are (a) the low temperature fit parameter T_L , (b) the time constant $A t_0$ controlling the turn-on for the linear portion of $A(t)$, (c) the most probable or peak value and (d) the initial value of the integrated residual divided by the transmission profile of the atmosphere ($\Delta I_{mp}/\tau$ and $\Delta I_0/\tau$), and (e) the their ratio $R_{mp/0}$. X = static events. O = dynamic events. 10, 50, 100 kg represent A(S), B(M), and B(L), respectively.

of five events for testing and the remaining for training. After the 1000 cases, the mean of all class-conditional probability densities is tested by each event to determine the ability of the densities to distinguish between types. The best performing features, shown in Figure 75, are those associated with the CO₂ emission region.

Table 25. Prediction accuracies based upon the feature used. The results in the solid box refer to the ability to distinguish static and dynamic events if Type A(S). The dashed box contains the prediction accuracy to distinguish static and dynamic events independent of weight or type. The dotted box addresses the ability to distinguish small and large static events.

spectral features	T_L (°K)	A_{t0} (s)	$\Delta I_{mp}/\tau$ (W/Sr)	$\Delta I_{mp}/\tau$ (W/Sr)	$\Delta I_0/\tau$ (W/Sr)	$R_{mp/0}$
T_L	89%					
A_{t0}	89%					
$\Delta I_{mp}/\tau$	100%					
$\Delta I_{mp}/\tau$				86%		
$\Delta I_0/\tau$					100%	
$R_{mp/0}$						90%

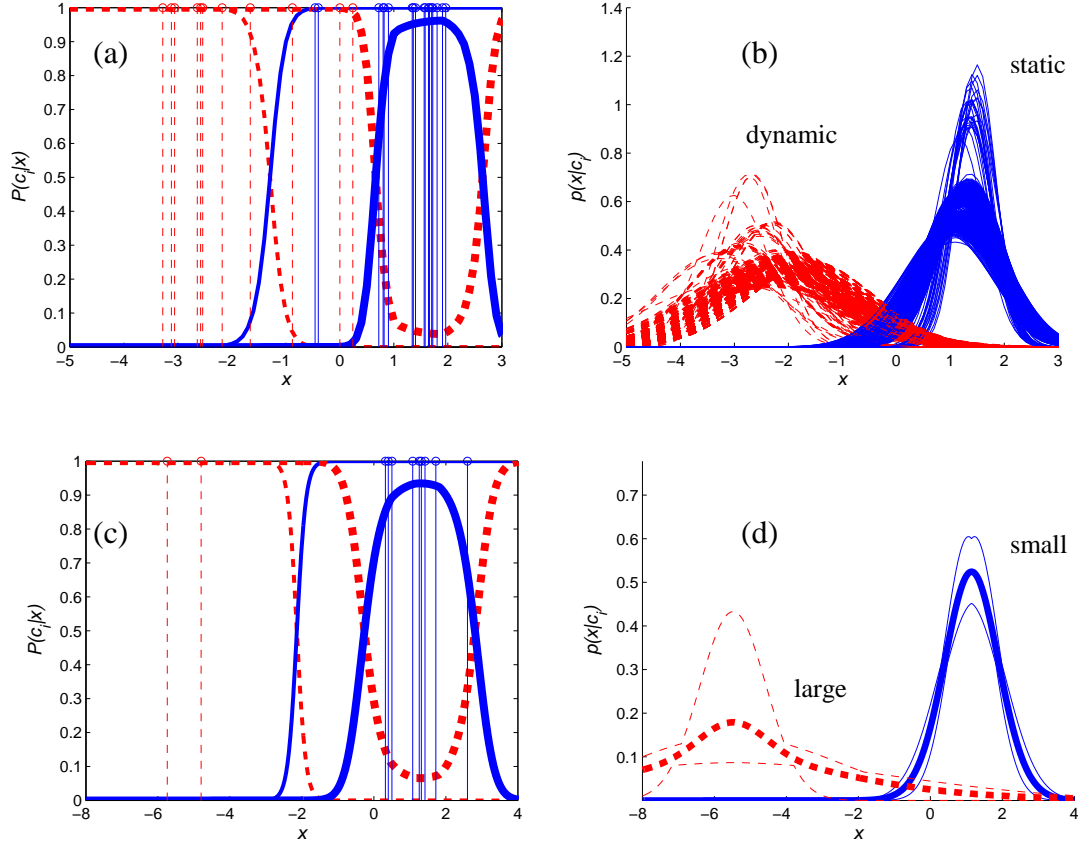


Figure 75. Class-conditional probabilities (right column) and resulting range of posteriors (left column) with test data identified as vertical stems illustrates class separation and reason for high accuracies in placing a new event into the right class. Figures (a) and (b) are for the feature ΔI_{mp} which yielded a 86% accuracy of 998 test cases ($F = 11.0 \pm 1.0$) in determining if an event is static or dynamic, independently of weight. Figures (c) and (d) show the results of using ΔI_0 to distinguish large and small static events with 100% accuracy for 11 test cases ($F = 99 \pm 32$).

F. Conclusions to using spectra to discriminate munitions

For the first time, the Planck radiation function multiplied by an accurate atmospheric model is applied to the emissions from cased munitions collected during the Radiant test series. As a result, this novel approach shows reducibility in three time-dependent parameters that represent the intensity data as a function of wavenumber and

time: the area-emissivity product, the temperature, and the integrated residual of the fit from 1950 to 2250 cm^{-1} . These fit parameters demonstrate differences between the static events, dynamic events, and weights. Twenty three features are further extracted from these time-dependent parameters, and pattern recognitions tools quantify these features' ability to classify events. The best two features come from the integrated residual $\Delta I(\sigma)$ in the 1950 to 2250 cm^{-1} spectral band and provide an ability to classify some of the event types collected during the Radiant test. The integrated residual initial magnitude at detonation ΔI_0 seems to scale with weight—particularly the static events of which this feature predicts the weight with 100% accuracy and large class separation represented by a Fisher ratio of $F = 99 \pm 32$. The second feature is the peak of the integrated residual ΔI_{mp} which does not scale with weight but does distinguish between static and dynamically dropped ordnances with 86% accuracy and a Fisher ratio of $F = 11.0 \pm 1.0$, given similar test conditions. If *a priori* information is that the event type is Type A Small, then this same feature can absolutely determine if the event was statically detonated or dynamically dropped.

VI. Conclusions

A. Impact of this research on classification

Significant progress towards the classification of battlespace detonation events has been achieved, including (1) acquisition of reliable signatures for specific event classes under field conditions, (2) enhanced characterization of event phenomenology for key feature extraction, (3) apply quantitative classification methodology using class conditional probability densities, (4) selection of key features that offer reproducibility within a class and distinguishability between classes, and (5) demonstration of successful classification within a defined subset of event types. For the first time among the small community involved in munitions classification, pattern recognition tools have been applied to a set of key image and spectral features to exploit class-conditional probability densities and establish that classification potential is high among the event types investigated. Additionally, these features provide valuable insights for newly documented bomb/fireball phenomenology.

Two new field tests were designed and conducted with the objective of classification between uncased conventional munitions as represented by trinitrotoluene (TNT) and an enhanced novel explosive (ENE) material of interest to the military intelligence community. Signatures for 95 events, including mid-infrared spectra, near-infrared imagery, and three-band visible imagery, were acquired over approximately 30 days during two separate field deployments.

Detonation fireballs from cased munitions are largely Planckian in the mid-infrared with initial temperatures of 1200 – 1800 °K, attenuated by atmospheric

absorption. Temperatures often decay exponentially to ambient within 1 – 3 s for large charges of cased munitions and in less than 1 s for uncased or smaller weight charges. Occasionally, temperature profiles exhibit secondary maxima at 0.5 – 1 s after detonation. Non-Planckian spectra features, particularly in the 1950 – 2250 cm^{-1} band, are observed with 10% deviation from Planckian behavior for cased munitions and often greater than 50% for uncased munitions. Fireballs from uncased explosives typically attain a maximum area in the near infrared of 100 – 200 m^2 at 20 – 200 ms after detonation. Fireball size depends on imaging frequency band, with smaller, shorter lived fireballs in the blue. The combination of decaying temperature and growing fireball size often produce irradiance profiles with secondary maxima at 0.25 – 0.5 s.

Discrimination tools based on standard pattern recognition techniques quantify the classification potential of the extracted features using (1) the Fisher ratio and (2) the area under the receiver operating characteristic curve (ROC) to capture class separation and clustering of class-conditional probability densities, and (3) a performance percentage value of correct classification during cross-validation. Classification stability is also captured by the standard deviation of the Fisher ratio or that of the area under the ROC curve, A_{ROC} . Thus, a good feature is independent of training and testing data selection and is one that consistently generates a high Fisher ratio (or A_{ROC}), a low standard deviation in the Fisher ratio (or area A_{ROC}) and small standard deviations in the locations of the class-conditional probability densities. Feature stability is also independent of training and testing data selection and is measured by a consistent ordered ranking of features by either the Fisher ratio or the area under the ROC curve. Interestingly, some features produce a relatively high Fisher ratio, yet the class-

conditional probability densities overlap significantly because one density is nearly a delta function in the vicinity of the other class density. This case may be useful in some applications where high discrimination confidence is required.

This research has shown that a more appropriate method of employing pattern recognition tools is to use a committee of classifiers which first examines each extracted feature for scaling law properties. Features that scale with weight or type of munition not only best perform classification but also provide the pool of features from which feature saliency, or ranking of features, is determined. Based upon the current findings in projecting a multidimensional feature-space into a one-dimensional Fisher line for discrimination, a set of two features is the limit before feature stability declines. Higher dimensional discrimination along Bayesian decision boundaries defined by hyperquadric lines or three-dimensional surfaces may provide the dimensionality necessary to discriminate using three or more features. In effect, the committee of classifiers is a step toward multivariate discrimination using two-dimensional probability densities.

Using the developed tools for quantifying classification potential for cased munitions emission spectra, the mid-infrared spectra from cased munitions can be reduced to a set of features including fireball temperature, area, and residuals to Planckian fits in selected spectral bands as a function of time. The residuals in the $1950 - 2250 \text{ cm}^{-1}$ ($4.4\text{-}5.1 \text{ }\mu\text{m}$) band corresponding to hot CO_2 emissions are typically less than 10% and provide the best discrimination between explosive type, size, and method of detonation (static or aircraft delivered). Indeed, discrimination based only on the peak residual provides 100% accurate classification and $F = 14 \pm 1$ between static and dynamic detonation for one type and size of munitions and 86% accuracy independent of type and

size ($F = 11.0 \pm 1.0$). Equally impressive is the ability to distinguish between large and small weights for static detonations at 100% accuracy and $F = 99 \pm 32$ using the residual immediately after detonation. Uncased munitions exhibit highly non-Planckian behavior, offering strong classification potential for TNT and ENE materials.

Uncased munitions, on the other hand, are not Planckian, yet the fireball size derived from near-infrared and color imagery shows sufficient reproducibility and class distinguishability to warrant quantification. The areas derived from the images are phenomenologically different from those derived from the Planckian fit in that areas from the imagery quickly rise before falling to background. As discovered with the cased munitions, only one or two features from the fireball area are useful in classifying explosion types and weights while maintaining stable class-conditional probabilities.

Three *a priori* conditions are examined for an unknown event being an uncased explosive device made of either TNT or an enhanced material: (1) all events weigh 50 kg and are either TNT or ENE, (2) the weight is unknown and the type is either TNT or ENE, and (3) neither the weight nor the type is known. Overall, the features related to the time to peak (t_{mp}) of the fireball area in the near-infrared provide the best classification for each of the three *a priori* conditions. For TNT, $t_{mp} = 40 - 160$ ms and for ENE materials, $t_{mp} = 0 - 60$ ms. Feature saliency from Fisher discrimination techniques always yields t_{mp} as the most important feature, with duration of the fireball and symmetry of its area, as measured by the standard deviation in the median time and the skew in the residual of a parametric fit of the area, as secondary features. The single feature t_{mp} yields a Fisher ratio of $F = 2.9 \pm 0.3$ and 89% accuracy in robust testing of explosive type classification if the weight is known *a priori* (at 50 kg) and 87% and

$F = 2.5 \pm 0.1$ if the weight is unknown. Similarly, the single best feature from the 3-band visible imagery is the maximum area in the blue band, A_{mp} , of $10 - 60 \text{ m}^2$ for TNT and $40 - 280 \text{ m}^2$ for ENE. This feature provides 93% and 79% correct classification and $F = 5.4 \pm 0.2$ and 4.4 ± 0.1 for the 50 kg and unspecified weights, respectively.

Combining the time to peak size in the near IR and maximum area in the blue does not significantly improve the classification performance. For a five class problem of two types and three weights, combining these two features improves the classification performance to 74% from 54% for either feature alone. The single best feature for the five class problem is the time integrated area in the blue band, but this feature is highly correlated with the corresponding peak area. Linear combinations of two or more features do not improve classification and decrease stability in the locations and peaks of the class-conditional probability densities.

In general, image data contains more information about the type of explosive than about the weight. Even so, success in discriminating cased munitions with spectral content leads one to believe that classification of uncased explosives will improve as a phenomenological model is developed to capture features related to the peak of the fireball area and other unique features from the spectra. Additionally, the imagery features examined in this effort are limited to those associated with the fireball area, which is only a small portion of potential information in the image. Other important features could possibly be associated with the shape of the fireball, structure due to fluid dynamics immediately surrounding the fireball (*e.g.* vortices and turbulence), or the reflected signal from the ground or air.

B. Recommendations and opportunities

Further study is necessary to understand the phenomenology behind the emissions from uncased explosives. As one develops this knowledge, source intensity could be derived after appropriately compensating for the atmospheric effects. The challenge is decoupling the atmospheric effects and the uncased emission effects. Currently, it is unknown whether the area of a fireball grows because it is getting bigger or because the emissions in certain spectral regions drive an apparent growth. Likewise, a disconnect exists between the time dependent area derived from imagery and the spectra. The relationship between these two behaviors may lie in a proper description of the fireball emissive properties. In addition to phenomenology driving the area time dependence, it is also responsible for other information, such as the time evolving shape of the fireball as seen in the images.

Once these issues are resolved in the phenomenological description of the fireball, the source intensity should be accurately determined. Then clear differences in the spectra, images, etc. of explosive type should be easily observed. These differences could contain information about the emissions one observes in the 1950 to 2250 cm^{-1} region and other absorption effects, which in turn should further improve the phenomenological model.

Coupled with a phenomenological model is a need for better understanding of the limits of the instrumentation. Accurate and frequent calibration is vital to ensure quality data and analysis results. Both teams have significantly improved their ability to acquire accurate data, validate calibrations, and cross-validate with other collection instruments fielded for the same event. Even with good calibration, none of the currently deployed

instruments frame fast enough to capture the first part of the explosion, which may contain critical phenomenological features. Likewise, the emissions from an explosion change rapidly in time, which challenges the accuracy of an FTIR instrument scanning the spectrum with a moving mirror. For this reason, one needs to study the effects of fast transient signatures recorded by an FTIR as a function of mirror velocity. While recording at a slower rate, near-infrared and color imagery have proved to be effective sources for discrimination. Techniques presented in this research allow the coupling of image and spectral information to aid classification. Yet to better understand the kinetics of a fireball, one needs to investigate the spectral content of a fireball as a function of position on the fireball with high temporal resolution. For this reason, future studies should include an instrument capable of recording spatial dependent spectra at fast framing rates.

Even without new instruments, much more can be done to quantify the classification capability of various bomb or explosive types. For example, pattern recognition techniques go well beyond those discussed in this research project. This research utilizes one-dimensional linear approaches to define decision boundaries between classes, yet better discrimination, especially for a multiple class problem, may be achieved with multi-dimensional decision boundaries based upon two-dimensional class-conditional probability densities. Even so, pattern recognition techniques are limited in effectiveness and accuracy when the problem is data starved. Even though the presented work demonstrates a strong classification potential, more trials for each event type is needed to further quantify the objective proposed at the beginning of this work.

The amount of testing should be planned carefully to ensure the desired results. Each test series should have a classification and discrimination goal. For example, if discriminating weight is the goal, then at least ten to fifteen [55] explosives of each type of interest should be detonated over each of the desired weight range and repeated over several different days. Likewise, if type discrimination is the goal, one needs to consider if the weight is known *a priori*. Otherwise, many repetitions of each type at each weight are needed. As seen in the present study, the width and thus the potential class overlap of the class-conditional probability densities depends more on systematic errors between test series and test days than on statistical errors within the data. Thus, a more adequate data set for the present study would include fifteen detonations of TNT and fifteen detonations of an ENE mixture, all at 50 kg. To examine the classification potential at different weights and to determine if weight is distinguishable, then another set of thirty detonations should be at 10 kg and finally a set at 100 kg. As one can see, tests to determine if enhanced explosives and TNT explosives are distinguishable are not simple and require time to collect adequate data for statistically valid answers. Thus, an overall test plan should be established to meet objectives.

Finally, the methods and conclusions presented in this research may contribute significantly to the classification ability of current operational remote sensing systems, allowing better target discrimination for both military and commercial customers. These findings can aid program managers in the design of future remote sensors that capitalize on the discrimination strengths of imagery and spectra.

Appendix A: NIR Fireball Areas for Brilliant Flash I

The figures in this appendix compliments Figure 18 by providing the fireball areas from the near-infrared images for types A, C, and D, all from Brilliant Flash I test series.

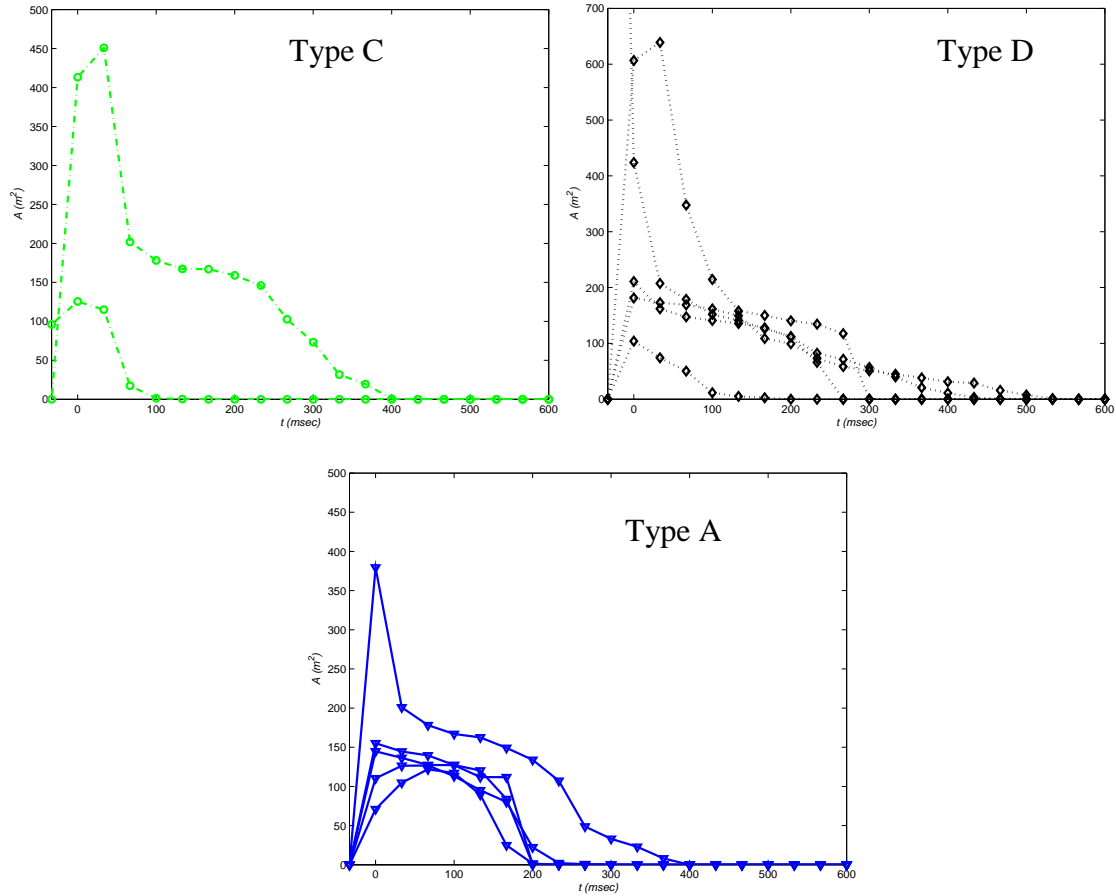


Figure 76. The fireball area in the near-infrared as a function of time for the three types represented in the Brilliant Flash I test series.

Appendix B: Imagery Features from Brilliant Flash test series

The tables in this appendix provide the feature values derived from the imagery collected during both Brilliant Flash test series. Each feature has a value from each of the near-infrared (0.6-1.7 μm), red (approx. 0.7 μm), green (approx. 0.54 μm), and blue (approx. 0.45 μm) spectral bands. The following tables are included:

- Table 26. NIR imagery feature values from Brilliant Flash II test.
- Table 27. NIR imagery feature values from Brilliant Flash I test.
- Table 28. Red imagery feature values from Brilliant Flash II test.
- Table 29. Green imagery feature values from Brilliant Flash II test.
- Table 30. Blue imagery feature values from Brilliant Flash II test.
- Table 31. Red imagery feature values from Brilliant Flash I test.
- Table 32. Green imagery feature values from Brilliant Flash I test.
- Table 33. Blue imagery feature values from Brilliant Flash I test.

Table 26. NIR imagery feature values from Brilliant Flash II test.

Event No.	Type	W	A	t _{median}	t _{medianstd}	t _{mp}	A _{median}	A _{medianstd}	A _{mp}	C ₁	C ₂	C ₃	μ ₁	μ ₂	μ ₃	μ ₄
		(kg)	(m ² msec)	(msec)	(msec)	(msec)	(m ²)	(m ²)	(m ²)	(m ² msec ⁻²)	(m ² msec ⁻¹)	(m ²)				
1	TNT	10	12154	33	118	67	73	11	74	-0.00162	0.24	50	27.8	3722	3.6	13.1
2	TYPEF	10	786	-33	118	33	0	0	12	0.00000	-0.17	13	33.3	0	NA	NA
3	TYPEC	10	10543	0	118	0	77	12	77	-0.00083	-0.18	75	28.0	5408	2.6	6.5
4	TYPED	10	10831	33	118	33	75	11	75	-0.00176	0.14	59	26.2	1525	6.5	38.1
5	TYPEC	50	58508	100	117	0	162	23	168	-0.00119	0.20	159	28.5	12020	4.1	16.3
7	TNT	10	16678	33	118	67	82	12	87	-0.00117	0.12	69	29.3	3735	3.5	12.4
8	TNT	50	63092	133	116	100	156	21	162	-0.00101	0.28	136	27.8	15978	4.8	21.8
9	TYPEC	50	70151	133	116	0	192	27	194	-0.00137	0.26	183	29.0	11144	4.7	21.4
10	TYPEC	50	75723	133	116	33	194	27	211	-0.00090	0.06	205	32.9	14762	4.0	15.9
12	TYPED	50	85187	133	116	0	196	26	209	-0.00079	0.11	198	28.5	15233	4.7	21.4
13	TYPEB	50	22928	33	118	33	128	19	128	-0.00183	0.17	99	29.6	3332	3.7	13.5
14	TYPEB	50	20117	33	118	33	132	20	132	-0.00135	-0.07	111	28.1	2836	4.6	20.3
15	TNT	10	16858	33	118	33	105	16	105	-0.00179	0.00	98	29.2	2563	3.1	9.5
17	TYPEB	50	17907	33	118	33	116	18	116	-0.00060	-0.33	117	30.8	2418	3.2	10.0
18	TYPEB	50	19552	33	118	33	126	19	126	-0.00180	0.09	99	27.5	3827	4.1	16.1
19	TYPED	50	64883	100	117	33	189	26	204	-0.00133	0.19	184	30.3	13074	3.9	14.4
20	TYPED	50	64306	133	116	33	169	23	183	-0.00137	0.36	148	29.9	12380	4.5	18.9
21	TNT	10	16691	67	118	67	99	15	99	-0.00123	0.23	55	27.8	3850	4.3	19.0
22	TYPEC	100	128670	167	115	0	268	35	271	-0.00126	0.36	251	30.9	15914	4.8	22.2
23	TYPEC	100	118150	167	115	100	256	34	262	-0.00139	0.45	222	28.5	14979	5.3	27.1
24	TNT	50	57521	133	116	100	143	19	153	-0.00157	0.48	121	32.4	15655	3.6	12.7
25	TNT	50	61372	167	115	100	140	19	149	-0.00128	0.47	108	29.9	10607	4.6	21.7
26	TYPEB	100	42289	67	118	33	162	24	200	-0.00069	-0.12	160	29.8	5930	4.0	16.0
27	TYPEB	100	46242	100	117	33	144	20	195	-0.00076	-0.03	153	28.7	4130	4.9	25.7
28	TYPED	100	147610	233	112	33	249	31	271	-0.00072	0.25	234	29.1	21142	5.8	31.6
29	TYPED	100	153340	233	112	0	258	32	295	-0.00057	0.09	271	30.7	15191	5.3	27.5
30	TYPEC	100	141500	200	114	33	267	34	286	-0.00094	0.27	256	28.7	9330	6.2	38.5
31	TNT	50	64733	167	115	100	147	20	161	-0.00133	0.59	87	28.0	5704	5.1	30.4
32	TNT	1000	496480	333	106	400	675	78	689	-0.00187	1.27	472	30.2	24681	6.2	37.6

Event No.	Type	W	A	t _{median}	t _{medianstd}	t _{mp}	A _{median}	A _{medianstd}	A _{mp}	C ₁	C ₂	C ₃	μ ₁	μ ₂	μ ₃	μ ₄
		(kg)	(m ² msec)	(msec)	(msec)	(msec)	(m ²)	(m ²)	(m ²)	(m ² msec ⁻²)	(m ² msec ⁻¹)	(m ²)				
33	TYPED	1000	543250	367	103	533	720	81	752	-0.00264	2.05	386	31.2	21953	5.9	34.2
34	TNT	100	97704	200	114	167	211	28	215	-0.00123	0.48	162	32.5	20689	4.2	17.3
35	TYPEC	1000	574130	300	108	367	820	95	830	-0.00272	1.58	644	32.8	25458	5.1	25.7
36	TNT	100	125790	233	112	167	219	28	226	-0.00070	0.31	178	30.9	28276	5.0	23.6
37	TYPED	1000	253220	167	115	33	558	75	651	-0.00135	-0.07	584	28.0	11881	5.5	30.3
38	TYPED	100	63673	100	117	33	191	27	218	-0.00103	0.16	168	28.9	4557	4.6	22.2
39	TYPED	50	32415	67	118	0	101	14	151	-0.00005	-0.29	136	28.5	7307	4.0	16.5
40	TNT	50	41563	133	116	167	116	16	116	-0.00130	0.33	101	31.3	14432	3.8	13.6
41	TYPEE	50	44550	100	117	33	131	18	139	-0.00088	0.14	123	25.6	7251	6.0	35.3
42	TYPEE	50	48161	100	117	33	136	19	152	-0.00095	0.19	124	27.7	4235	6.0	39.1
43	TYPEE	50	48170	100	117	67	147	21	155	-0.00118	0.14	149	31.2	11683	3.3	10.6
44	TNT	50	39680	133	116.07	166.67	113	16	117	-0.00146	0.45	83	28.0	5539	5.7	31.4

NA is placed in the third and fourth moment values when the numerical calculations are unrealistic, e.g. when the second moment is zero.

Table 27. NIR imagery feature values from Brilliant Flash I test.

Event No.	Type	W	A	t _{median}	t _{medianstd}	t _{mp}	A _{median}	A _{medianstd}	A _{mp}	C ₁	C ₂	C ₃	μ ₁	μ ₂	μ ₃	μ ₄
		(kg)	(m ² msec)	(msec)	(msec)	(msec)	(m ²)	(m ²)	(m ²)	(m ² msec ⁻²)	(m ² msec ⁻¹)	(m ²)				
2	TYPEC	50	10248	-33	118	0	96	14	126	-0.01143	-0.13	114	31.1	1551	2.2	3.2
3	TYPEC	50	70369	33	118	33	451	69	451	0.00311	-2.07	414	31.8	5687	3.5	12.9
5	TNT	1	409	-33	118	0	0	0	8	0.00000	-0.12	8	33.3	0	NA	NA
9	TYPED	5	5253	0	118	0	48	7	48	-0.00039	-0.24	50	29.9	3787	2.1	4.4
10	TYPEC	5	3152	-33	118	0	1	0	34	-0.00100	-0.14	35	30.9	3703	1.7	2.9
11	TYPEC	5	13291	-33	118	0	0	0	290	0.00000	-4.35	278	33.3	0	NA	NA
12	TYPEC	5	35307	-33	118	0	0	0	593	0.08601	-13.78	583	33.3	1111	2.5	4.0
13	TNT	1	11683	167	115	-33	20	2	52	0.00006	-0.08	31	27.3	6367	8.5	64.1
14	TNT	1	499	-33	118	0	0	0	14	0.00000	-0.42	14	0.0	0	0.0	0.0
15	TNT	5	4304	33	118	33	23	3	23	-0.00069	0.07	21	29.5	5427	2.8	7.1
17	TNT	5	5255	33	118	0	26	4	31	0.00002	-0.10	30	29.6	6270	3.6	13.0
18	TYPED	50	8255	-33	118	0	0	0	104	0.00204	-1.05	106	30.4	3586	1.8	3.0
19	TYPED	50	83601	0	118	33	607	93	639	0.00809	-4.32	642	30.1	6209	3.6	12.9
20	TYPED	50	46394	67	118	0	169	25	181	0.00040	-0.58	198	30.8	9224	3.8	15.5
21	TNT	1	12901	633	62	1267	9	0	11	0.00000	0.00	8	31.7	25495	6.8	50.5
22	TNT	1	3	-33	118	-33	0	0	0	0.00000	-0.01	0	0.0	0	0.0	0.0
23	TNT	50	17685	33	118	67	105	16	122	-0.00793	1.16	75	28.1	6322	2.5	6.0
24	TNT	50	25715	33	118	0	145	21	155	-0.00547	0.45	145	27.7	5701	2.6	6.5
25	TNT	50	53038	33	118	0	201	28	379	0.00184	-1.40	307	28.1	4225	4.2	16.8
26	TNT	1	926	-33	118	0	0	0	21	0.00000	-0.32	20	33.3	0	NA	NA
27	TNT	1	941	-33	118	33	0	0	12	-0.00144	0.02	11	33.3	1111	2.5	4.0
29	TYPED	50	93227	-33	118	-33	2338	365	2338	0.00000	-31.96	990	33.3	-2222	0	-2
30	TYPED	50	36742	33	118	0	162	24	211	-0.00181	-0.13	185	27.8	5549	3.4	11.3
31	TNT	50	22574	33	118	67	126	19	127	-0.00389	0.39	114	29.2	7952	2.8	7.0
32	TNT	50	25315	33	118	0	136	20	145	-0.00538	0.54	132	27.3	5615	2.8	7.1
34	TNT	1	883	0	118	0	9	1	9	-0.00023	-0.03	9	31.4	3467	1.9	3.3
35	TNT	1	219	-33	118	33	0	0	5	0.00000	-0.03	3	33.3	0	NA	NA
36	TYPEC	5	8488	0	118	0	101	16	101	0.00194	-0.78	87	27.6	1671	4.4	16.8
37	TYPEC	5	2815	-33	118	0	0	0	33	-0.00031	-0.23	34	29.9	2872	2.2	4.3

Event No.	Type	W	\underline{A}	t_{median}	$t_{\text{medianstd}}$	t_{mp}	A_{median}	$A_{\text{medianstd}}$	A_{mp}	c_1	c_2	c_3	μ_1	μ_2	μ_3	μ_4
		(kg)	(m^2 msec)	(msec)	(msec)	(msec)	(m^2)	(m^2)	(m^2)	(m^2 msec ⁻²)	(m^2 msec ⁻¹)	(m^2)				
39	TYPED	5	5512	0	118	0	47	7	47	-0.00099	-0.07	44	28.6	2795	3.1	8.4
40	TYPED	5	5928	0	118	0	58	9	58	0.00040	-0.37	57	31.0	2969	2.4	5.3
41	TYPED	5	4536	-33	118	0	0	0	56	0.00074	-0.47	53	28.5	2417	2.5	5.4
42	TNT	1	20	-33	118	0	0	0	1	0.00000	-0.02	1	0.0	0	0.0	0.0
43	TNT	5	5708	0	118	0	66	10	66	0.00185	-0.62	59	27.7	2002	3.9	13.4
44	TNT	5	7416	0	118	0	72	11	72	0.00037	-0.49	74	32.9	2822	2.6	6.3
45	TNT	5	5336	0	118	0	54	8	54	-0.00216	-0.09	52	28.0	2232	2.6	5.9
46	TYPED	5	3683	0	118	0	37	6	37	-0.00113	-0.11	37	31.3	1463	2.5	5.2
48	TYPED	5	3282	-33	118	0	0	0	37	-0.00042	-0.23	38	27.9	2192	2.6	6.0
50	TYPEC	5	3703	-33	118	0	0	0	45	-0.00459	0.00	45	33.3	1111	2.5	4.0
51	TYPEC	5	17208	-33	118	0	0	0	253	0.00853	-2.64	215	27.4	2992	3.5	11.5

NA is placed in the third and fourth moment values when the numerical calculations are unrealistic, e.g. when the second moment is zero.

Table 28. Red imagery feature values from Brilliant Flash II test.

Event No.	Type	W	A	t _{median}	t _{medianstd}	t _{mp}	A _{median}	A _{medianstd}	A _{mp}	C ₁	C ₂	C ₃	μ ₁	μ ₂	μ ₃	μ ₄
		(kg)	(m ² msec)	(msec)	(msec)	(msec)	(m ²)	(m ²)	(m ²)	(m ² msec ⁻²)	(m ² msec ⁻¹)	(m ²)				
1	TNT- 10	10	1.5E+05	167	251	200	334	24	345	-0.0032	1.31	213	29.3	4858	9.0	67.8
5	ENE- 50	50	2.8E+04	33	251	33	162	12	162	-0.0011	-0.31	161	29.8	4227	3.7	13.0
6	ENE- 50	50	1.5E+05	133	251	133	381	28	381	-0.0036	1.11	294	29.5	7840	5.5	26.8
8	TNT- 50	50	8.9E+04	167	251	233	205	15	213	-0.0014	0.51	154	29.9	21560	4.3	17.3
9	ENE- 50	50	1.5E+05	133	251	167	389	28	393	-0.0035	1.08	314	31.3	14620	4.4	18.8
10	ENE- 50	50	1.7E+05	133	251	200	402	29	403	-0.0032	1.12	304	27.2	8860	6.7	39.1
11	ENE- 50	50	1.5E+05	133	251	0	337	24	372	-0.0023	0.69	286	28.6	5226	8.2	53.6
12	ENE- 50	50	1.8E+05	167	251	33	383	28	396	-0.0023	0.74	339	32.6	17841	4.4	18.7
13	ENE- 50	50	5.2E+04	67	251	167	175	13	187	-0.0045	1.03	135	28.3	5120	5.8	26.1
14	ENE- 50	50	4.7E+04	67	251	33	187	14	200	-0.0033	0.39	186	31.8	8126	3.0	9.0
15	TNT- 10	10	1.2E+04	33	251	67	76	6	78	-0.0037	0.44	63	32.3	4523	2.3	5.3
17	ENE- 50	50	6.9E+04	67	251	67	258	19	258	-0.0042	0.83	214	29.2	3766	4.3	18.7
18	ENE- 50	50	1.8E+05	167	251	133	451	33	452	-0.0030	1.14	316	28.4	10210	5.0	25.8
19	ENE- 50	50	1.7E+05	167	251	133	395	29	400	-0.0018	0.41	363	32.2	19608	4.0	15.2
21	TNT- 10	10	2.7E+04	33	251	33	144	11	144	0.0000	-0.35	131	28.3	3514	4.5	22.0
22	ENE-100	100	3.3E+05	267	251	300	633	46	634	-0.0033	1.93	335	27.6	18967	5.9	33.2
23	ENE-100	100	2.8E+05	200	251	200	562	40	562	-0.0025	0.97	459	29.3	19119	5.2	26.2
24	TNT- 50	50	8.3E+04	133	251	233	195	14	211	-0.0027	0.98	132	31.6	10636	4.6	19.2
25	TNT- 50	50	8.4E+04	167	251	300	182	13	194	-0.0018	0.70	134	30.0	14972	4.1	16.6
27	ENE-100	100	1.2E+05	133	251	0	253	18	282	-0.0027	0.93	208	29.2	7314	6.2	34.9
28	ENE-100	100	3.1E+05	267	251	33	464	33	514	-0.0009	0.19	490	31.2	31492	5.2	25.4
29	ENE-100	100	3.6E+05	233	251	200	592	42	598	-0.0016	0.74	470	28.7	16299	6.3	37.9
30	ENE-100	100	3.3E+05	233	251	267	580	42	588	-0.0028	1.41	414	32.0	14560	4.7	23.3
31	TNT- 50	50	8.7E+04	167	251	100	185	13	194	-0.0013	0.52	146	30.1	12089	4.4	20.0
34	TNT-100	100	2.4E+05	300	250	233	348	25	365	-0.0012	0.70	245	28.9	20701	5.4	29.0
36	TNT-100	100	3.1E+05	367	250	433	401	28	407	-0.0009	0.73	254	30.9	38466	5.9	33.5
38	ENE-100	100	3.0E+05	233	251	167	527	38	537	-0.0018	0.70	461	28.3	10290	6.8	45.7
39	ENE- 50	50	1.7E+05	167	251	33	369	27	378	-0.0015	0.45	322	29.1	10678	5.1	26.5
40	TNT- 50	50	9.0E+04	200	251	267	187	13	193	-0.0014	0.58	140	32.2	15783	4.3	18.2
44	TNT- 50	50	8.1E+04	167	251	200	193	14	195	-0.0015	0.52	154	30.0	15074	4.4	18.6

Table 29. Green imagery feature values from Brilliant Flash II test.

Event No.	Type	W	A	t _{median}	t _{medianstd}	t _{mp}	A _{median}	A _{medianstd}	A _{mp}	C ₁	C ₂	C ₃	μ ₁	μ ₂	μ ₃	μ ₄
		(kg)	(m ² msec)	(msec)	(msec)	(msec)	(m ²)	(m ²)	(m ²)	(m ² msec ⁻²)	(m ² msec ⁻¹)	(m ²)				
1	TNT- 10	10	87948	100	251	200	221	16	262	-0.0033	1.02	176	29.6	6907	5.6	27.5
5	ENE- 50	50	18868	33	251	0	118	9	119	-0.0015	-0.19	122	29.7	6845	2.7	6.9
6	ENE- 50	50	95149	100	251	0	255	19	276	-0.0030	0.78	215	28.1	3305	10.3	73.1
8	TNT- 50	50	40112	67	251	167	149	11	155	-0.0036	0.87	105	29.2	11467	3.4	10.7
9	ENE- 50	50	98541	133	251	167	272	20	275	-0.0028	0.70	244	31.0	8851	3.8	14.8
10	ENE- 50	50	108580	100	251	0	288	21	313	-0.0026	0.67	244	27.0	6294	7.2	42.2
11	ENE- 50	50	95600	100	251	0	229	17	303	-0.0022	0.54	214	29.4	5717	6.7	38.2
12	ENE- 50	50	114150	133	251	33	270	19	309	-0.0019	0.46	265	32.0	10593	4.3	19.4
13	ENE- 50	50	25335	33	251	33	119	9	119	-0.0041	0.70	88	27.1	5569	4.3	15.1
14	ENE- 50	50	22272	33	251	33	120	9	120	-0.0029	0.18	119	29.9	8034	2.6	6.4
15	TNT- 10	10	7003	0	251	33	46	3	60	-0.0035	0.26	50	28.0	4107	2.6	6.0
17	ENE- 50	50	42147	67	251	0	175	13	181	-0.0029	0.30	174	31.4	8800	3.0	8.6
18	ENE- 50	50	124410	133	251	33	304	22	355	-0.0019	0.35	309	31.5	14811	4.2	17.0
19	ENE- 50	50	121750	133	251	0	284	21	344	-0.0023	0.66	244	28.0	3164	10.8	81.6
21	TNT- 10	10	15959	33	251	33	103	8	103	-0.0002	-0.29	98	27.5	3493	4.0	15.8
22	ENE-100	100	198020	200	251	267	412	30	430	-0.0035	1.70	229	29.8	14120	5.2	26.8
23	ENE-100	100	179280	167	251	233	399	29	407	-0.0028	0.94	341	30.9	13182	4.3	19.0
24	TNT- 50	50	41394	67	251	67	154	11	154	-0.0035	0.79	112	27.2	5341	5.7	26.1
25	TNT- 50	50	42306	100	251	33	139	10	143	-0.0023	0.55	112	28.8	4599	4.6	22.0
27	ENE-100	100	60983	100	251	0	159	11	204	-0.0023	0.59	141	29.3	3390	8.5	54.4
28	ENE-100	100	198770	200	251	33	352	25	402	-0.0009	0.18	361	31.5	20753	5.0	25.2
29	ENE-100	100	214140	200	251	0	379	27	447	-0.0014	0.49	335	27.3	12141	7.5	48.4
30	ENE-100	100	195900	200	251	267	389	28	397	-0.0022	0.87	324	31.0	14274	4.6	21.5
31	TNT- 50	50	36197	67	251	100	144	11	154	-0.0025	0.58	100	28.0	8192	3.8	14.5
34	TNT-100	100	121090	167	251	167	278	20	278	-0.0010	0.31	225	30.6	18630	4.7	22.0
36	TNT-100	100	153080	233	251	200	290	21	299	-0.0015	0.71	202	31.4	25058	4.6	20.1
38	ENE-100	100	190420	200	251	33	338	24	482	-0.0011	0.22	370	31.4	11542	5.1	27.4
39	ENE- 50	50	110300	133	251	0	233	17	332	-0.0007	-0.10	289	29.8	12815	4.7	21.8
40	TNT- 50	50	54011	133	251	200	153	11	155	-0.0018	0.48	126	31.2	14224	3.7	12.9
44	TNT- 50	50	47118	100	251	167	147	11	154	-0.0019	0.44	127	29.7	12554	3.5	11.6

Table 30. Blue imagery feature values from Brilliant Flash II test.

Event No.	Type	W	A	t _{median}	t _{medianstd}	t _{mp}	A _{median}	A _{medianstd}	A _{mp}	C ₁	C ₂	C ₃	μ ₁	μ ₂	μ ₃	μ ₄
		(kg)	(m ² msec)	(msec)	(msec)	(msec)	(m ²)	(m ²)	(m ²)	(m ² msec ⁻²)	(m ² msec ⁻¹)	(m ²)				
1	TNT- 10	10	18047	0	251	0	127	9	127	-0.0008	-0.14	88	31.3	555	24.7	127.5
5	ENE- 50	50	11191	0	251	0	85	6	85	-0.0029	0.03	83	31.7	3442	2.3	4.7
6	ENE- 50	50	49234	67	251	0	169	12	193	-0.0032	0.55	154	27.1	4375	6.6	32.3
8	TNT- 50	50	1013	-33	251	0	0	0	28	0.0000	-0.79	28	0.0	0	0.0	0.0
9	ENE- 50	50	51886	100	251	0	168	12	181	-0.0024	0.43	164	30.5	9891	3.6	12.4
10	ENE- 50	50	53814	67	251	0	175	13	216	-0.0022	0.30	169	27.6	5363	6.0	28.5
11	ENE- 50	50	49328	67	251	0	152	11	209	-0.0026	0.46	147	29.9	3163	7.3	36.4
12	ENE- 50	50	56482	100	251	0	169	12	213	-0.0015	0.10	192	30.6	9804	3.5	12.3
13	ENE- 50	50	1295	-67	251	-33	0	0	37	0.0000	-1.12	0	0.0	0	0.0	0.0
14	ENE- 50	50	1589	-33	251	0	0	0	45	0.0000	-1.34	45	0.0	0	0.0	0.0
15	TNT- 10	10	116	0	251	33	0	0	3	0.0000	-0.05	4	33.3	2222	1.4	2.0
17	ENE- 50	50	13153	33	251	100	49	4	84	-0.0033	0.49	56	30.0	5010	3.1	9.0
18	ENE- 50	50	61632	100	251	33	184	13	223	-0.0035	0.94	145	31.6	7699	3.9	14.8
19	ENE- 50	50	63413	100	251	0	185	13	232	-0.0021	0.32	196	29.3	8631	3.8	14.0
21	TNT- 10	10	5752	0	251	33	47	3	65	-0.0049	0.22	53	28.3	2352	2.5	5.5
22	ENE-100	100	96497	133	251	67	239	17	253	-0.0032	1.15	164	31.6	12167	4.1	16.6
23	ENE-100	100	96732	133	251	167	265	19	272	-0.0031	0.84	225	30.2	11108	4.0	15.6
24	TNT- 50	50	486	-33	251	33	1	0	8	-0.0013	0.07	5	31.1	1206	2.7	4.1
25	TNT- 50	50	194	-33	251	0	0	0	3	0.0002	-0.04	3	33.3	1111	2.5	4.0
27	ENE-100	100	5141	-33	251	0	49	4	52	0.0013	-0.42	38	30.8	-289	NA	250.1
28	ENE-100	100	98537	133	251	33	251	18	262	-0.0011	0.10	251	29.7	18197	4.3	17.3
29	ENE-100	100	107330	133	251	0	257	19	295	-0.0015	0.30	241	28.6	13777	4.9	21.8
30	ENE-100	100	97860	133	251	33	222	16	261	-0.0015	0.29	240	31.0	11106	3.8	15.3
31	TNT- 50	50	498	0	251	33	2	0	9	-0.0022	0.18	3	33.3	1111	2.5	4.0
34	TNT-100	100	4853	0	251	0	58	4	58	0.0010	-0.41	47	28.1	1729	5.2	26.0
36	TNT-100	100	4903	0	251	0	62	5	62	0.0013	-0.47	50	28.5	1407	3.6	10.7
38	ENE-100	100	84763	133	251	33	204	15	300	-0.0015	0.36	201	28.5	5908	5.9	35.2
39	ENE- 50	50	48303	100	251	33	135	10	180	-0.0011	0.14	146	30.8	7560	4.1	17.1
40	TNT- 50	50	2467	0	251	67	5	0	34	-0.0058	0.69	7	30.4	3584	1.8	3.0
44	TNT- 50	50	2113	0	251	0	30	2	30	0.0004	-0.22	25	30.0	943	3.2	6.7

Table 31. Red imagery feature values from Brilliant Flash I test.

Event No.	Type	W	A	t _{median}	t _{medianstd}	t _{mp}	A _{median}	A _{medianstd}	A _{mp}	C ₁	C ₂	C ₃	μ ₁	μ ₂	μ ₃	μ ₄
		(kg)	(m ² msec)	(msec)	(msec)	(msec)	(m ²)	(m ²)	(m ²)	(m ² msec ⁻²)	(m ² msec ⁻¹)	(m ²)				
2	ENE- 50	50	41603	67	179	33	168	17	174	-0.0030	0.51	145	27.6	8896	3.7	13.0
3	ENE- 50	50	29863	100	179	200	84	8	94	-0.0010	0.26	73	30.4	12044	3.9	14.8
4	ENE- 50	50	31854	33	179	0	152	15	169	-0.0011	-0.20	161	30.9	7403	3.0	9.2
18	ENE- 50	50	56380	67	179	0	161	15	310	-0.0032	0.58	165	27.8	1004	21.8	186.3
19	ENE- 50	50	140050	100	179	33	400	39	455	-0.0018	0.22	343	28.5	7183	5.4	27.9
20	ENE- 50	50	47895	67	179	167	150	15	174	-0.0033	0.86	111	27.0	5971	5.7	26.2
23	TNT- 50	50	18918	67	179	133	85	8	98	-0.0039	0.79	54	30.3	9510	2.7	7.1
24	TNT- 50	50	5849	0	179	33	45	5	51	-0.0057	0.47	38	28.1	1280	6.8	15.3
25	TNT- 50	50	27855	67	179	100	91	9	95	-0.0012	0.29	68	27.8	7124	4.9	21.6
29	ENE- 50	50	99552	100	179	0	248	24	348	-0.0012	0.00	271	27.9	5604	7.2	43.3
30	ENE- 50	50	32173	67	179	100	139	14	148	-0.0026	0.48	108	28.0	7451	3.5	12.4
31	TNT- 50	50	18190	33	179	33	104	10	104	-0.0041	0.62	74	27.8	2823	3.7	13.0

Table 32. Green imagery feature values from Brilliant Flash I test.

Event No.	Type	W	A	t _{median}	t _{medianstd}	t _{mp}	A _{median}	A _{medianstd}	A _{mp}	C ₁	C ₂	C ₃	μ ₁	μ ₂	μ ₃	μ ₄
		(kg)	(m ² msec)	(msec)	(msec)	(msec)	(m ²)	(m ²)	(m ²)	(m ² msec ⁻²)	(m ² msec ⁻¹)	(m ²)				
2	ENE- 50	50	29192	33	179	33	157	16	157	-0.0030	0.21	143	27.8	6812	3.3	9.9
3	ENE- 50	50	23027	67	179	33	80	8	90	-0.0007	0.03	86	31.1	9944	3.4	11.8
4	ENE- 50	50	22585	0	179	0	200	20	200	0.0017	-1.15	185	28.3	3429	3.3	10.4
18	ENE- 50	50	46079	33	179	0	205	20	323	-0.0038	0.40	176	27.8	635	29.6	227.9
19	ENE- 50	50	127490	67	179	33	405	40	409	-0.0023	0.30	338	28.7	8288	4.8	22.1
20	ENE- 50	50	34066	33	179	0	129	13	149	-0.0036	0.68	106	27.1	4326	5.8	25.1
23	TNT- 50	50	8930	33	179	67	54	5	64	-0.0039	0.54	41	27.9	6059	2.6	6.3
24	TNT- 50	50	362	-33	179	0	3	0	4	-0.0003	-0.01	3	31.2	-1212	NA	-3.5
25	TNT- 50	50	18493	33	179	67	71	7	73	-0.0004	-0.01	61	28.0	6952	5.0	22.5
29	ENE- 50	50	94042	67	179	0	306	30	357	-0.0006	-0.48	316	27.4	5459	6.9	38.8
30	ENE- 50	50	17692	33	179	67	103	10	105	-0.0028	0.25	92	27.9	5055	2.8	7.5
31	TNT- 50	50	7025	0	179	33	46	5	61	-0.0029	0.16	51	27.7	2555	3.2	9.0

Table 33. Blue imagery feature values from Brilliant Flash I test.

Event No.	Type	W	A	t _{median}	t _{medianstd}	t _{mp}	A _{median}	A _{medianstd}	A _{mp}	C ₁	C ₂	C ₃	μ ₁	μ ₂	μ ₃	μ ₄
		(kg)	(m ² msec)	(msec)	(msec)	(msec)	(m ²)	(m ²)	(m ²)	(m ² msec ⁻²)	(m ² msec ⁻¹)	(m ²)				
2	ENE- 50	50	17912	33	179	33	125	13	125	-0.0031	0.23	102	26.7	3832	3.6	12.2
3	ENE- 50	50	13065	67	179	33	59	6	64	-0.0015	0.29	44	26.6	5539	4.2	16.2
4	ENE- 50	50	13767	0	179	0	114	12	114	0.0000	-0.59	119	27.3	1417	5.0	21.6
18	ENE- 50	50	26637	33	179	0	123	12	161	-0.0037	0.52	103	27.1	3410	5.8	22.9
19	ENE- 50	50	79000	67	179	33	225	22	301	-0.0015	0.17	217	27.9	2952	9.6	69.1
20	ENE- 50	50	14988	0	179	0	107	11	107	-0.0028	0.28	70	27.6	1922	6.9	27.3
23	TNT- 50	50	97	-33	179	0	0	0	2	0.0000	-0.03	2	33.3	0	1.7e7	2.0e5
24	TNT- 50	50	0	-100	179	-100	0	0	0	0.0000	0.00	0	0.0	0	0.0	0.0
25	TNT- 50	50	1117	-33	179	0	4	0	11	-0.0010	0.05	8	30.1	95	213.1	753.0
29	ENE- 50	50	60137	67	179	0	160	16	216	-0.0010	0.00	176	29.2	8066	4.7	20.2
30	ENE- 50	50	3366	0	179	33	24	2	34	-0.0037	0.30	25	28.4	2382	2.5	5.5
31	TNT- 50	50	412	-33	179	0	0	0	12	0.0000	-0.37	12	0.0	0	0.0	0.0

Appendix C: Brilliant Flash II Area Fits

The time-dependence of a fireball area is extracted from each image recorded in the near-infrared. The plots in this appendix show the Brilliant Flash II fireball areas at each time step (\bullet), the peak value (Δ), the area value associated with the median time (\square), and the curve that fits the equation, $f(t) = c_1t^2 + c_2t + c_3$. The following figures are included in this appendix:

- Figure 77. These figures represent the fireball area in the near-infrared band for events recorded during the Brilliant Flash II test series. Figures (a) through (e) are for events 1 through 5 and Fig. (f) is for event 7.
- Figure 78. These figures represent the fireball area in the near-infrared band for events recorded during the Brilliant Flash II test series. Figures (a) through (c) are for events 8-10 and Figs. (d) through (f) are for event 12-14.
- Figure 79. These figures represent the fireball area in the near-infrared band for events recorded during the Brilliant Flash II test series. Figures (a) through (f) are for events 15, 17-21.
- Figure 80. These figures represent the fireball area in the near-infrared band for events recorded during the Brilliant Flash II test series. Figures (a) through (f) are for events 22-27.
- Figure 81. These figures represent the fireball area in the near-infrared band for events recorded during the Brilliant Flash II test series. Figures (a) through (f) are for events 28-33.

- Figure 82. These figures represent the fireball area in the near-infrared band for events recorded during the Brilliant Flash II test series. Figures (a) through (f) are for events 34-39.
- Figure 83. These figures represent the fireball area in the near-infrared band for events recorded during the Brilliant Flash II test series. Figures (a) through (e) are for events 40-44.

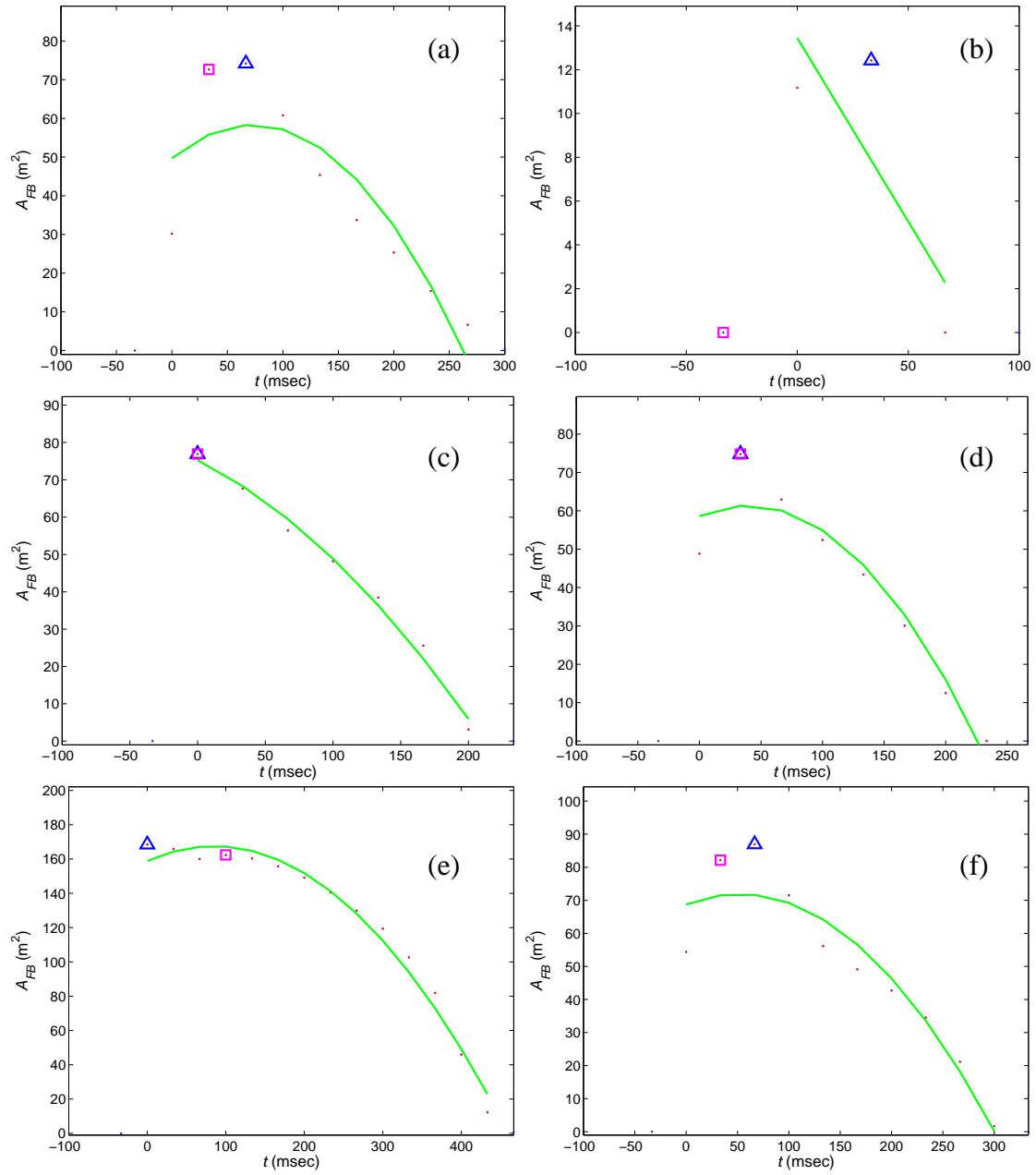


Figure 77. These figures represent the fireball area in the near-infrared band for events recorded during the Brilliant Flash II test series. Figures (a) through (e) are for events 1 through 5 and Fig. (f) is for event 7.

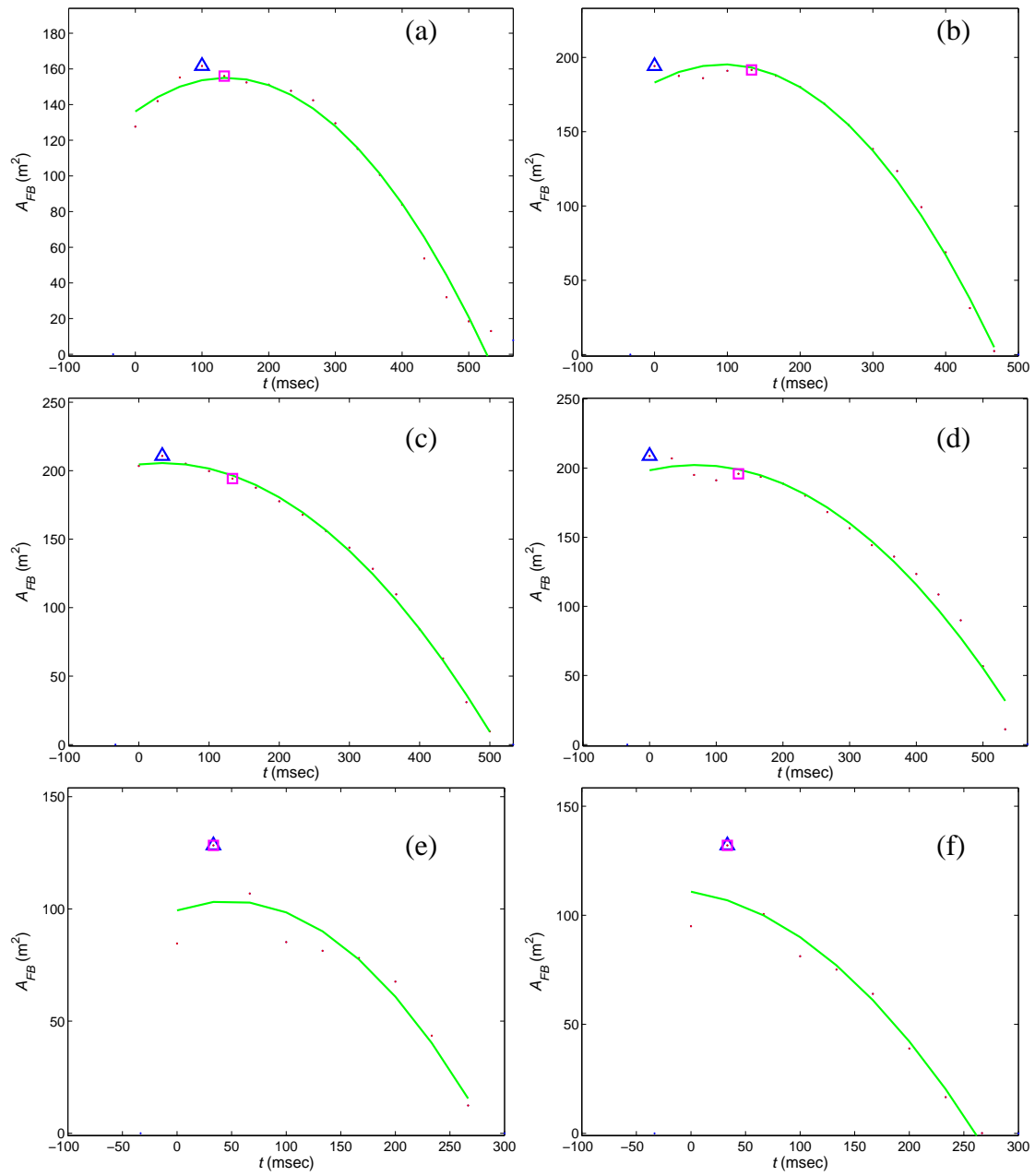


Figure 78. These figures represent the fireball area in the near-infrared band for events recorded during the Brilliant Flash II test series. Figures (a) through (c) are for events 8-10 and Figs. (d) through (f) are for event 12-14.

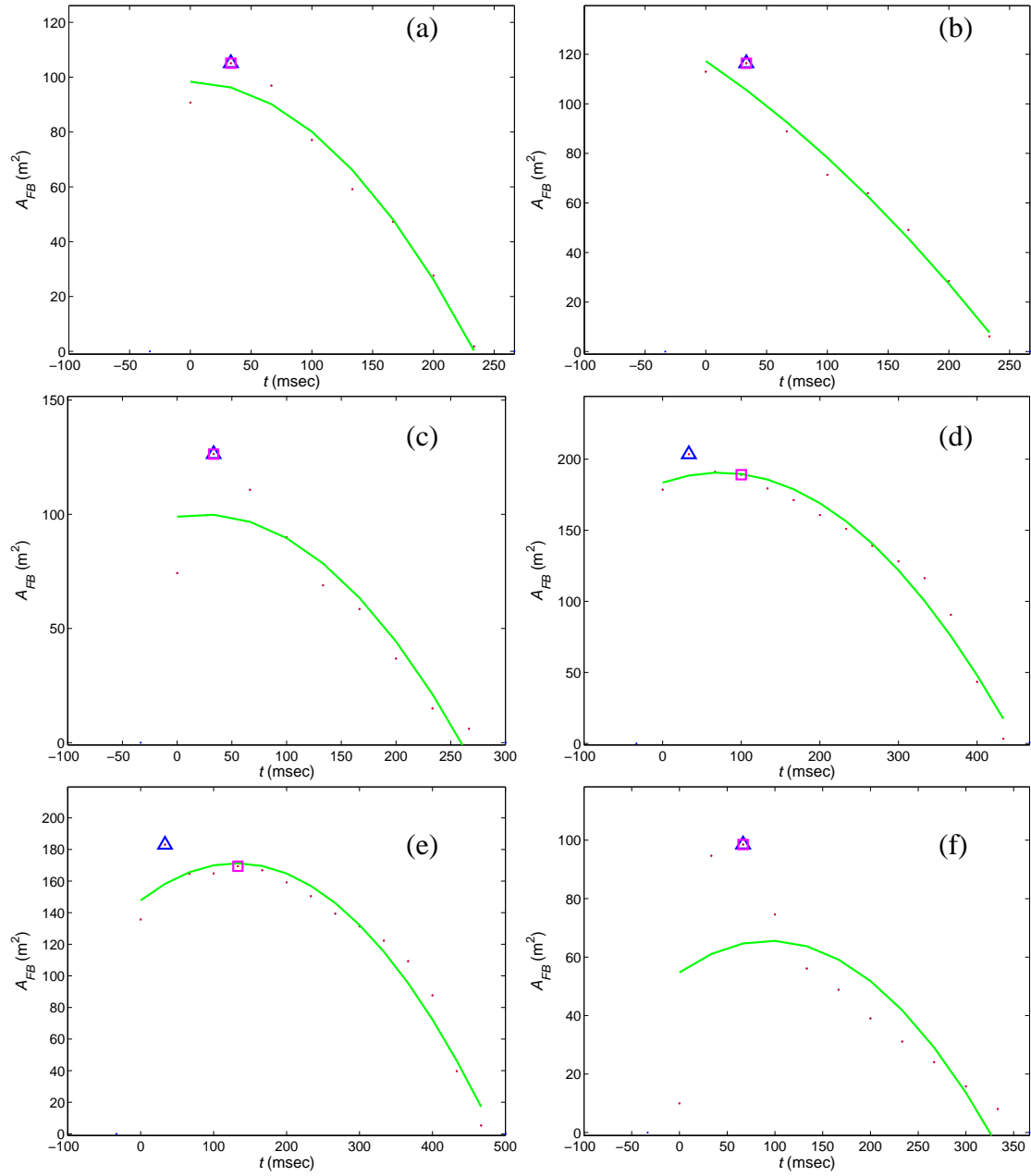


Figure 79. These figures represent the fireball area in the near-infrared band for events recorded during the Brilliant Flash II test series. Figures (a) through (f) are for events 15, 17-21.

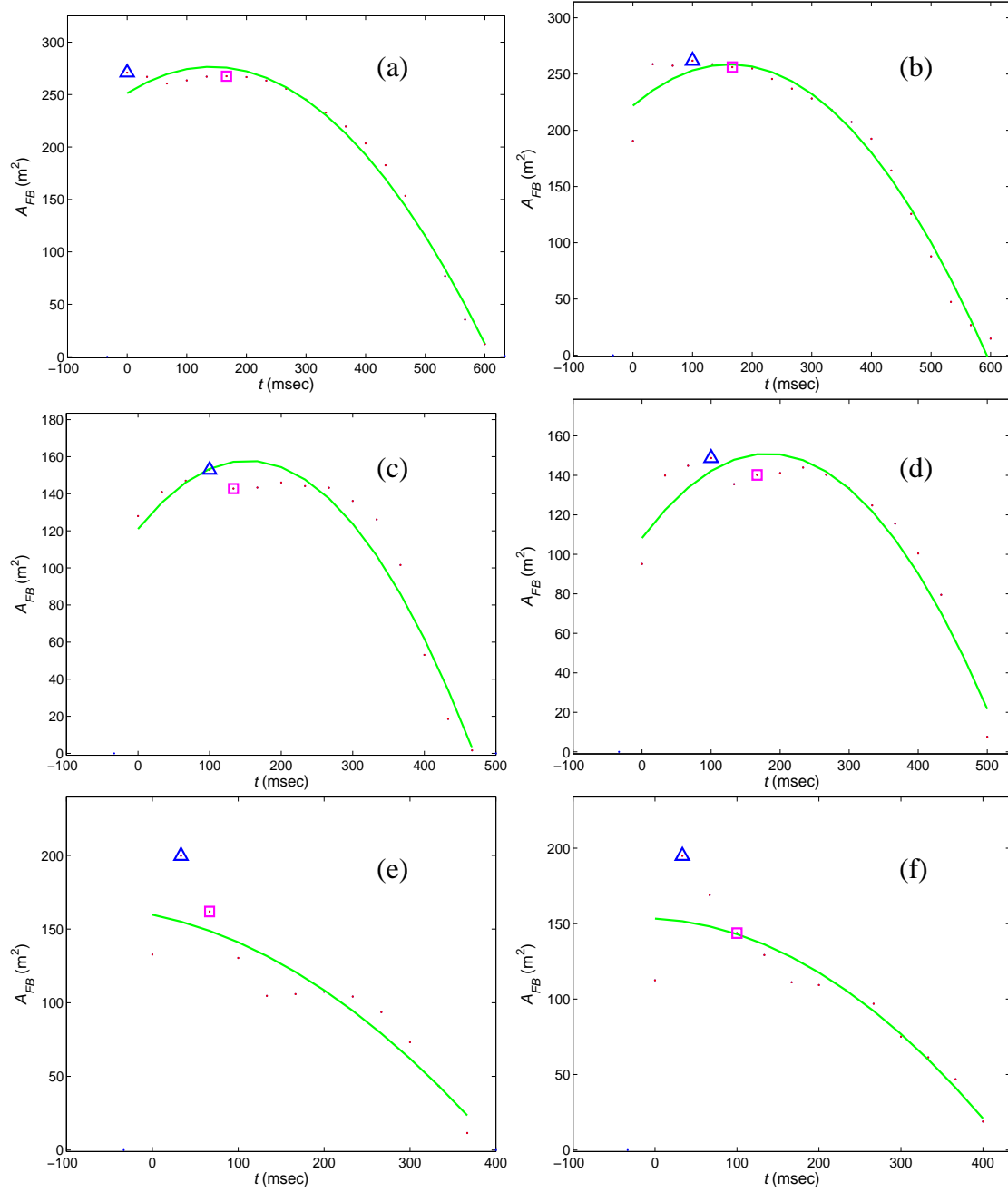


Figure 80. These figures represent the fireball area in the near-infrared band for events recorded during the Brilliant Flash II test series. Figures (a) through (f) are for events 22-27.

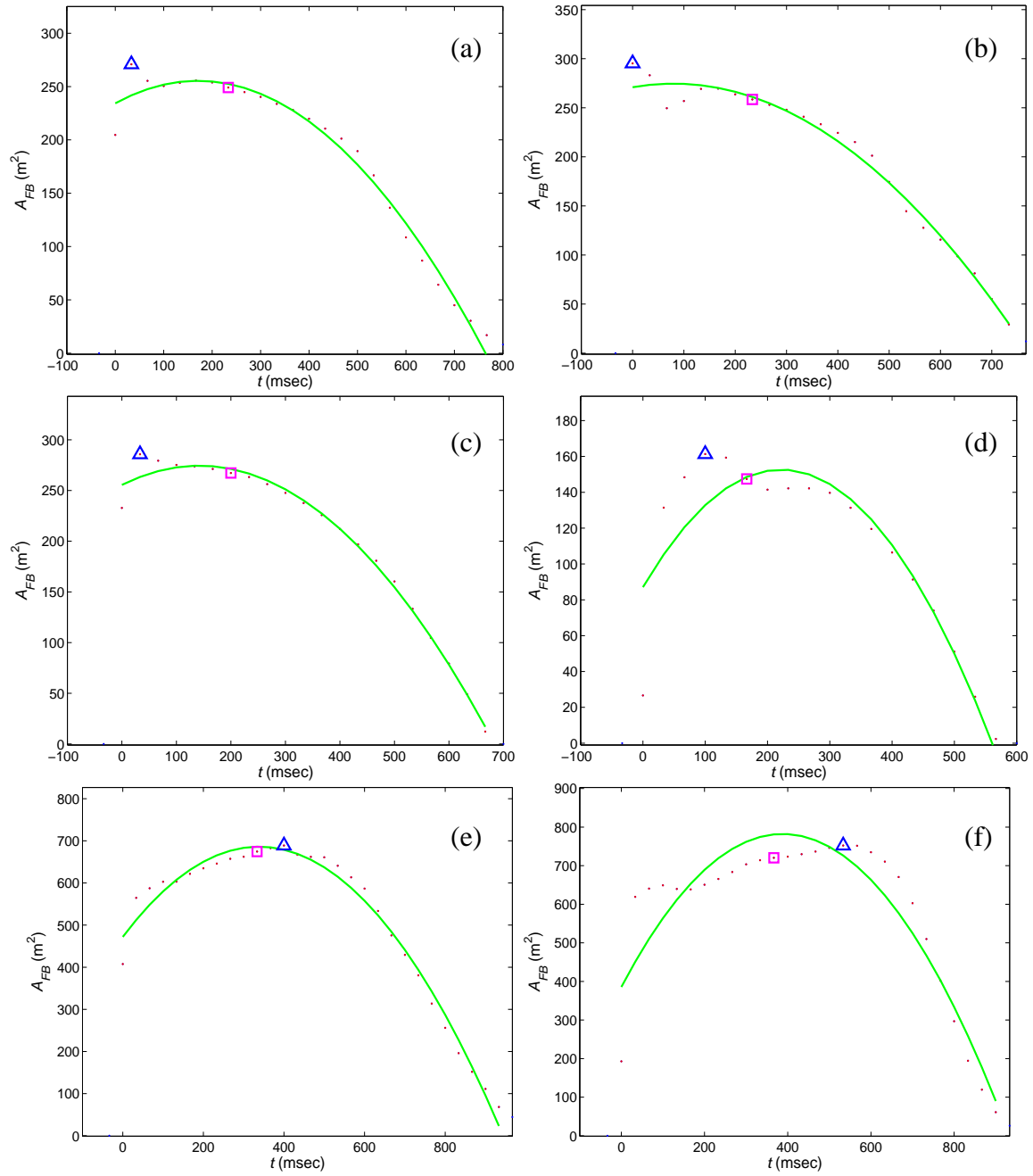


Figure 81. These figures represent the fireball area in the near-infrared band for events recorded during the Brilliant Flash II test series. Figures (a) through (f) are for events 28-33.

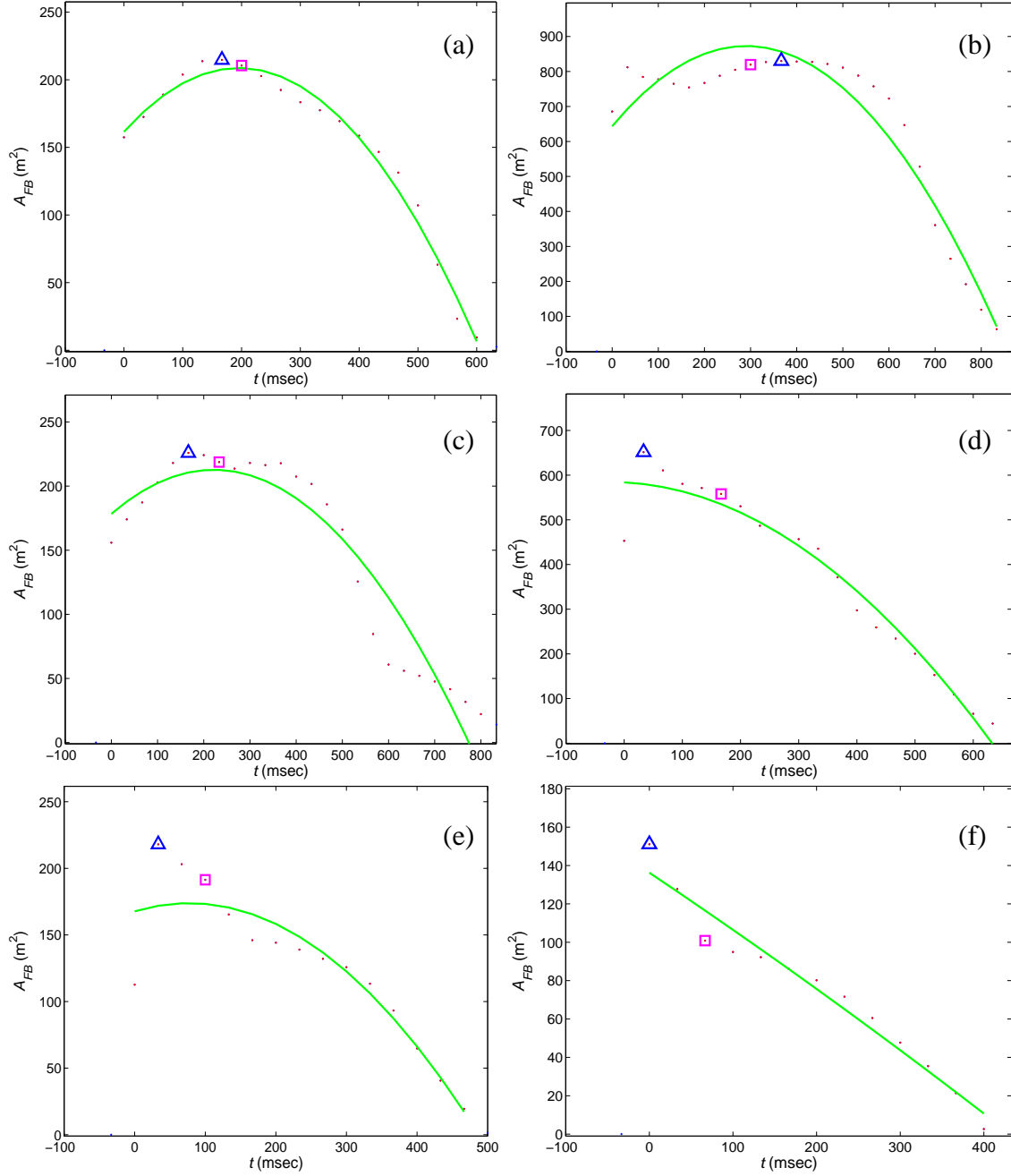


Figure 82. These figures represent the fireball area in the near-infrared band for events recorded during the Brilliant Flash II test series. Figures (a) through (f) are for events 34-39.

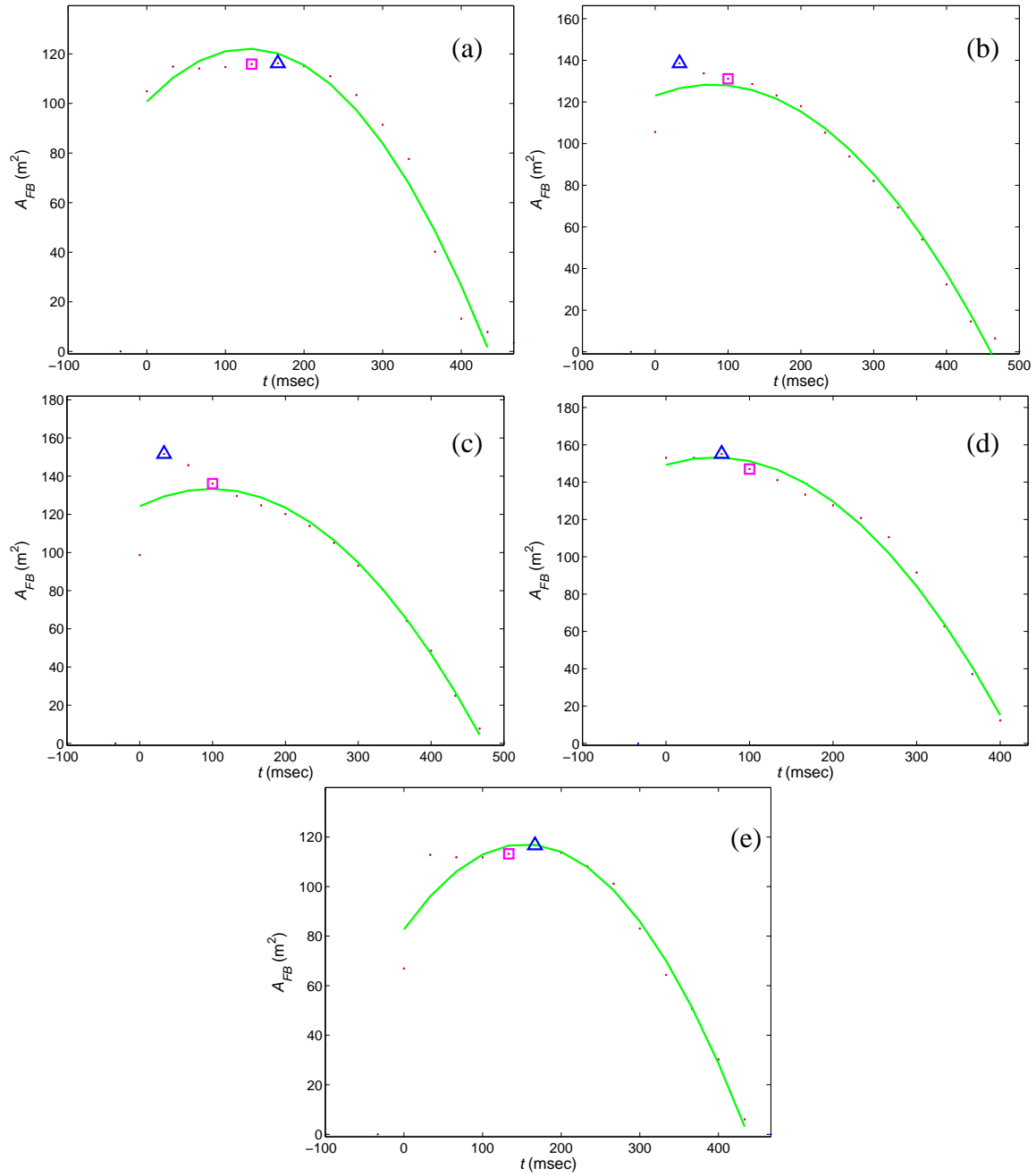


Figure 83. These figures represent the fireball area in the near-infrared band for events recorded during the Brilliant Flash II test series. Figures (a) through (e) are for events 40-44.

Appendix D: Brilliant Flash I IR Areas

The time-dependence of a fireball area is extracted from each image recorded in the near-infrared. The plots in this appendix show the Brilliant Flash I fireball areas at each time step (\bullet), the peak value (Δ), the area value associated with the median time (\square), and the curve that fits the equation, $f(t) = c_1t^2 + c_2t + c_3$. The following figures are included in this appendix:

- Figure 84. These figures represent the fireball area in the near-infrared band for events recorded during the Brilliant Flash I test series. Figures (a) through (f) are for events 2, 3, 5, 9-11.
- Figure 85. These figures represent the fireball area in the near-infrared band for events recorded during the Brilliant Flash I test series. Figures (a) through (f) are for events 12-15, 17-18.
- Figure 86. These figures represent the fireball area in the near-infrared band for events recorded during the Brilliant Flash I test series. Figures (a) through (f) are for events 19-24.
- Figure 87. These figures represent the fireball area in the near-infrared band for events recorded during the Brilliant Flash I test series. Figures (a) through (f) are for events 25-27, 29-31.
- Figure 88. These figures represent the fireball area in the near-infrared band for events recorded during the Brilliant Flash I test series. Figures (a) through (f) are for events 32, 34-37, 39.
- Figure 89. These figures represent the fireball area in the near-infrared band for events recorded during the Brilliant Flash I test series. Figures (a) through (f) are for events 40-45.

- Figure 90. These figures represent the fireball area in the near-infrared band for events recorded during the Brilliant Flash I test series. Figures (a) through (d) are for events 46, 48, 50-51.

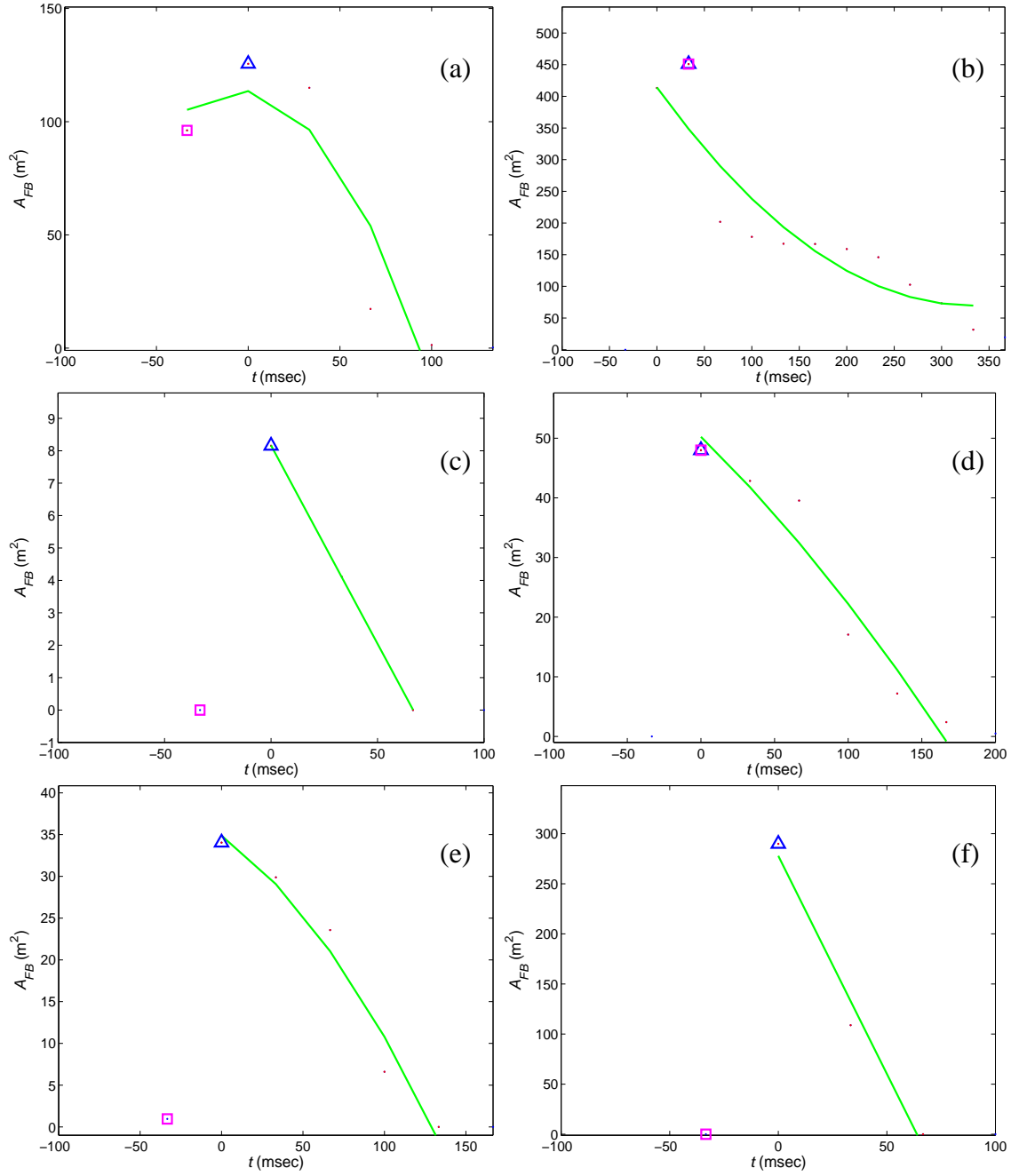


Figure 84. These figures represent the fireball area in the near-infrared band for events recorded during the Brilliant Flash I test series. Figures (a) through (f) are for events 2, 3, 5, 9-11.

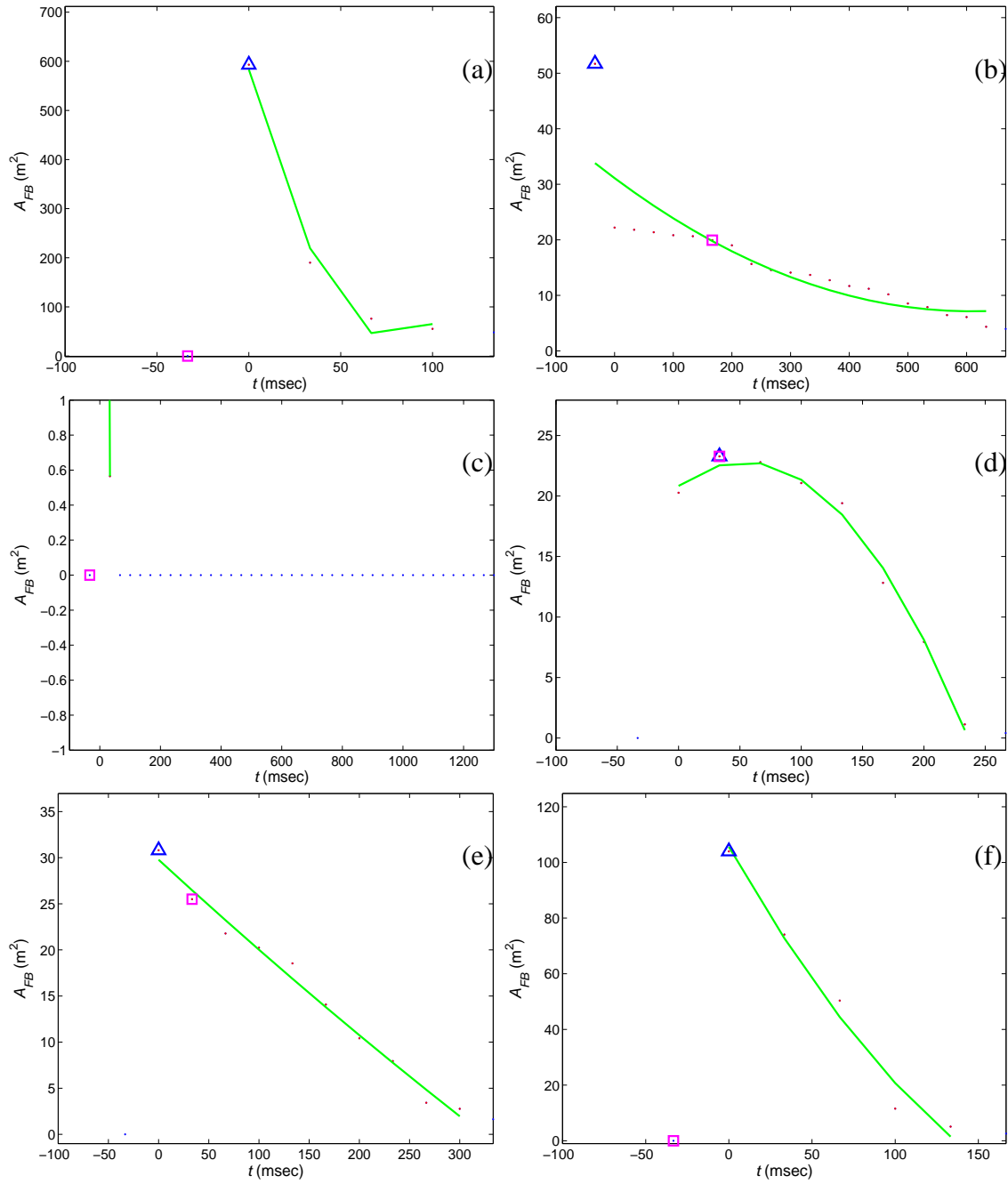


Figure 85. These figures represent the fireball area in the near-infrared band for events recorded during the Brilliant Flash I test series. Figures (a) through (f) are for events 12-15, 17-18.

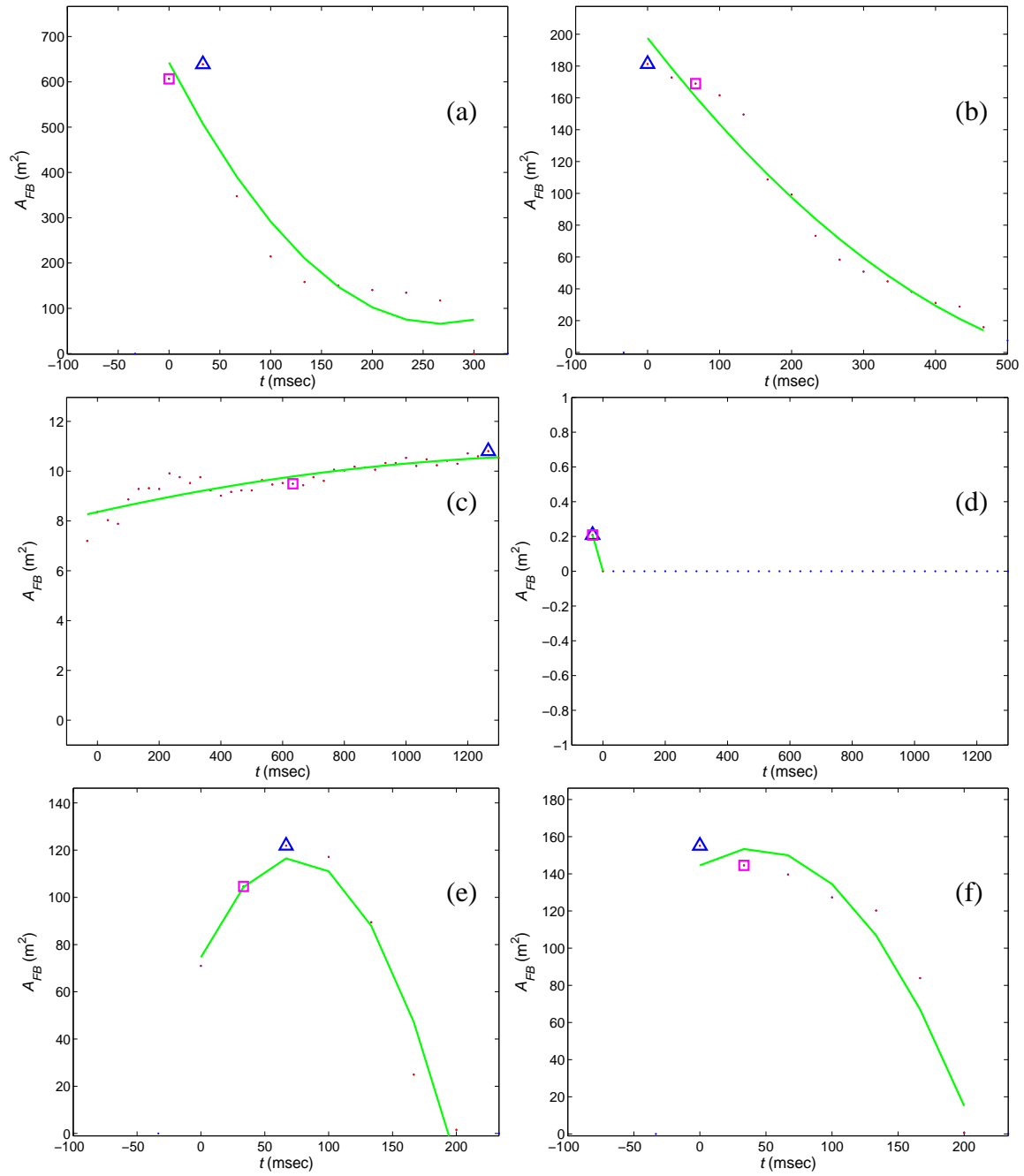


Figure 86. These figures represent the fireball area in the near-infrared band for events recorded during the Brilliant Flash I test series. Figures (a) through (f) are for events 19-24.

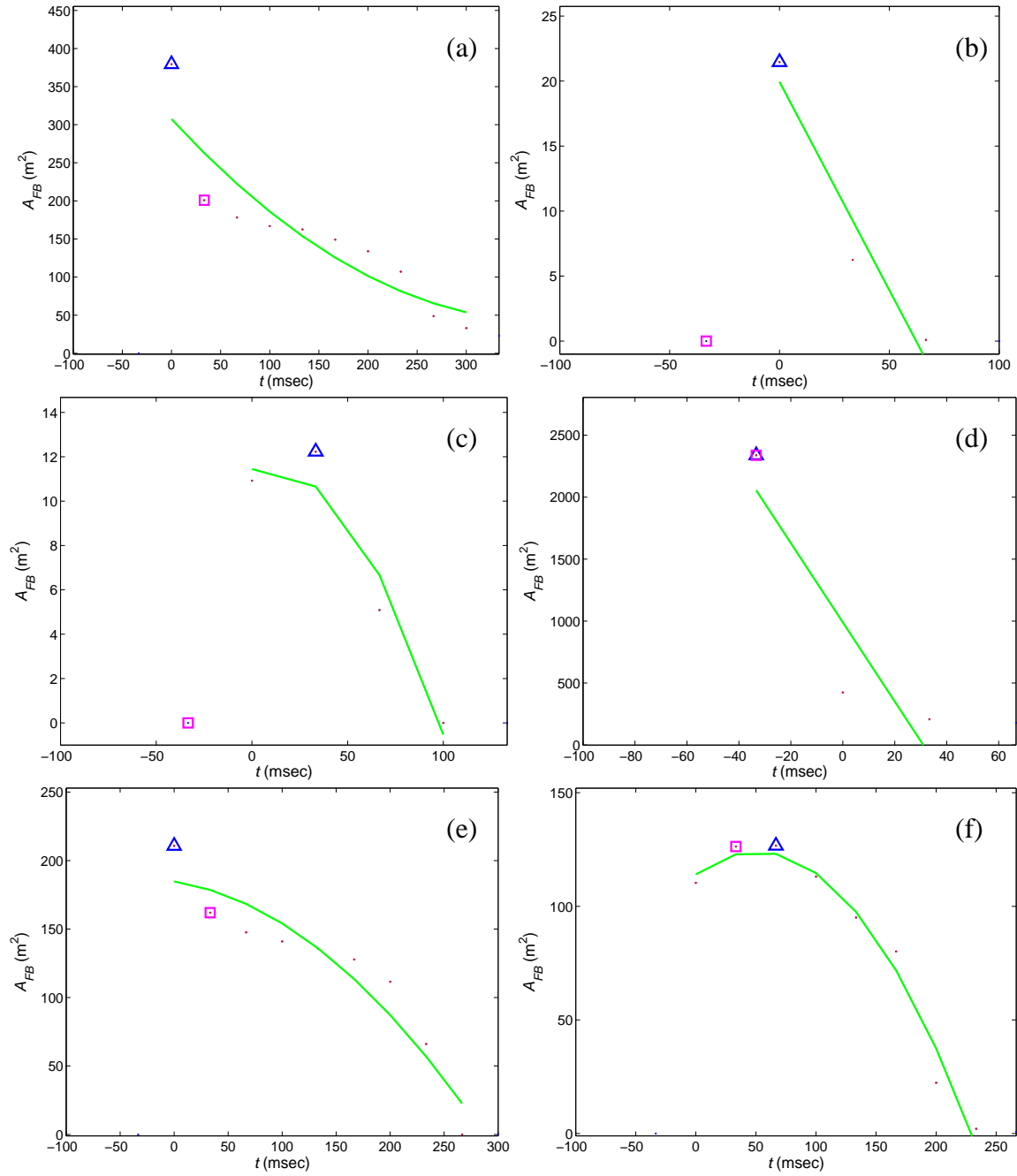


Figure 87. These figures represent the fireball area in the near-infrared band for events recorded during the Brilliant Flash I test series. Figures (a) through (f) are for events 25-27, 29-31.

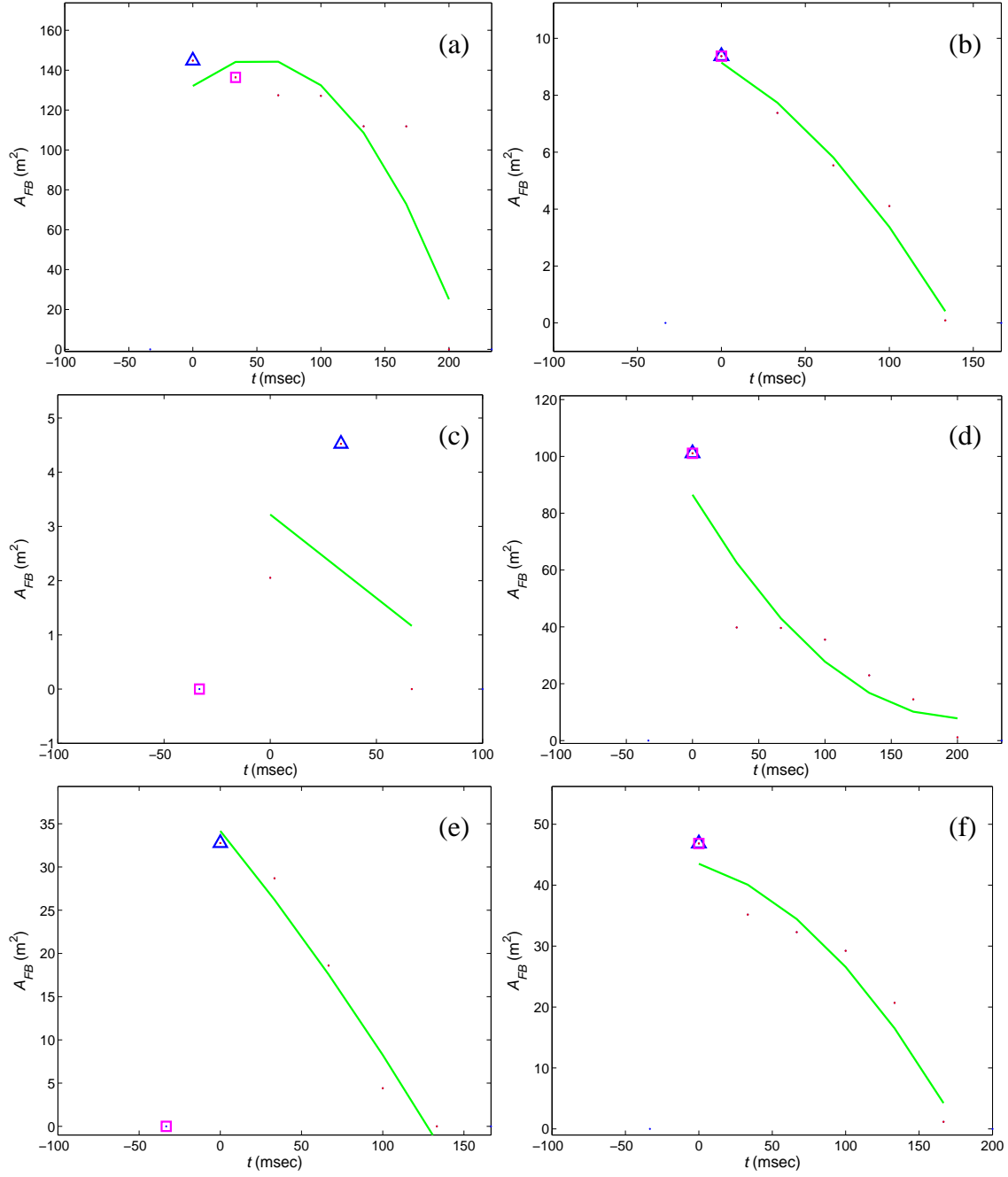


Figure 88. These figures represent the fireball area in the near-infrared band for events recorded during the Brilliant Flash I test series. Figures (a) through (f) are for events 32, 34-37, 39.

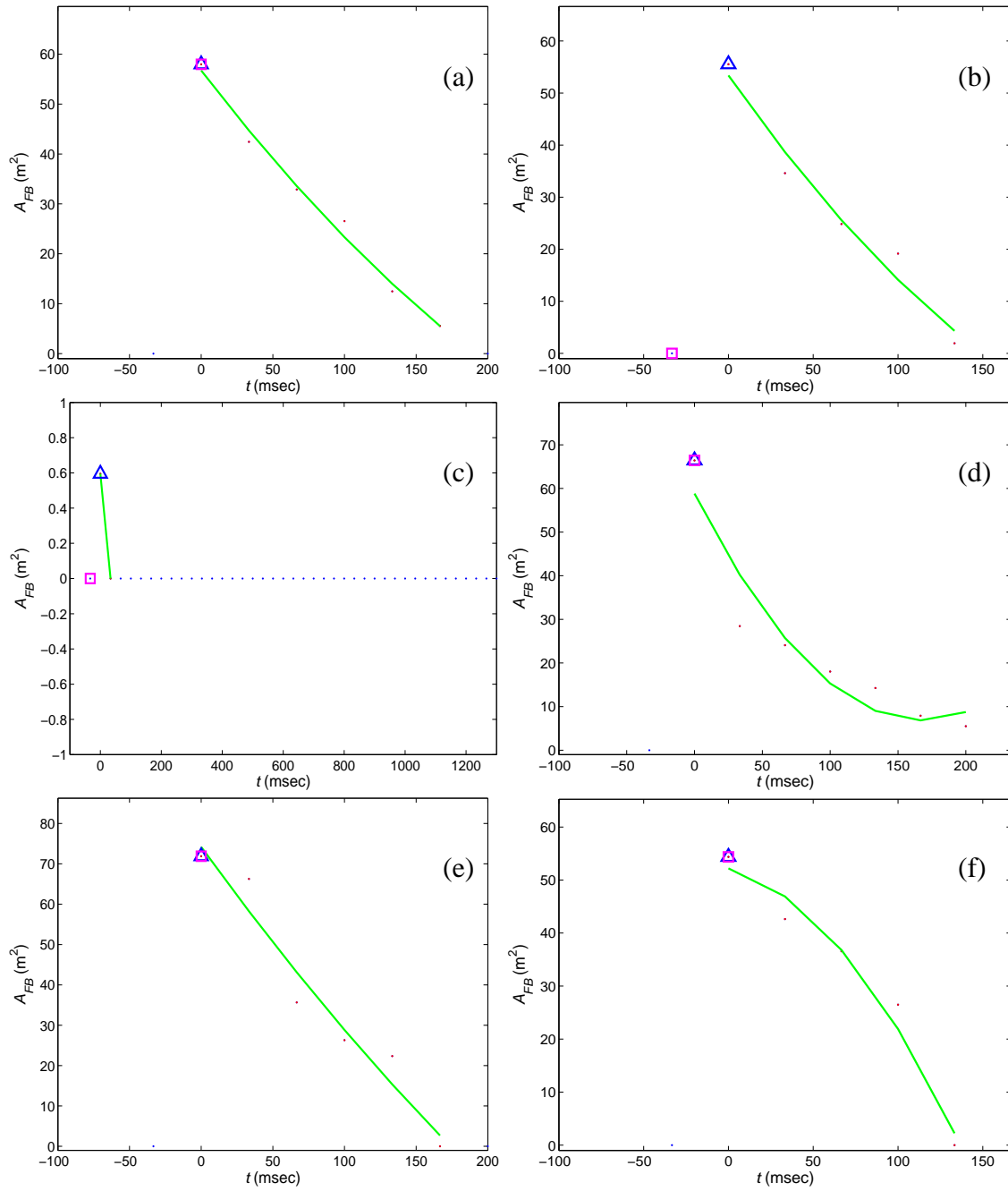


Figure 89. These figures represent the fireball area in the near-infrared band for events recorded during the Brilliant Flash I test series. Figures (a) through (f) are for events 40-45.

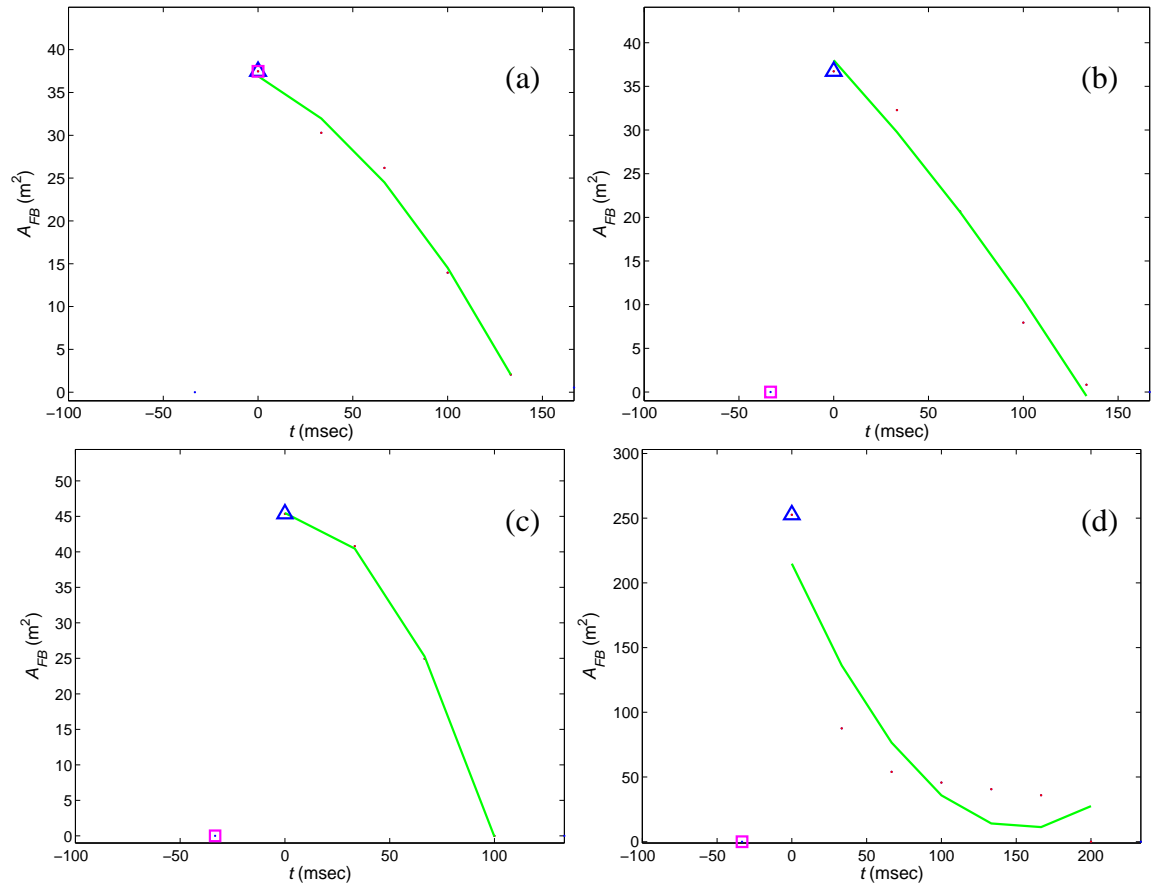


Figure 90. These figures represent the fireball area in the near-infrared band for events recorded during the Brilliant Flash I test series. Figures (a) through (d) are for events 46, 48, 50-51.

Appendix E: Brilliant Flash II 3-Chip Areas

The time-dependence of a fireball area is extracted from each image recorded by the 3-chip color camera. The plots in this appendix show the Brilliant Flash II fireball areas for each color at each time step (\bullet), the peak value (Δ), the area value associated with the median time (\square), and the curve that fits the equation, $f(t) = c_1t^2 + c_2t + c_3$. The following figures are included in this appendix:

- Figure 91. These figures represent the fireball area for each of the three color bands for events recorded during the Brilliant Flash II test series. Figures (a) through (e) are for events 1-5.
- Figure 92. These figures represent the fireball area for each of the three color bands for events recorded during the Brilliant Flash II test series. Figures (a) through (e) are for events 6, 8-11.
- Figure 93. These figures represent the fireball area for each of the three color bands for events recorded during the Brilliant Flash II test series. Figures (a) through (e) are for events 12-15, 17.
- Figure 94. These figures represent the fireball area for each of the three color bands for events recorded during the Brilliant Flash II test series. Figures (a) through (e) are for events 18-19, 21-23.
- Figure 95. These figures represent the fireball area for each of the three color bands for events recorded during the Brilliant Flash II test series. Figures (a) through (e) are for events 24-25, 27-29.
- Figure 96. These figures represent the fireball area for each of the three color bands for events recorded during the Brilliant Flash II test series. Figures (a) through (e) are for events 30-34.

- Figure 97. These figures represent the fireball area for each of the three color bands for events recorded during the Brilliant Flash II test series. Figures (a) through (e) are for events 35-39.
- Figure 98. These figures represent the fireball area for each of the three color bands for events recorded during the Brilliant Flash II test series. Figures (a) through (e) are for events 40-44.

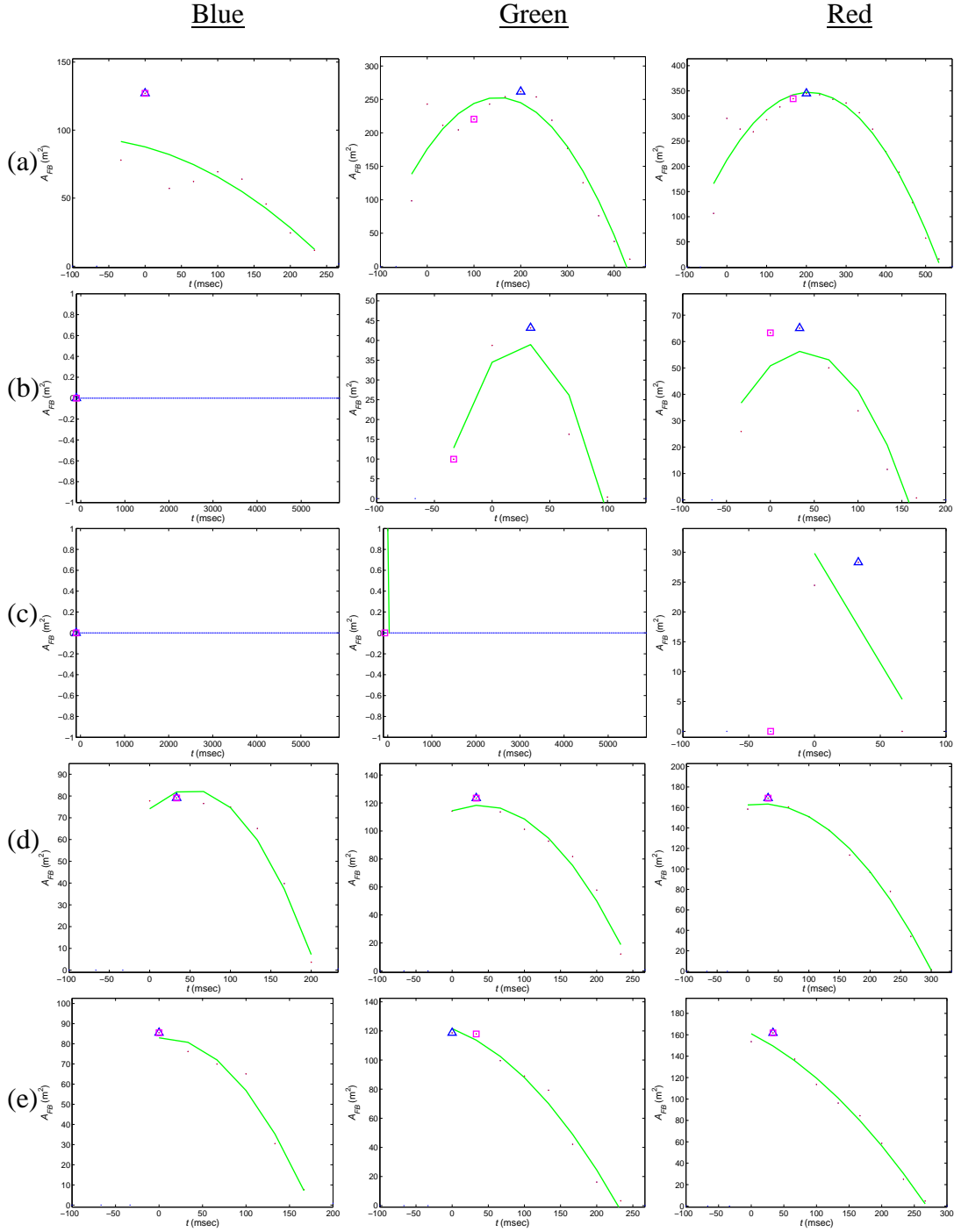


Figure 91. These figures represent the fireball area for each of the three color bands for events recorded during the Brilliant Flash II test series. Figures (a) through (e) are for events 1-5.

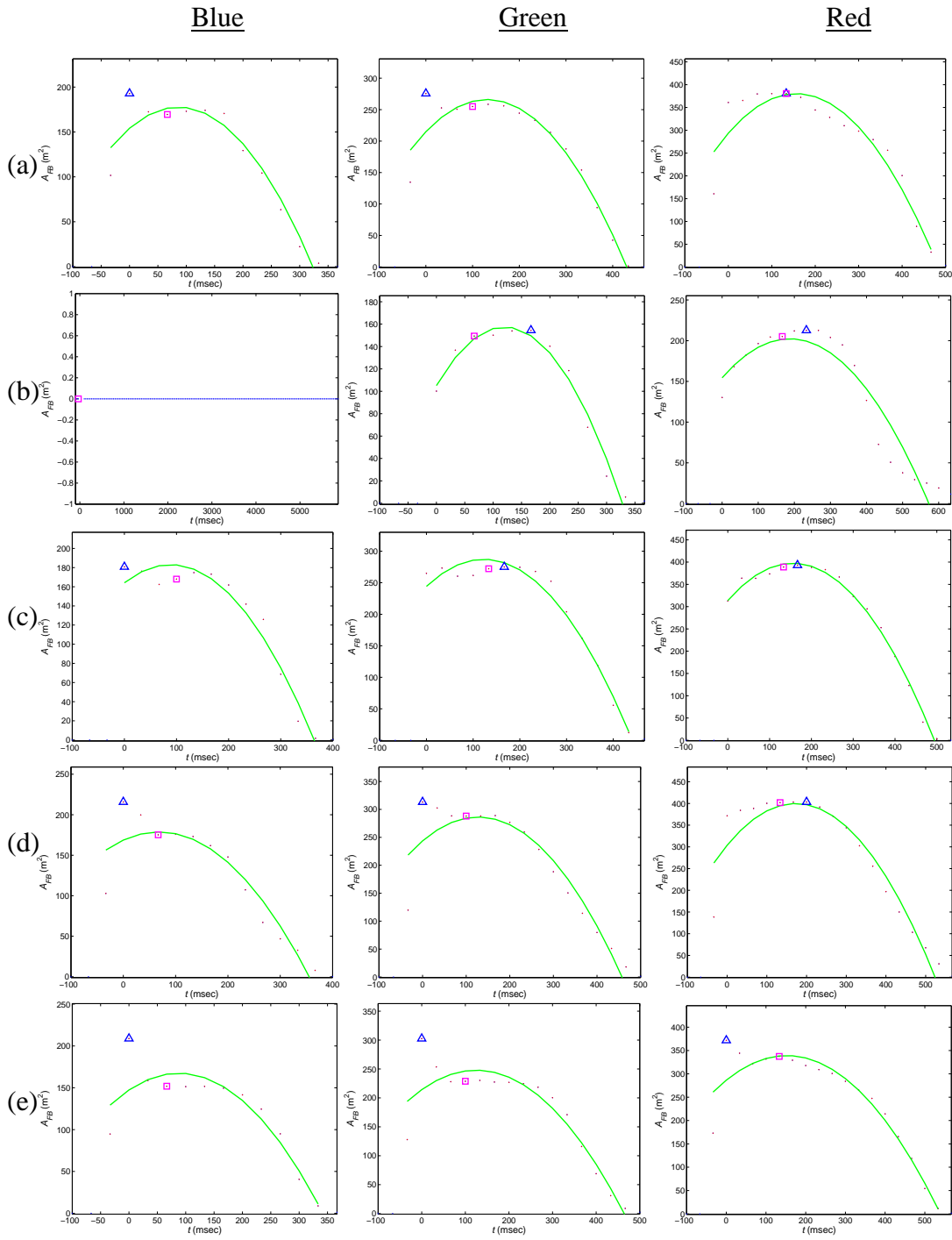


Figure 92. These figures represent the fireball area for each of the three color bands for events recorded during the Brilliant Flash II test series. Figures (a) through (e) are for events 6, 8-11.

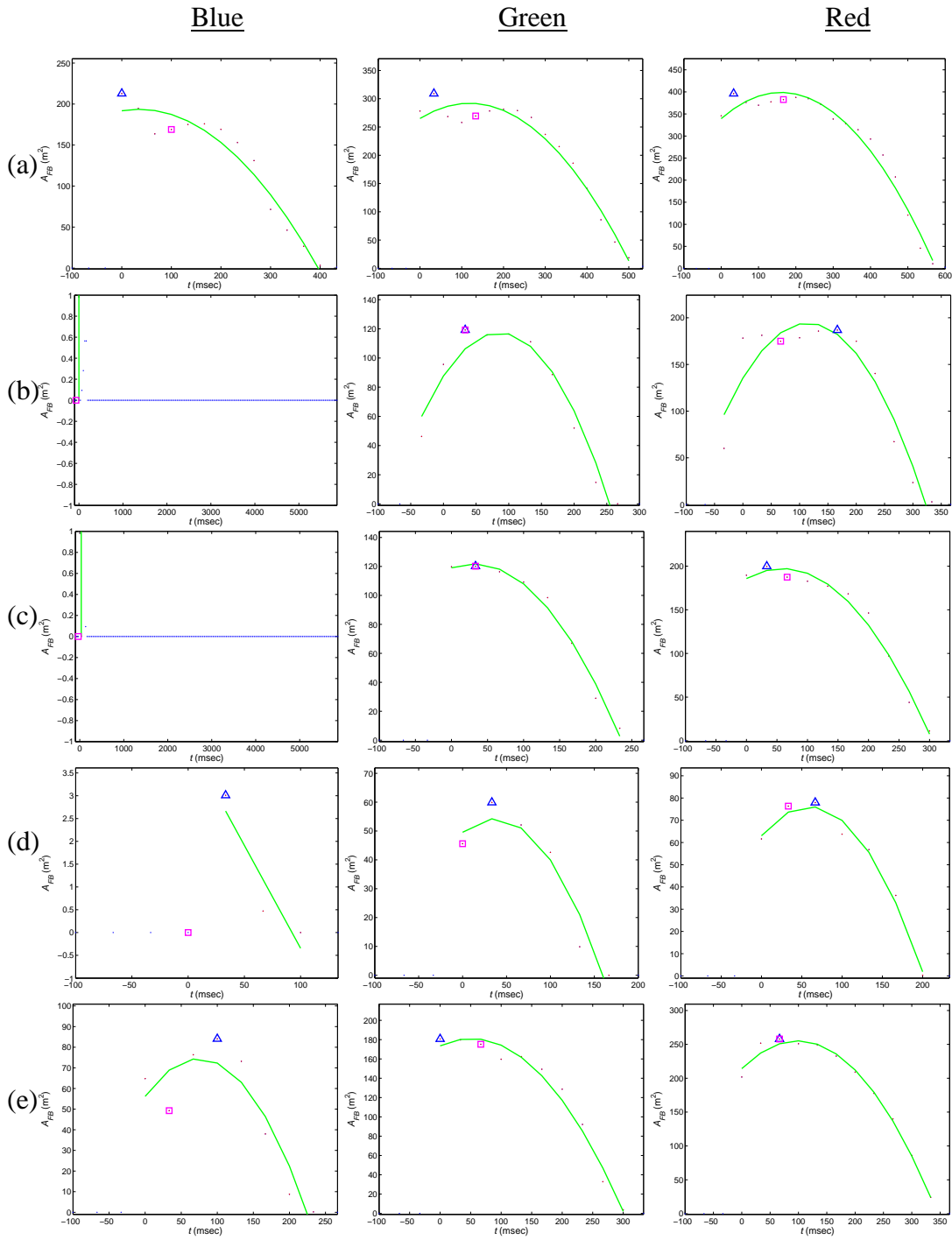


Figure 93. These figures represent the fireball area for each of the three color bands for events recorded during the Brilliant Flash II test series. Figures (a) through (e) are for events 12-15, 17.

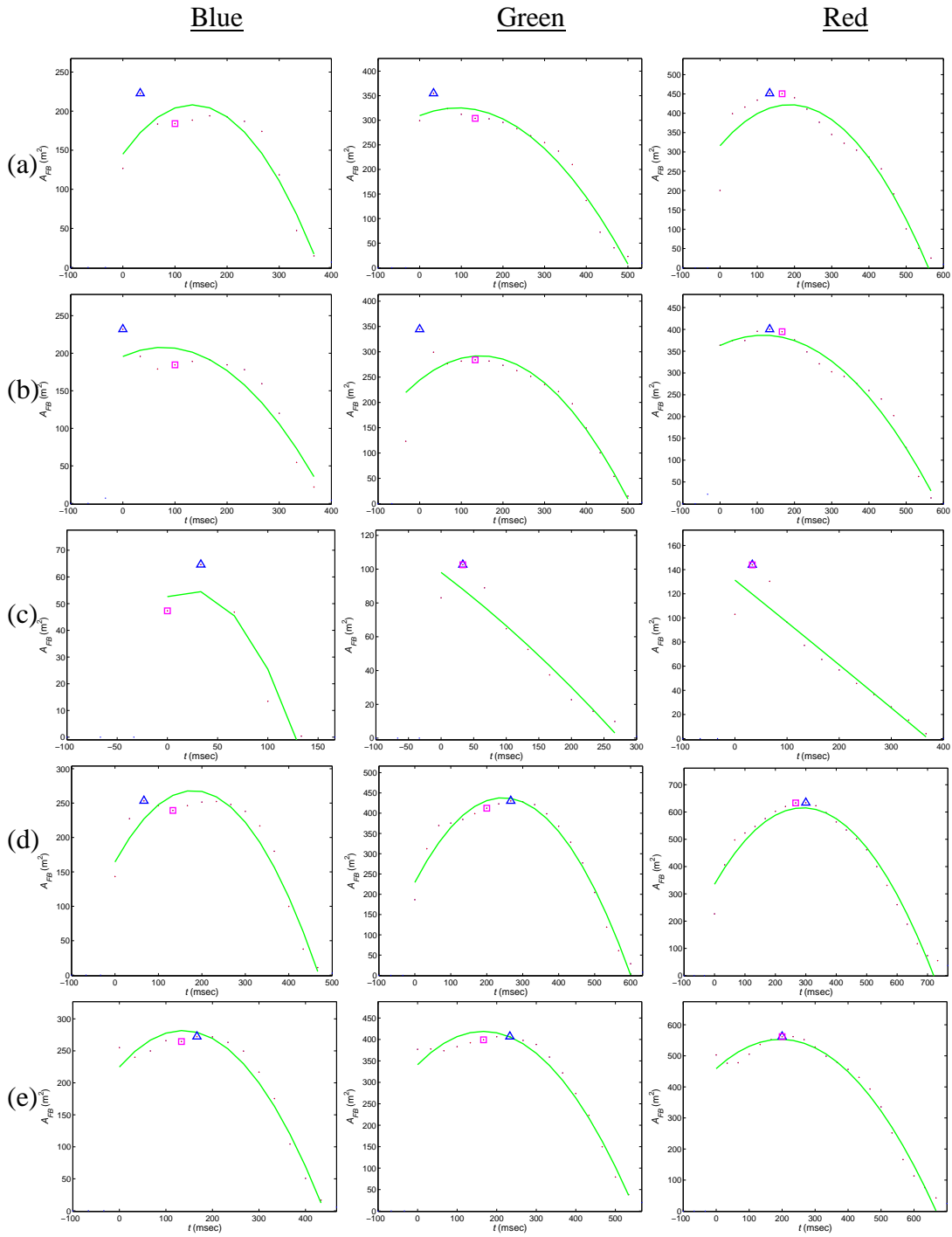


Figure 94. These figures represent the fireball area for each of the three color bands for events recorded during the Brilliant Flash II test series. Figures (a) through (e) are for events 18-19, 21-23.

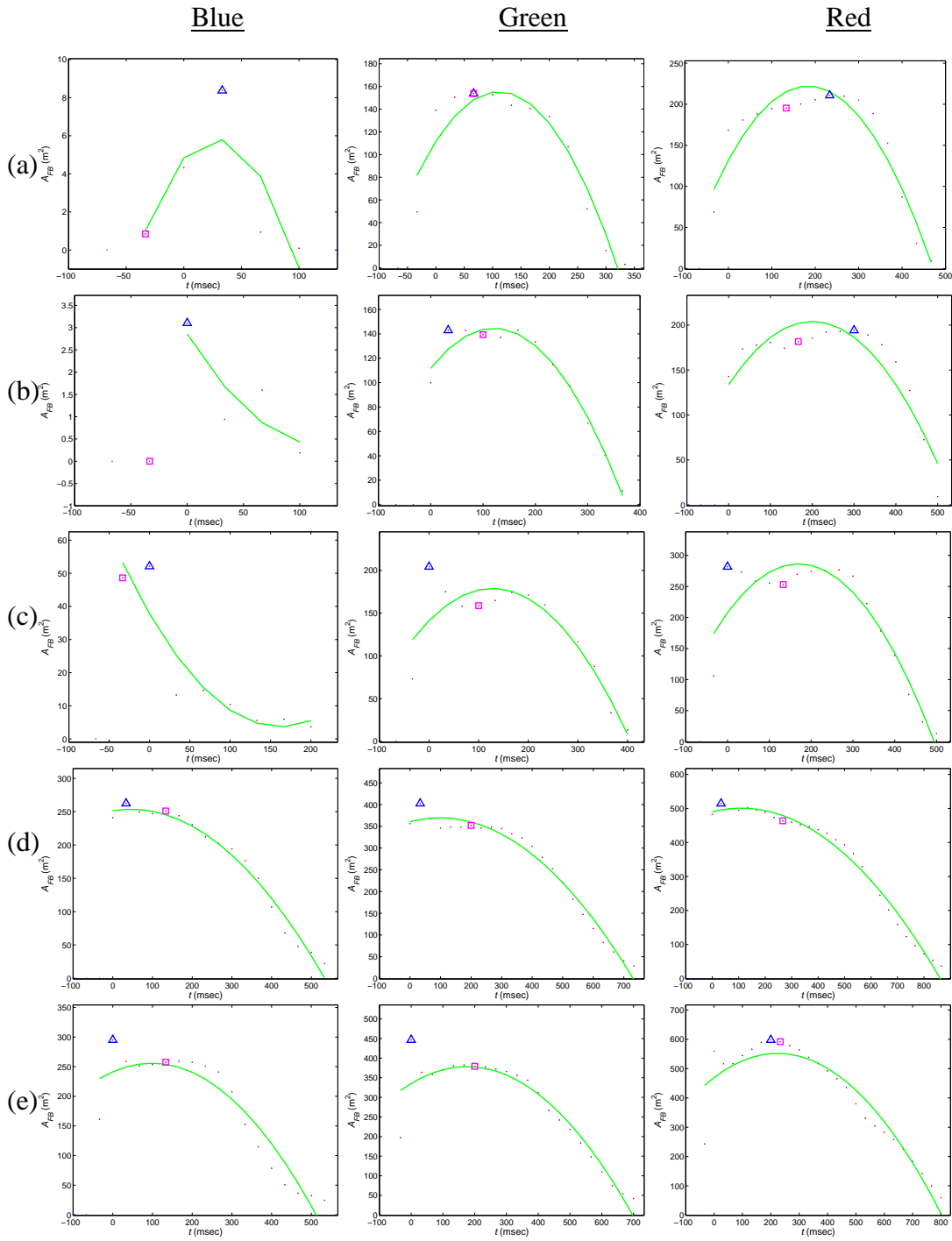


Figure 95. These figures represent the fireball area for each of the three color bands for events recorded during the Brilliant Flash II test series. Figures (a) through (e) are for events 24-25, 27-29.

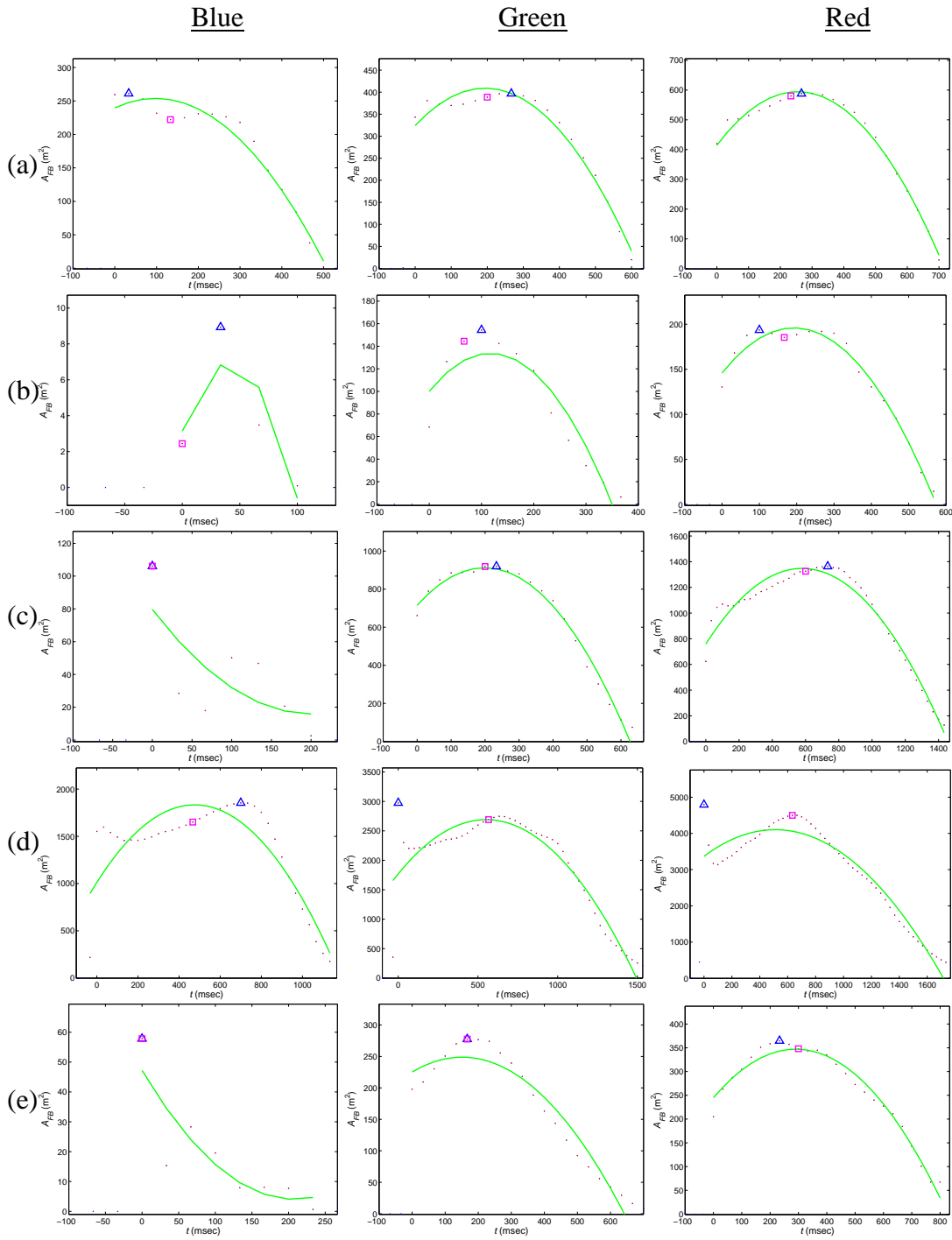


Figure 96. These figures represent the fireball area for each of the three color bands for events recorded during the Brilliant Flash II test series. Figures (a) through (e) are for events 30-34.

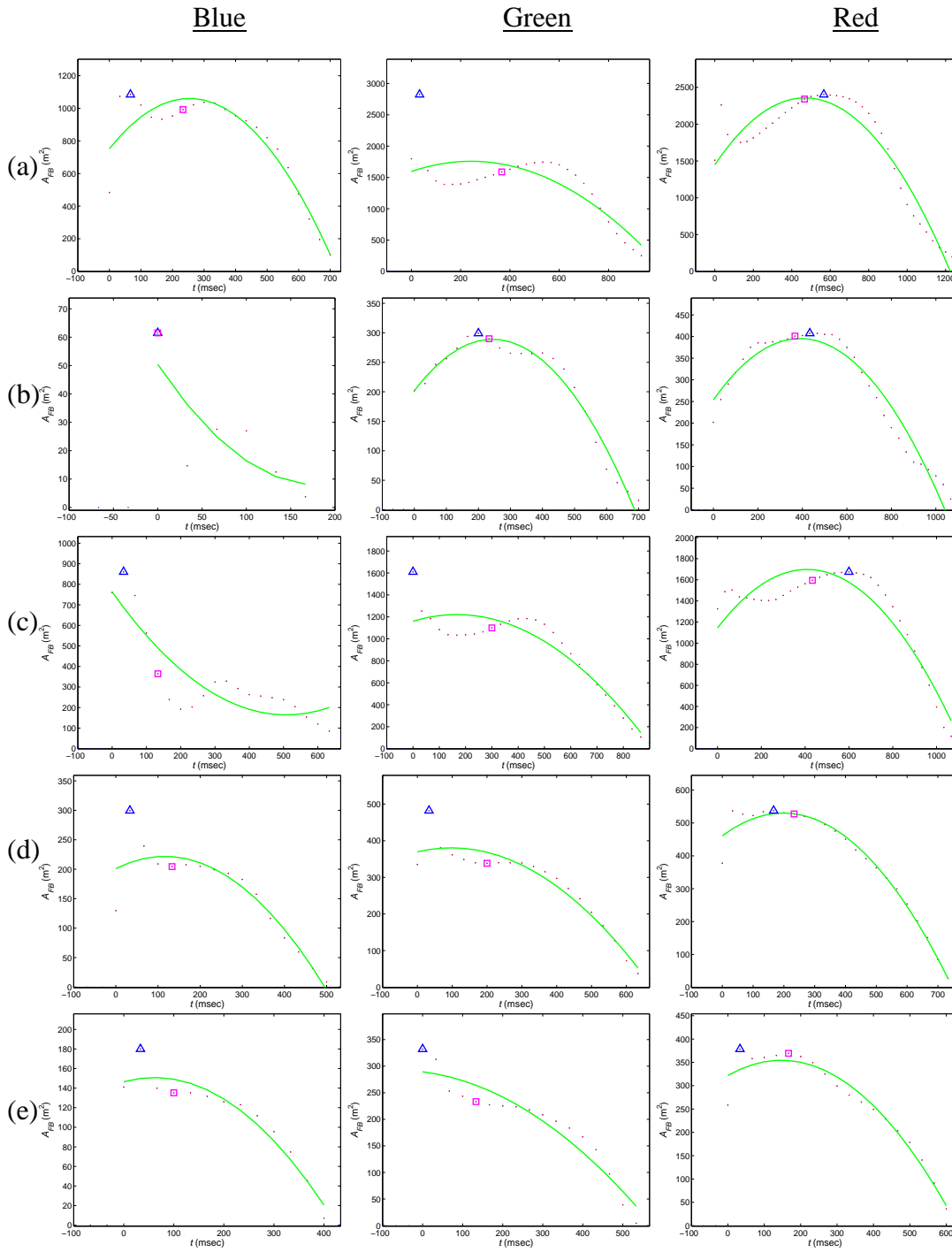


Figure 97. These figures represent the fireball area for each of the three color bands for events recorded during the Brilliant Flash II test series. Figures (a) through (e) are for events 35-39.

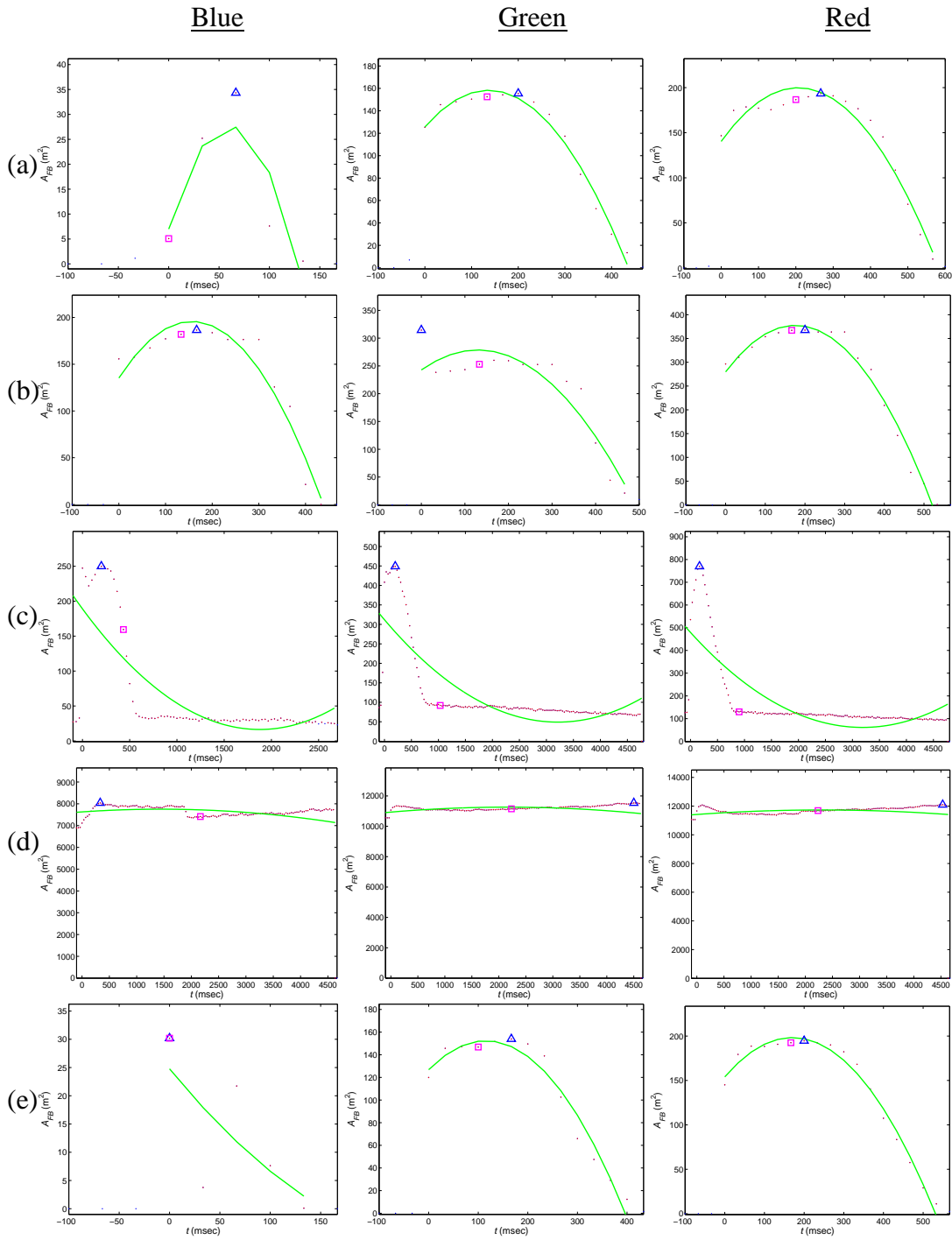


Figure 98. These figures represent the fireball area for each of the three color bands for events recorded during the Brilliant Flash II test series. Figures (a) through (e) are for events 40-44.

Appendix F: Brilliant Flash I 3-Chip Areas

The time-dependence of a fireball area is extracted from each image recorded by the 3-chip color camera. The plots in this appendix show the Brilliant Flash I fireball areas for each color at each time step (\bullet), the peak value (Δ), the area value associated with the median time (\square), and the curve that fits the equation, $f(t) = c_1t^2 + c_2t + c_3$. The following figures are included in this appendix:

- Figure 99. These figures represent the fireball area for each of the three color bands for events recorded during the Brilliant Flash I test series. Figures (a) through (e) are for events 1-5.
- Figure 100. These figures represent the fireball area for each of the three color bands for events recorded during the Brilliant Flash I test series. Figures (a) through (e) are for events 7-11.
- Figure 101. These figures represent the fireball area for each of the three color bands for events recorded during the Brilliant Flash I test series. Figures (a) through (e) are for events 13-17.
- Figure 102. These figures represent the fireball area for each of the three color bands for events recorded during the Brilliant Flash I test series. Figures (a) through (e) are for events 18-22.
- Figure 103. These figures represent the fireball area for each of the three color bands for events recorded during the Brilliant Flash I test series. Figures (a) through (e) are for events 23-25, 29-30.
- Figure 104. These figures represent the fireball area for each of the three color bands for events recorded during the Brilliant Flash I test series. Figures (a) through (e) are for events 31, 34, 38-40.
- Figure 105. These figures represent the fireball area for each of the three color bands for events recorded during the Brilliant Flash I test series. Figures (a) through (e) are for events 41-45.
- Figure 106. These figures represent the fireball area for each of the three color bands for events recorded during the Brilliant Flash I test series. Figures (a) through (e) are for events 46-50.
- Figure 107. These figures represent the fireball area for each of the three color bands for events recorded during the Brilliant Flash I test series. Figures (a) through (c) are the blue, green, and red spectral bands, respectively, for event 51.

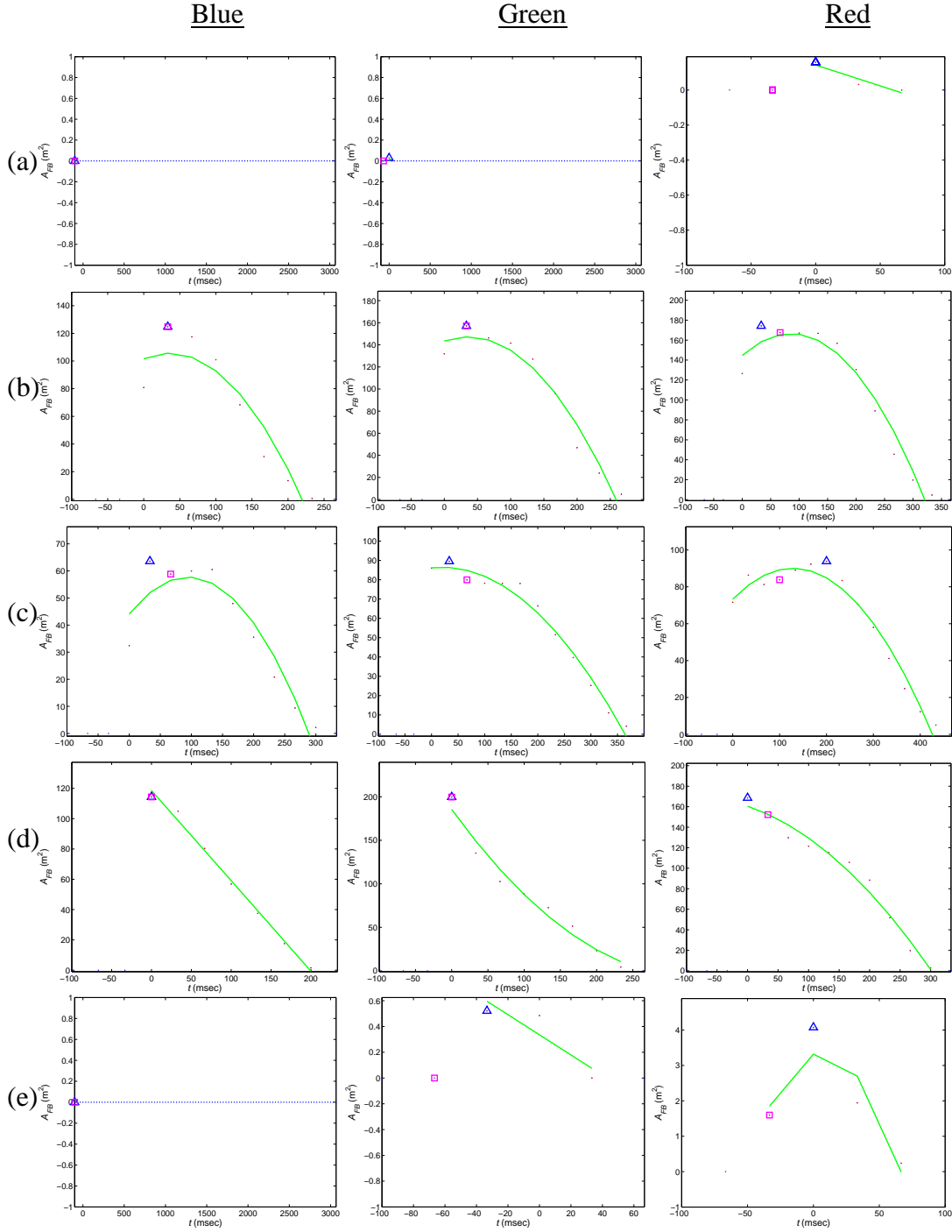


Figure 99. These figures represent the fireball area for each of the three color bands for events recorded during the Brilliant Flash I test series. Figures (a) through (e) are for events 1-5.

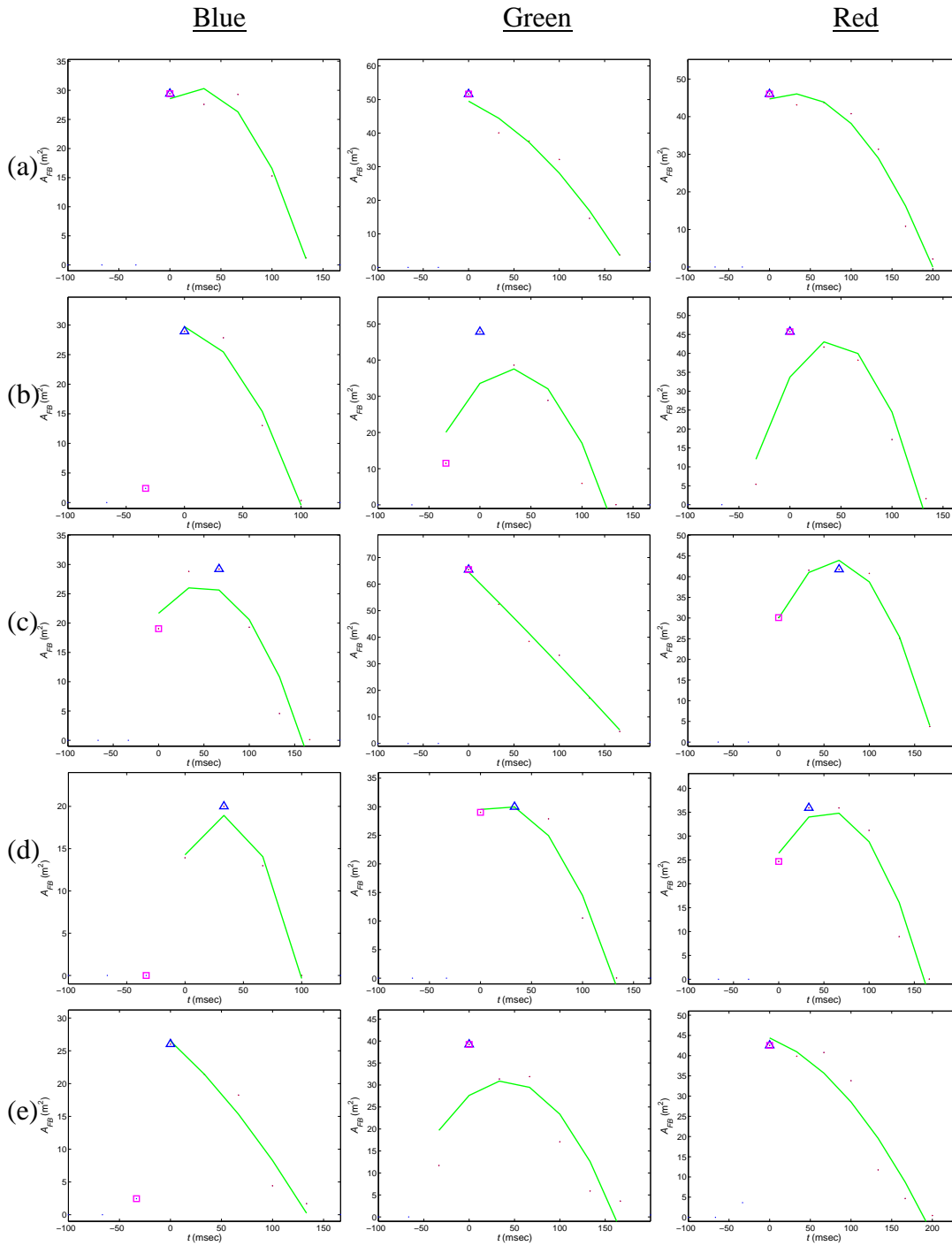


Figure 100. These figures represent the fireball area for each of the three color bands for events recorded during the Brilliant Flash I test series. Figures (a) through (e) are for events 7-11.

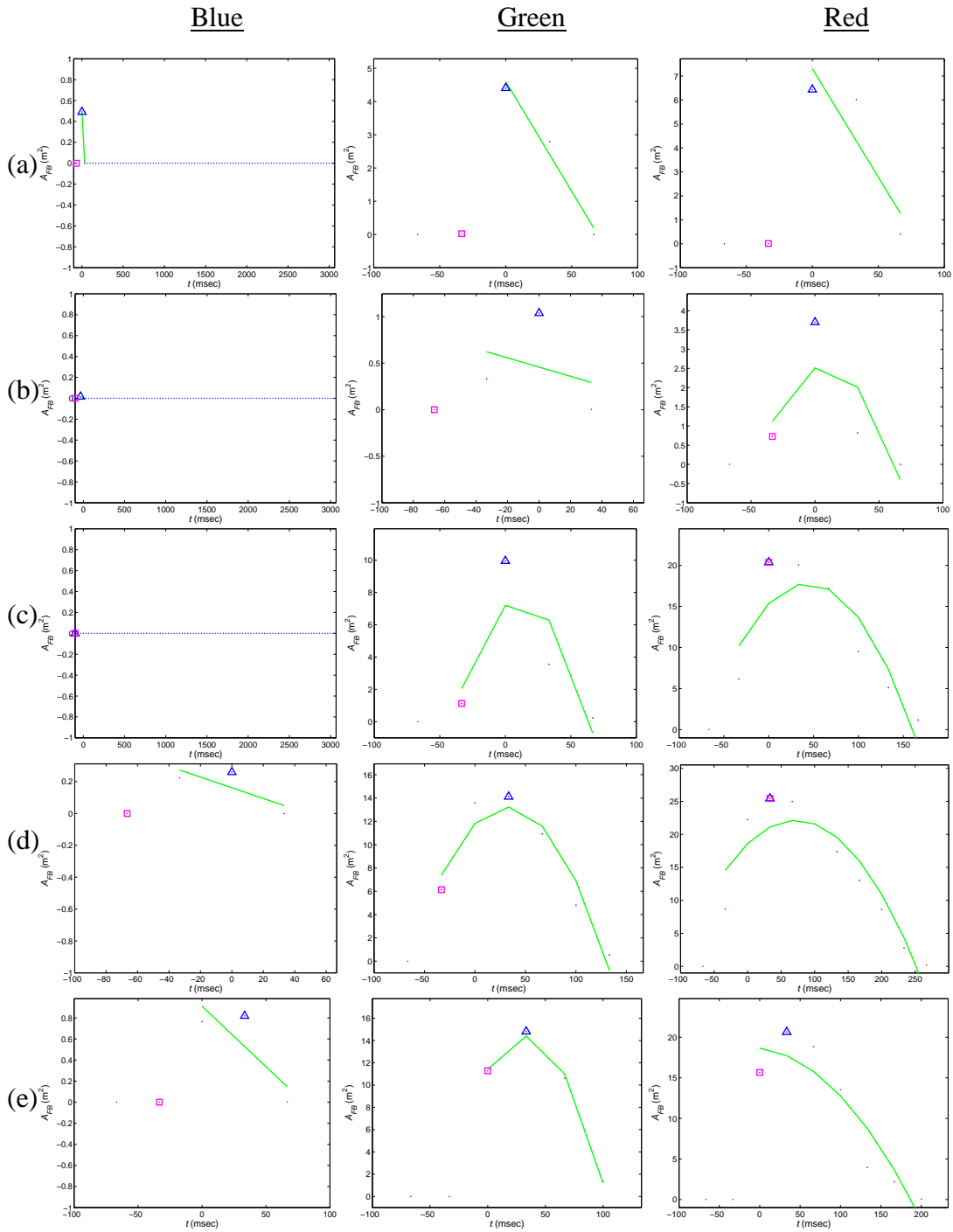


Figure 101. These figures represent the fireball area for each of the three color bands for events recorded during the Brilliant Flash I test series. Figures (a) through (e) are for events 13-17.

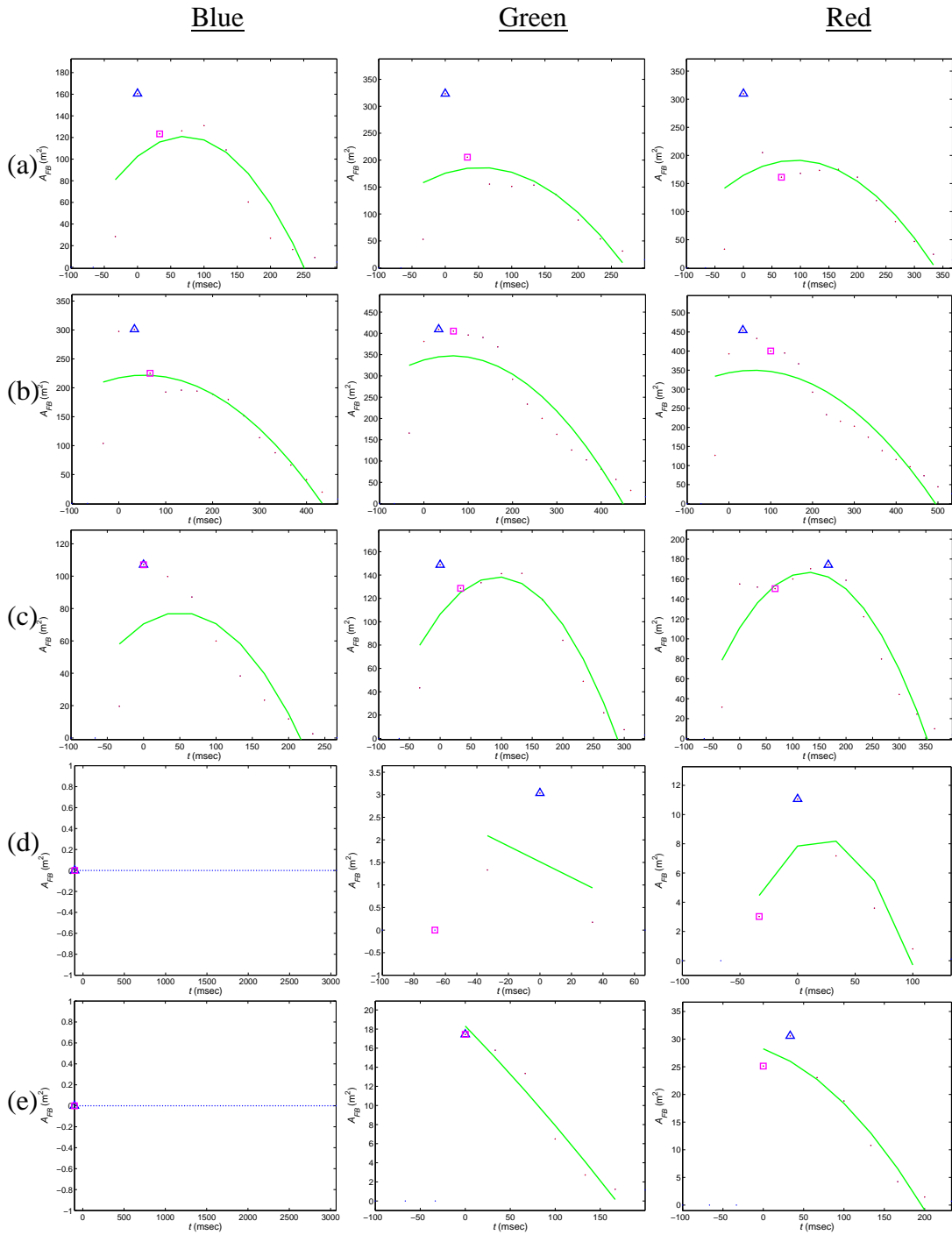


Figure 102. These figures represent the fireball area for each of the three color bands for events recorded during the Brilliant Flash I test series. Figures (a) through (e) are for events 18-22.

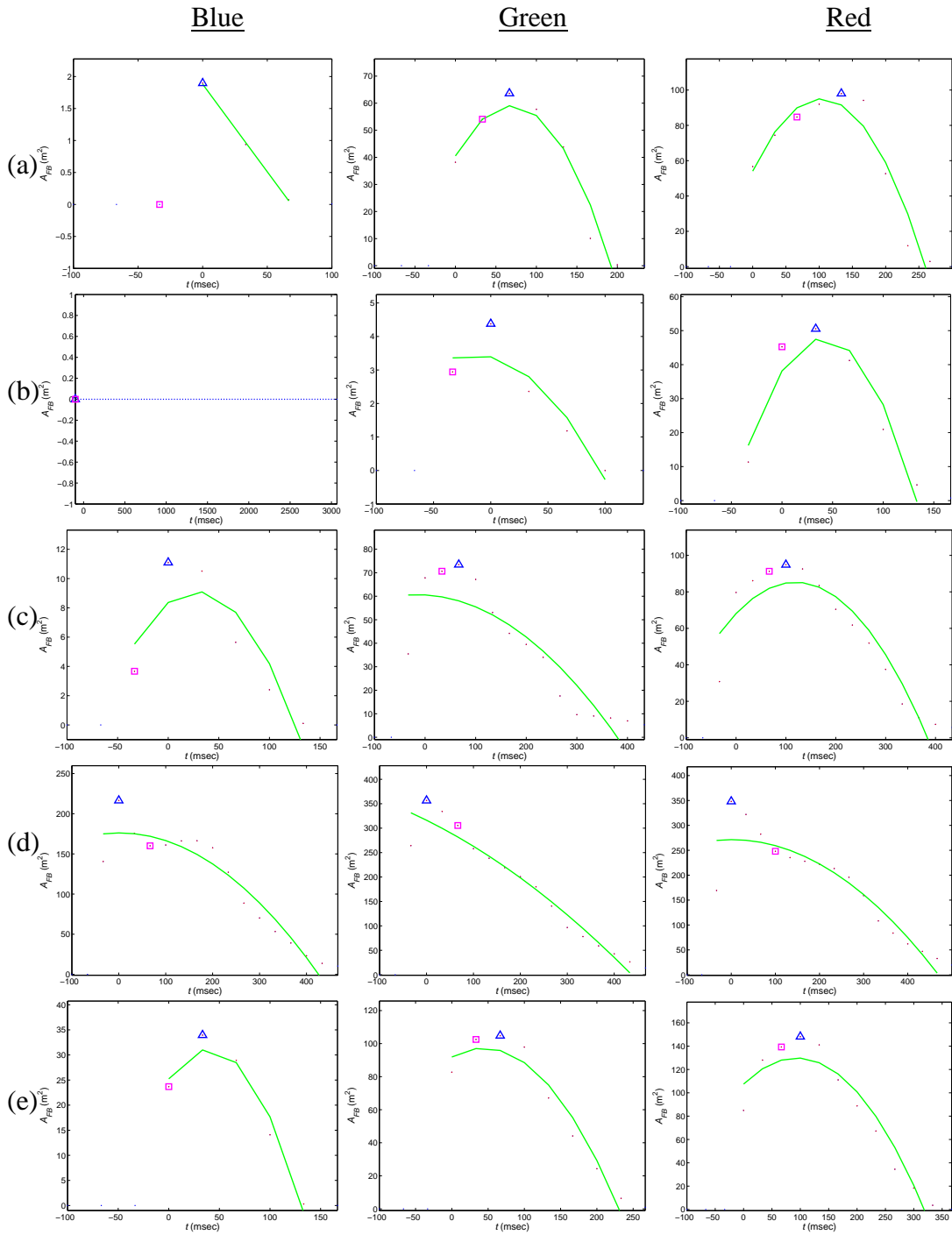


Figure 103. These figures represent the fireball area for each of the three color bands for events recorded during the Brilliant Flash I test series. Figures (a) through (e) are for events 23-25, 29-30.

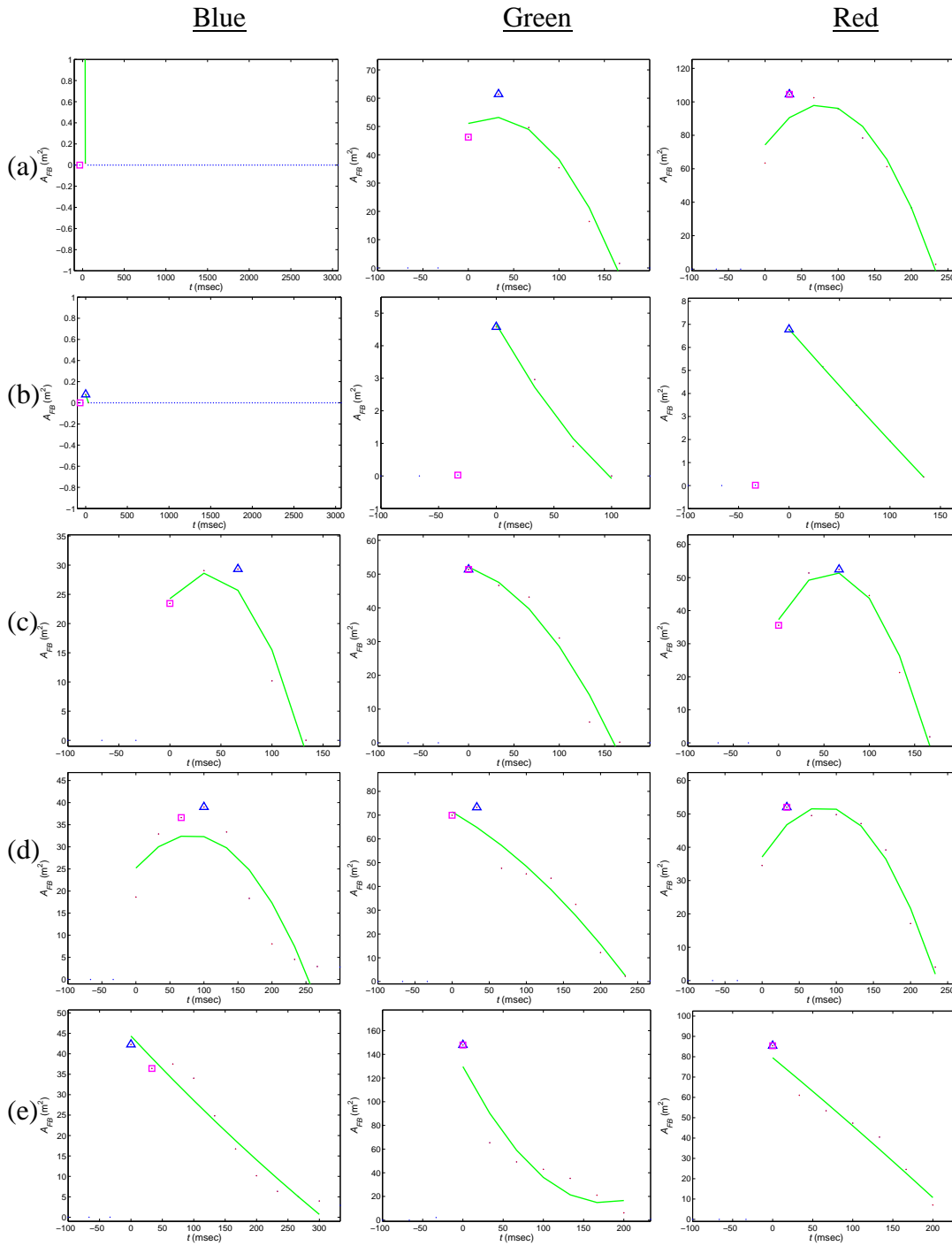


Figure 104. These figures represent the fireball area for each of the three color bands for events recorded during the Brilliant Flash I test series. Figures (a) through (e) are for events 31, 34, 38-40.

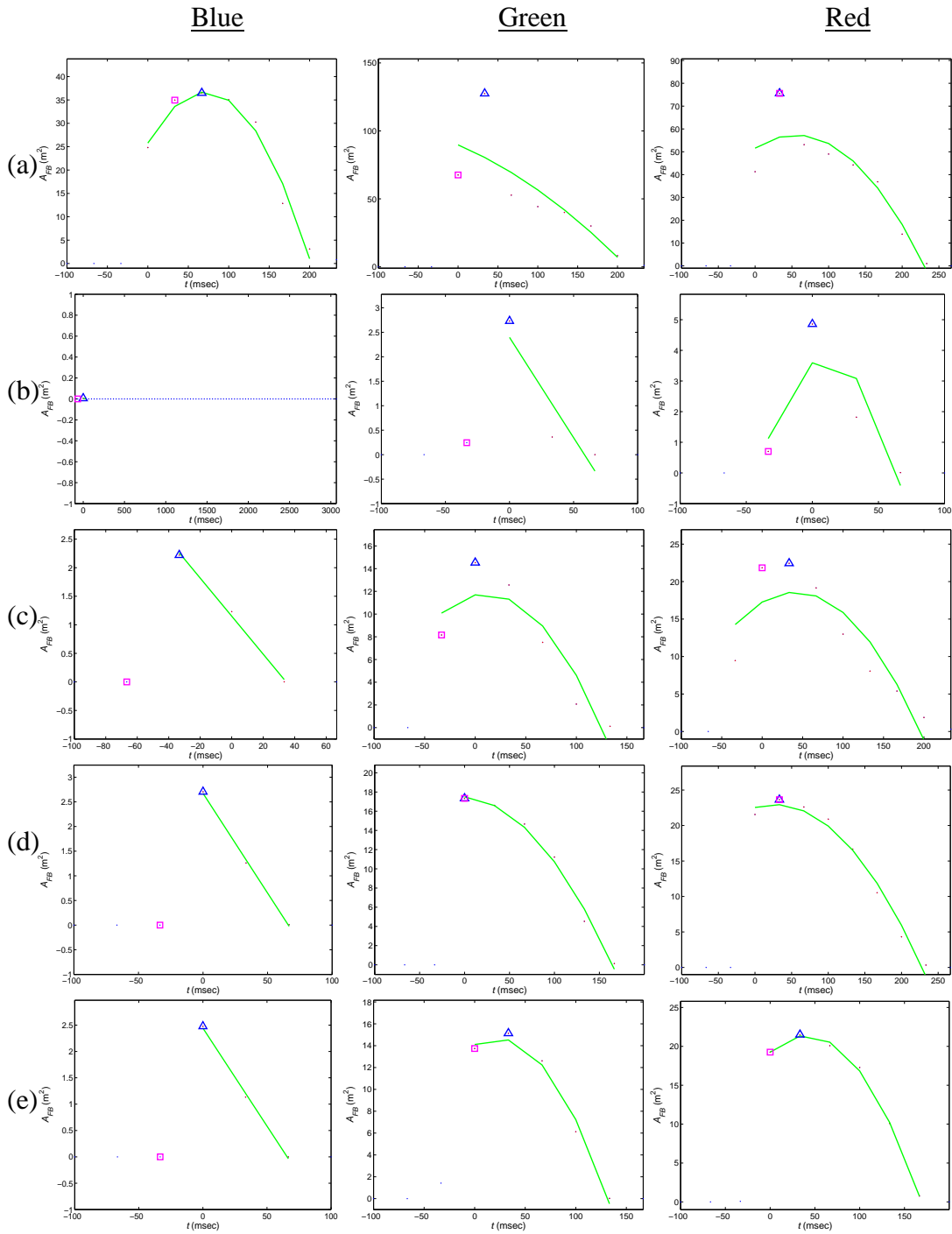


Figure 105. These figures represent the fireball area for each of the three color bands for events recorded during the Brilliant Flash I test series. Figures (a) through (e) are for events 41-45.

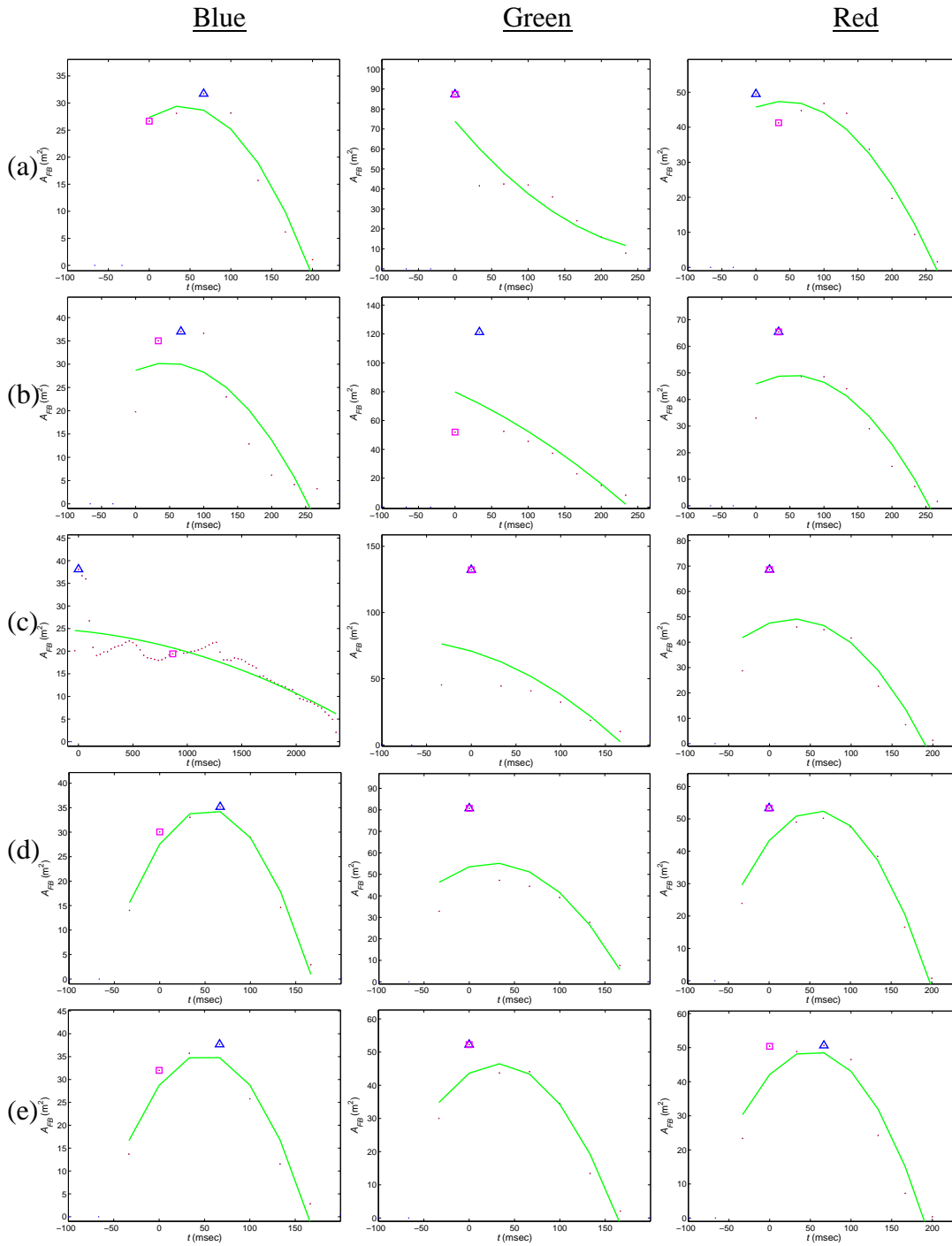


Figure 106. These figures represent the fireball area for each of the three color bands for events recorded during the Brilliant Flash I test series. Figures (a) through (e) are for events 46-50.

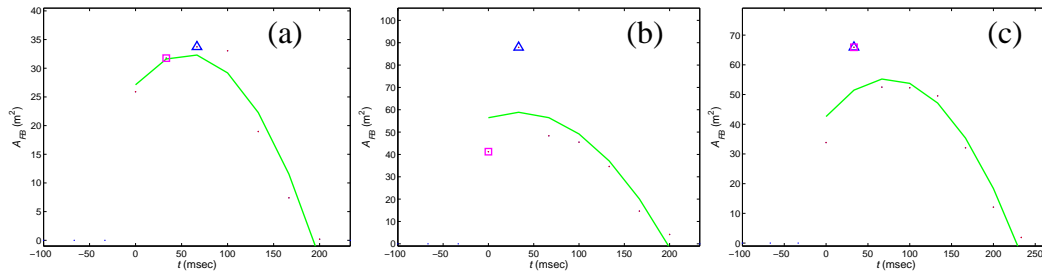


Figure 107. These figures represent the fireball area for each of the three color bands for events recorded during the Brilliant Flash I test series. Figures (a) through (c) are the blue, green, and red spectral bands, respectively, for event 51.

Appendix G: Scaling Laws, NIR features, BFI & BFII

Each extracted feature derived from the near-infrared image is examined for weight scaling relationships. The first figure presented in this appendix is an overall summary of all the features while each of the individual plots is given in the remaining figures. The data points marked as “x” are the enhanced novel explosive (ENE) events (Types B through E) and marked as “o” are Type A (TNT) events. The weights are 10 kg, 50 kg, and 100 kg. The least square fit lines have error bars which are described in Chapter IV, Section H; the errors associated with ENE are dotted lines, while those associated with Type A are dash-dotted lines. The following is a list of figures for this appendix:

- Figure 108. Each feature extracted from the fireball NIR image is plotted here as a function of weight, showing potential scaling relationships.
- Figure 109. Potential scaling relationships exhibit fireball area features dependence upon weight (W). Figures (a) through (f) contain features A , t_{median} , $\sigma\tau_{\mu\epsilon\delta\iota\alpha\nu}$, A_{median} , t_{mp} , and A_{mp} .
- Figure 110. Potential scaling relationships exhibit fireball area features dependence upon weight (W). Figures (a) through (f) contain features $\sigma A_{\mu\epsilon\delta\iota\alpha\nu}$, $.c1$, $c2$, $c3$, $\mu1$, and $\mu1$.
- Figure 111. Potential scaling relationships exhibit fireball area features dependence upon weight (W). Figures (a) through (b) contain features $\mu3$ and $\mu4$

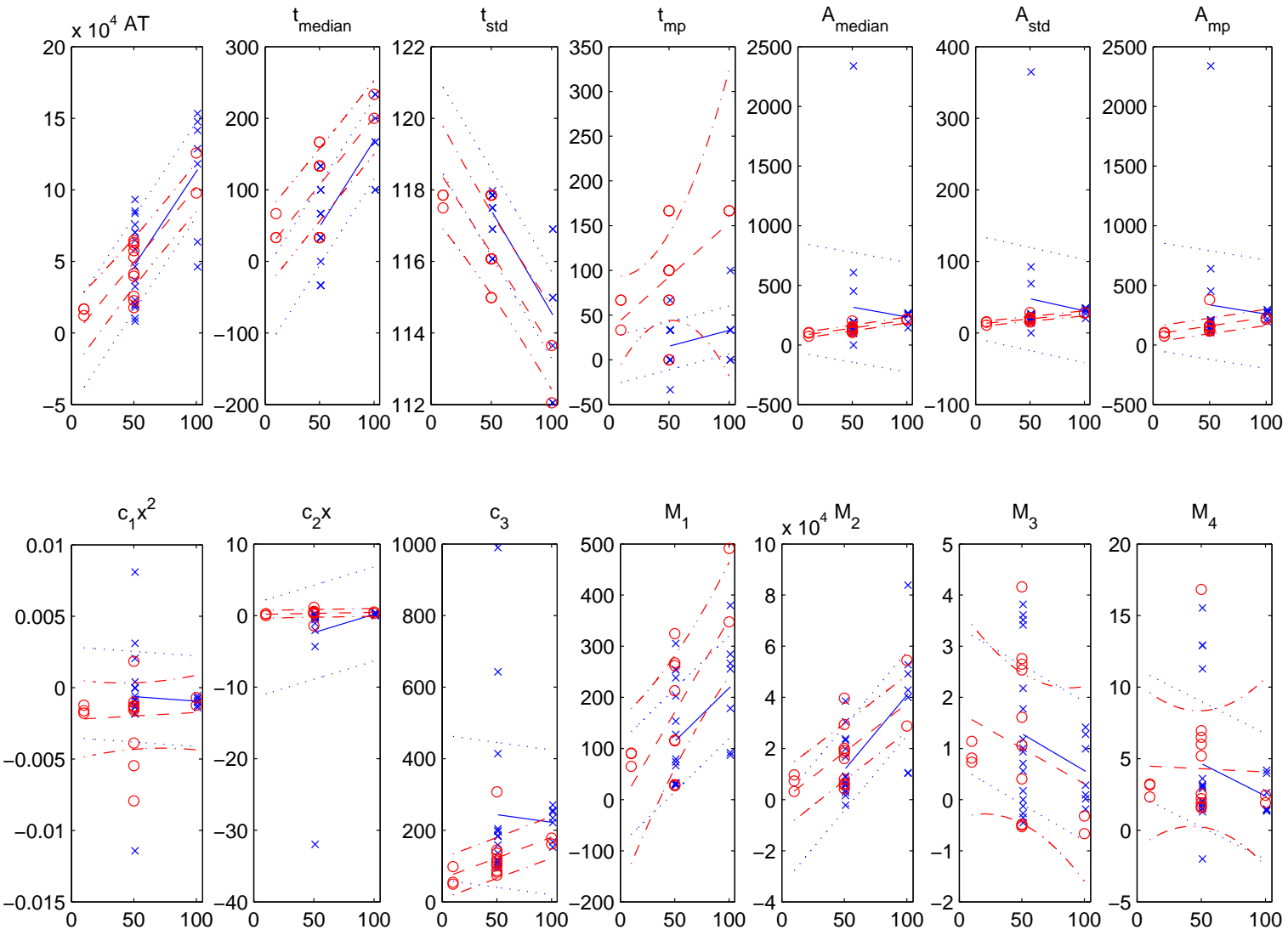


Figure 108. Each feature extracted from the fireball NIR image is plotted here as a function of weight, showing potential scaling relationships.

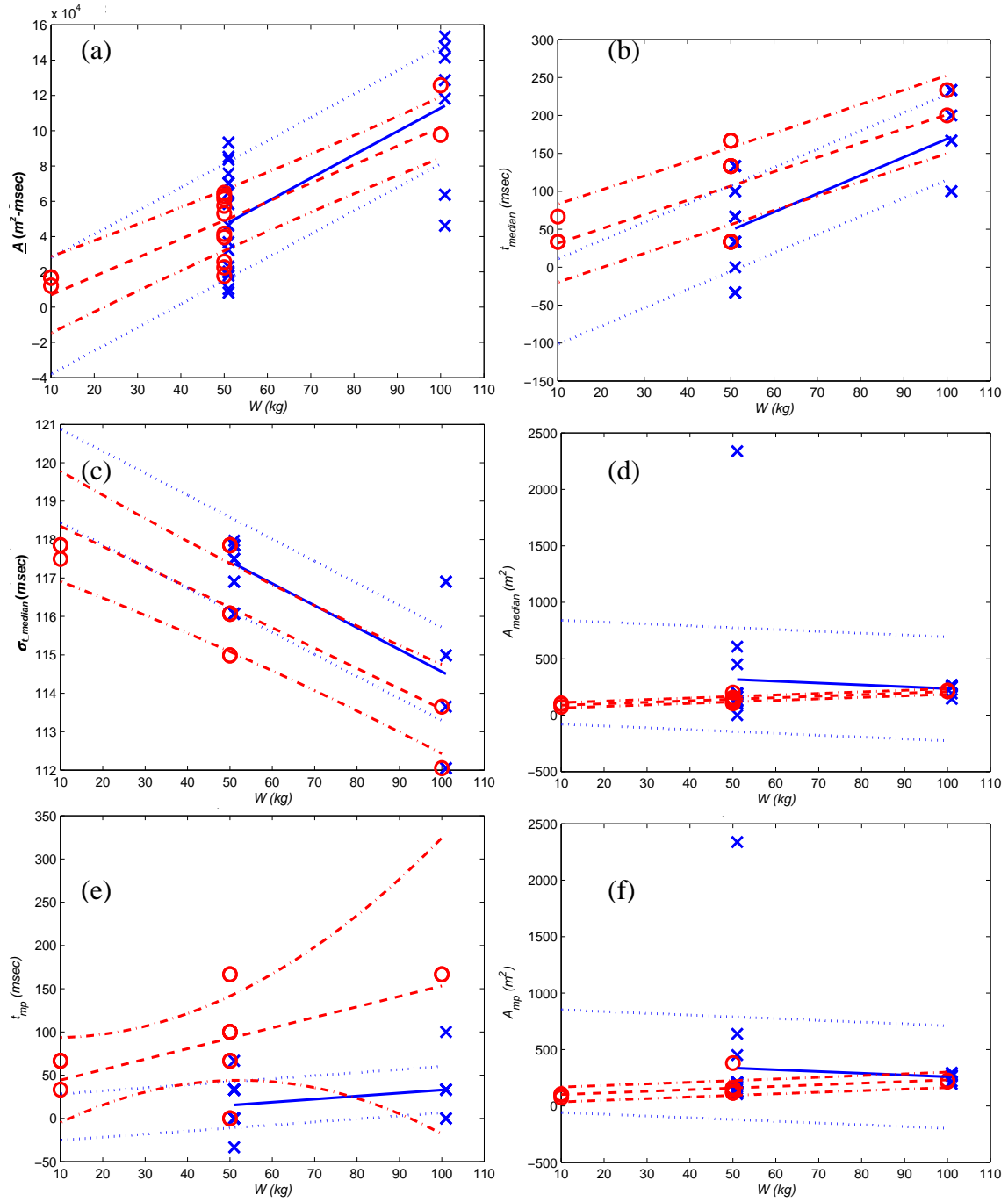


Figure 109. Potential scaling relationships exhibit fireball area features dependence upon weight (W). Figures (a) through (f) contain features \bar{A} , t_{median} , $\sigma_{t_{median}}$, A_{median} , t_{mp} , and A_{mp} .

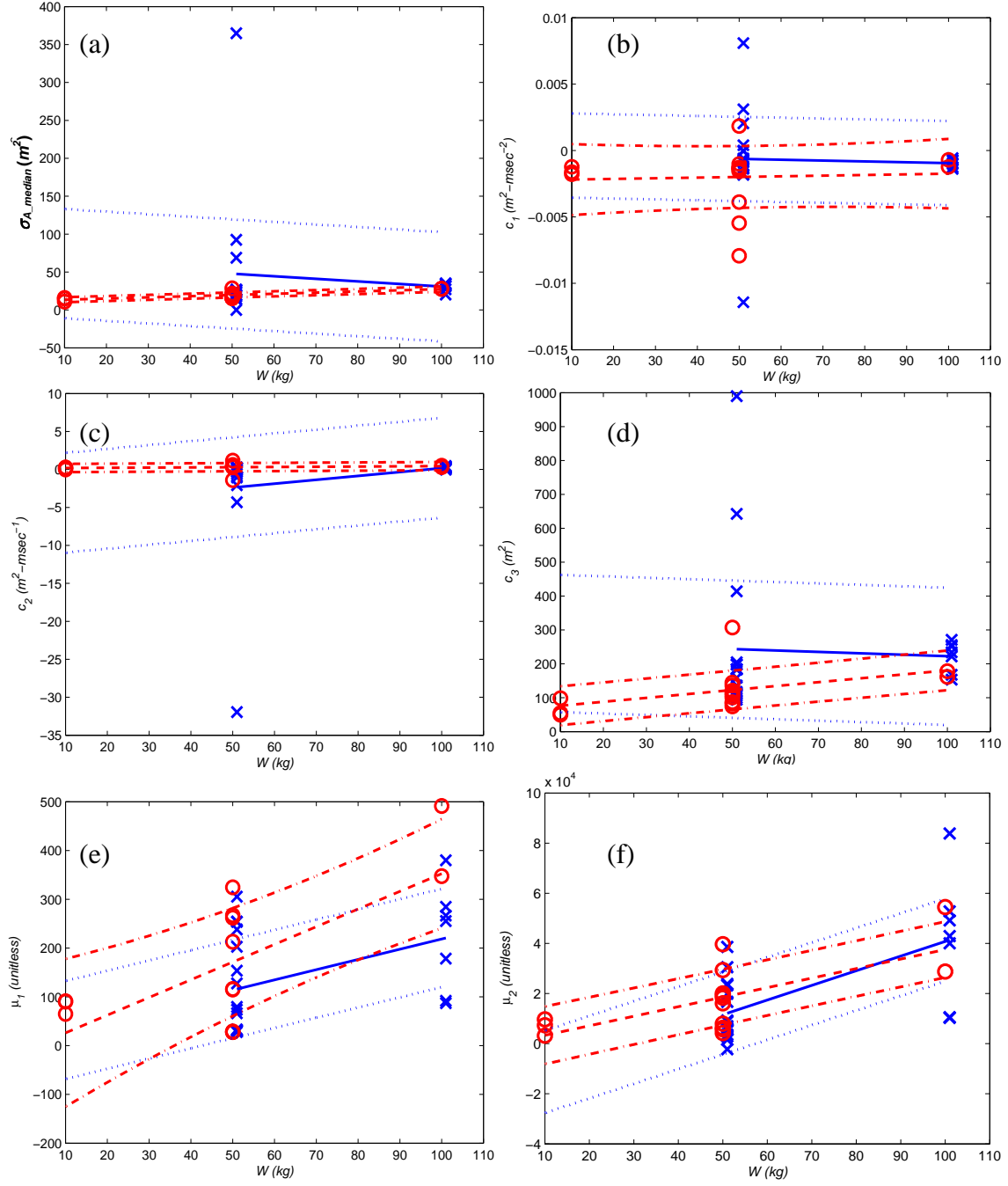


Figure 110. Potential scaling relationships exhibit fireball area features dependence upon weight (W). Figures (a) through (f) contain features σ_{A_median} , c_1 , c_2 , c_3 , μ_1 , and μ_2 .

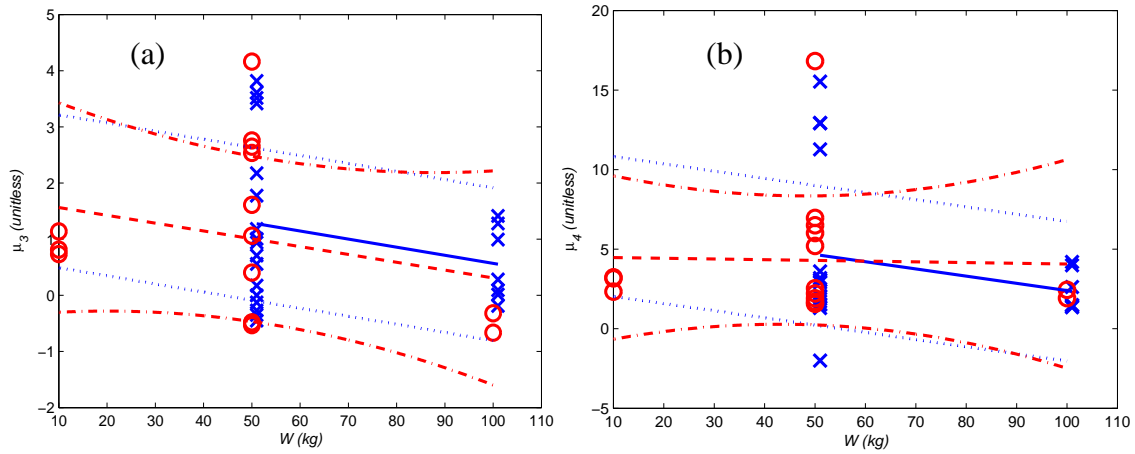


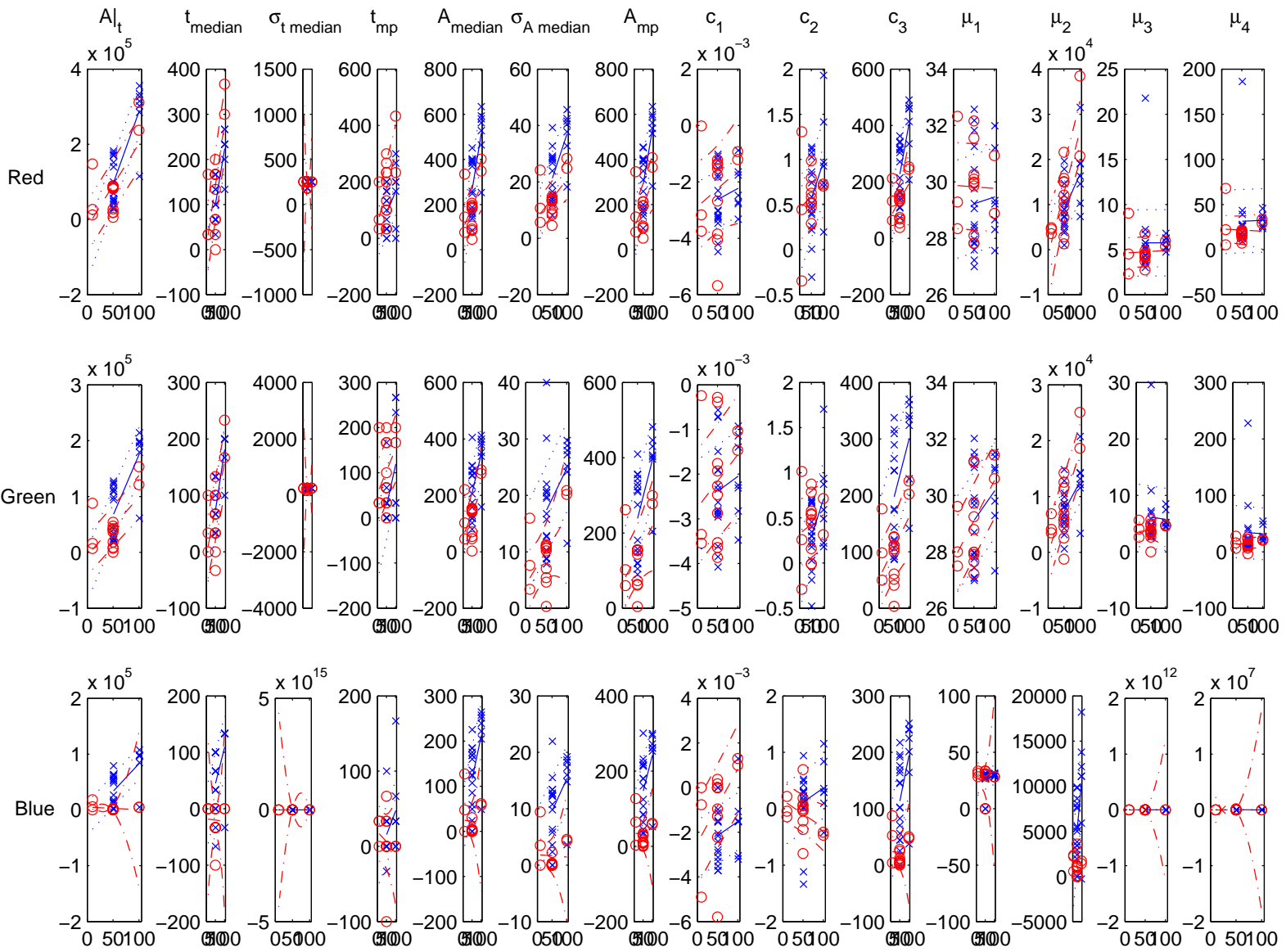
Figure 111. Potential scaling relationships exhibit fireball area features dependence upon weight (W). Figures (a) through (b) contain features μ_3 and μ_4

Appendix H: Scaling Laws, 3-Chip features, BFI & BFII

Each extracted feature derived from the 3-chip color image is examined for weight scaling relationships. The first figure presented in this appendix is an overall summary of all the features for each color while each of the individual plots is given in the remaining figures. The data points marked as “x” are the enhanced novel explosive (ENE) events (Types B through E) and marked as “o” are Type A (TNT) events. The weights are 10 kg, 50 kg, and 100 kg. The least square fit lines have error bars which are described in Chapter IV, Section H; the errors associated with ENE are dotted lines, while those associated with Type A are dash-dotted lines. The following is a list of figures for this appendix:

- Figure 112. Each feature extracted from the fireball color image is plotted here as a function of weight, showing potential scaling relationships.
- Figure 113. Potential scaling relationships exhibit fireball area features dependence upon weight (W). Figures (a) through (f) contain the red band features for A , t_{median} , $\sigma\tau_{\mu\epsilon\delta\iota\alpha\nu}$, t_{mp} , A_{median} , $\sigma A_{\mu\epsilon\delta\iota\alpha\nu}$.
- Figure 114. Potential scaling relationships exhibit fireball area features dependence upon weight (W). Figures (a) through (f) contain the red band features for A_{mp} , $c1$, $c2$, $c3$, $\mu1$, and $\mu2$.
- Figure 115. Potential scaling relationships exhibit fireball area features dependence upon weight (W). Figures (a) and (b) contain the red band features for the third and fourth moments, while Figures (c) through contain the green band features for A , t_{median} , $\sigma\tau_{\mu\epsilon\delta\iota\alpha\nu}$, t_{mp} , and A_{median} .

- Figure 116. Potential scaling relationships exhibit fireball area features dependence upon weight (W). Figures (a) through (f) contain the green band features for *tmp*, $\sigma A_{\mu\epsilon\delta\iota\omicron\nu}$, *Amp*, *c1*, *c2*, and *c3*.
- Figure 117. Potential scaling relationships exhibit fireball area features dependence upon weight (W). Figures (a) through (d) contain the green band features for the four moments, while Figures (e) and (f) contain the blue band features for *A* and *tmedian*.
- Figure 118. Potential scaling relationships exhibit fireball area features dependence upon weight (W). Figures (a) through (f) contain the blue band features for $\sigma\tau_{\mu\epsilon\delta\iota\omicron\nu}$, *tmp*, *Amedian*, $\square A_{median}$, $A\mu\pi$, and *c1*.
- Figure 119. Potential scaling relationships exhibit fireball area features dependence upon weight (W). Figures (a) through (f) contain the blue band features for *c1*, *c2*, and the first four moments.



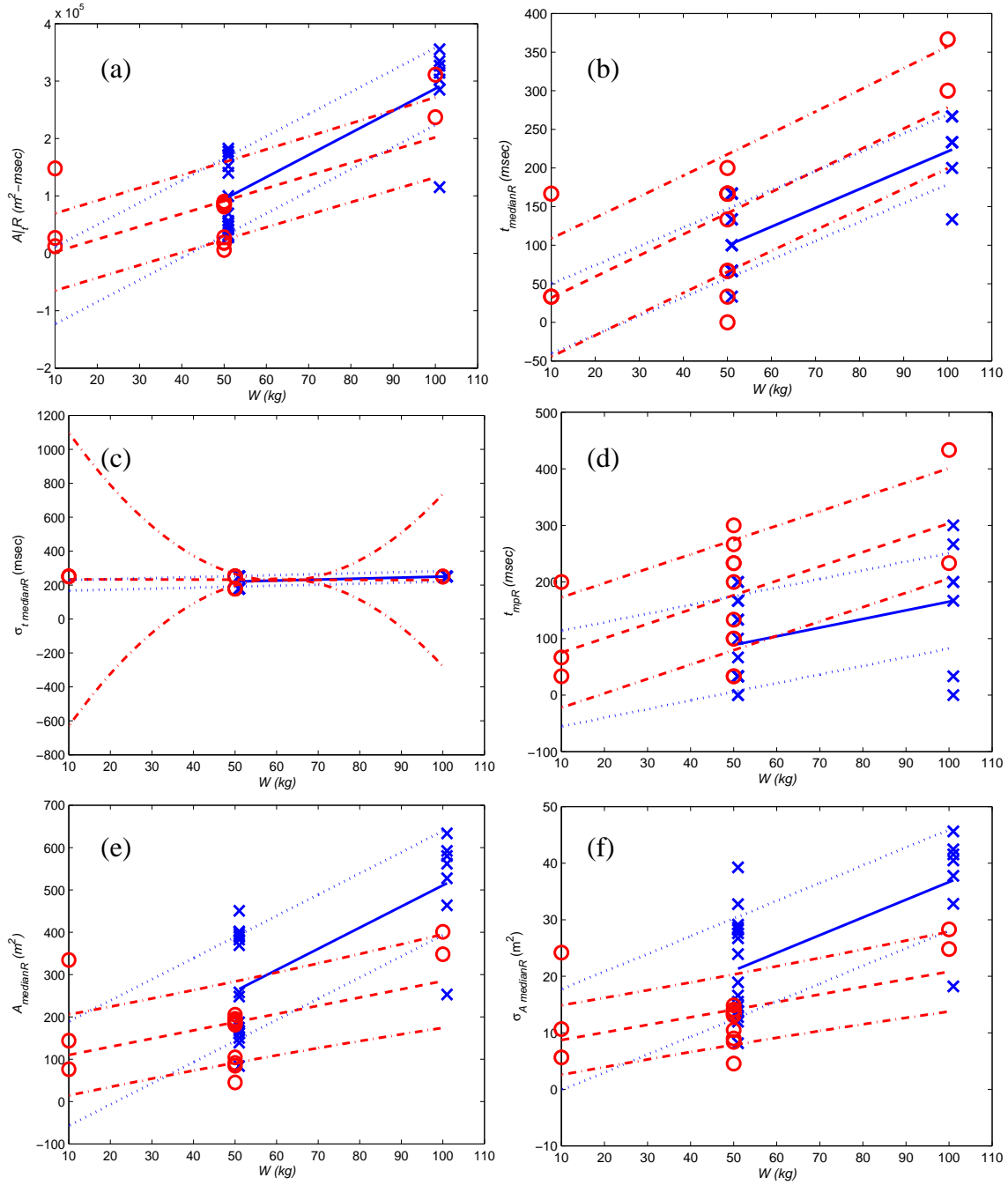


Figure 113. Potential scaling relationships exhibit fireball area features dependence upon weight (W). Figures (a) through (f) contain the red band features for \underline{A} , t_{median} , $\sigma_{t_{median}}$, t_{mp} , A_{median} , $\sigma_{A_{median}}$.

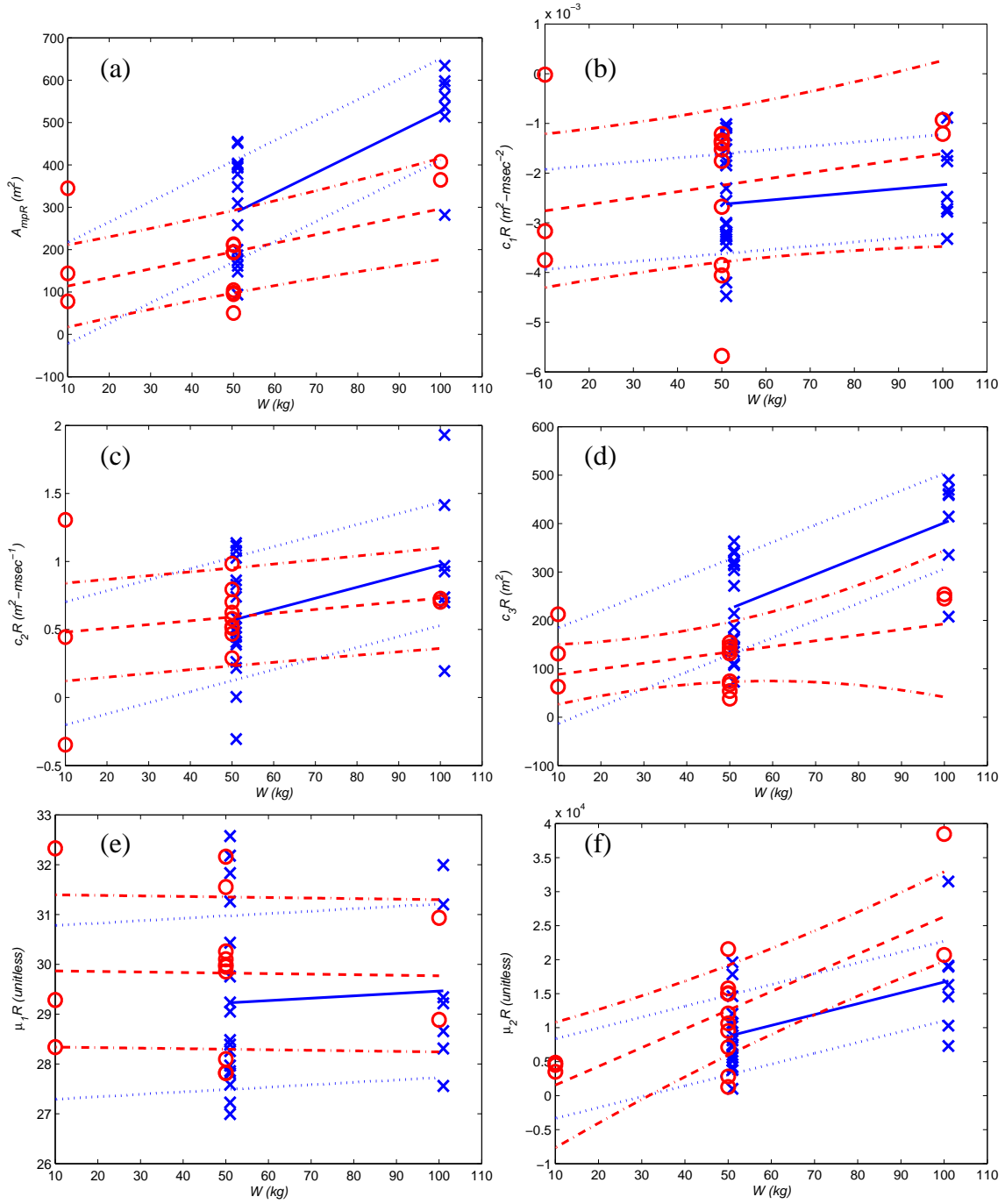


Figure 114. Potential scaling relationships exhibit fireball area features dependence upon weight (W). Figures (a) through (f) contain the red band features for A_{mp} , c_1 , c_2 , c_3 , μ_1 , and μ_2 .

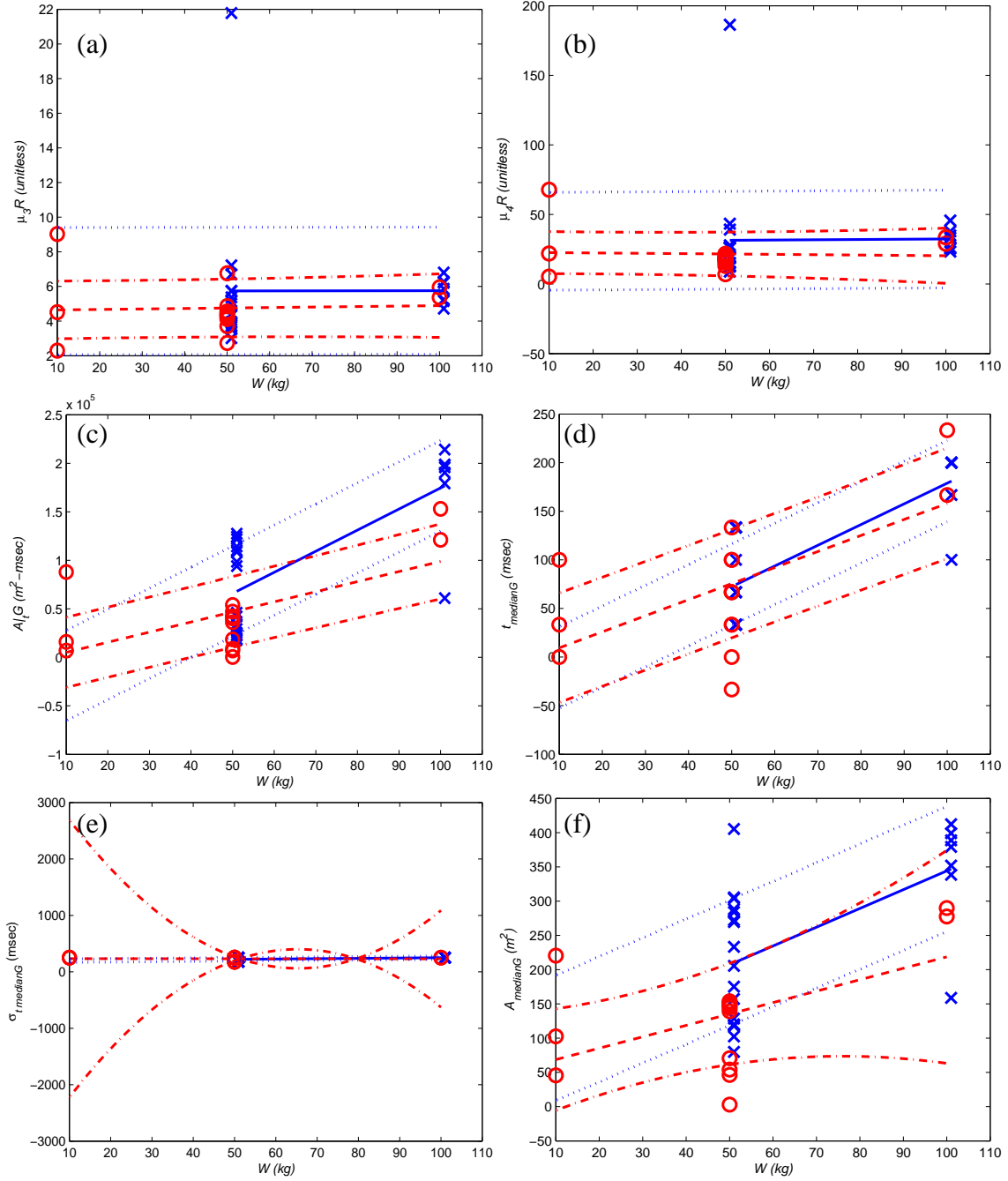


Figure 115. Potential scaling relationships exhibit fireball area features dependence upon weight (W). Figures (a) and (b) contain the red band features for the third and fourth moments, while Figures (c) through (f) contain the green band features for \underline{A} , t_{median} , $\sigma_{t_{median}}$, t_{mp} , and A_{median} .

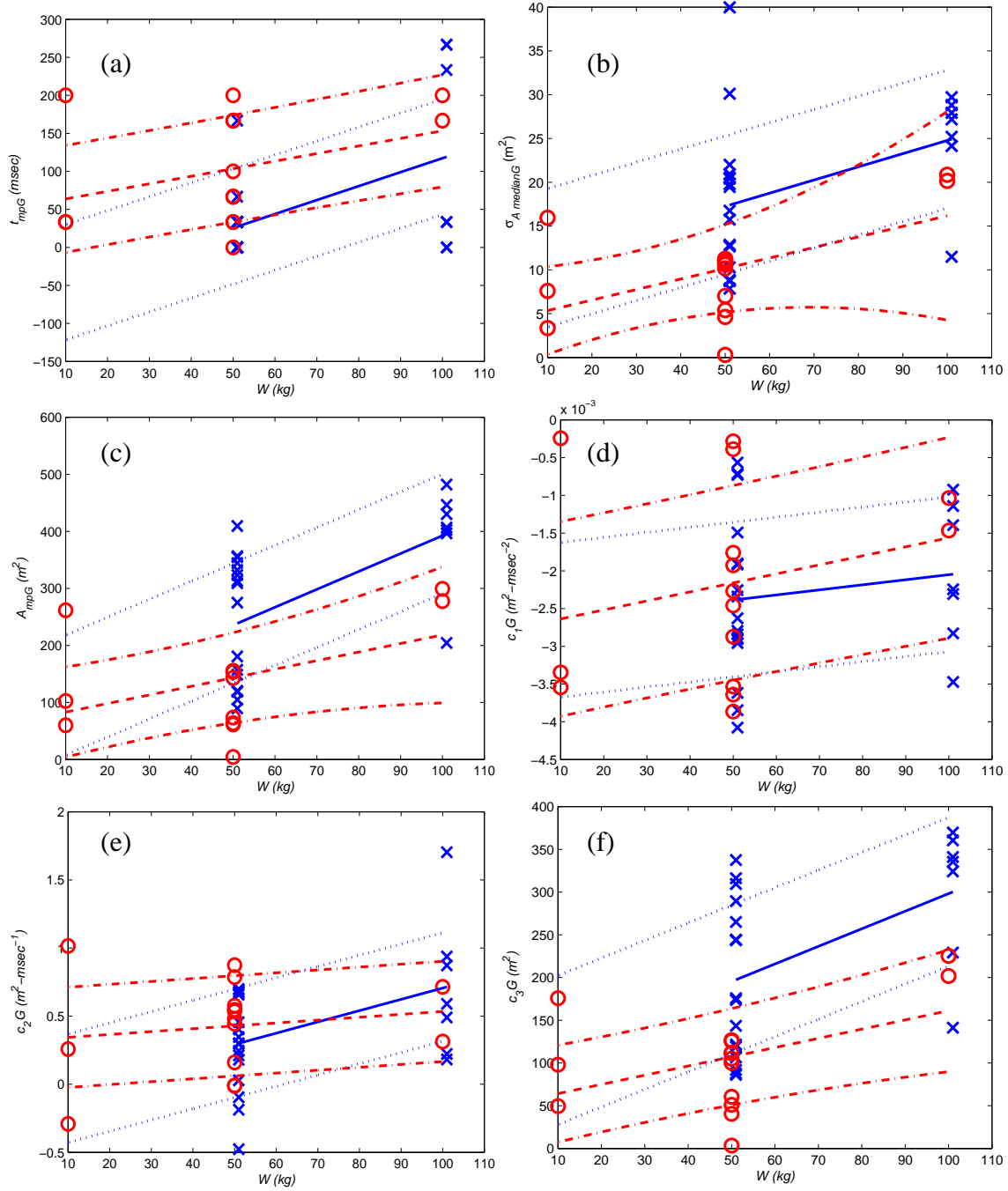


Figure 116. Potential scaling relationships exhibit fireball area features dependence upon weight (W). Figures (a) through (f) contain the green band features for t_{mp} , σ_{A_median} , A_{mp} , c_1 , c_2 , and c_3 .

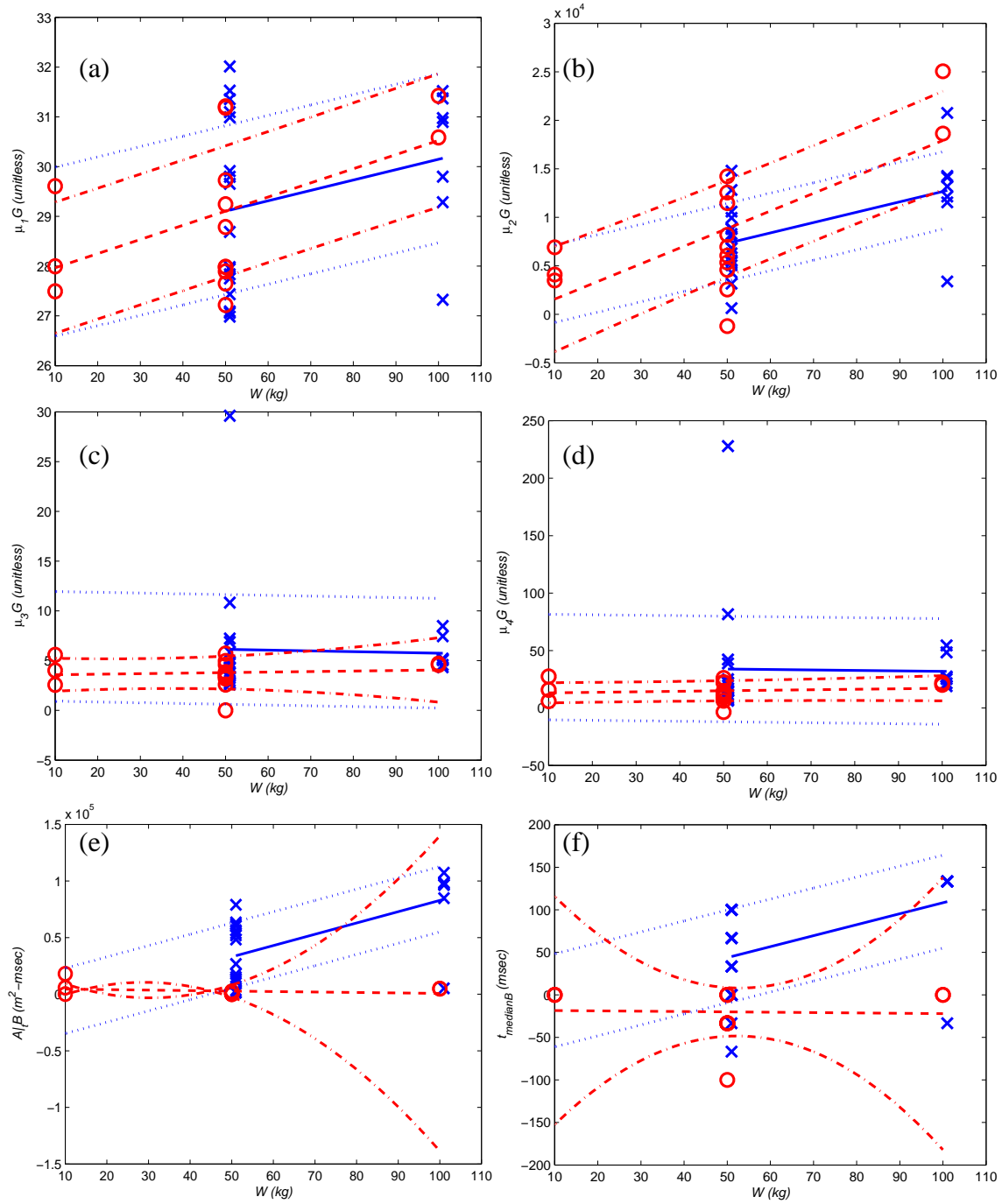


Figure 117. Potential scaling relationships exhibit fireball area features dependence upon weight (W). Figures (a) through (d) contain the green band features for the four moments, while Figures (e) and (f) contain the blue band features for A/B and t_{median} .

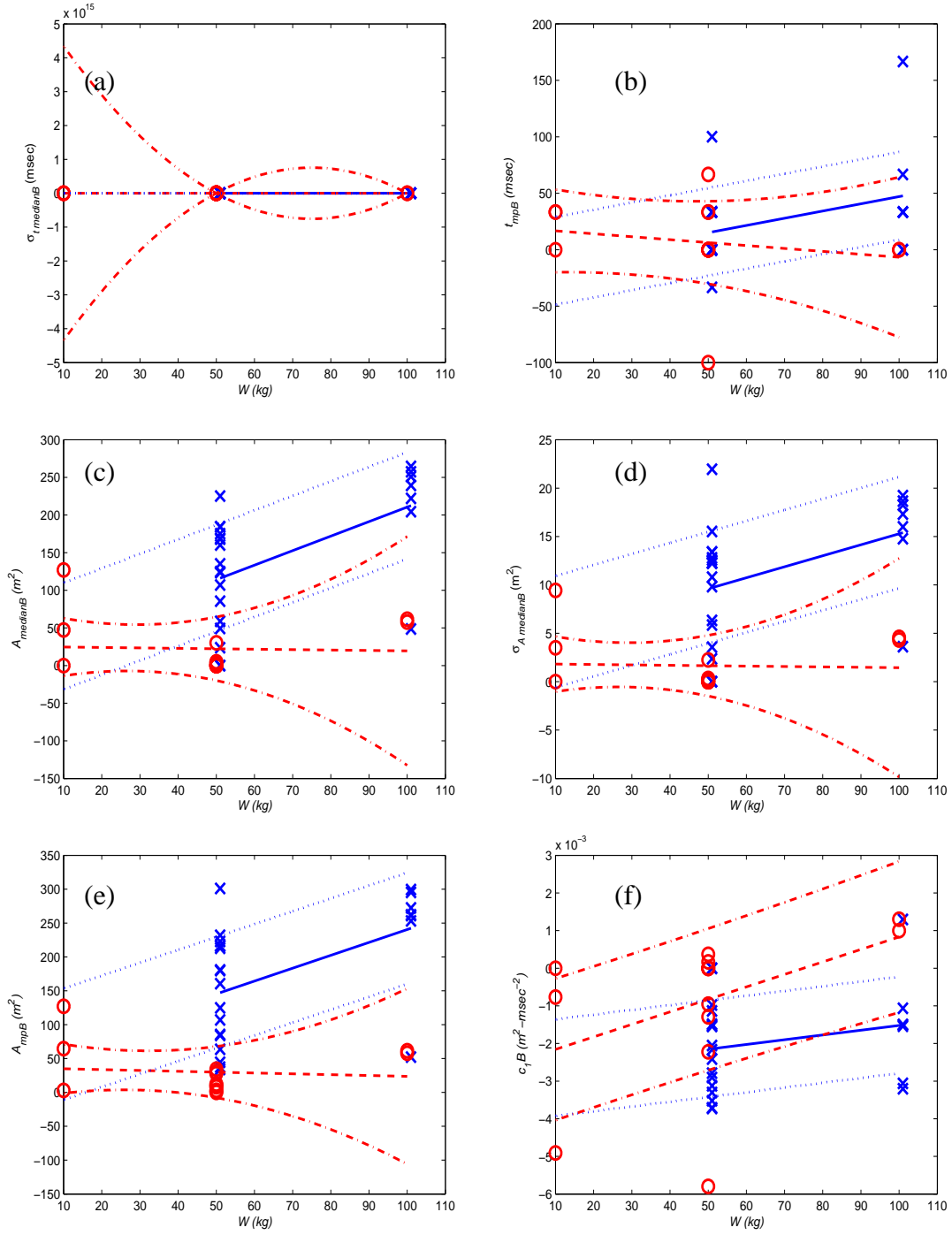


Figure 118. Potential scaling relationships exhibit fireball area features dependence upon weight (W). Figures (a) through (f) contain the blue band features for σ_{t_median} , t_{mp} , A_{median} , σ_{A_median} , A_{mp} , and c_1 .

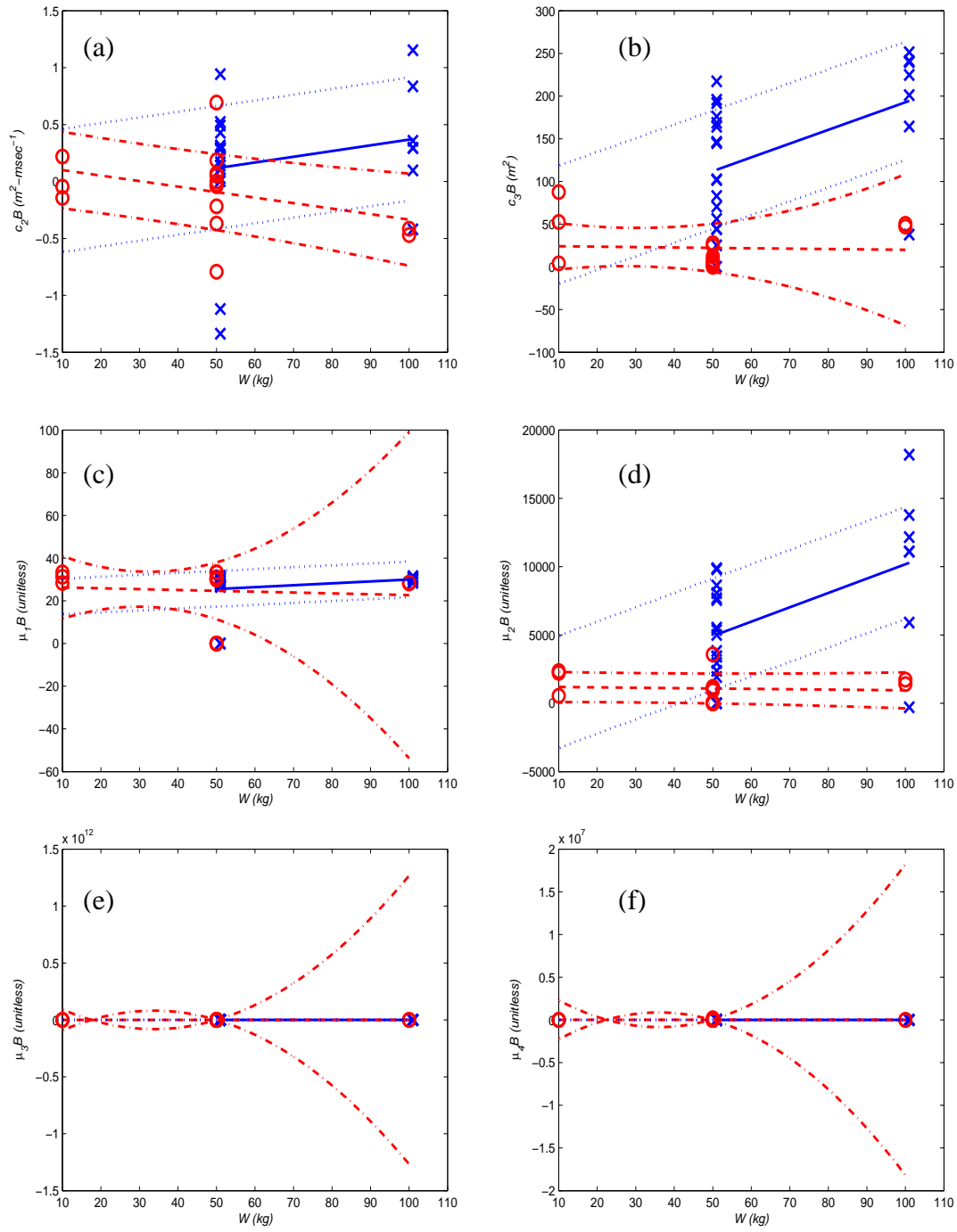


Figure 119. Potential scaling relationships exhibit fireball area features dependence upon weight (W). Figures (a) through (f) contain the blue band features for c_1 , c_2 , and the first four moments.

Appendix I: Scaling Laws, Spectral Data, Radiant

Each extracted feature derived from the spectra collected on the Radiant events is examined for weight and scaling relationships. The first figure presented in this appendix is an overall summary of all the features while each of the individual plots is given in the remaining figures. The data points marked as “x” are the static events and marked as “o” are dynamically dropped events. Each of the plots abscissa axis is labeled as 10, 50, and 100, which are actually numerical symbols for Type A Small, Type B Medium, and Type B Large, respectively. The least square fit lines have error bars which are described in Chapter IV, Section H; the errors associated with static events are dotted lines, while those associated with the dynamics events are dash-dotted lines. The following is a list of figures for this appendix:

- Figure 120. Each feature extracted from the fireball spectra is plotted here as a function of weight, showing potential scaling relationships.
- Figure 121. Potential scaling relationships exhibit fireball area features dependence upon weight (W). Figures (a) through (f) contain the spectral features for TH , TL , Γ , σTH , $\sigma T\Lambda$, and $\sigma \Gamma$.
- Figure 122. Potential scaling relationships exhibit fireball area features dependence upon weight (W). Figures (a) through (f) contain the spectral features for AA , $ASwitch$, Aka , AB , Akb , and AC .
- Figure 123. Potential scaling relationships exhibit fireball area features dependence upon weight (W). Figures (a) through (f) contain the spectral features for $At0$, $\Delta I\mu\pi/\tau$, tmp , $\Delta I0/\tau$, $\Delta I2/\tau$, and $\Delta I0.5/\tau$.

- Figure 124. Potential scaling relationships exhibit fireball area features dependence upon weight (W). Figures (a) through (c) contain the spectral features for $R2/0$, $R2/0.5$, and $Rmp/0$.

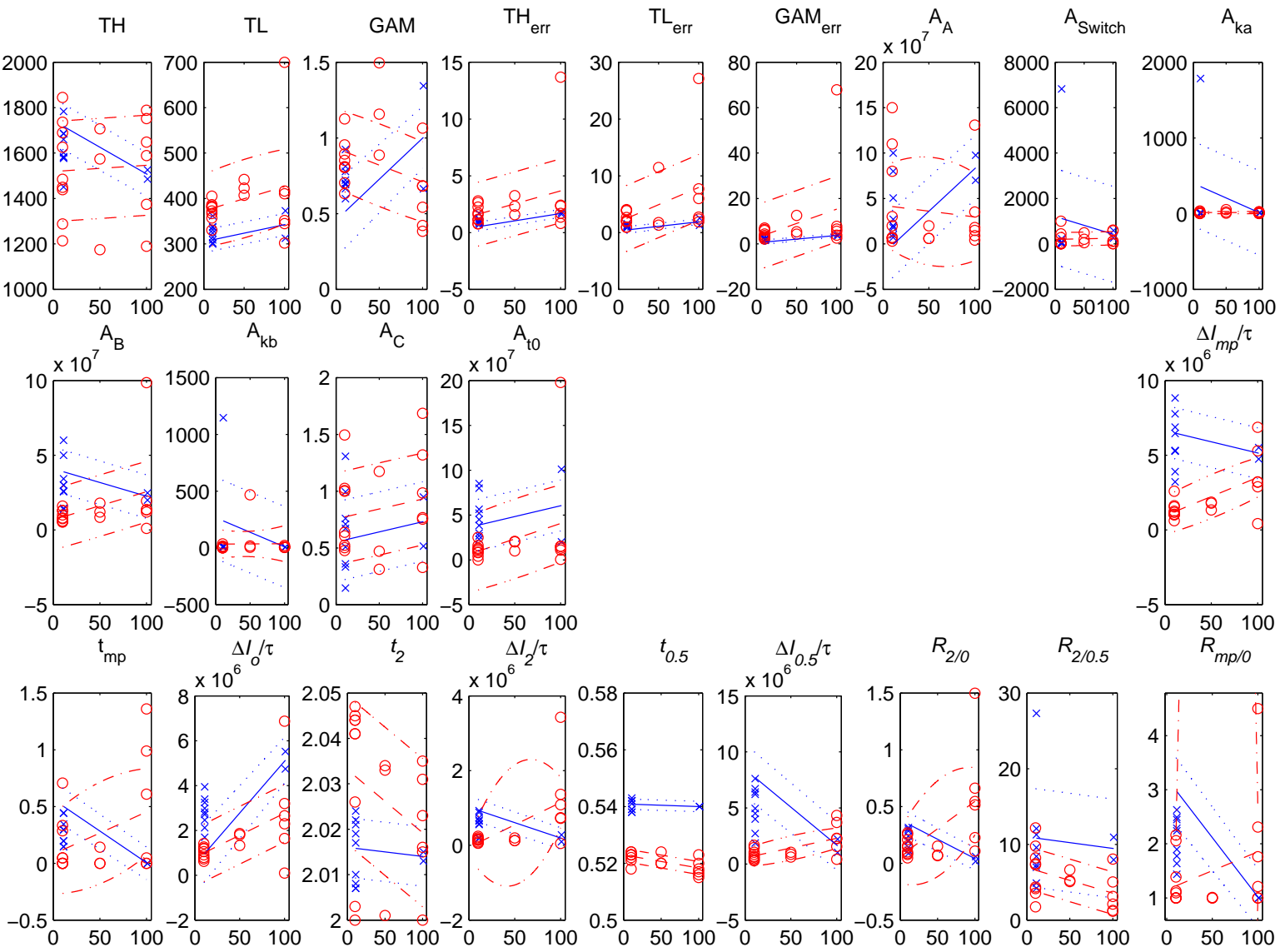


Figure 120. Each feature extracted from the fireball spectra is plotted here as a function of weight, showing potential scaling relationships.

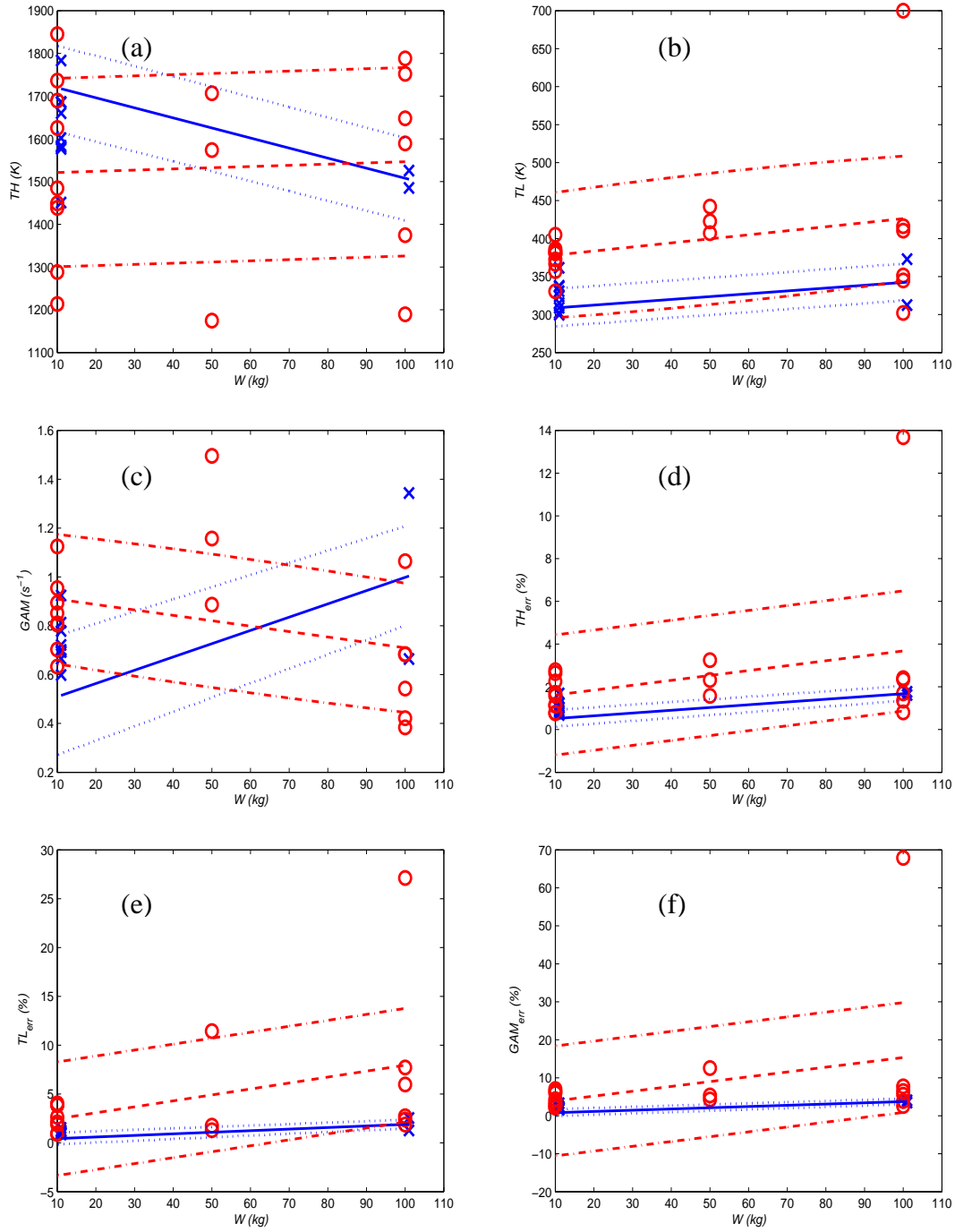


Figure 121. Potential scaling relationships exhibit fireball area features dependence upon weight (W). Figures (a) through (f) contain the spectral features for T_H , T_L , Γ , σ_{TH} , σ_{TL} , and σ_{Γ} .

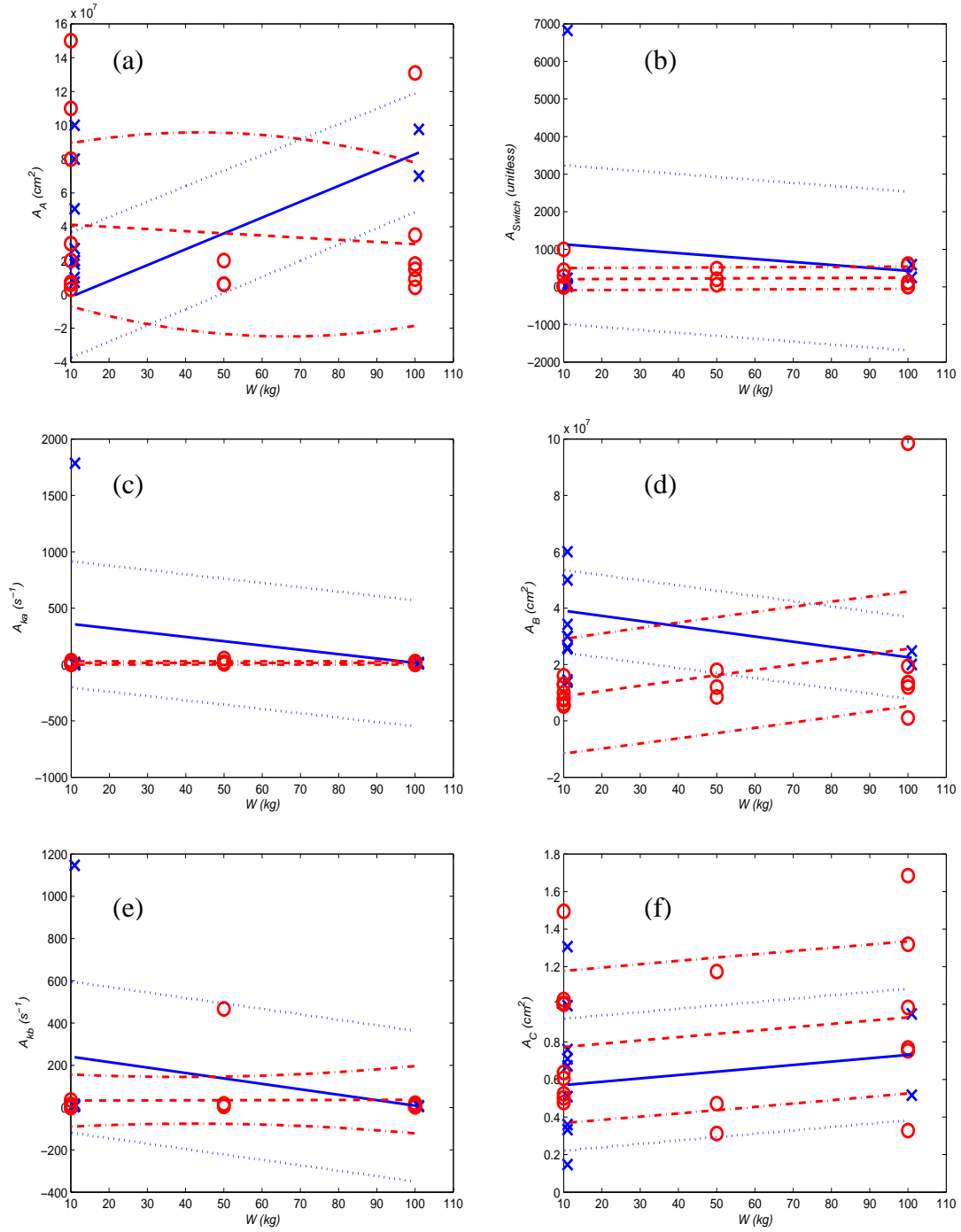


Figure 122. Potential scaling relationships exhibit fireball area features dependence upon weight (W). Figures (a) through (f) contain the spectral features for A_A , A_{Switch} , A_{ka} , A_B , A_{kb} , and A_C .

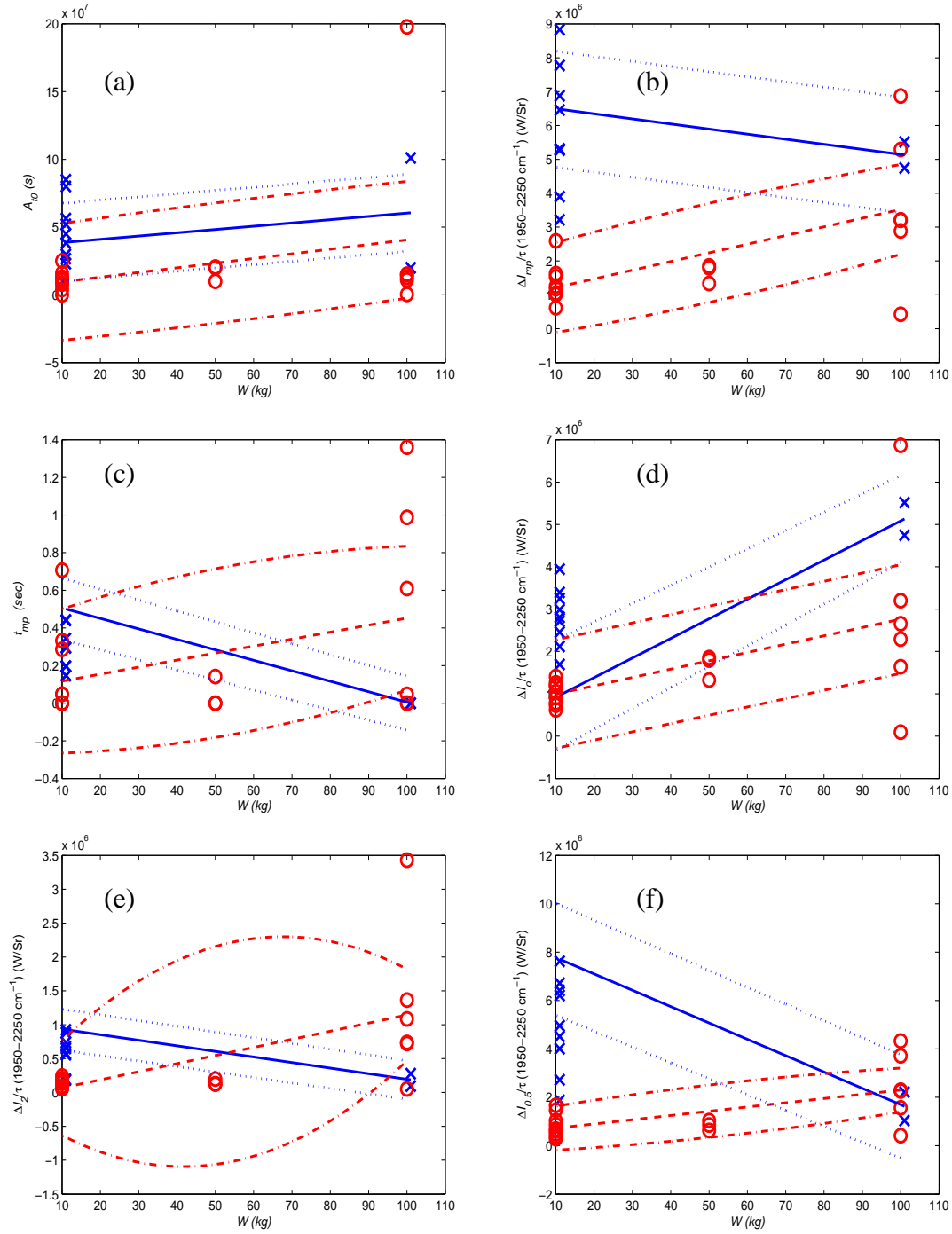


Figure 123. Potential scaling relationships exhibit fireball area features dependence upon weight (W). Figures (a) through (f) contain the spectral features for A_{t0} , $\Delta I_{mp}/\tau$, t_{mp} , $\Delta I_o/\tau$, $\Delta I_2/\tau$, and $\Delta I_{0.5}/\tau$.

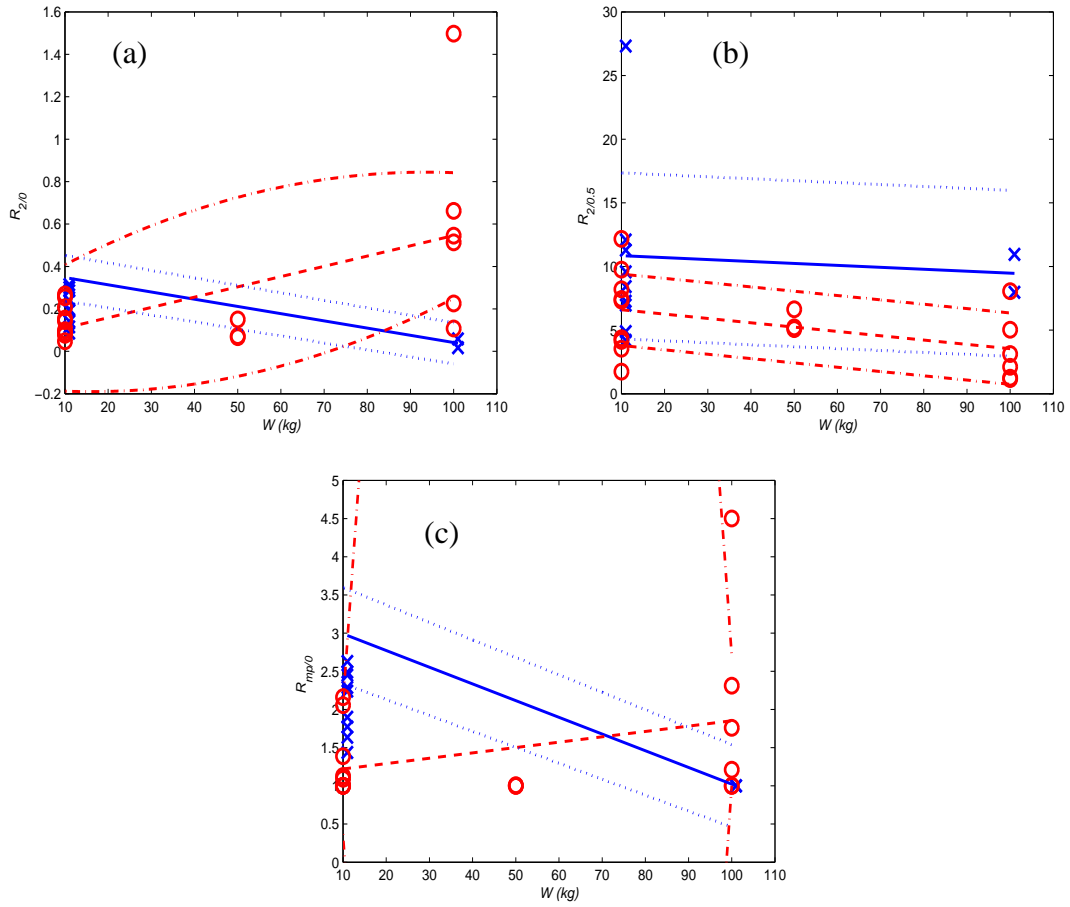


Figure 124. Potential scaling relationships exhibit fireball area features dependence upon weight (W). Figures (a) through (c) contain the spectral features for $R_{2/0}$, $R_{2/0.5}$, and $R_{mp/0}$.

Appendix J: Spectral Features from Radiant test series

One method to represent each recorded event spectra from the Radiant test series is by a Planckian multiplied by an appropriate atmospheric transmission function. The result generates area and temperature temporal profiles along with a residual between the fit and the data. Extracted feature values from these profiles and residual are listed in the following tables included in this appendix:

- Table 34. Temperature fit values to the Radiant data.
- Table 35. Area fit values from Radiant data.
- Table 36. Features derived from the residuals for the Radiant data. The residuals are the differences between the Planckian fit and the data. These residuals are integrated from 1950 to 2250 cm^{-1} .

Table 34. Temperature fit values to the Radiant data.

Event ID	Type	Angle	Test	T_H (K)	T_L (K)	Γ (s ⁻¹)	σ_{TH} (%)	σ_{TL} (%)	σ_T (%)
e214_03b	A (S)	155° Perpendicular	RB3A	1439	357	0.63	2.8	3.9	7.0
e214_04b	A (S)	155° Perpendicular	RB3A	1736	331	0.70	1.7	3.9	4.4
e214_05b	A (S)	155° Perpendicular	RB3A	1625	373	0.85	2.3	4.1	6.0
e214_06b	A (S)	155° Perpendicular	RB3A	1690	386	0.89	1.6	2.0	3.7
e214_07b	A (S)	155° Perpendicular	RB3A	1485	405	1.13	2.6	2.7	6.4
e215_22b	A (S)	335° Toward	RB3A	1845	384	0.81	1.1	2.1	2.8
e216_30b	A (S)	65° Away	RB3A	1449	367	0.81	1.2	1.9	3.2
e216_32b	A (S)	65° Away	RB3A	1214	381	0.81	0.8	1.0	2.2
e216_33b	A (S)	65° Away	RB3A	1288	381	0.95	0.8	0.9	2.1
e298_04b	A (S)	45° Tower	RB3B	1687	331	0.69	1.0	1.1	2.1
e298_05b	A (S)	45° Tower	RB3B	1783	338	0.70	1.0	1.0	2.0
e298_06b	A (S)	45° Tower	RB3B	1685	324	0.81	1.7	1.5	3.3
e298_07b	A (S)	45° Tower	RB3B	1660	337	0.69	0.9	1.2	2.0
e298_08b	A (S)	45° Tower	RB3B	1580	300	0.78	1.0	1.0	2.1
e298_10b	A (S)	45° Tower	RB3B	1584	302	0.72	1.0	1.0	2.0
e301_12b	A (S)	45° Tower	RB3B	1602	315	0.67	1.2	1.3	2.4
e301_18b	A (S)	45° Tower	RB3B	1577	361	0.92	0.7	0.9	1.6
e301_21b	A (S)	45° Tower	RB3B	1451	309	0.60	0.8	0.9	1.7
e214_10b	B (L)	155° Perpendicular	RB3A	1375	345	0.42	2.3	6.0	7.7
e214_13b	B (L)	155° Perpendicular	RB3A	1589	410	0.68	1.4	2.4	3.9
e215_18b	B (L)	335° Toward	RB3A	1648	700	0.68	13.7	27.1	67.9
e215_20b	B (L)	335° Toward	RB3A	1788	302	0.38	1.7	7.7	5.5
e215_21b	B (L)	335° Toward	RB3A	1752	351	0.54	0.8	2.7	2.6
e216_43b	B (L)	65° Away	RB3A	1190	416	1.06	2.4	1.9	6.5
e301_15b	B (L)	30° Elevation	RB3B	1485	313	0.66	1.8	2.5	4.0
e301_16b	B (L)	10° Elevation	RB3B	1526	373	1.34	1.6	1.3	3.5
e214_14b	B (M)	155° Perpendicular	RB3A	1707	423	0.89	3.2	11.4	12.6
e214_15b	B (M)	155° Perpendicular	RB3A	1574	442	1.50	2.3	1.8	5.4
e216_39b	B (M)	65° Away	RB3A	1175	407	1.16	1.6	1.3	4.3

Table 35. Area fit values from Radiant data.

Event ID	Type	A_A (cm ²)	A_{Switch} (unitless)	A_{k_a} (s ⁻¹)	A_B (cm ²)	A_{k_b} (s ⁻¹)	A_C (cm ² s ⁻¹)	A_{t_0} (s)
e214_03b	A (S)	8.0E+07	8	6.4	7513800	1.0	1.5	13008000
e214_04b	A (S)	1.1E+08	7	6.3	6000000	0.8	0.6	8500100
e214_05b	A (S)	6.0E+06	37	13.0	5300000	15.6	0.6	16000000
e214_06b	A (S)	7.0E+06	1000	2.8	5500000	0.6	0.5	4000000
e214_07b	A (S)	7.0E+06	445	34.1	7958100	8.8	1.0	0
e215_22b	A (S)	3.0E+06	281	25.8	10000000	3.5	0.5	8000100
e216_30b	A (S)	1.5E+08	12	7.6	12892000	10.3	1.0	10541000
e216_32b	A (S)	3.0E+07	12	6.4	16000000	36.0	0.5	12000000
e216_33b	A (S)	2.0E+07	0	1.6	13000000	9.6	1.0	25000000
e298_04b	A (S)	2.0E+07	85	2.1	26000000	7.4	0.5	45000000
e298_05b	A (S)	5.1E+07	21	1.8	14540000	1146.4	0.4	29778000
e298_06b	A (S)	1.8E+07	39	2.3	34253000	6.5	0.1	38222000
e298_07b	A (S)	2.7E+07	42	1.4	30000000	5.9	0.7	52000000
e298_08b	A (S)	2.0E+07	12	2.9	50000000	10.5	0.8	80000000
e298_10b	A (S)	8.0E+07	16	17.9	60000000	5.7	1.0	85000000
e301_12b	A (S)	1.0E+07	228	7.6	30000000	7.6	0.3	23000000
e301_18b	A (S)	7.1E+06	34	2.0	13782000	16.9	0.7	26736000
e301_21b	A (S)	1.0E+08	6823	1785.3	25578000	13.6	1.3	56353000
e214_10b	B (L)	3.5E+07	581	25.3	19364000	9.8	1.3	15204000
e214_13b	B (L)	1.8E+07	113	3.1	12000000	5.2	0.8	13000000
e215_18b	B (L)	4.2E+06	9	4.3	1034300	5.4	0.3	382070
e215_20b	B (L)	1.5E+07	9	0.7	13475000	21.1	1.7	10962000
e215_21b	B (L)	9.1E+06	120	11.3	13543000	4.3	1.0	15000000
e216_43b	B (L)	1.3E+08	608	22.5	98547000	6.4	0.8	197780000
e301_15b	B (L)	7.0E+07	253	5.3	20000000	5.3	0.9	20000000
e301_16b	B (L)	9.8E+07	590	16.6	24755000	8.7	0.5	101070000
e214_14b	B (M)	6.0E+06	56	21.0	8500500	17.8	1.2	10000000
e214_15b	B (M)	6.0E+06	203	5.1	12000000	5.8	0.3	20000000
e216_39b	B (M)	2.0E+07	486	53.3	17968000	467.0	0.5	20576000

Table 36. Features derived from the residuals for the Radiant data. The residuals are the differences between the Plankian fit and the data. These residuals are integrated from 1950 to 2250 cm^{-1} .

Event ID	Type	CO I_{mp} (W/Sr)	CO t_{mp} (sec)	CO I_o (W/Sr)	CO t_2 (sec)	CO I_2 (W/Sr)	CO $t_{0.5}$ (sec)	CO $I_{0.5}$ (W/Sr)	CO $R_{12/10}$	CO $R_{2/0.5}$	CO $R_{mp/0}$
e214_03b	A (S)	6.2E+05	0.000	6.2E+05	2.041	1.7E+05	0.522	2.9E+05	0.27	1.74	1.00
e214_04b	A (S)	1.0E+06	0.048	9.1E+05	2.045	1.4E+05	0.523	6.1E+05	0.15	4.36	1.13
e214_05b	A (S)	1.2E+06	0.000	1.2E+06	2.044	2.4E+05	0.523	8.7E+05	0.21	3.54	1.00
e214_06b	A (S)	1.3E+06	0.000	1.3E+06	2.044	6.0E+04	0.523	4.9E+05	0.05	8.21	1.00
e214_07b	A (S)	1.1E+06	0.000	1.1E+06	2.041	9.1E+04	0.521	3.8E+05	0.09	4.16	1.00
e215_22b	A (S)	1.6E+06	0.707	7.9E+05	2.026	2.0E+05	0.518	1.5E+06	0.25	7.31	2.06
e216_30b	A (S)	2.6E+06	0.333	1.2E+06	2.047	1.7E+05	0.523	1.7E+06	0.14	9.76	2.16
e216_32b	A (S)	1.5E+06	0.048	1.4E+06	2.000	1.4E+05	0.524	1.0E+06	0.10	7.44	1.09
e216_33b	A (S)	1.0E+06	0.286	7.3E+05	2.003	5.6E+04	0.524	6.9E+05	0.08	12.17	1.39
e298_04b	A (S)	5.3E+06	0.196	3.0E+06	2.007	5.8E+05	0.538	4.0E+06	0.19	6.97	1.77
e298_05b	A (S)	6.5E+06	0.440	2.5E+06	2.007	7.4E+05	0.538	6.2E+06	0.30	8.42	2.63
e298_06b	A (S)	5.3E+06	0.344	2.1E+06	2.017	1.8E+05	0.541	5.0E+06	0.09	27.32	2.49
e298_07b	A (S)	6.9E+06	0.296	2.8E+06	2.022	8.8E+05	0.543	6.4E+06	0.31	7.27	2.45
e298_08b	A (S)	8.8E+06	0.197	3.9E+06	2.024	5.6E+05	0.542	6.7E+06	0.14	12.07	2.24
e298_10b	A (S)	7.8E+06	0.443	3.4E+06	2.019	6.8E+05	0.542	7.6E+06	0.20	11.28	2.29
e301_12b	A (S)	5.3E+06	0.294	3.2E+06	2.008	9.3E+05	0.539	4.5E+06	0.29	4.88	1.64
e301_18b	A (S)	3.2E+06	0.147	1.7E+06	2.010	2.0E+05	0.539	1.9E+06	0.12	9.58	1.90
e301_21b	A (S)	3.9E+06	0.147	2.7E+06	2.021	6.5E+05	0.542	2.7E+06	0.24	4.19	1.44
e214_10b	B (L)	3.2E+06	0.047	2.7E+06	2.035	1.4E+06	0.520	1.6E+06	0.51	1.15	1.21
e214_13b	B (L)	3.2E+06	0.000	3.2E+06	2.031	7.2E+05	0.518	2.3E+06	0.23	3.13	1.00
e215_18b	B (L)	4.3E+05	0.609	9.5E+04	2.015	5.2E+04	0.515	4.2E+05	0.55	8.05	4.50
e215_20b	B (L)	5.3E+06	1.360	2.3E+06	2.016	3.4E+06	0.516	4.3E+06	1.50	1.26	2.31
e215_21b	B (L)	2.9E+06	0.988	1.6E+06	2.023	1.1E+06	0.517	2.3E+06	0.66	2.11	1.76
e216_43b	B (L)	6.9E+06	0.000	6.9E+06	2.000	7.4E+05	0.523	3.7E+06	0.11	5.02	1.00
e301_15b	B (L)	4.7E+06	0.000	4.7E+06	2.015	2.8E+05	0.540	2.2E+06	0.06	7.97	1.00
e301_16b	B (L)	5.5E+06	0.000	5.5E+06	2.013	9.5E+04	0.540	1.0E+06	0.02	10.95	1.00
e214_14b	B (M)	1.3E+06	0.142	1.3E+06	2.034	2.0E+05	0.520	1.0E+06	0.15	5.21	1.01
e214_15b	B (M)	1.8E+06	0.000	1.8E+06	2.033	1.3E+05	0.520	8.6E+05	0.07	6.63	1.00
e216_39b	B (M)	1.9E+06	0.000	1.9E+06	2.001	1.2E+05	0.524	6.3E+05	0.07	5.07	1.00

Appendix K:

Comparison plots of MR154 and MR354 InSb spectrometer data

with radiometers for Brilliant Flash II events

One method of comparing spectrometer and radiometer instruments is to integrate and scale the spectrometer data for each radiometer spectral band (see Table 8 in Chapter III. The scaling factor and the temporal profile provide a quantitative comparison. This appendix contains the scaling factors for each event followed by the temporal profiles for each individual event.

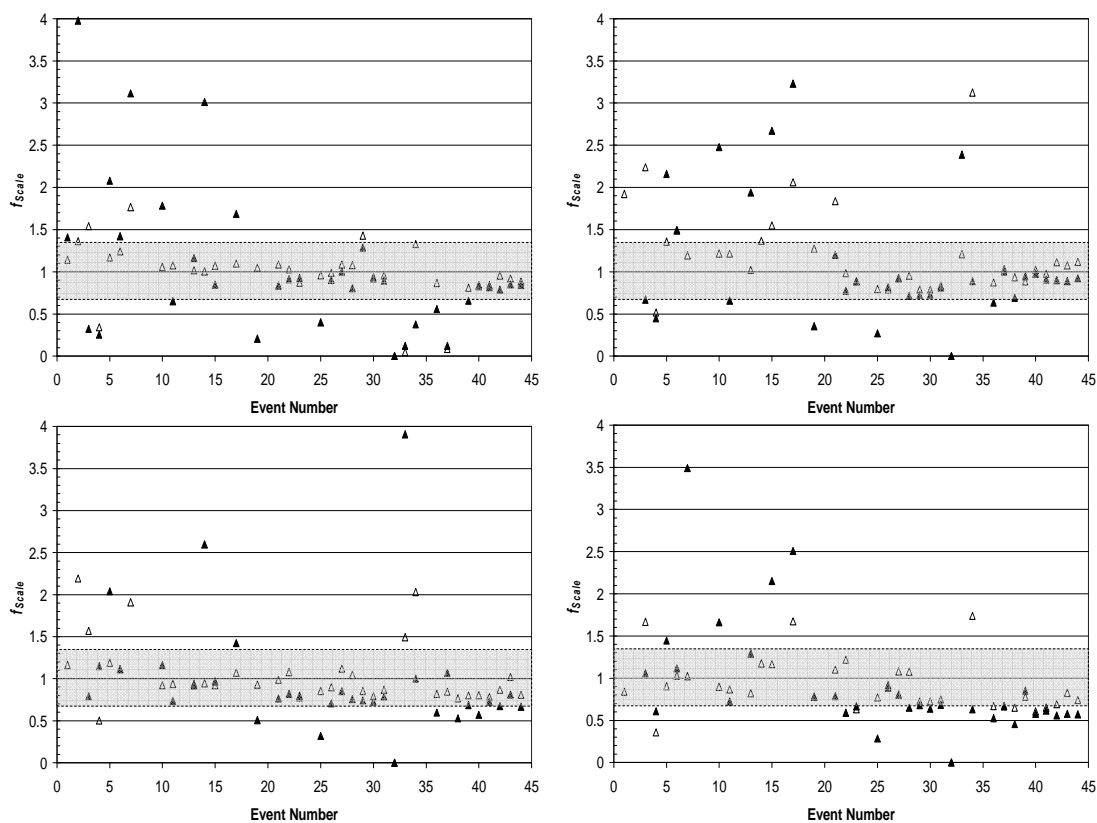


Figure 125. Integrating the spectra over a specific radiometer spectral band and scaling it such that the peak value matches the peak radiometer value provides a simple instrument comparison. These figures contain the results of scaling both the MR154 data (\blacktriangle) and MR354 data (\triangle) and also show the 33% accuracy window for each spectral band (a) band I, (b) band II, (c) band IV, and (d) band V.

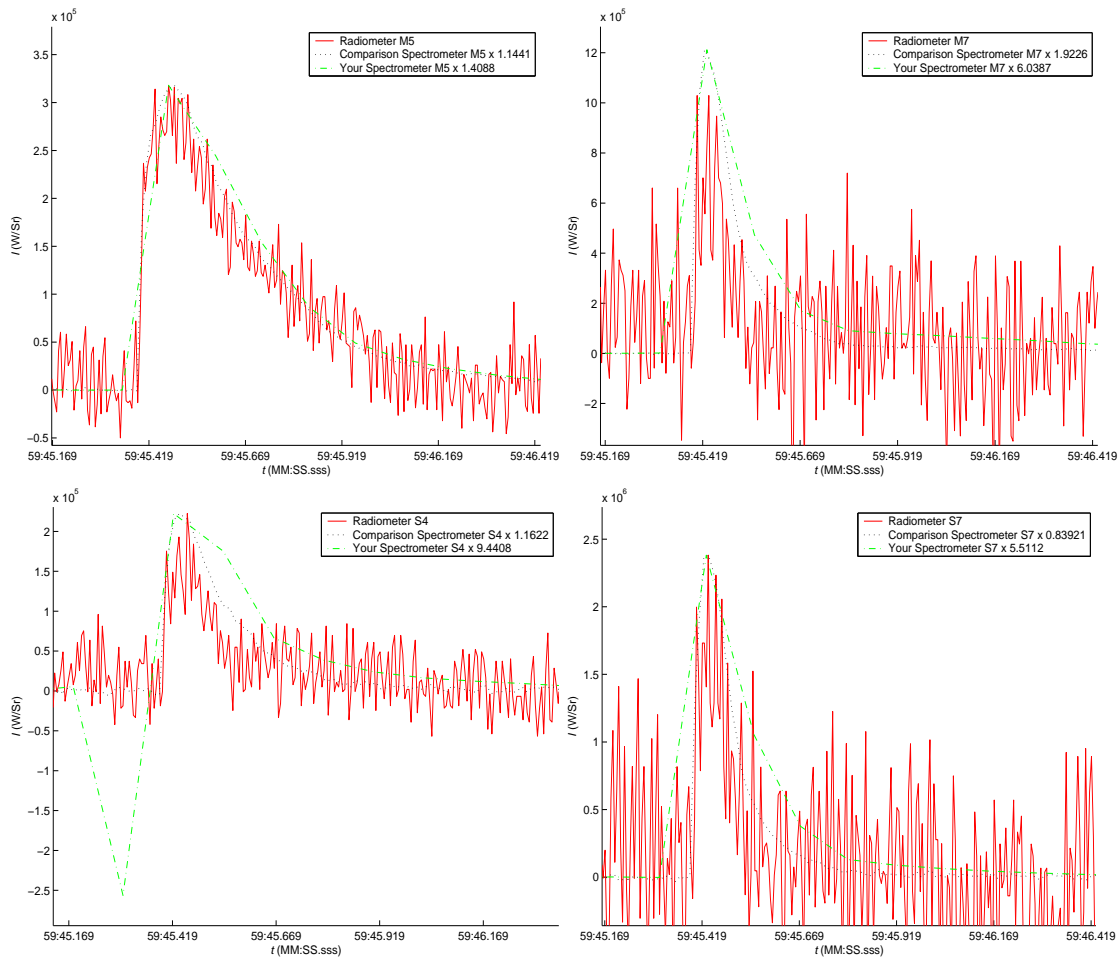


Figure 126. Band comparison for event 1. “Comparison Spectrometer” is from the MR354 FTIR and “Your Spectrometer” is from the MR154 FTIR.

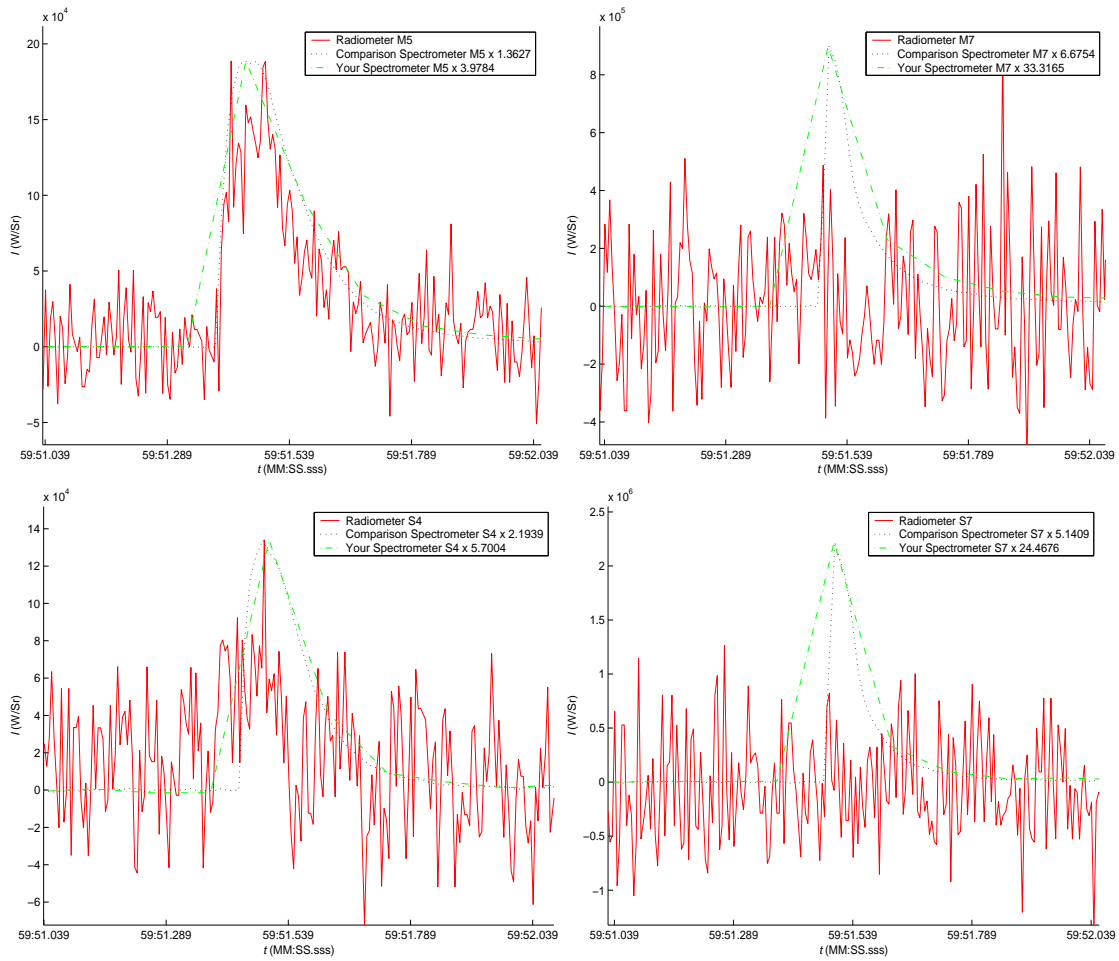


Figure 127. Band comparison for event 2. “Comparison Spectrometer” is from the MR354 FTIR and “Your Spectrometer” is from the MR154 FTIR.

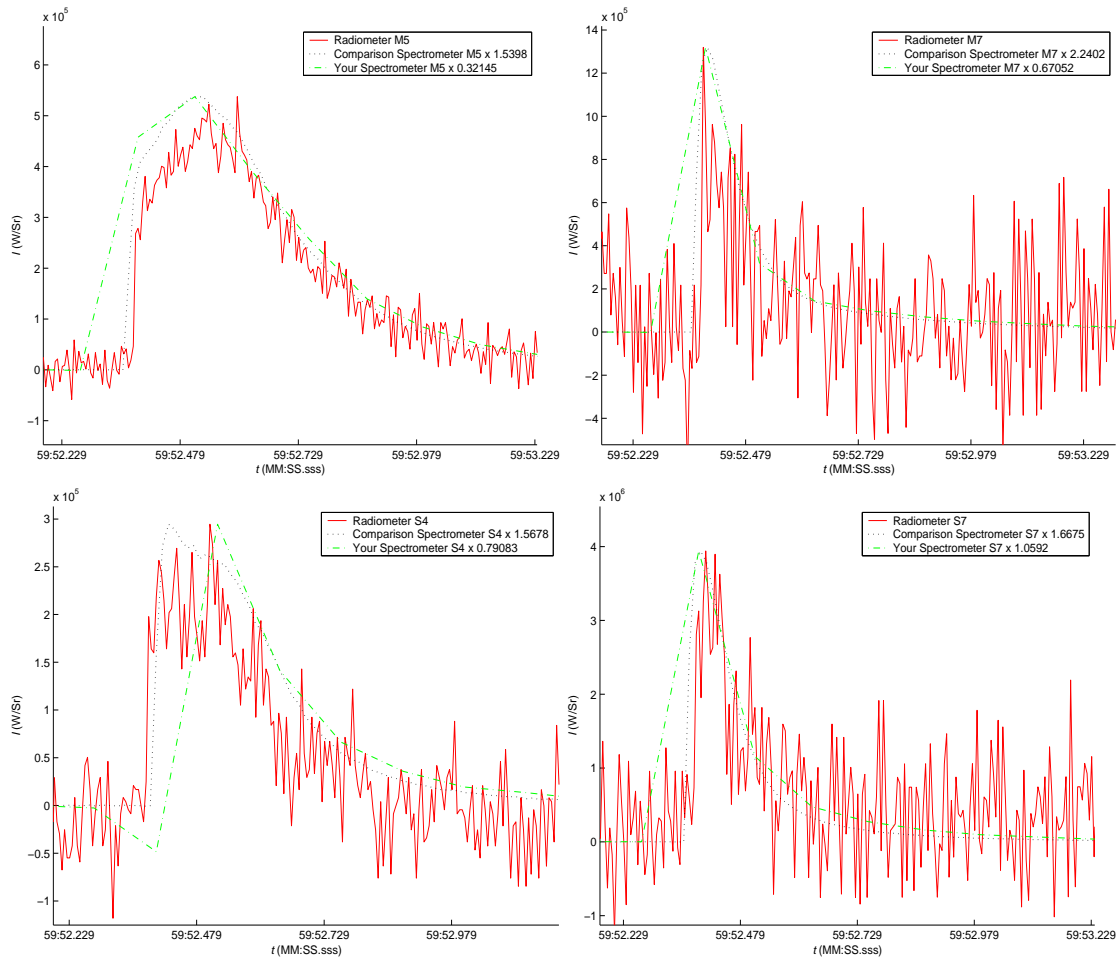


Figure 128. Band comparison for event 3. “Comparison Spectrometer” is from the MR354 FTIR and “Your Spectrometer” is from the MR154 FTIR.

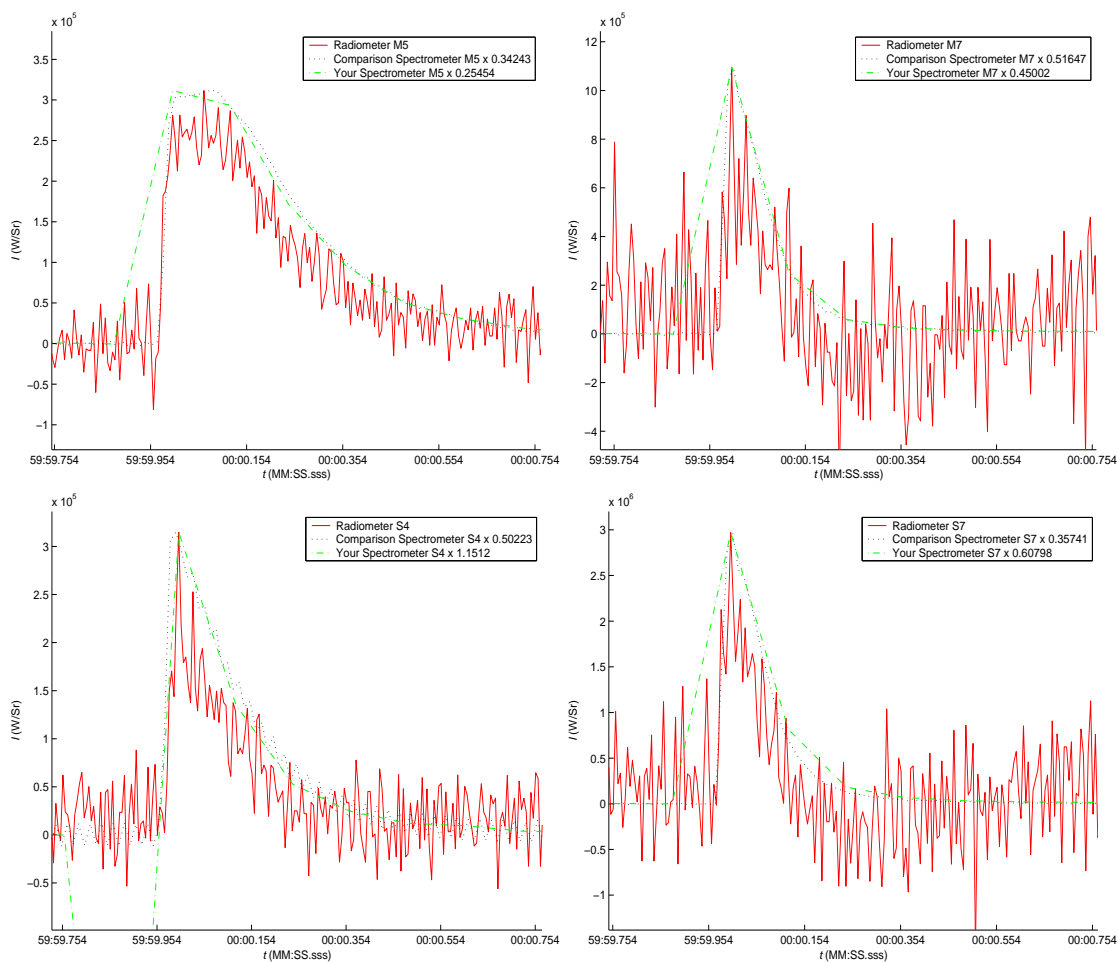


Figure 129. Band comparison for event 4. “Comparison Spectrometer” is from the MR354 FTIR and “Your Spectrometer” is from the MR154 FTIR.

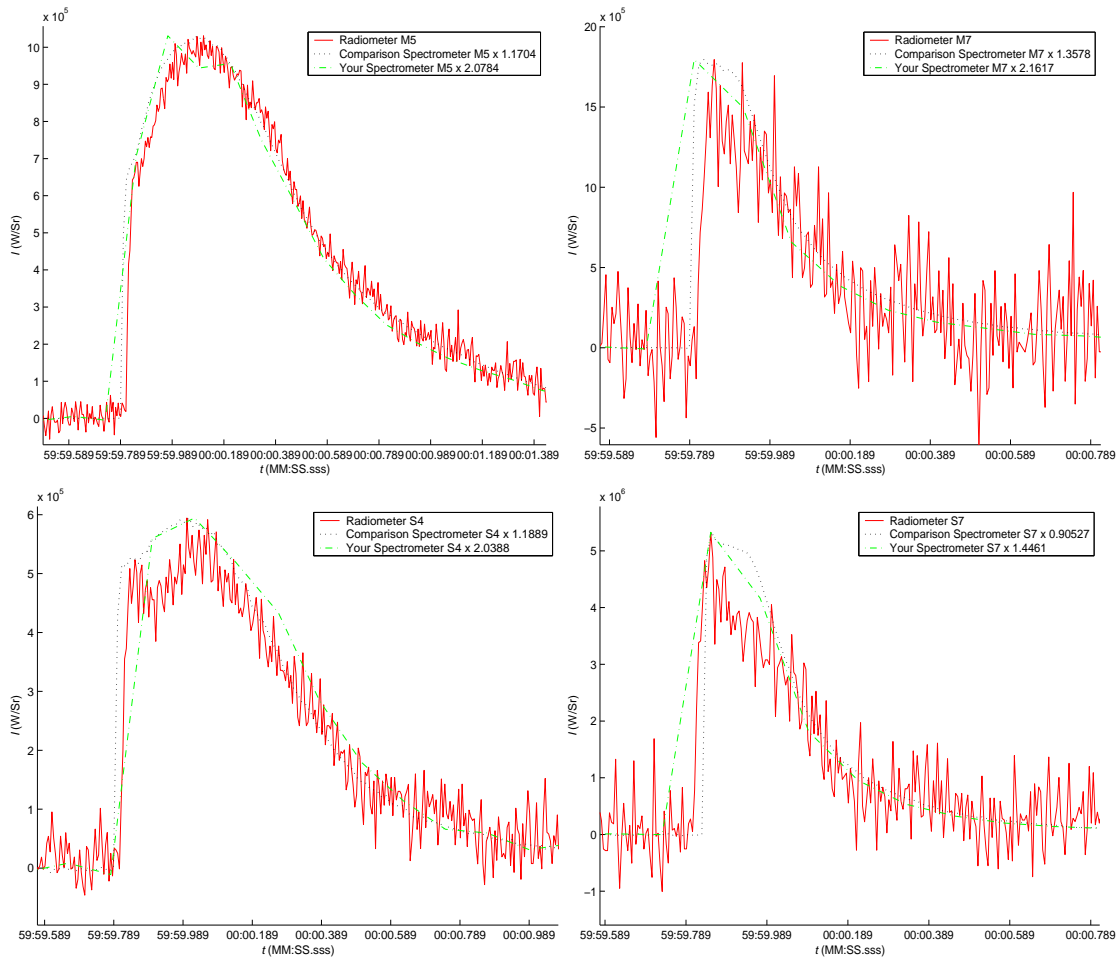


Figure 130. Band comparison for event 5. “Comparison Spectrometer” is from the MR354 FTIR and “Your Spectrometer” is from the MR154 FTIR.

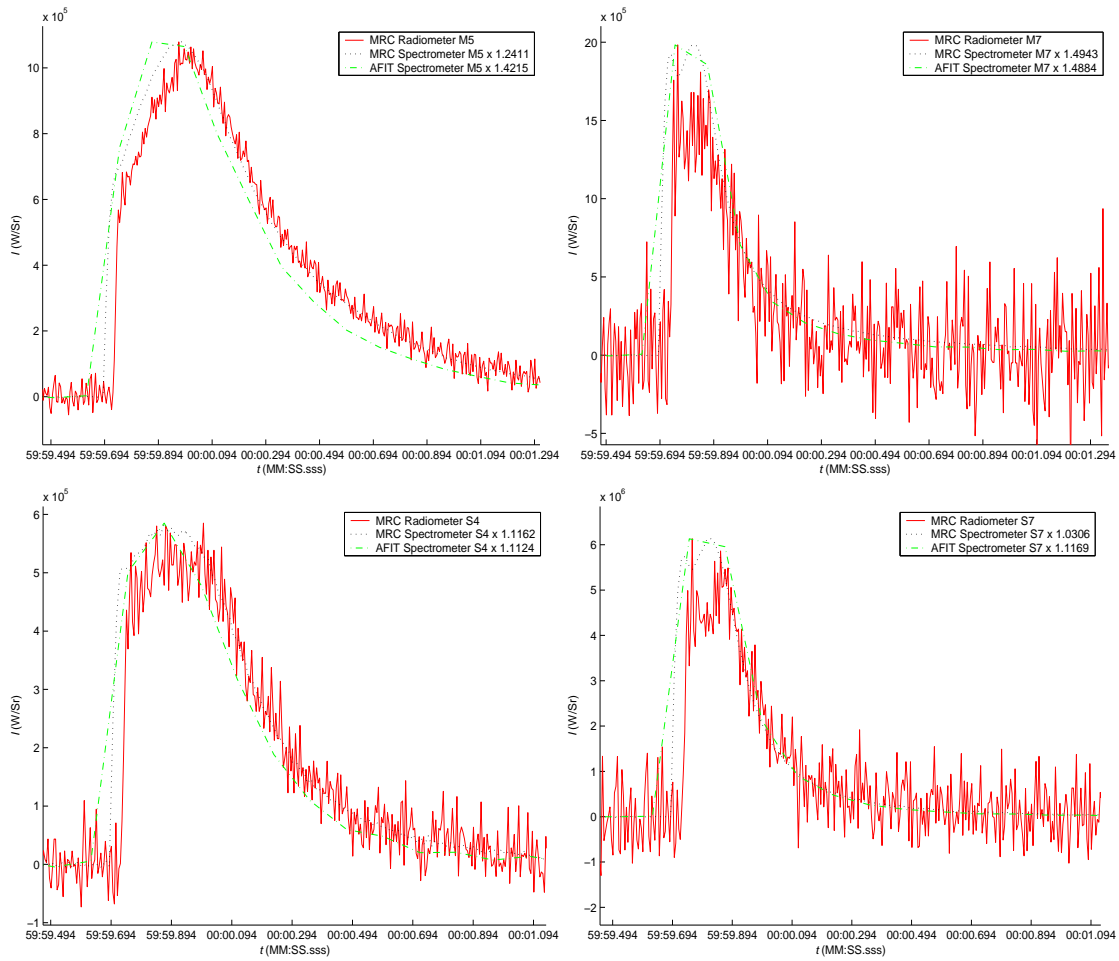


Figure 131. Band comparison for event 6. “Comparison Spectrometer” is from the MR354 FTIR and “Your Spectrometer” is from the MR154 FTIR.

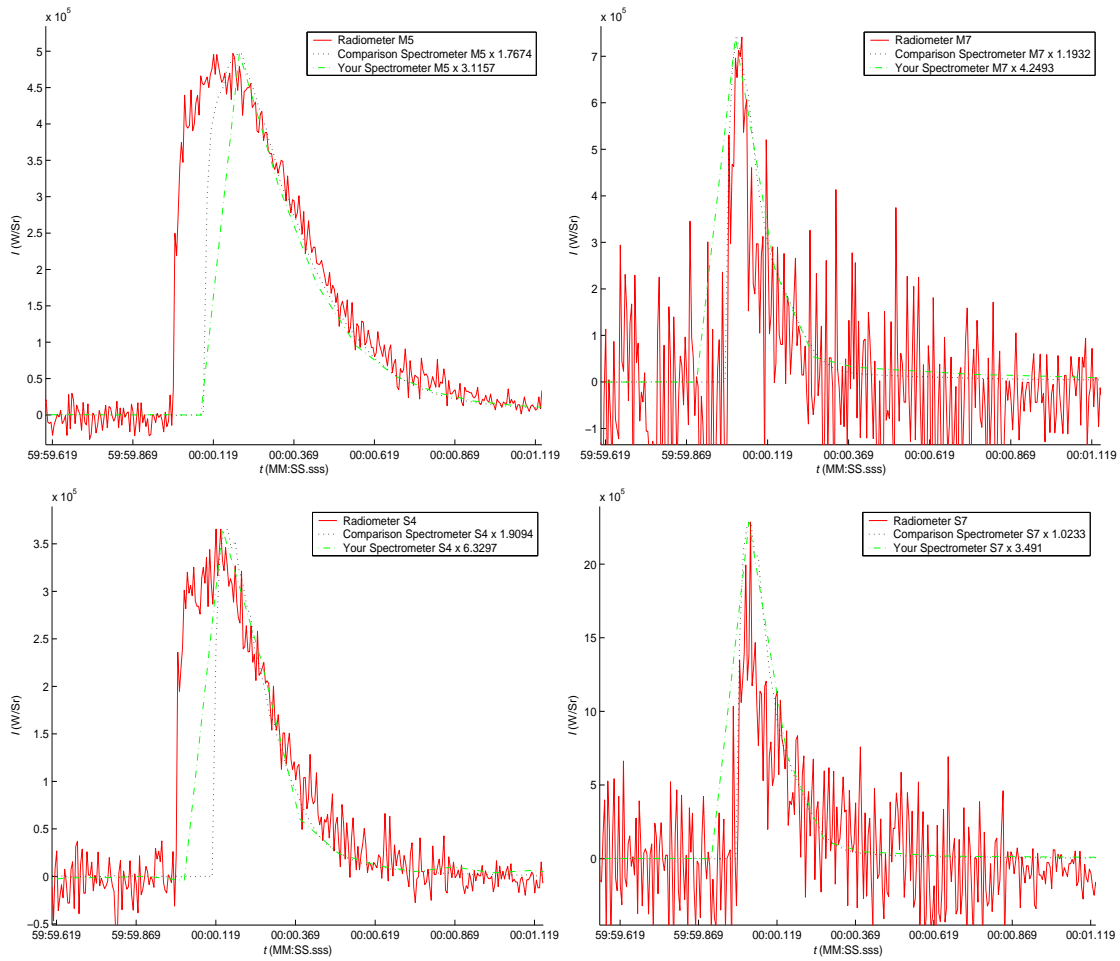


Figure 132. Band comparison for event 7. “Comparison Spectrometer” is from the MR354 FTIR and “Your Spectrometer” is from the MR154 FTIR.

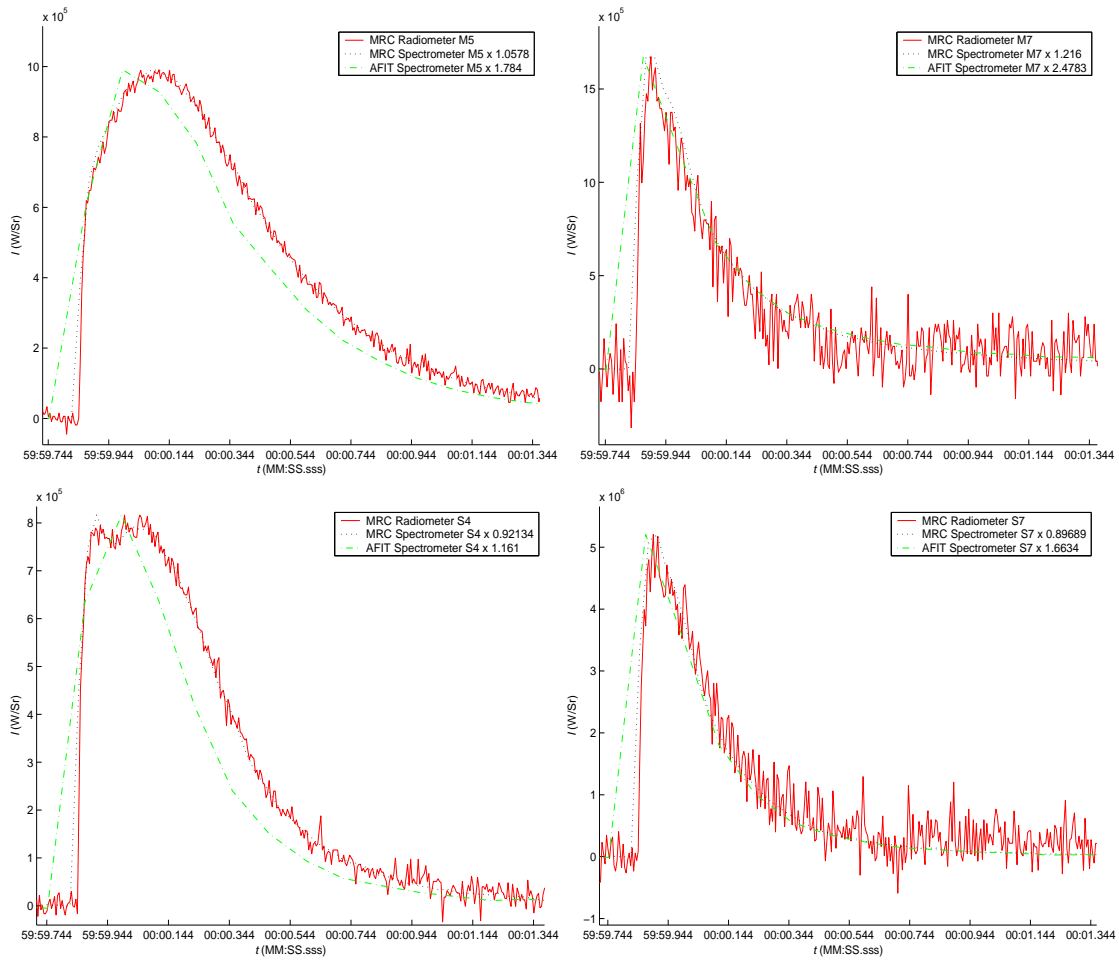


Figure 133. Band comparison for event 10. “Comparison Spectrometer” is from the MR354 FTIR and “Your Spectrometer” is from the MR154 FTIR.

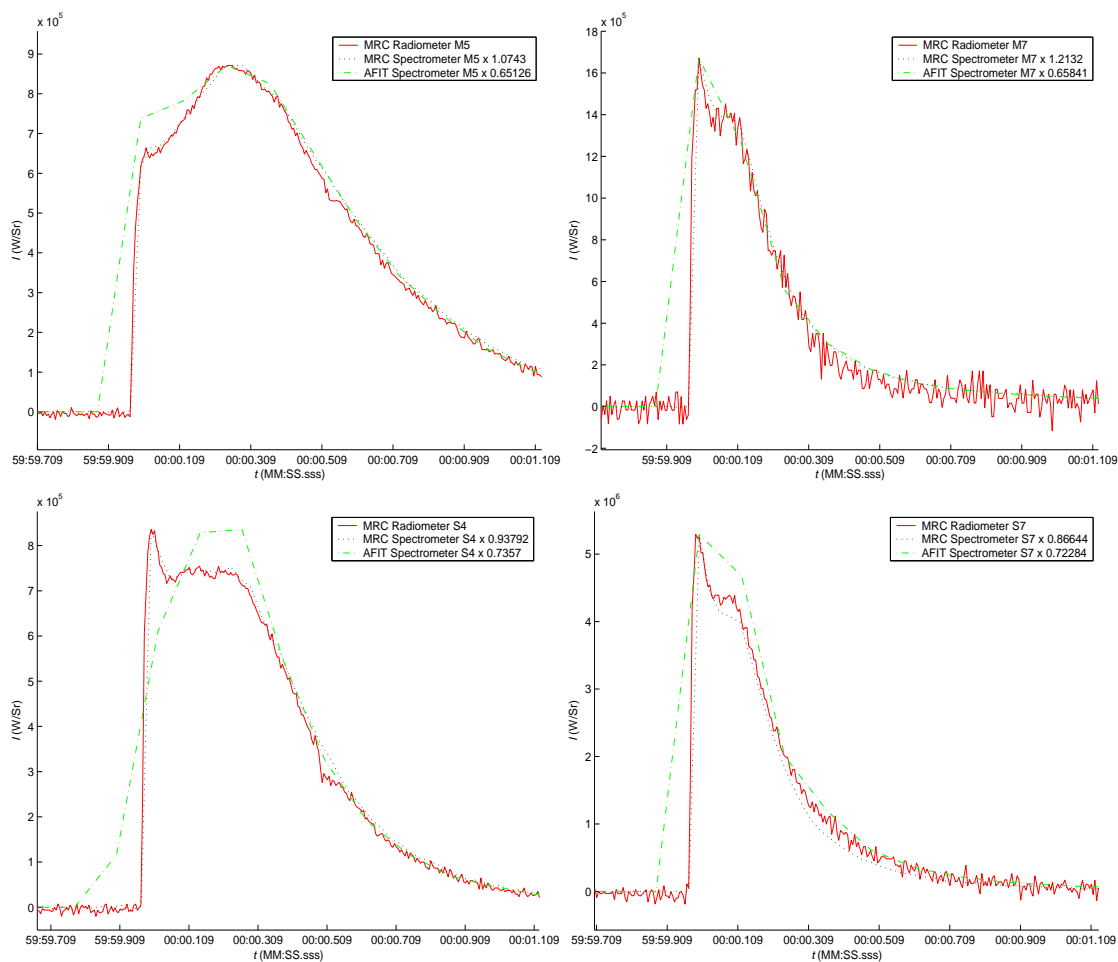


Figure 134. Band comparison for event 11. “Comparison Spectrometer” is from the MR354 FTIR and “Your Spectrometer” is from the MR154 FTIR.

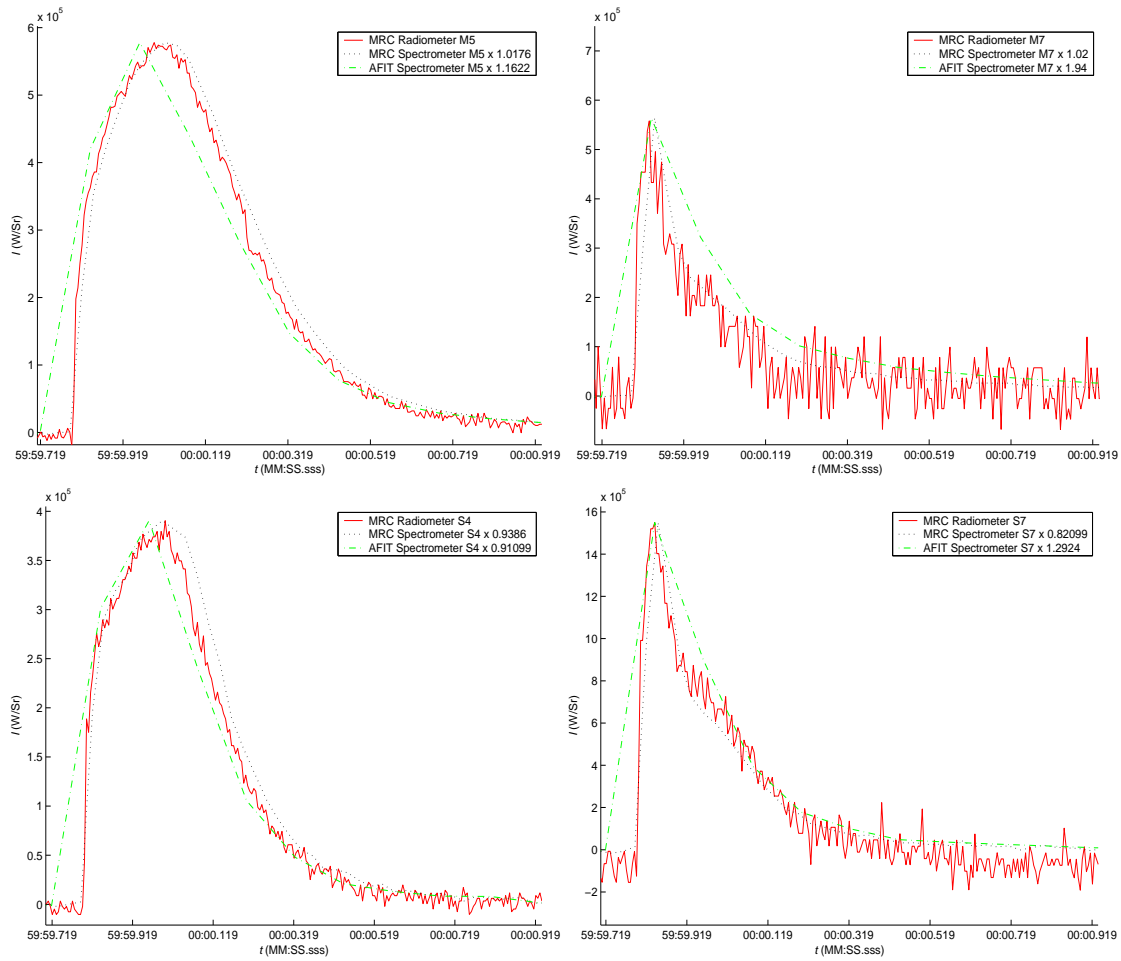


Figure 135. Band comparison for event 13. “Comparison Spectrometer” is from the MR354 FTIR and “Your Spectrometer” is from the MR154 FTIR.

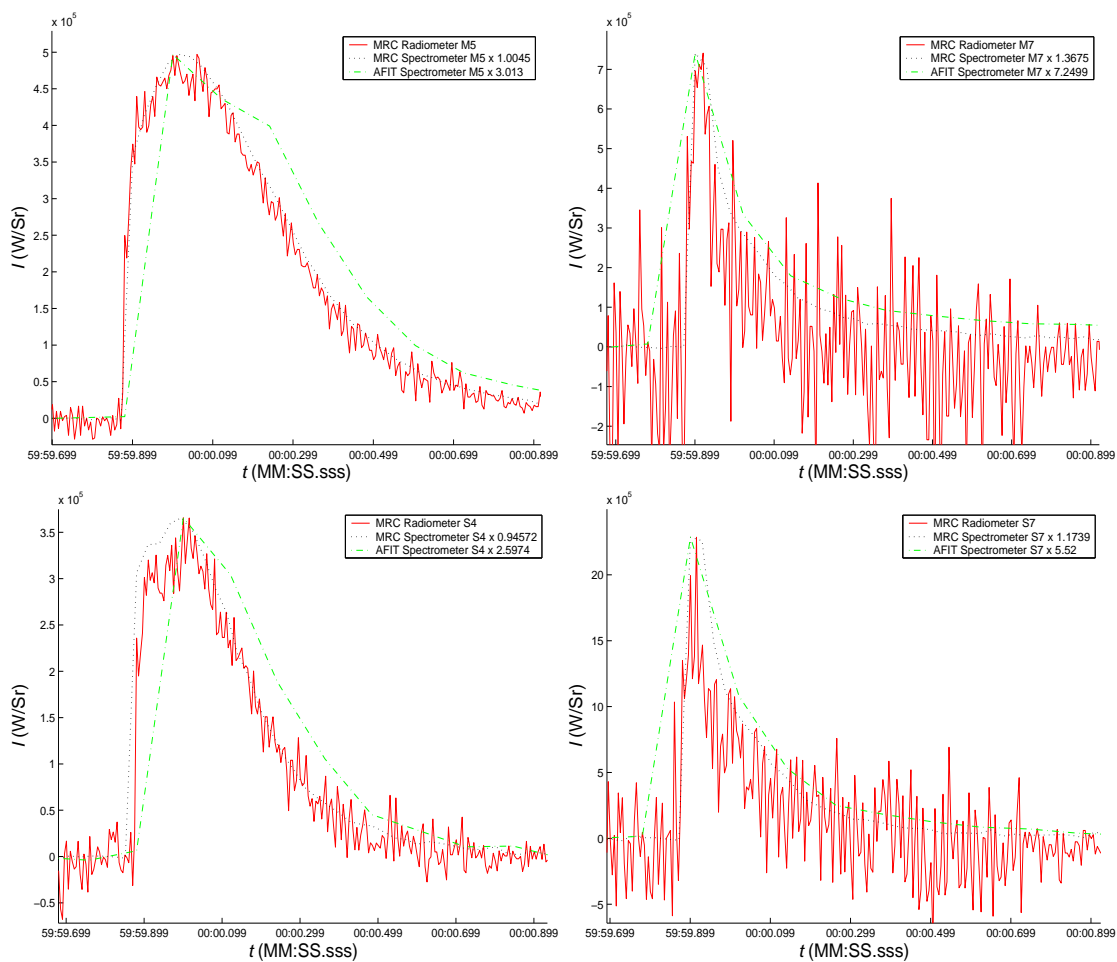


Figure 136. Band comparison for event 14. “Comparison Spectrometer” is from the MR354 FTIR and “Your Spectrometer” is from the MR154 FTIR.

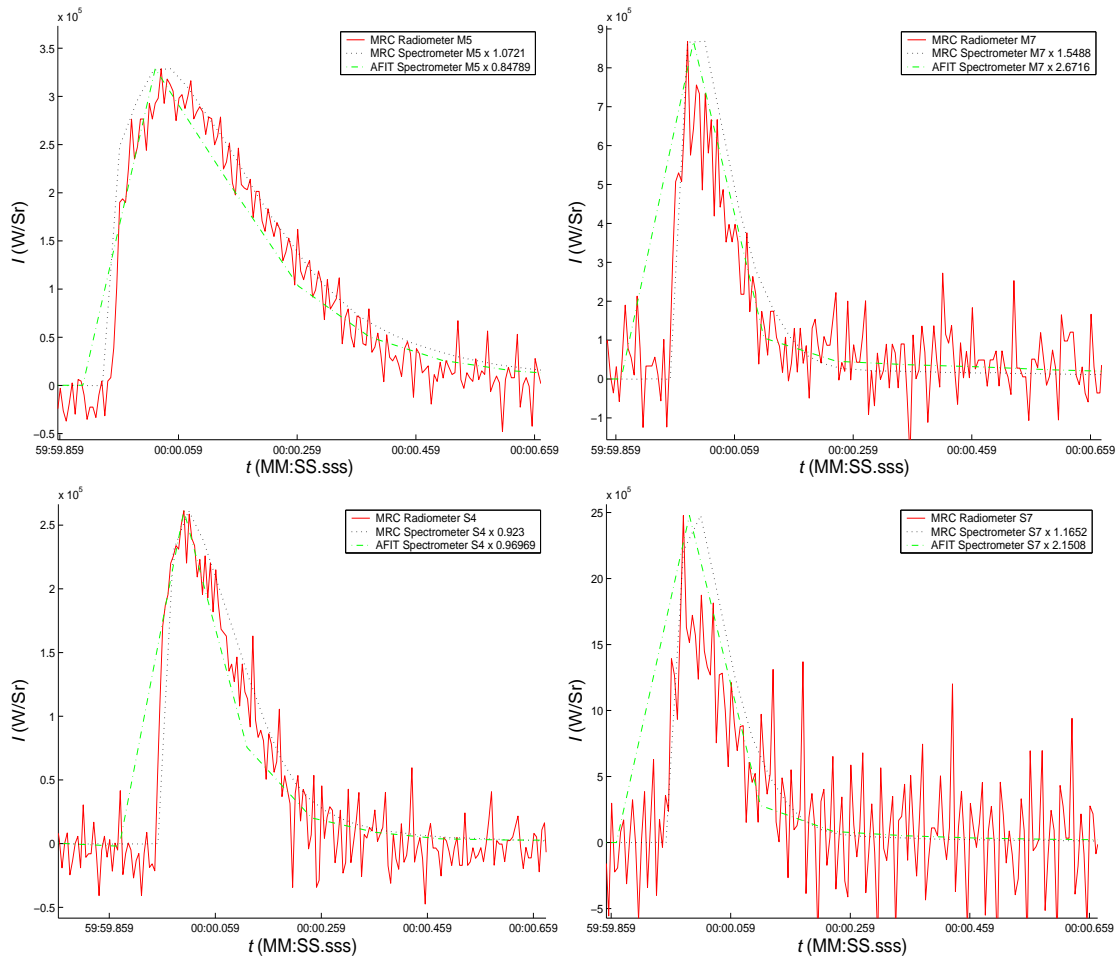


Figure 137. Band comparison for event 15. “Comparison Spectrometer” is from the MR354 FTIR and “Your Spectrometer” is from the MR154 FTIR.

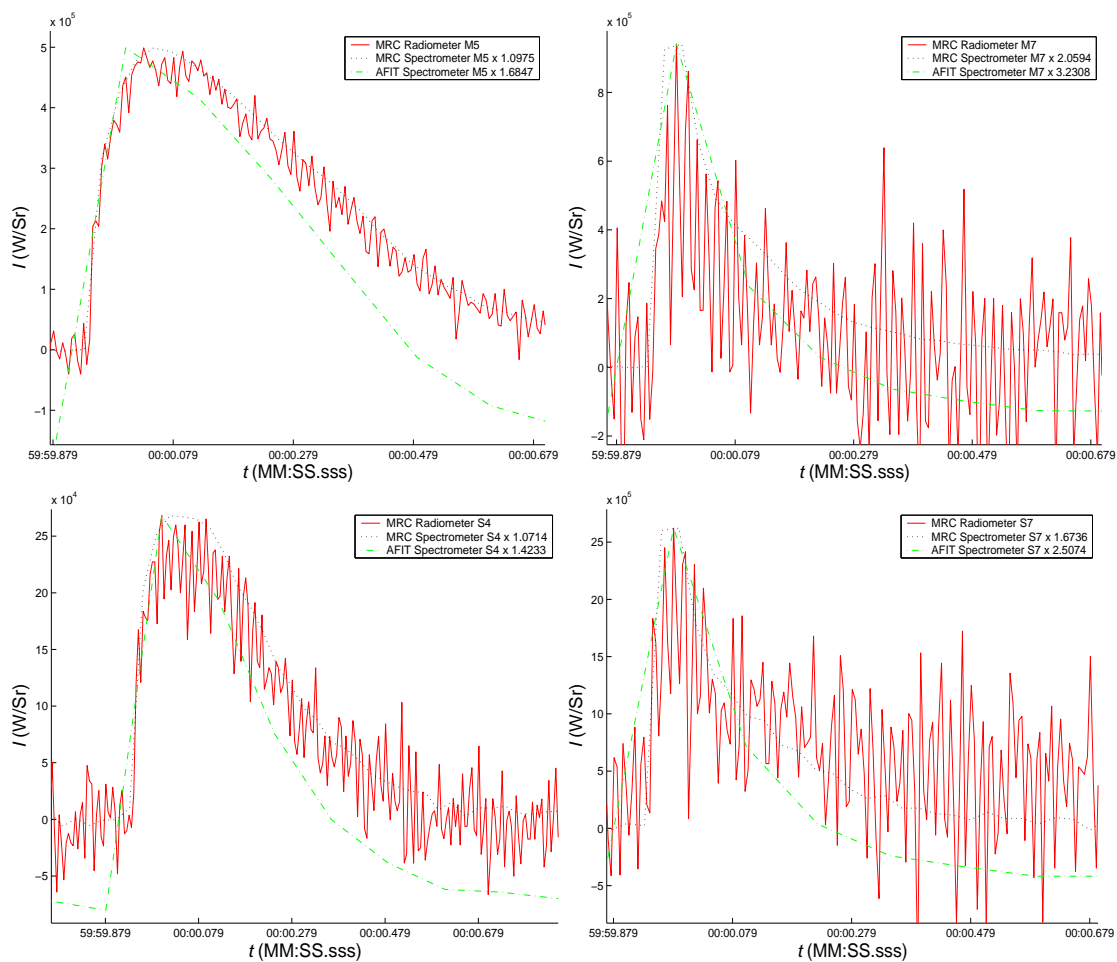


Figure 138. Band comparison for event 17. “Comparison Spectrometer” is from the MR354 FTIR and “Your Spectrometer” is from the MR154 FTIR.

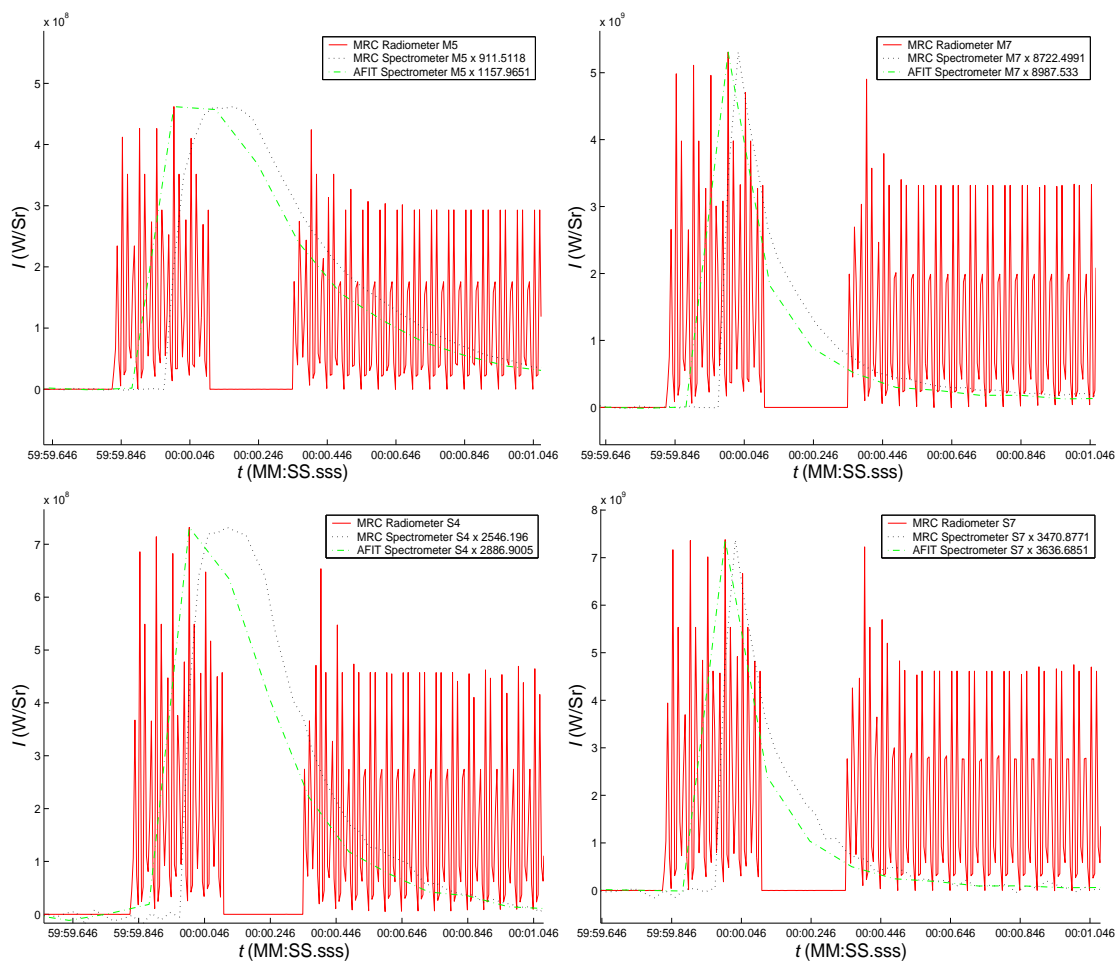


Figure 139. Band comparison for event 18. “Comparison Spectrometer” is from the MR354 FTIR and “Your Spectrometer” is from the MR154 FTIR.

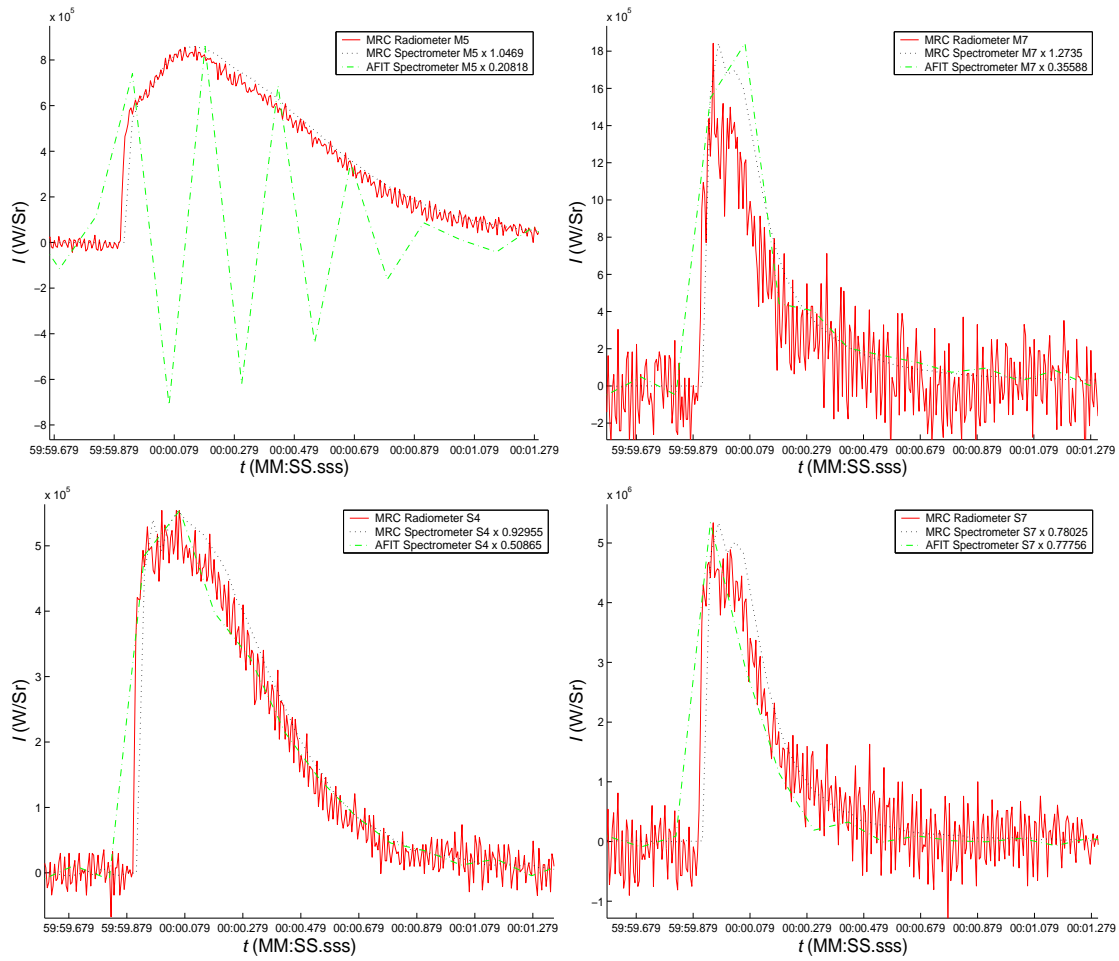


Figure 140. Band comparison for event 19. “Comparison Spectrometer” is from the MR354 FTIR and “Your Spectrometer” is from the MR154 FTIR.

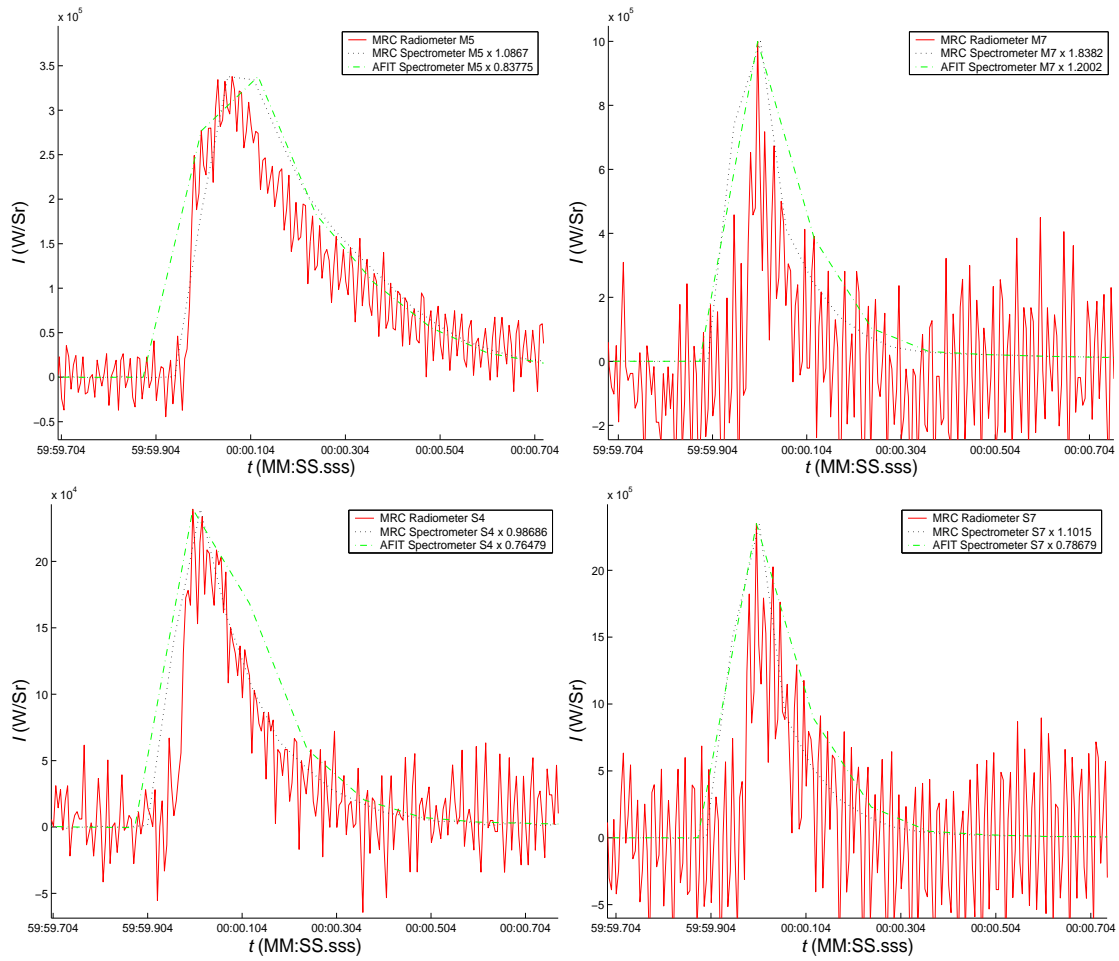


Figure 141. Band comparison for event 21. “Comparison Spectrometer” is from the MR354 FTIR and “Your Spectrometer” is from the MR154 FTIR.

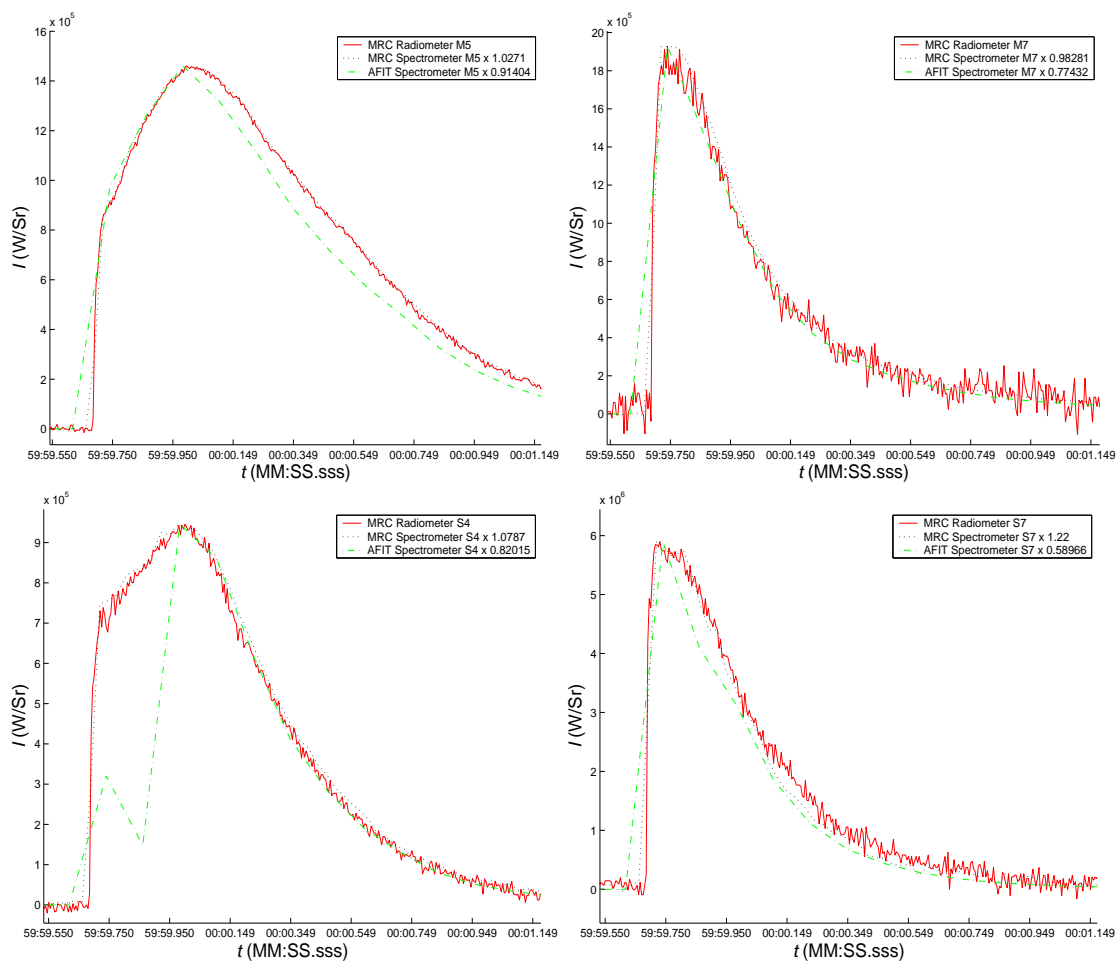


Figure 142. Band comparison for event 22. “Comparison Spectrometer” is from the MR354 FTIR and “Your Spectrometer” is from the MR154 FTIR.

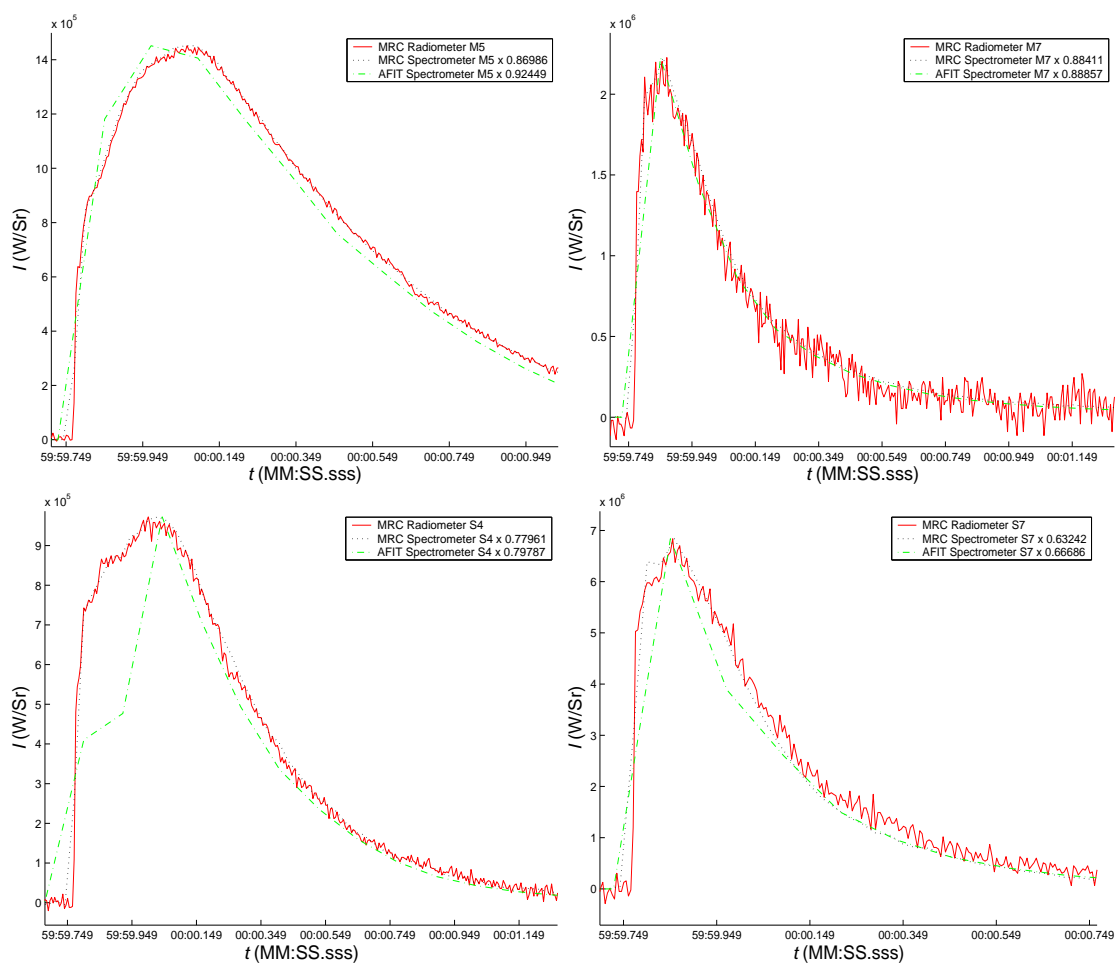


Figure 143. Band comparison for event 23. “Comparison Spectrometer” is from the MR354 FTIR and “Your Spectrometer” is from the MR154 FTIR.

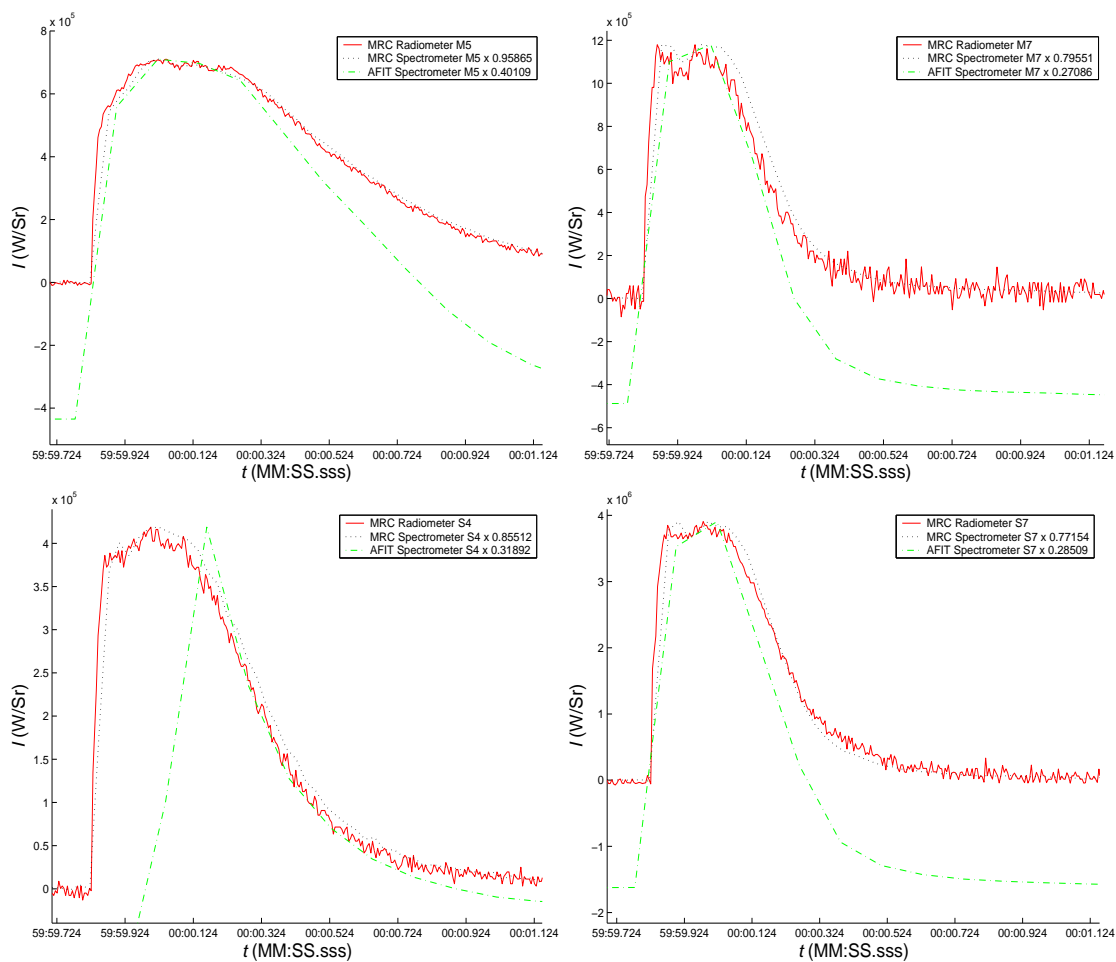


Figure 144. Band comparison for event 25. “Comparison Spectrometer” is from the MR354 FTIR and “Your Spectrometer” is from the MR154 FTIR.

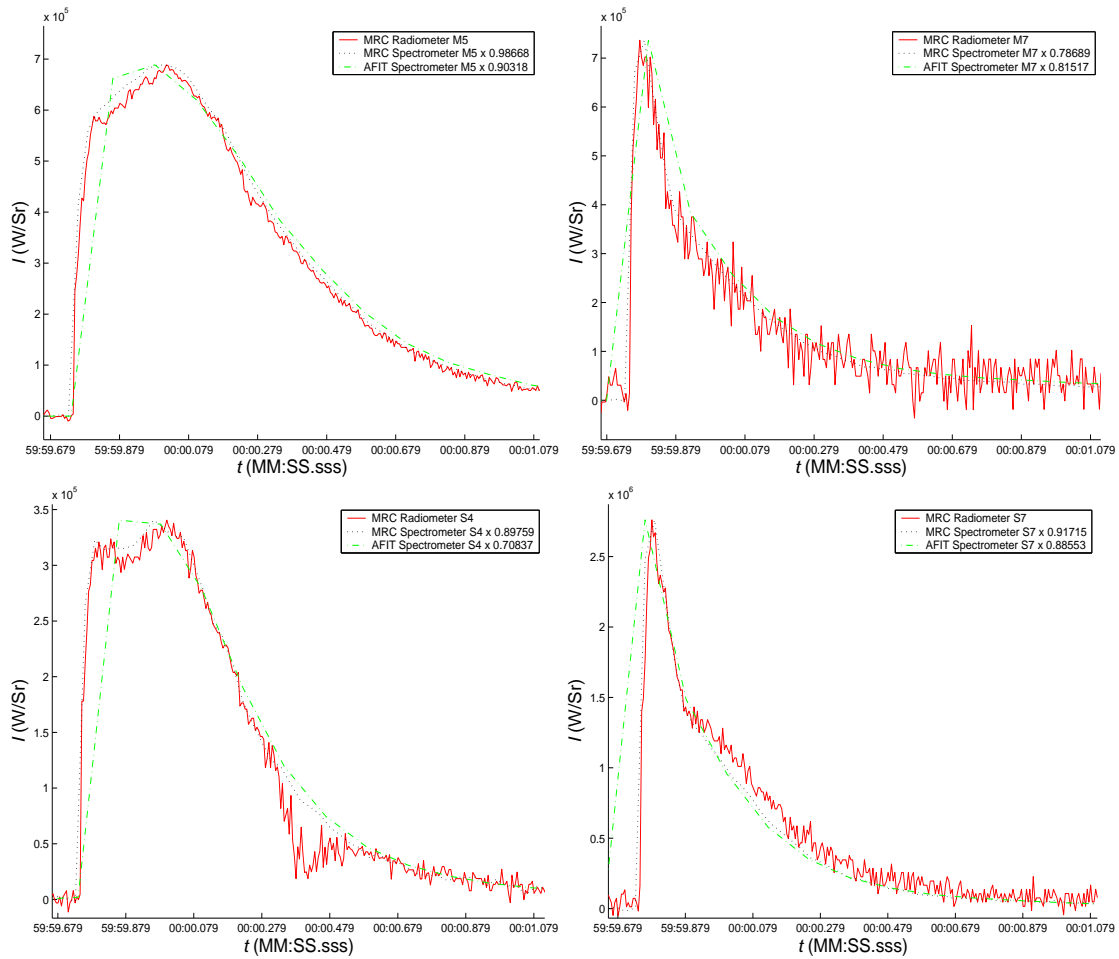


Figure 145. Band comparison for event 26. “Comparison Spectrometer” is from the MR354 FTIR and “Your Spectrometer” is from the MR154 FTIR.

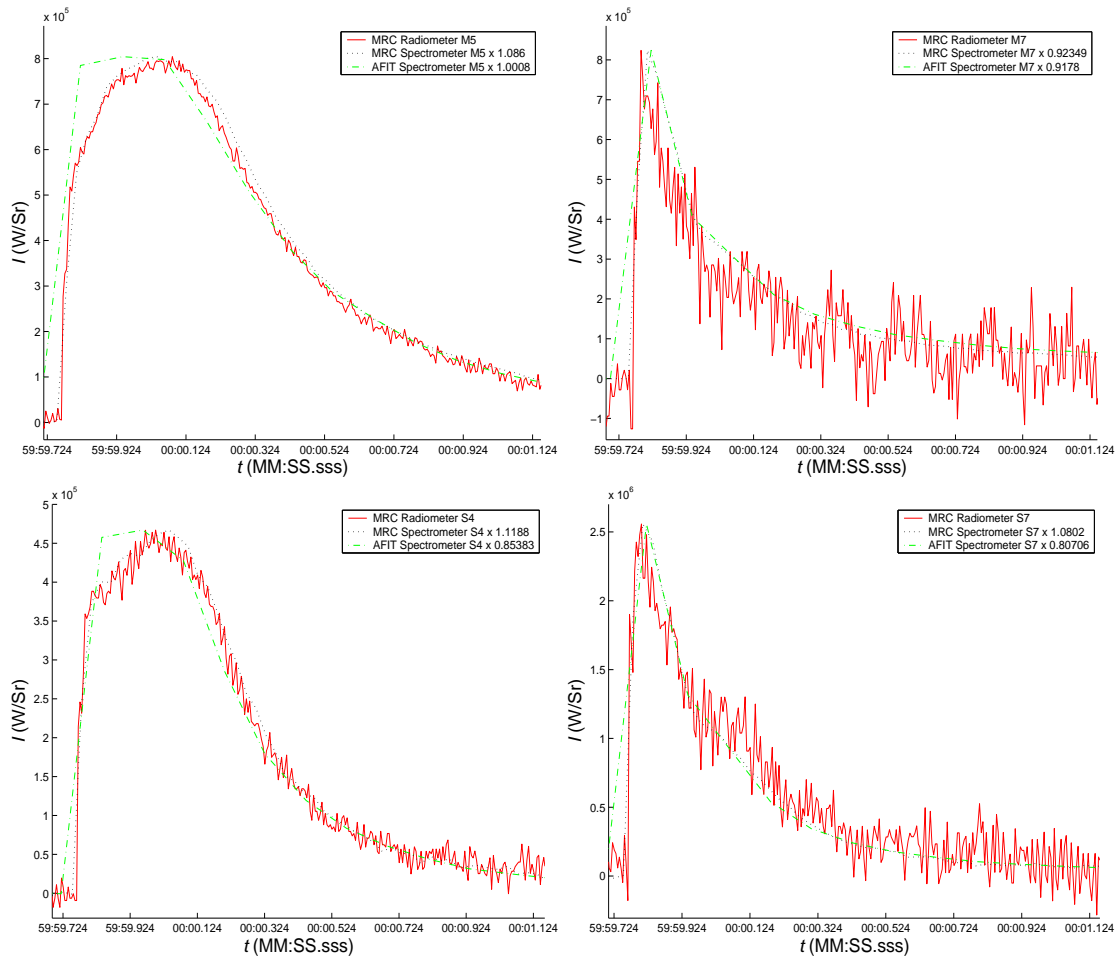


Figure 146. Band comparison for event 27. “Comparison Spectrometer” is from the MR354 FTIR and “Your Spectrometer” is from the MR154 FTIR.

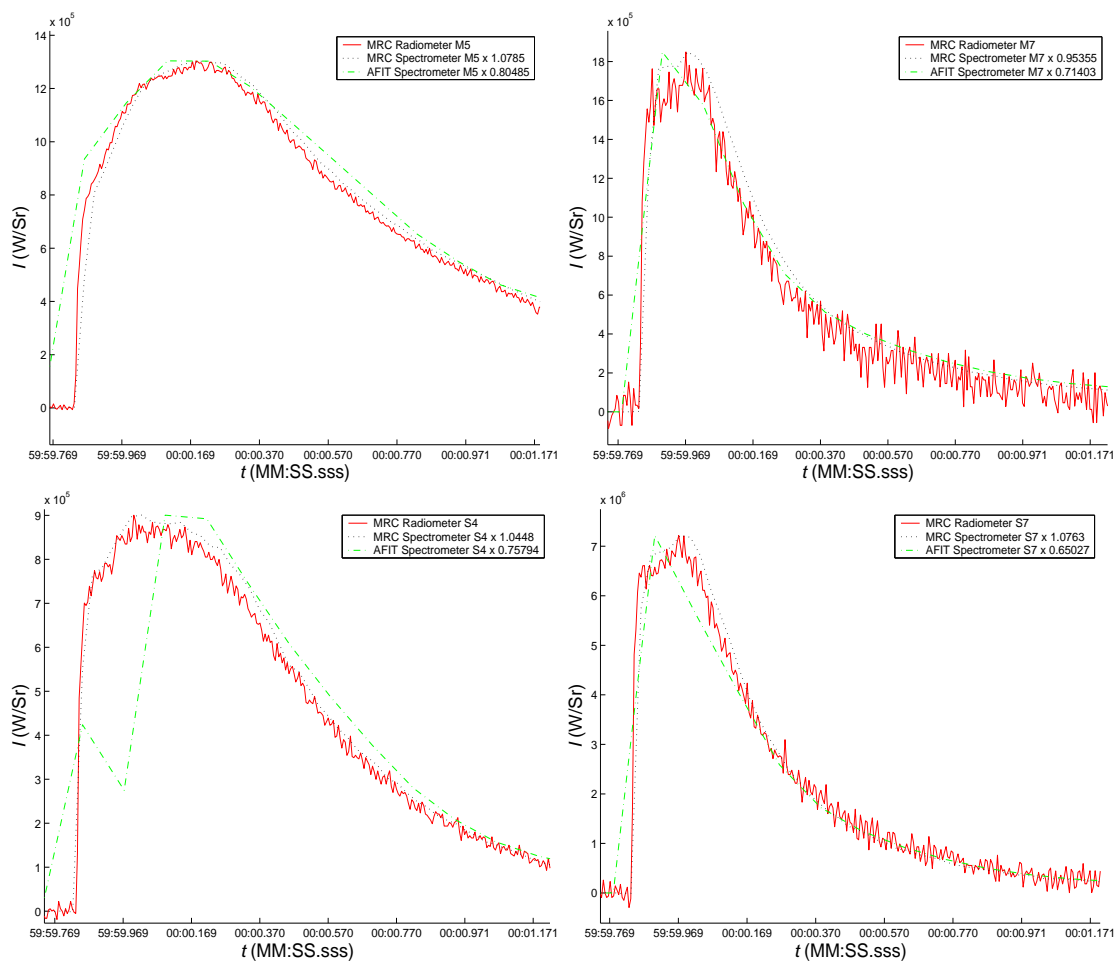


Figure 147. Band comparison for event 28. “Comparison Spectrometer” is from the MR354 FTIR and “Your Spectrometer” is from the MR154 FTIR.

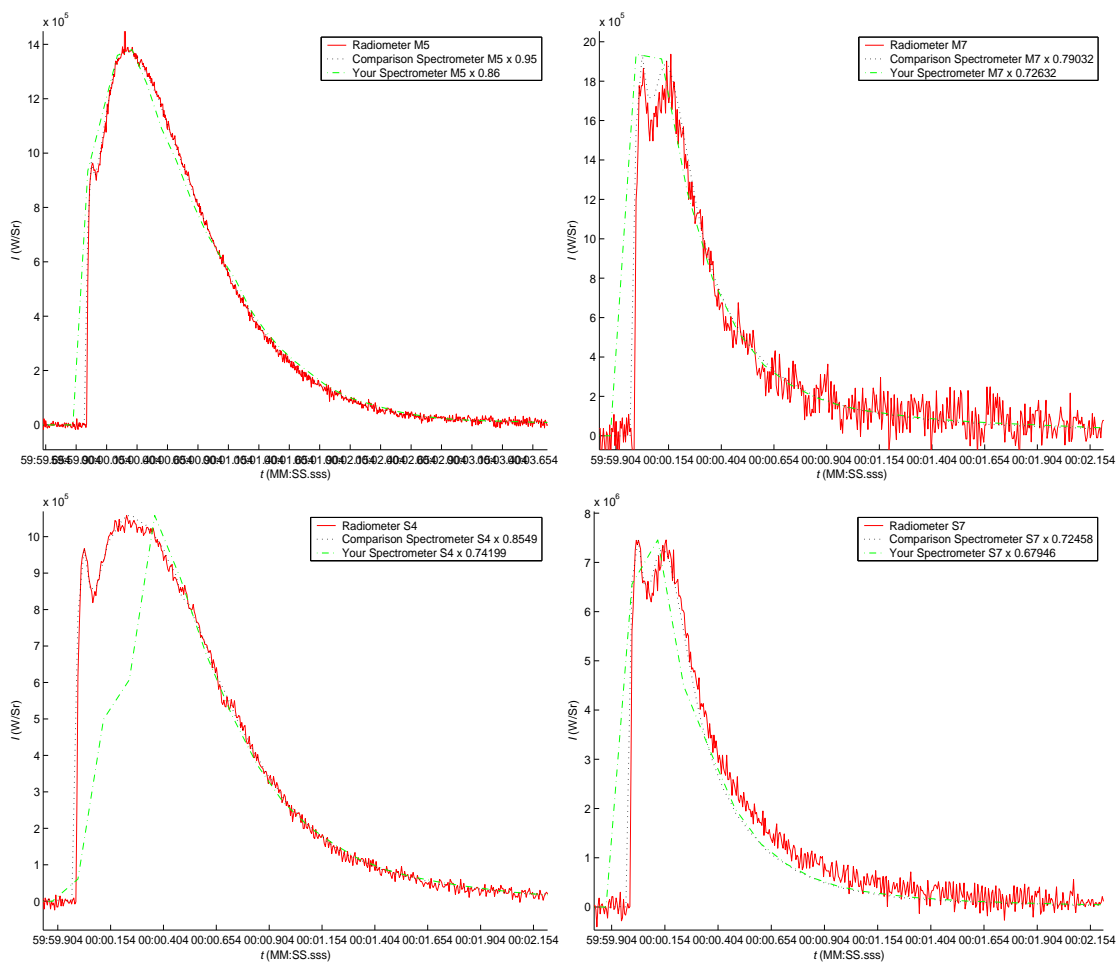


Figure 148. Band comparison for event 29. “Comparison Spectrometer” is from the MR354 FTIR and “Your Spectrometer” is from the MR154 FTIR.

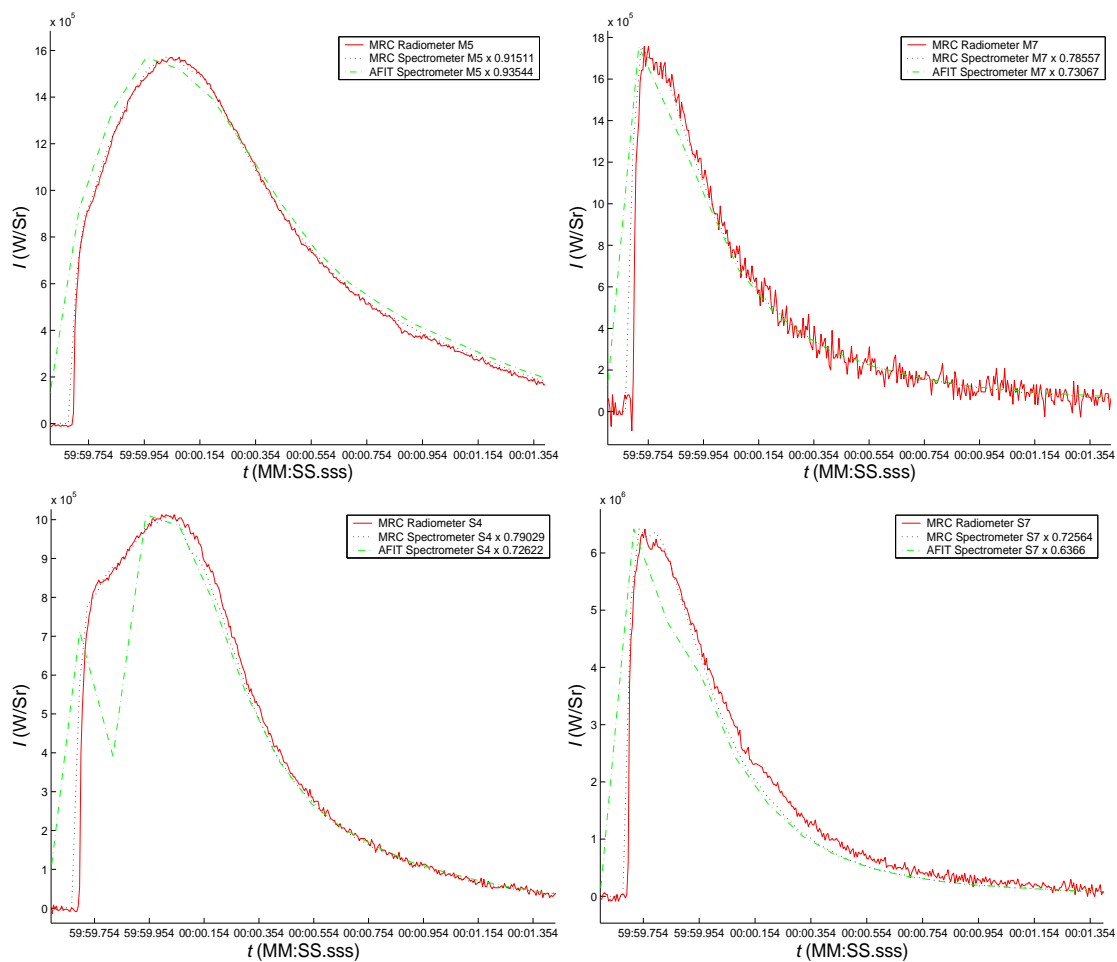


Figure 149. Band comparison for event 30. “Comparison Spectrometer” is from the MR354 FTIR and “Your Spectrometer” is from the MR154 FTIR.

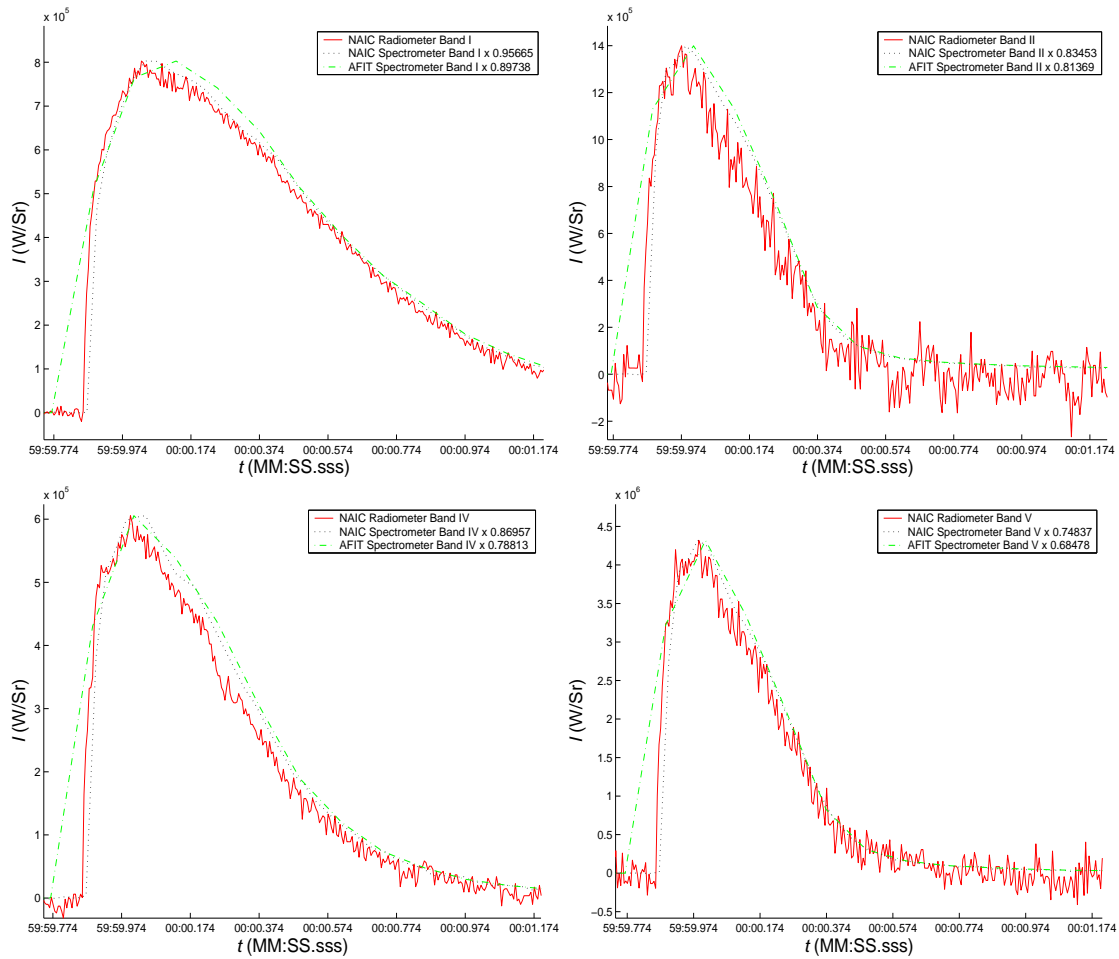


Figure 150. Band comparison for event 31. “Comparison Spectrometer” is from the MR354 FTIR and “Your Spectrometer” is from the MR154 FTIR.

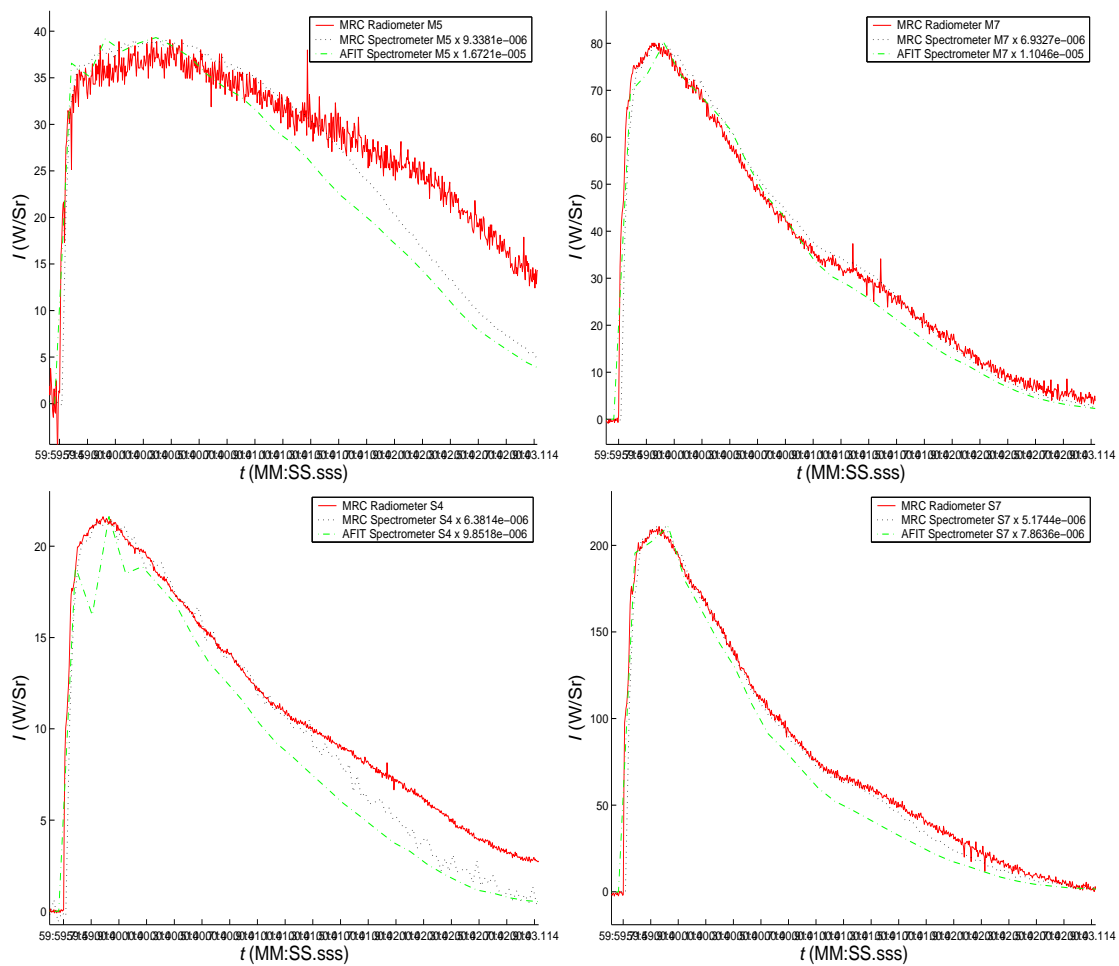


Figure 151. Band comparison for event 32. “Comparison Spectrometer” is from the MR354 FTIR and “Your Spectrometer” is from the MR154 FTIR.

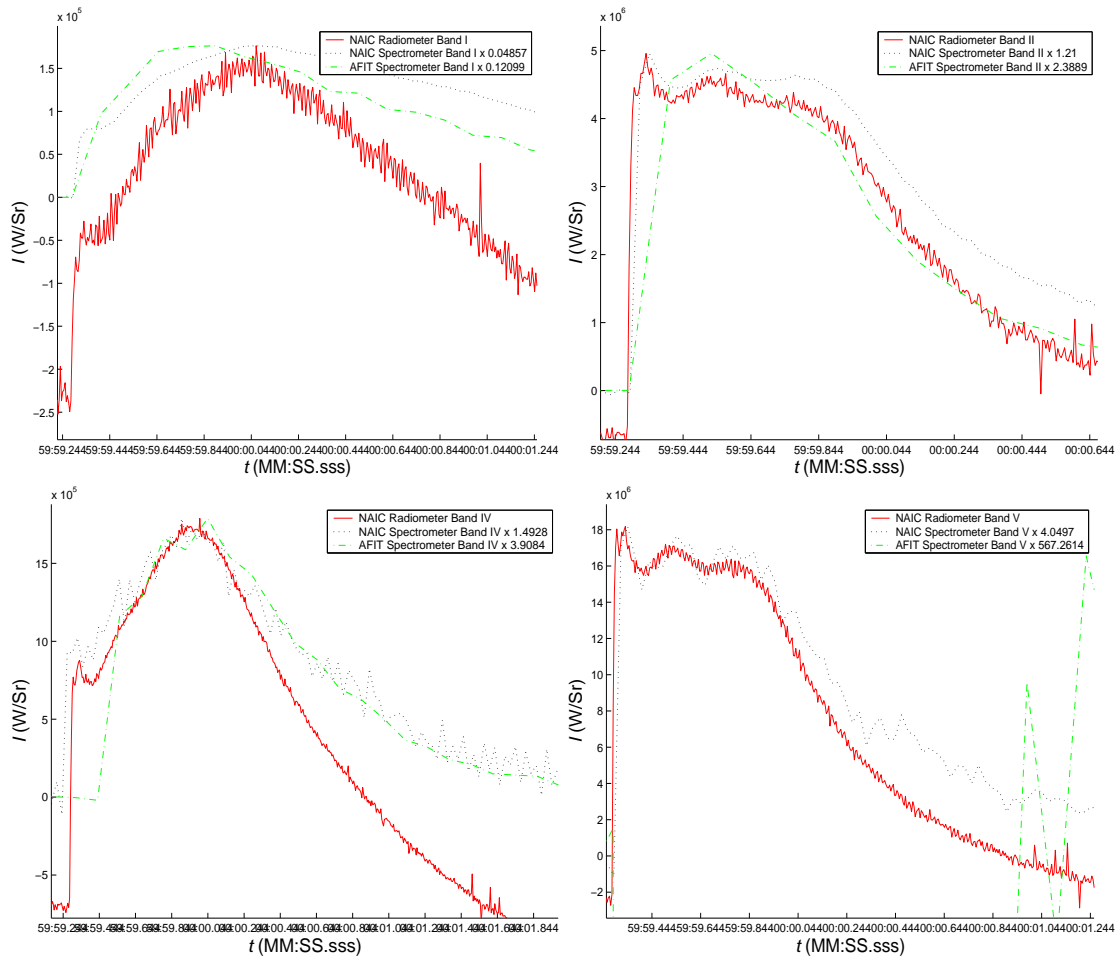


Figure 152. Band comparison for event 33. “Comparison Spectrometer” is from the MR354 FTIR and “Your Spectrometer” is from the MR154 FTIR.

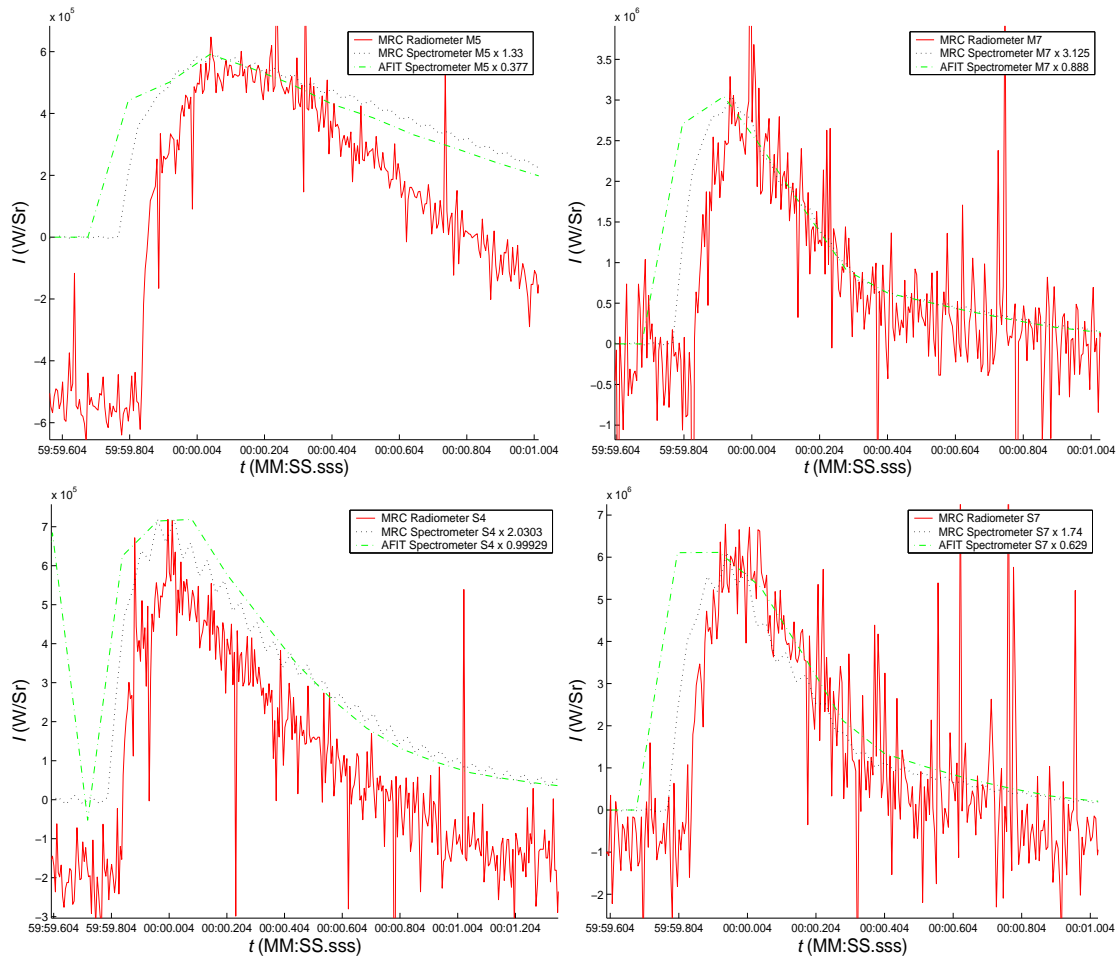


Figure 153. Band comparison for event 34. “Comparison Spectrometer” is from the MR354 FTIR and “Your Spectrometer” is from the MR154 FTIR.

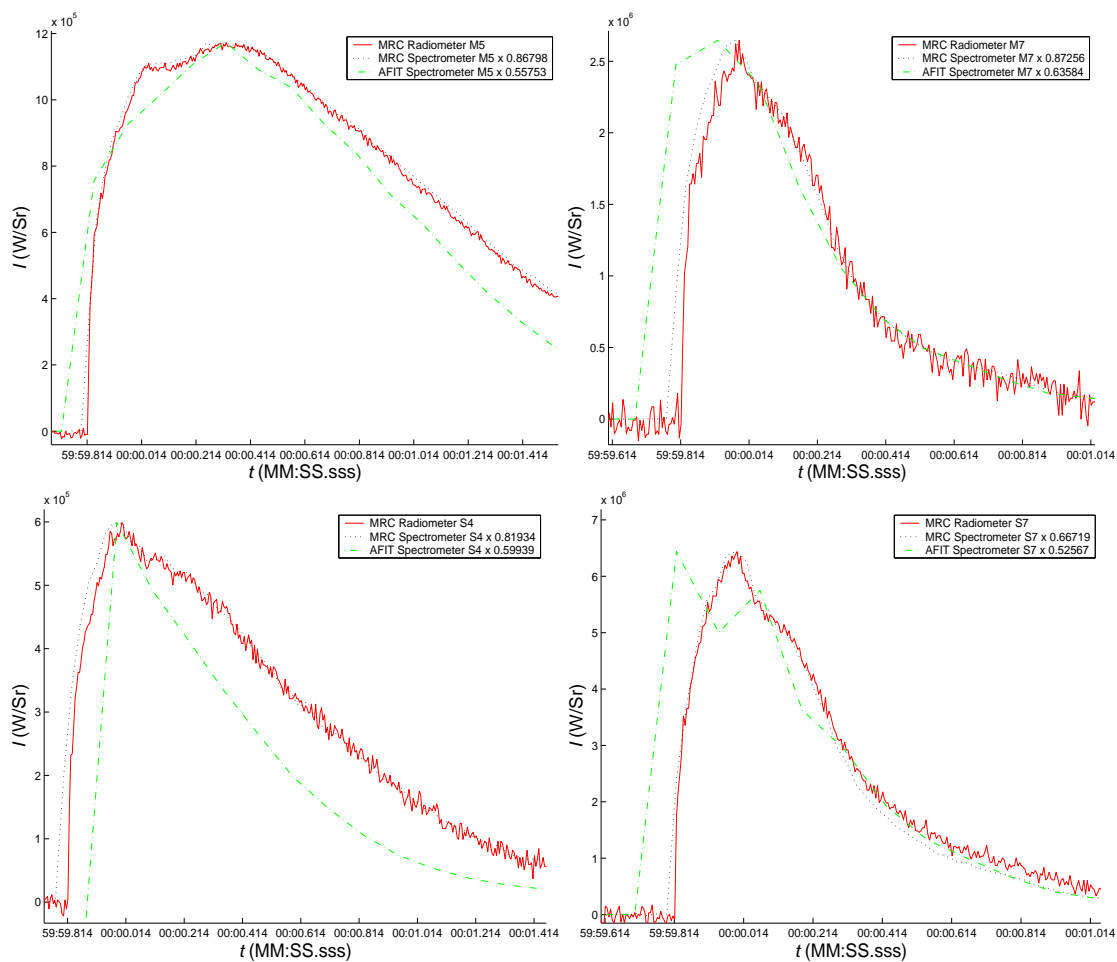


Figure 154. Band comparison for event 36. “Comparison Spectrometer” is from the MR354 FTIR and “Your Spectrometer” is from the MR154 FTIR.

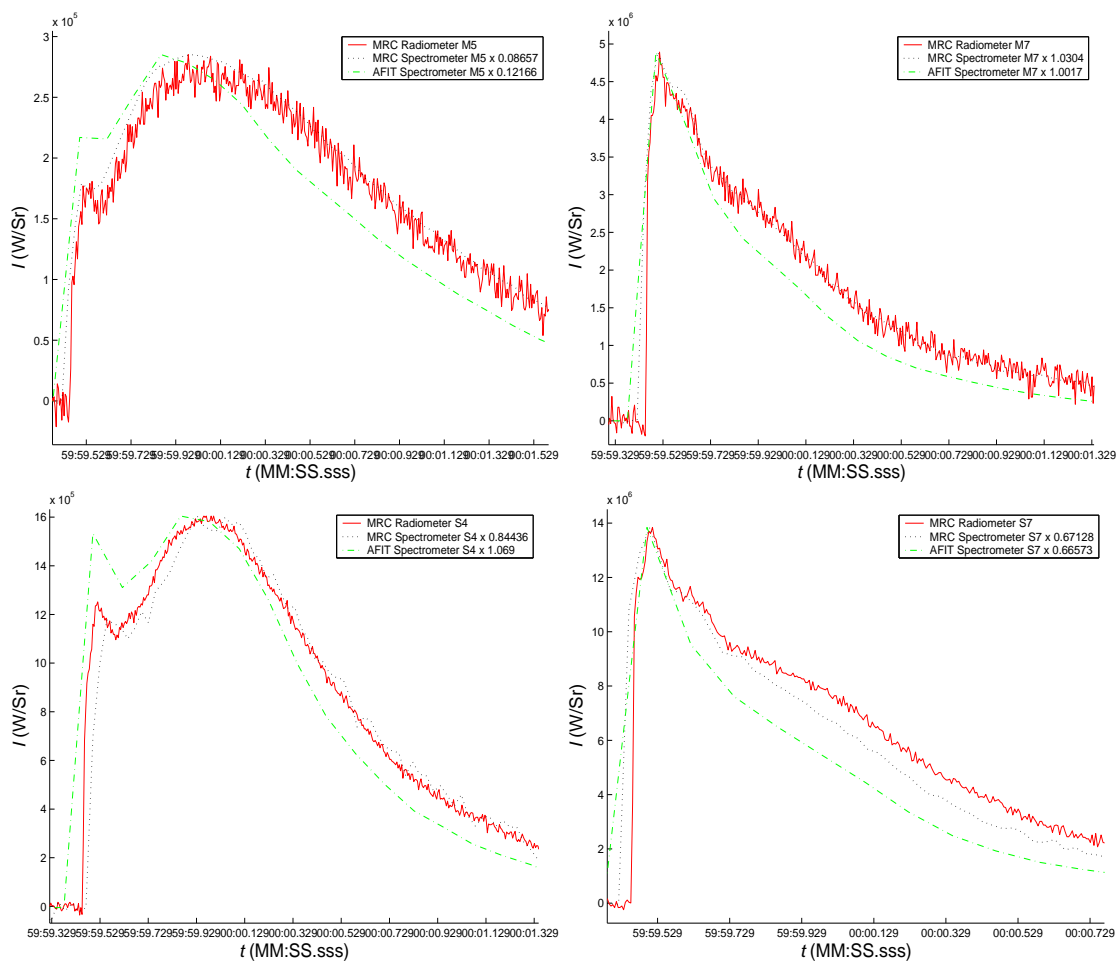


Figure 155. Band comparison for event 37. “Comparison Spectrometer” is from the MR354 FTIR and “Your Spectrometer” is from the MR154 FTIR.

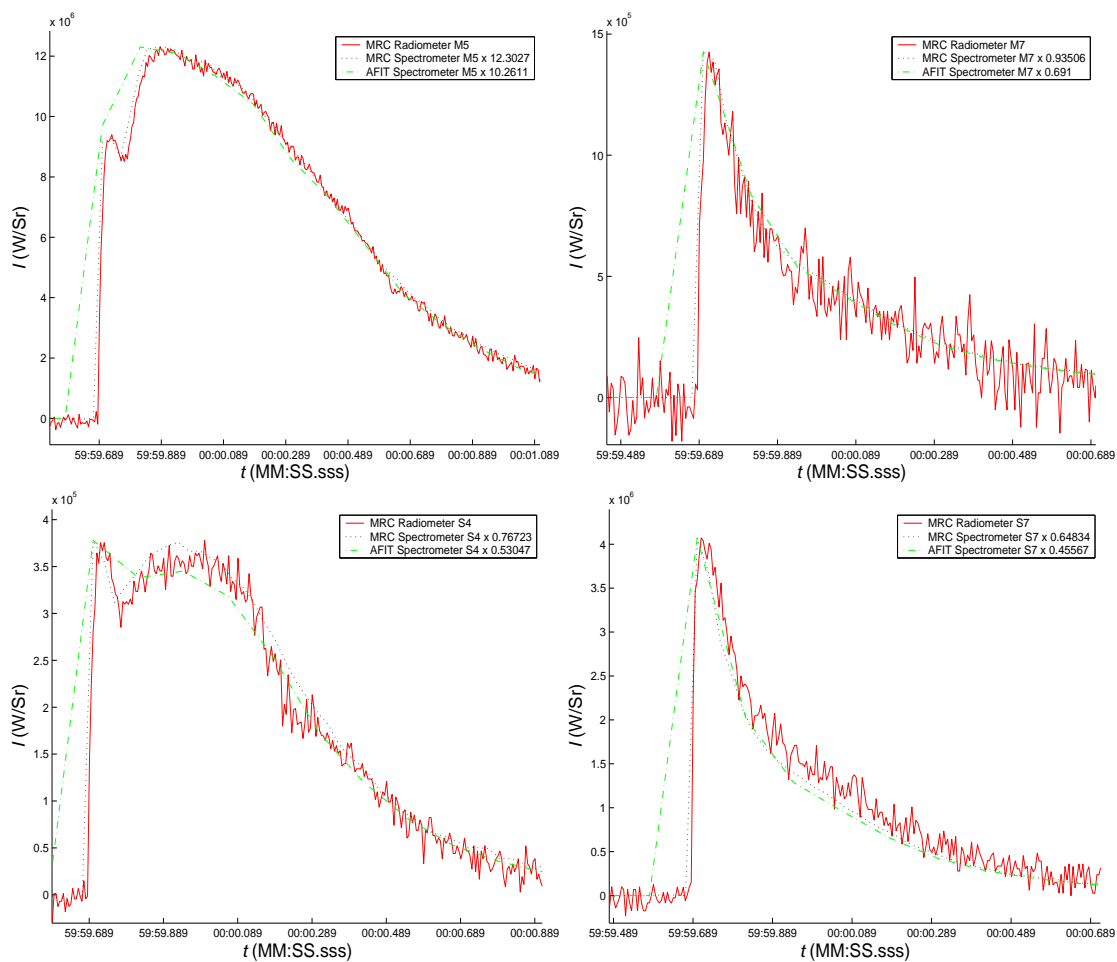


Figure 156. Band comparison for event 38. “Comparison Spectrometer” is from the MR354 FTIR and “Your Spectrometer” is from the MR154 FTIR.

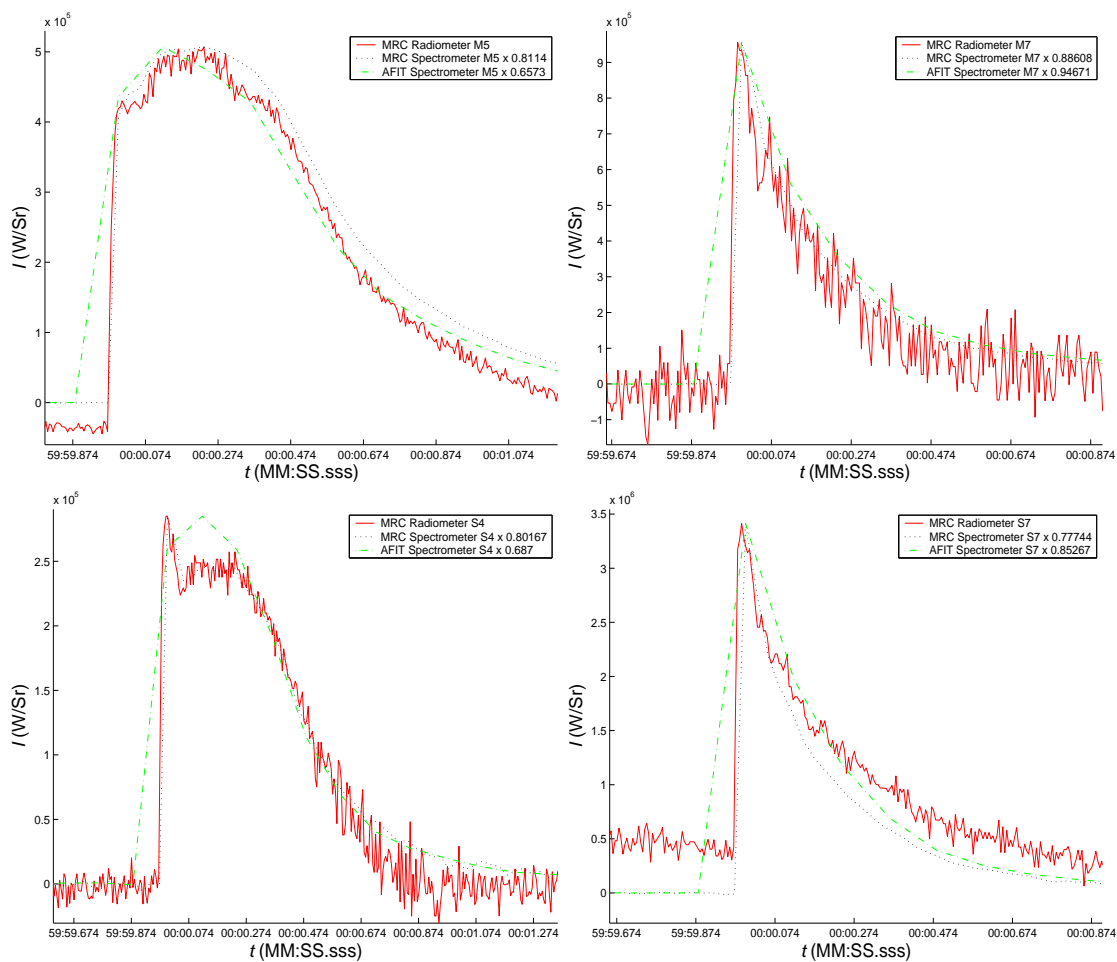


Figure 157. Band comparison for event 39. “Comparison Spectrometer” is from the MR354 FTIR and “Your Spectrometer” is from the MR154 FTIR.

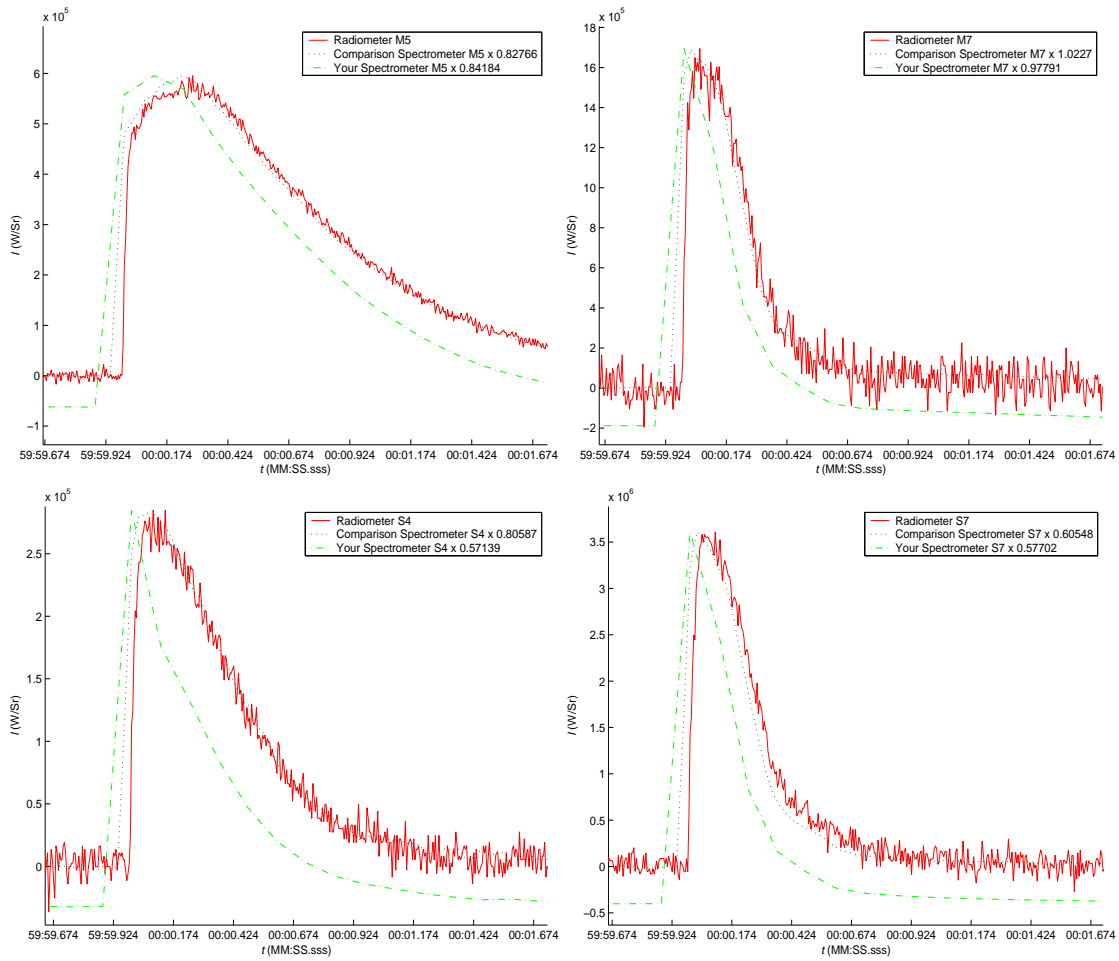


Figure 158. Band comparison for event 40. “Comparison Spectrometer” is from the MR354 FTIR and “Your Spectrometer” is from the MR154 FTIR.

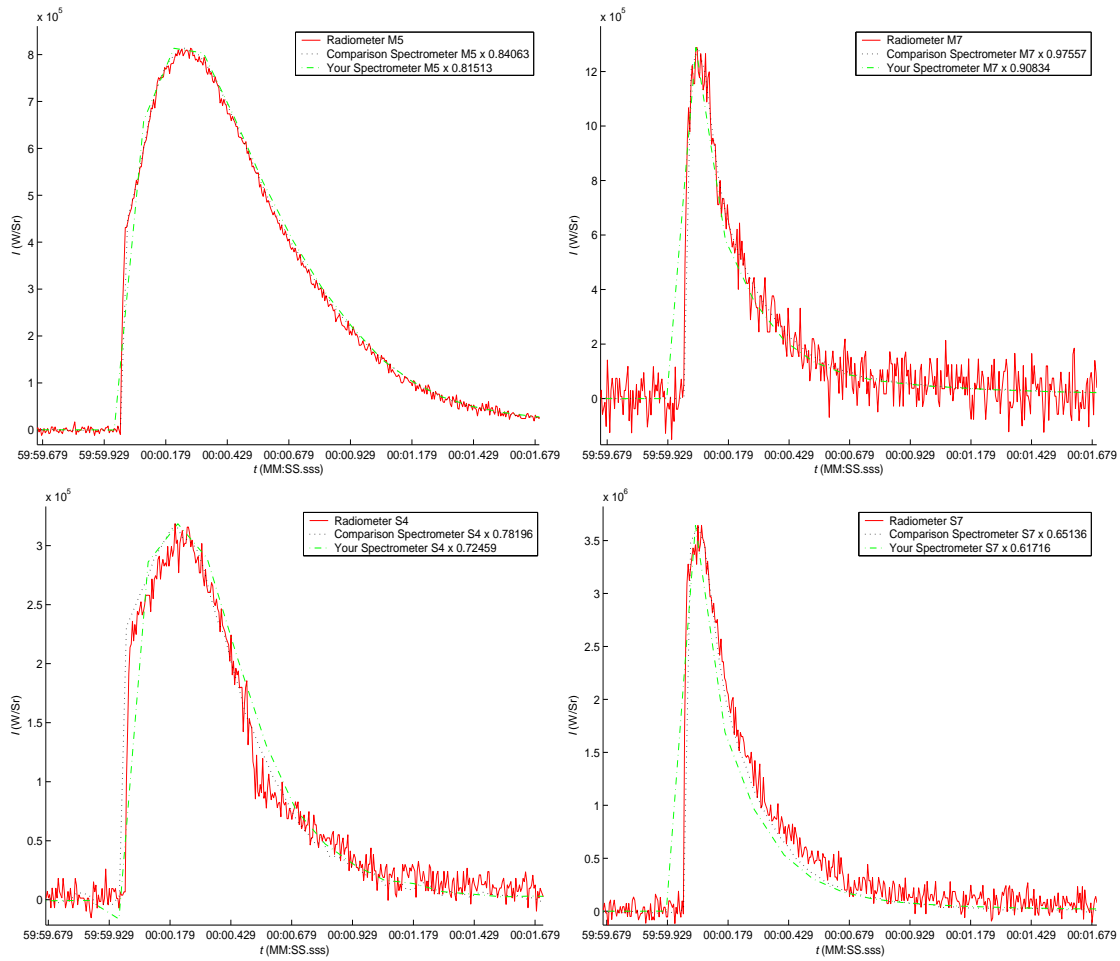


Figure 159. Band comparison for event 41. “Comparison Spectrometer” is from the MR354 FTIR and “Your Spectrometer” is from the MR154 FTIR.

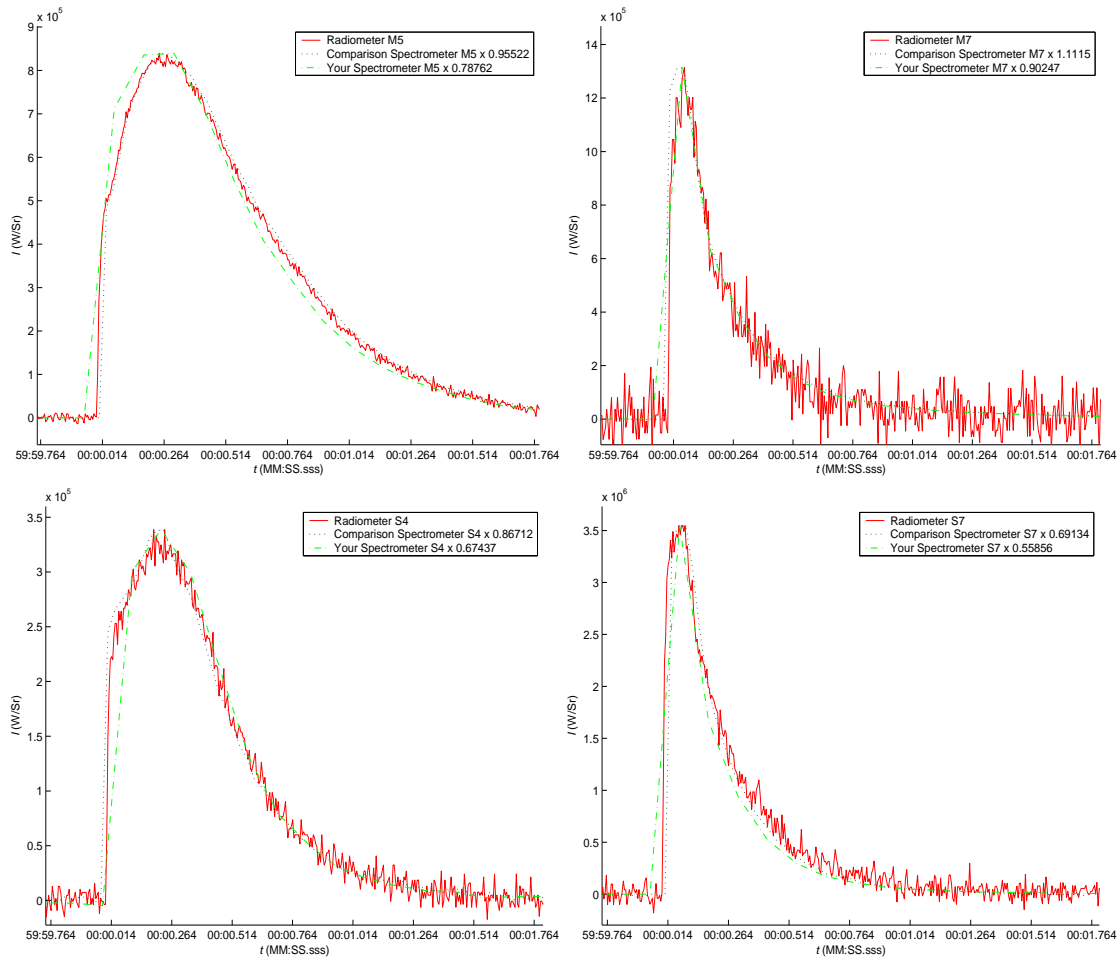


Figure 160. Band comparison for event 42. “Comparison Spectrometer” is from the MR354 FTIR and “Your Spectrometer” is from the MR154 FTIR.

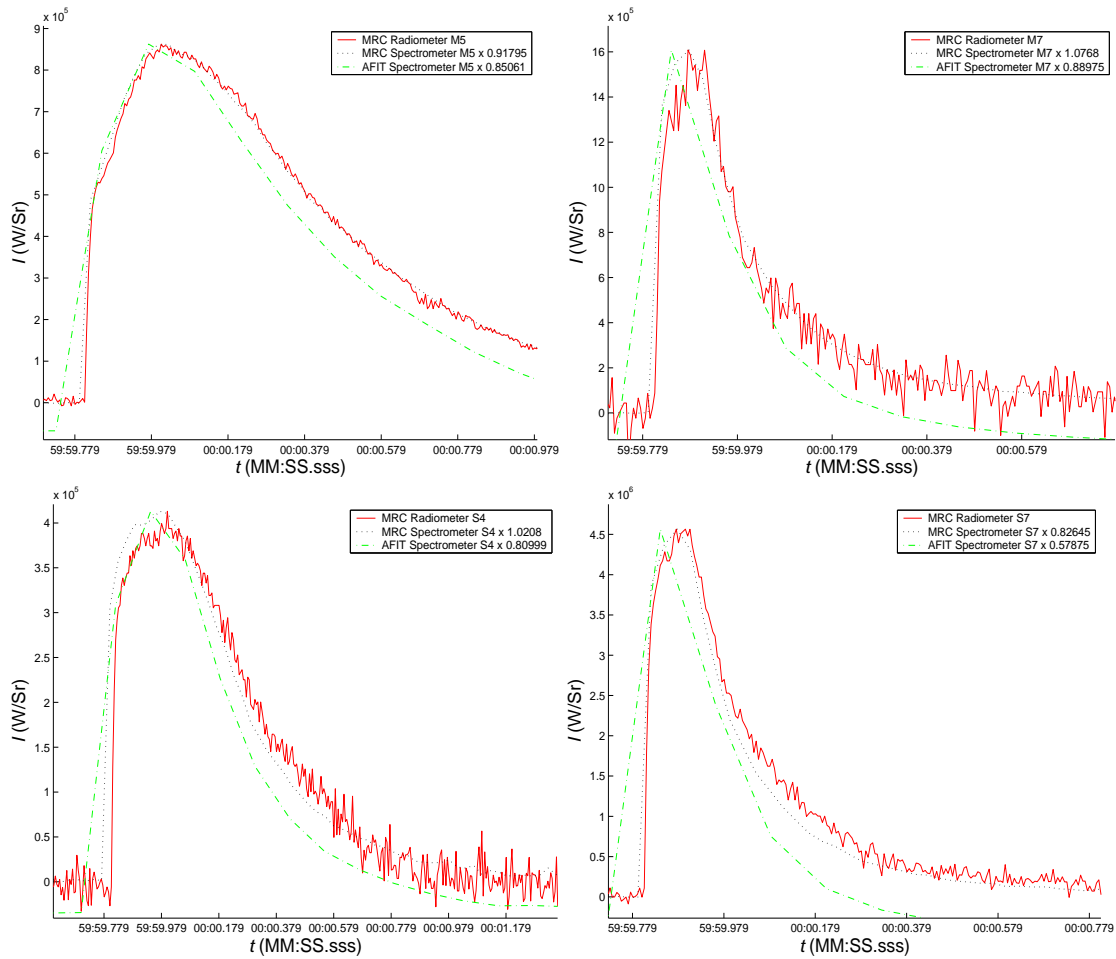


Figure 161. Band comparison for event 43. “Comparison Spectrometer” is from the MR354 FTIR and “Your Spectrometer” is from the MR154 FTIR.

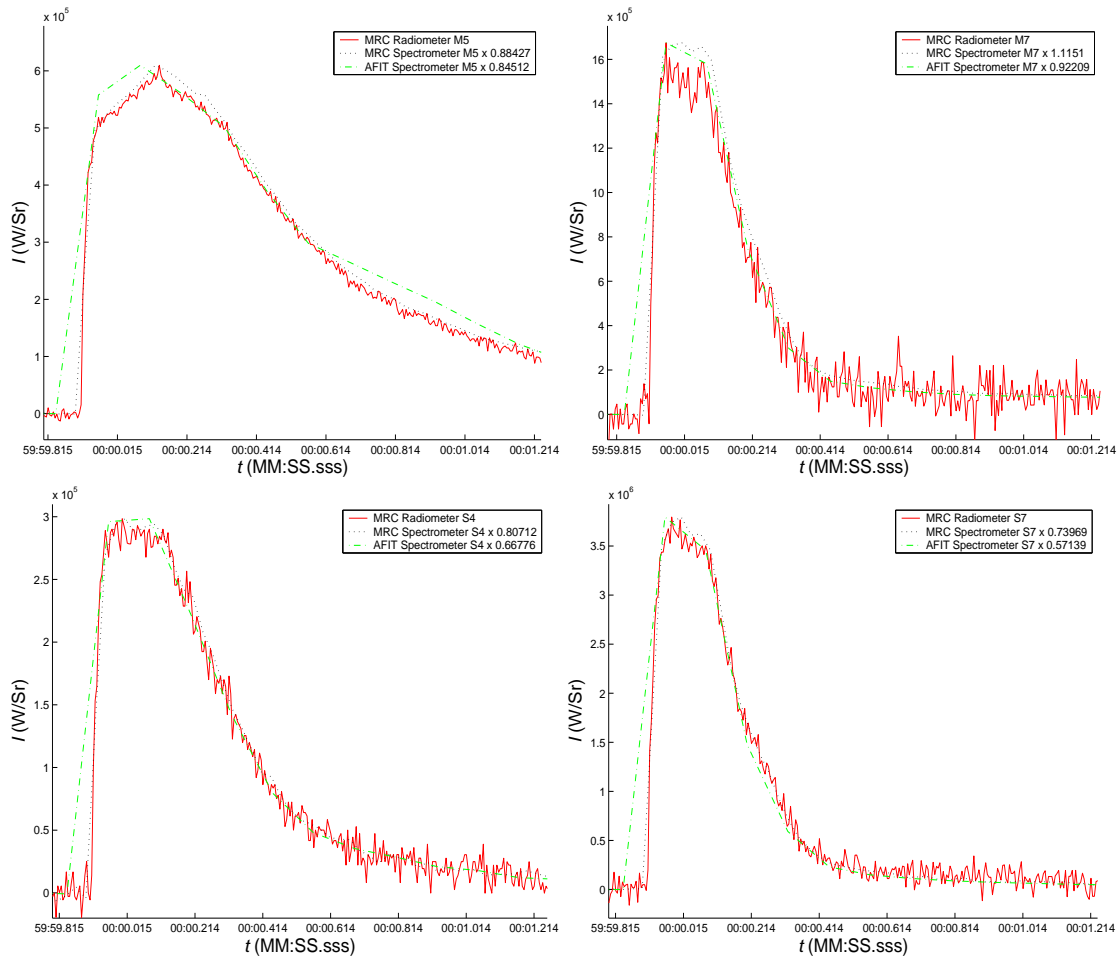


Figure 162. Band comparison for event 44. “Comparison Spectrometer” is from the MR354 FTIR and “Your Spectrometer” is from the MR154 FTIR.

Bibliography

- 1 S. N. Goward, *et al.*, "Enhanced Landsat capturing all the Earth's land areas," EOS 80 (26), 289-293 (1999).
- 2 P. C. Doraiswamy *et al.*, "Crop condition and yield simulations using Landsat and MODIS," Remote Sens.Environ. 92 (4), 548-559 (2004).
- 3 Dengsheng Lu *et al.*, "Relationships between forest stand parameters and Landsat TM spectral responses in the Brazilian Amazon Basin," For.Ecol.Manage. 198 (1-3), 149-167 (2004).
- 4 Hyeungu Choi and Robert Bindschadler, "Cloud detection in Landsat imagery of ice sheets using shadow matching technique and automatic normalized difference snow index threshold value decision," Remote Sens.Environ. 91 (2), 237-242 (2004).
- 5 Jeremy I. Fisher and John F. Mustard, "High spatial resolution sea surface climatology from Landsat thermal infrared data," Remote Sens.Environ. 90 (3), 293-307 (2004).
- 6 Matthew Patrick, Kenneson Dean and Jonathan Dehn, "Active mud volcanism observed with Landsat 7 ETM+," J.Volcanol.Geotherm.Res. 131 (3-4), 307-320 (2004).
- 7 M. A. Wulder *et al.*, "Estimating time since forest harvest using segmented Landsat ETM+ imagery," Remote Sens.Environ. 93 (1-2), 179-187 (2004).
- 8 J. P. Aguttes, D. Massonnet and O. Grosjean, "A new radar system for the French program in the 2000s," Acta Astronautica 25 (1), 43-50 (1991)
- 9 P. Henry , T. Gentet, M. Arnaud and C. Andersson, "The VEGETATION system: A global earth monitoring from SPOT satellites," Acta Astronautica 38 (4-8), 487-492 (1996).
- 10 S. R. Falke, R. B. Husar and B. A. Schichtel, "Fusion of SeaWiFS and TOMS satellite data with surface observations and topographic data during extreme aerosol events," J.Air Waste Manag.Assoc. 51 (11), 1579-1585 (2001).
- 11 C. C. Goillot, "Airborne thermography or infrared remote sensing," Bibl.Radiol. 6 (6), 237-248 (1975).

- 12 Tahir Husain and Suhail M. Khan, "Impact assessment and forecasting of soot from Kuwaiti oil fires using a modeling approach," *Atmos. Environ.* 28 (13), 2175-2196 (1994).
- 13 Jeffery T. McQueen and Roland R. Draxler, "Evaluation of model back trajectories of the Kuwait oil fires smoke plume using digital satellite data," *Atmos. Environ.* 28 (13), 2159-2174 (1994).
- 14 Department of the Air Force. "Defense Support Program Satellites," <http://www.af.mil/factsheets/factsheet.asp?fsID=96>. 22 October 2004 (unpublished).
- 15 Department of the Air Force. *Defense Support Program*. DTIC PE Number 0305911F. February 2000.
- 16 P. G. Sanderson, "The application of satellite remote sensing to coastal management in Singapore," *Ambio* 30 (1), 43-48 (2001).
- 17 X. Zhang *et al.*, "Optical influence of ship wakes," *Appl. Opt.* 43 (15), 3122-3132 (2004).
- 18 A. Goldberg, "Infrared signatures of the muzzle flash of a 120 mm tank gun and their implications for Kinetic Energy Active Protection System (KEAPS)," ARL-TR-909. (Army Research Laboratory, October 2001).
- 19 A. Fontijn, "Kinetics of Propellant Combustion and Muzzle Flash Reactions," ADA146109 (DTIC, 28 Nov 1990).
- 20 Military.com. "BRINGING DOWN THE HOUSE: Military Demolitions and Explosives," http://www.military.com/soldiertech/0,14632,Soldiertech_Explosives,,00.html. 22 October 2004 (unpublished)
- 21 W.C. Moss, "A method to estimate the yield of an underground nuclear explosion," *J. App. Phys.* 63 (9), 4771-4773 (1988).
- 22 H.A. Bethe, "The fireball in air," *J. Quantitative Spectroscopy and Radiative Transfer* 5 (1), 9-12 (1965).
- 23 L. E. Fried, W. M. Howard, P. C. Souers, and P.A. Vitello. computer code CHEETAH 3.0 (cheetah@llnl.gov, Energetic Materials Center, Lawrence Livermore National Laboratory, Livermore, CA 94551)

- 24 R.E. Setchell, "Optical studies of chemical energy release during shock initiation of granular explosives", Dynamics of Explosions, Progress in Astronautics and Aeronautics, J.R. Bowen, J.-C. Leyer, I.R. Soloukhin (Eds.), 106, pp. 607-628 (Chapter 7), AIAA, Washington, DC, 1986.
- 25 W.G. Von Holle, C.M. Traver, "Temperature measurements of shocked explosives by time resolved infrared radiometry—a new technique to measure shock-induced reaction", Seventh Symposium on Detonation, pp. 993-1003, Annapolis, MD, 1981.
- 26 B.W. Assay, D.J. Funk, G.W. Laabs, P.J. Howe, "Measurements of strain and temperature fields during dynamics shear of explosives, shock compression of condensed matter", American Physical Society Topical Conference, AIP Press, Melville, NY, 1995.
- 27 G. Klingenberg, J.M. Heimerl, "Gun Muzzle Blast and Flash", Progress in Astronautics and Aeronautics, A. Richard Seebass (EIC), 139, pp. 3-14 (Chapter 1), AIAA, Washington, DC, 1992.
- 28 J.A Orson, "Collection of detonation signatures and characterization of spectral signatures." MS thesis, AFIT/GSO/ENP/00M-01. Graduate School of Engineering and Management, Air Force Institute of Technology (AU), Wright-Patterson AFB OH, March 2000 (ADA381528)
- 29 J. A Orson, W. F. Bagby, and G. P. Perram, "Infrared signatures from bomb detonations," Infrared Physics & Technology 44: 101-107 (2003).
- 30 W. F. Bagby, "Spectral and Temporal Characterization of High-Temperature Events." MS thesis, AFIT/GAP/ENP/01M-01, Graduate School of Engineering and Management, Air Force Institute of Technology (AU), Wright-Patterson AFB OH, March 2001 (ADA392540)
- 31 A. N. Dills, K. C. Gross, and G. P. Perram. "Detonation discrimination techniques using a Fourier Transform Infrared Spectrometer system and a Near-Infrared Focal Plane Array," Targets And Backgrounds IX: Characterization And Representation, SPIE's AeroSense, 2003.
- 32 P. W. Cooper, Explosives Engineering. (New York City NY: Wiley-VCH, 1996).

- 33 G. Klingenberg, J.M. Heimerl. "Gun Muzzle Blast and Flash", Progress in Astronautics and Aeronautics, A. Richard Seebass (EIC), 139, pp. 3-14 (Chapter 1), AIAA, Washington, DC, 1992.
- 34 Ya. B. Zel'dovich and Yu. P. Raizer. Physics of Shock Waves and High-Temperature Hydrodynamic Phenomena. (New York City NY: Academic Press, 1967).
- 35 "Search for Species Data by Chemical Formula." An on-line searchable JANAF table. <http://webbook.nist.gov/chemistry/form-ser.html>. 18 October 2004.
- 36 Michael Hoke and Karen Doherty, "MODTRAN 4 Software," <http://www.vs.afrl.af.mil/Division/VSBYB/modtran4.html>. 31 January 2005.
- 37 Kevin C. Gross, Anthony N. Dills, and Glen P. Perram, "The dynamics and spectroscopy of fireballs arising from the detonation of conventional explosive materials," presented at the 7th Workshop on Infrared Emission Measurements by FTIR, Quebec, Canada, 2004 (unpublished).
- 38 Robert W. Boyd, Radiometry and the Detection of Optical Radiation. (New York City NY: John Wiley & Sons, Inc., 1983).
- 39 Non-Ideal Explosives Workshop. Socorro NM. May 2003 (workshop discussions).
- 40 C. L. Mader, Numerical Modeling of Explosives and Propellants, 2nd ed. (CRC Press, Boca Raton, FL, 1998), p. 70.
- 41 Alpha NIR. Product Brochure. (Goleta CA: Indigo Systems Corporation, 2002).
- 42 Digital Video Camcorder Instruction Manual. Canon XL1 A (NTSC). (Japan: Canon Inc., 1997).
- 43 C. A. Hollingsworth and G. P. Perram, "Brilliant Flash II Preliminary Test Report: AFIT Visible Spectrometer." Technical Report, Air Force Institute of Technology, Wright-Patterson AFB OH, 2003 (unpublished).
- 44 R. G. Hauser, "Survey of Military Applications for Fourier Transform Infrared (FTIR) Spectroscopy." MS thesis, AFIT/GM/ENP/99M-07. School of Engineering, Air Force Institute of Technology (AU), Wright-Patterson AFB OH, February 1999.
- 45 S. C. Miller, and W. J. Miller, Test Report. Florida: Science Applications International Corporation, August 1998.

- 46 J. Engle. NASIC/DXMJ Program Director. Technical discussions.
- 47 A. N. Dills, G. A. Zimmer, and G. P. Perram, "Preliminary Test Report from AFIT Sensors for Brilliant Flash Tests (July 2002)." Technical Report AFIT/EN-TR-03-02, Air Force Institute of Technology, Wright-Patterson AFB, OH, 2002.
- 48 Dictionary.com. <http://dictionary.reference.com/search?r=67&q=TNT>, 7 July 2004.
- 49 A. N. Dills and G. P. Perram, "Brilliant Flash II Preliminary Test Report from AFIT Sensors." Technical Report, Air Force Institute of Technology, Wright-Patterson AFB, OH, 2003 (unpublished).
- 50 NIMA Technical Report TR8350.2, "Department of Defense World Geodetic System 1984, Its Definition and Relationships With Local Geodetic Systems", 3rd ed. (4 July 1997).
- 51 Duda, Richard O., Peter E. Hart, David G. Stork. Pattern Classification, 2nd Ed., John Wiley & Sons, Inc., New York, 2001.
- 52 Bishop, Christopher M., Neural Networks for Pattern Recognition, Oxford University Press, Great Britain, 2000.
- 53 Fisher, Bob. "Fisher linear discriminant and dataset transformation." n. pag. http://homepages.inf.ed.ac.uk/rbf/CVonline/LOCAL_COPIES/FISHER/FLD/flld.html. 1 July 04.
- 54 Gross, Kevin C. "Developing a phenomenological model of fireball emissions for the purpose of explosive classification." Dissertation Prospectus. Air Force Institute of Technology.
- 55 P.H. Swain and S.M. Davis, (Eds.). Remote Sensing: The Quantitative Approach, McGraw-Hill, New York, 1978.

REPORT DOCUMENTATION PAGE				Form Approved OMB No. 074-0188	
<p>The public reporting burden for this collection of information is estimated to average 1 hour per response, including the time for reviewing instructions, searching existing data sources, gathering and maintaining the data needed, and completing and reviewing the collection of information. Send comments regarding this burden estimate or any other aspect of the collection of information, including suggestions for reducing this burden to Department of Defense, Washington Headquarters Services, Directorate for Information Operations and Reports (0704-0188), 1215 Jefferson Davis Highway, Suite 1204, Arlington, VA 22202-4302. Respondents should be aware that notwithstanding any other provision of law, no person shall be subject to an penalty for failing to comply with a collection of information if it does not display a currently valid OMB control number.</p> <p>PLEASE DO NOT RETURN YOUR FORM TO THE ABOVE ADDRESS.</p>					
1. REPORT DATE (DD-MM-YYYY) 21-03-2005		2. REPORT TYPE Doctoral Dissertation		3. DATES COVERED (From – To) Jun 2001 – March 2005	
4. TITLE AND SUBTITLE Classification Of Battlespace Detonations From Temporally Resolved Multi-Band Imagery And Mid-Infrared Spectra				5a. CONTRACT NUMBER	
				5b. GRANT NUMBER	
				5c. PROGRAM ELEMENT NUMBER	
				5d. PROJECT NUMBER	
				5e. TASK NUMBER	
6. AUTHOR(S) Dills, Anthony N., Major, USAF				5f. WORK UNIT NUMBER	
7. PERFORMING ORGANIZATION NAMES(S) AND ADDRESS(S) Air Force Institute of Technology Graduate School of Engineering and Management (AFIT/EN) 2950 Hobson Way WPAFB OH 45433-7765				8. PERFORMING ORGANIZATION REPORT NUMBER AFIT/DS/ENP/05-03	
9. SPONSORING/MONITORING AGENCY NAME(S) AND ADDRESS(ES) N/A				10. SPONSOR/MONITOR'S ACRONYM(S)	
				11. SPONSOR/MONITOR'S REPORT NUMBER(S)	
12. DISTRIBUTION/AVAILABILITY STATEMENT APPROVED FOR PUBLIC RELEASE; DISTRIBUTION UNLIMITED					
13. SUPPLEMENTARY NOTES					
14. ABSTRACT <p>The classification of battlespace detonations, specifically the determination of munitions type and size using temporal and spectral features, has been studied using near-infrared (NIR) and multi-color visible wavelength imagers. Key features from the time dependence of fireball size are identified for discriminating various types and sizes of detonation flashes. The five classes include three weights of trinitrotoluene (TNT) and two weights of an enhanced mixture, all of which are uncased and detonated with 10% C4. Using Fisher linear discriminant techniques, features are projected onto a line such that the projected points are maximally clustered for the different classes of detonations. Bayesian decision boundaries are then established on class-conditional probability densities. Feature saliency and stability are determined by selecting features that best discriminate while requiring low variations in class-conditional probability densities and high performance in independent testing. The most important and stable feature is the time to the maximum fireball area in the near-infrared wavelength band. Overall, the features related to the time to peak (t_{mp}) of the fireball provide the best classification for each of three a priori conditions. This feature correctly discriminates between TNT and ENE about 90% of the time, whether weight is known or not. The associated class-conditional probability densities separate the two classes with a Fisher ratio of 2.9 ± 0.3 and an area under the receiver operating characteristic, A_{ROC}, of 0.992. Also, t_{mp} achieves approximately 60% success rate at discerning both weight and type.</p>					
15. SUBJECT TERMS Bomb detonation, explosions, near-infrared and color imagery, fireball size, Fisher linear discriminant.					
16. SECURITY CLASSIFICATION OF:			17. LIMITATION OF ABSTRACT	18. NUMBER OF PAGES	19a. NAME OF RESPONSIBLE PERSON
REPORT U	ABSTRACT U	c. THIS PAGE U			Glen P. Perram, Dr. (ENP)
			UU	280	19b. TELEPHONE NUMBER (Include area code) (937) 255-3636, ext 4504; e-mail: glen.perram@afit.edu

Standard Form 298 (Rev. 8-98)

Prescribed by ANSI Std. Z39-18